PhD thesis

COMPUTER SIMULATIONS OF THE GAY-BERNE LIQUID
CRYSTAL MODEL AND OF PHYSICAL AGING
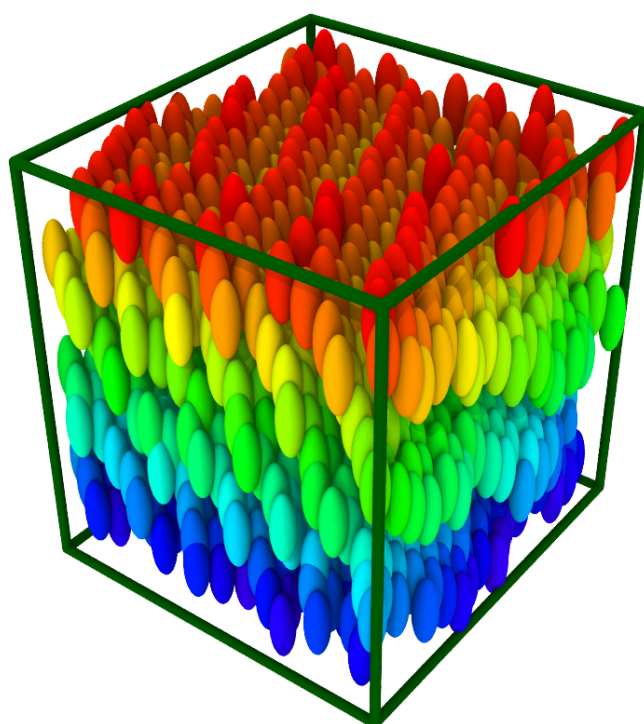
Saeed Mehri, *October 5, 2023*
supervisor: Trond S. Ingebrigtsen
co-supervisor: Jeppe C. Dyre

Glass and Time, IMFUFA
Department of Science and Environment,
Roskilde University, Denmark

Abstract

This thesis consists of two independent parts. In the first part, our primary focus is to investigate the existence of isomorphs in the Gay-Berne (GB) model's phase diagram. In the second part, we studied the validity of single-parameter aging through computer simulations.

Isomorph theory has been studied in the Glass and Time group at Roskilde University for the last decade. Roskilde simple systems, have invariant curves of structure and dynamics in their phase diagrams. These curves are called isomorphs.
In this thesis, we investigate the existence of isomorphs in the phase diagram of GB models. The GB model is a standard and popular model for studying liquid crystals' phase behavior through computer simulations. We first investigated the GB model with parametrization leading to discotic liquid crystals at low temperatures. In the isotropic phase and at high temperatures, we found a strong virial potential energy correlation which is the criterion for the existence of isomorphs. We studied one isomorph and showed that the reduced structure and dynamics are invariant along the isomorph. Afterward, we described the isomorph by the constant density scaling exponent equal to 11.5. This value is significantly larger than the density scaling exponent of various Lennard-Jones models that are often below 6.
In the next step, we studied the GB model with a choice of parameters corresponding to calamitic (rod-shaped) molecules. We focused on the isotropic, nematic, and smectic phases. We found strong correlations between virial and potential energy in the isotropic (close to nematic), nematic, and smectic phases. We investigate the level of invariance in dynamics by plotting the data for the reduced auto-correlation functions of mean-square displacement, velocity, angular velocity, etc. We demonstrate the invariance from the radial distribution function and second-ranked orientational pair-correlation function for the structure. It is worth mentioning that the investigation of the smectic phase is still ongoing and is not finished yet.

In the second part, we studied physical aging through computer simulations. Here we used standard Lennard-Jones to simulate the interactions between particles. We monitored the time evolution of the following quantities: potential energy, virial, averaged squared force, and the Laplacian of the potential energy. Although we studied significantly larger jumps compared to the experimental studies, our results confirm the single-parameter aging scenario to a good approximation. Finally, we demonstrate by computer simulations that physical aging can be predicted from thermal equilibrium fluctuations.

Resumé

Denne afhandling består af to uafhængige dele. I den første del er vores primære fokus at undersøge eksistensen af isomorfer i Gay-Berne (GB) modellens fasediagram. I den anden del har vi studeret validiteten af enkeltparameter aging ved hjælp af computersimuleringer.

Isomorfteori har været studeret i Glas og Tid gruppen på Roskilde Universitet i de sidste omkring 10 år. Roskilde simple systemer har invariante kurver af struktur og dynamik i deres fasediagram. Disse kurver kaldes isomorfer.

I denne afhandling undersøger vi eksistensen af isomorfer i fasediagrammet af GB modeller. GB modellen er en populær standardmodel til studiet af flydende krystallers fasediagram ved hjælp af computersimuleringer. Vi studerede først GB modellen ved parametrisering som førte til diskformede flydende krystaller ved lave temperaturer. I den isotropiske fase og ved høje temperaturer fandt vi en høj korrelation mellem virialet og den potentielle energi, hvilket er kriteriet for eksistensen af isomorfer. Vi studerede en isomorf og viste at den reducerede struktur og dynamikken er invatiante langs isomorfen. Dernæst beskrev vi isomorfen vha dens konstante densitetsskaleringseksponent på 11.5. Denne værdi er betydeligt højere end densitetsskaleringeksponenten af typiske Lennard-Jones modeller som oftest er under 6.

Vi studerede dernæst GB modellen med paramterværdier svarende til calamitic (stavformede) molekyler.Vi fokuserede på den isotropiske nematiske og smektiske fase. Vi fandt stærk korrelation mellem virial og potentiel energi i den isotropiske (tæt på nematisk), nematiske og smektiske fase. Vi undersøger graden af invarians i dynamikken ved at plotte data for den reducerede autokorrelationsfunktion af middelkvadratafvigelse, hastighed, vinkelhastighed, osv. Vi demonstrerer invariansen af den radiale fordelingsfunktion og andenrangs orienteringsmæssig par-korrelationsfunktion for strukturen. Det er værd at nævne, at undersøgelsen af den smektiske fase stadig er i gang og ikke er afsluttet.

I anden del studerede vi fysisk aging gennem computersimuleringer. Vi undersøgte tidsudviklingen af følgende størrelser: potentiel energi, virial, middelkvadreret kraft og Laplacian af den potentielle energi. Selvom vi studerede betydeligt større spring sammenlignet med de eksperimentelle studier, bekræftede vores resultater enkeltparameter aging scenariet med god tilnærmelse. Slutteligt demonstrerer vi gennem computersimuleringer at fysisk aging kan forudsiges ved hjælp af termiske ligevægtsfluktuationer.

Preface

This doctoral thesis describes some of the work done during the Danish PhD program, between Feb 1st 2019 and June 15th 2022. The work has been supervised by Trond S. Ingebrigtsen and Jeppe C. Dyre and was done in the *Glass and Time* group at Roskilde University.

Papers

The doctoral thesis has five companion papers which can be found in appendix E. The first four papers have been already published but the last one was accepted and in the process of being published at the same time of this doctoral thesis submission.

Paper I *Single-parameter aging in a binary Lennard-Jones system*
S. Mehri, T. S. Ingebrigtsen, and J. C. Dyre
Journal of Chemical Physics, **154**, 094504, 2021. Online

Paper II *Predicting nonlinear physical aging of glasses from equilibrium relaxation via the material time*
B. Riechers, L. A. Roed, S. Mehri, T. S. Ingebrigtsen, T. Hecksher, J. C. Dyre, K. Nissn
Science Advances, **8**, 9809, 2022. Online

Paper III *Lines of invariant physics in the isotropic phase of the discotic Gay-Berne model*
S. Mehri, M. A. Kolmangadi, J. C. Dyre, T. S. Ingebrigtsen
Journal of Non-Crystalline Solids: X, **14**, 100085, 2022. Online

Paper IV *Hidden scale invariance in the Gay-Berne model*
S. Mehri, J. C. Dyre, T. S. Ingebrigtsen
Physical Review E, **105**, 064703, 2022. Online

Paper V *Single-parameter aging in the weakly nonlinear limit*
S. Mehri, L. Costigliola, J. C. Dyre
Thermo, **160**, 2(3), 2022 Online

Paper VI *Hidden scale invariance in the Gay-Berne model. II. Smectic-B phase*
Saeed Mehri , Jeppe C. Dyre , and Trond S. Ingebrigtsen

Acknowledgements

My deep gratitude first goes to Trond, who has always been patient and kind to guide me expertly through my PhD study. His enthusiasm in research helped me constantly encouraged to push the project forward, and his personal generosity made my time at university enjoyable.

My heartfelt thanks go to Jeppe, who gave me a fantastic opportunity to be a member of the Glass and Time group. I had an amazing time with wonderful people at Roskilde University during these years.

My appreciates also extend to my colleagues in the Glass and Time group. Thanks also to the members of the simulation group who helped me in different aspects of my work: Nick, Ulf, Jesper, Heine, Søren, Shibu, Ian, Peter, Solvej, Emy. My special thanks go to Lorenzo, an excellent officemate, colleague, mentor, and friend. He always answered my question patiently, and I learned a lot from him.

I am grateful to have a wonderful family whose supports and encouragements help me to overcome challenges in my life, which would be impossible without them. Finally, I would like to express my deepest appreciations and thanks from the bottom of my heart to my girlfriend, Samaneh. Words can not express how grateful I am to have her who blessed me with a life of joy and happiness during these years.

In the end, I want to thank my friends Sam, Armin, Farhad, Kian, Niloofar, Shahrzad, Soheyla, and Zohreh for always staying true and supporting me all the time.

Contents

Chapter 1

Introduction

This thesis investigates two separate topics. In the first part, we study isomorph theory and liquid crystals, and in the second part, our primary focus is on physical aging. This chapter aims to provide a good storyline for the thesis and a brief introduction to the field of study and how the thesis contributes to it.

1.1 States of Matter

High school teaches that there are three classical states of matter: solid, liquid, and gas. One can distinguish these three states by looking at the properties of matter. All matter are made up of atoms and molecules regardless of what state the matter is in. Each constituent atom has a specific kinetic energy that allows the atom to move around [1].

In a solid state, the atoms are tightly bonded to form a single unit that often does not change shape. By heating up, the solid atoms can get more energy to move, which could weaken the bonds between atoms and gradually changes the solid into a liquid.

Compared to the solid state, atoms in a liquid are loosely bonded; this is a flexible bond that allows the atoms to move around. This explains why a liquid can change shape. Heating a liquid could give the atoms enough energy to break this bond and become a gas.

In a gas, there are no bonds between atoms. A gas can change shape and volume depending on the situation. All these explained processes are reversible, so one can change a gas to a liquid and a liquid to a solid. A good everyday example of changing state would be water. Below $0°C$, water freezes and becomes a solid, and heating it up to $100°C$ will change it

to a gas.

1.2 Phase diagram and phase transition

Generally, a phase diagram is a tool to show conditions at which thermodynamically distinct phases (states) occur and coexist at equilibrium. A phase contains lines of phase boundaries. Along these lines, multiple phases can coexist at equilibrium. Only one phase (solid, liquid, gas, etc.) can exist at any region separated by these lines. Phase diagrams are specific for each material and mixture.

Fig. 1.1 is the pressure-temperature phase diagram of water.
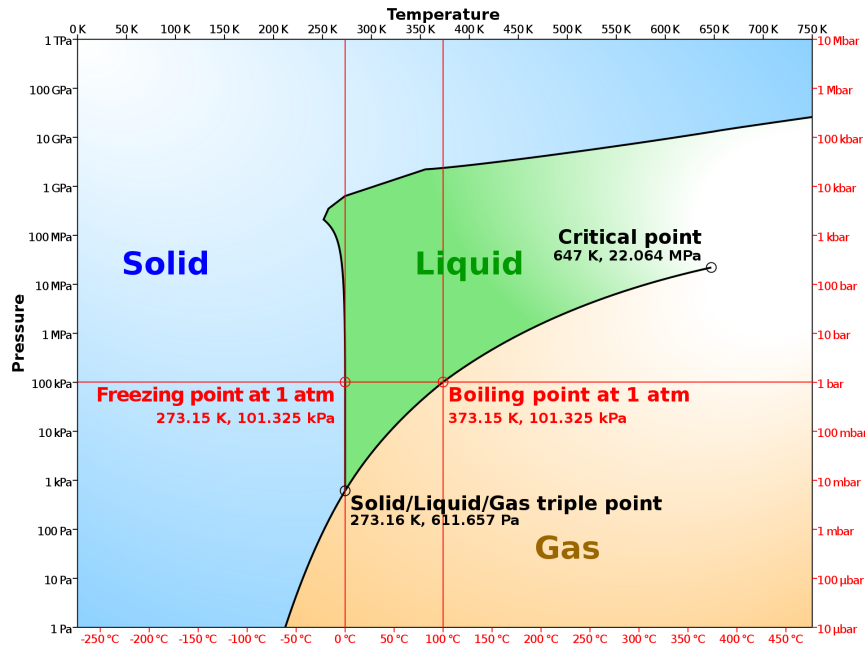
Figure 1.1: Simplified phase diagram of water taken from [2]
.

1.3 Liquid crystals

Going beyond typical high school teaching, there are also intermediate states of matter between solid and liquid, like plastic crystal, liquid crystal (LC), etc [3]. A plastic crystal is a crystal whose constituent atoms or molecules are weakly interacting and possess some orientational degrees of freedom. The name plastic here refers to mechanical softness. Liquid crystals are a class of materials that exhibit unique physical properties, including anisotropic

optical, electrical, and mechanical properties, that make them attractive for a wide range of applications in electronics, display technologies, and sensors [4–6]. However, the study and simulation of the phase diagram of liquid crystals are complicated by a number of factors, including the complexity of their molecular structure, the anisotropic nature of their intermolecular interactions, and the presence of multiple phases and phase transitions [7].

One of the key challenges in studying the phase diagram of liquid crystals is the complexity of their molecular structure. Liquid crystals are typically composed of elongated or disc-shaped molecules that exhibit anisotropic shapes and orientations. These molecules can form a variety of different phases, depending on the temperature, pressure, and other external factors. The phase behavior of liquid crystals is determined by the intermolecular interactions between the molecules, which can be highly anisotropic and dependent on the relative orientations of the molecules.

Another challenge in studying the phase diagram of liquid crystals is the presence of multiple phases and phase transitions. Liquid crystals can exhibit a wide range of different phases, including nematic, smectic, chiral, and columnar phases, each of which has its own unique physical properties [6]. In addition, liquid crystals can undergo a variety of phase transitions, including melting, solidification, and mesophase transitions, which can complicate the analysis of their phase behavior.

1.4 Density scaling and isomorph theory

Generally, a phase diagram is two-dimensional (pressure-temperature or density/volume temperature) and could be complicated depending on the system under study. Density scaling is a powerful approach in physics that can help to simplify the study and simulation of the phase diagram of liquid crystals. The density scaling approach is based on the observation that the dynamics of a system are invariant under rescaling of the interparticle separation, which is a fundamental length scale that governs the interactions between the molecules in the liquid crystal.

By rescaling the interparticle separation in a liquid crystal using a scaling parameter that is proportional to the density, the dependence of the phase behavior on the density can be eliminated, allowing for a more accurate and efficient description of the system. Simply saying, plotting data (for the dynamics) as a function of a single thermodynamic parameter, ρ^γ/T, results in a collapse, where γ is the density scaling exponent and, in most cases, determined by fitting [8–11]. In particular, the density scaling approach can be used to describe the thermodynamic properties of a wide range of liquid crystals, including those with different intermolecular potentials and different molecular structures.

The density scaling approach can also be used to study the behavior of liquid crystals near critical points, where the thermodynamic properties exhibit universal behavior that is independent of the specific details of the system. In this way, the density scaling approach can provide insights into the underlying physics of liquid crystals and help to guide the design of new materials with tailored properties [12, 13].

The glass and time research group at Roskilde University introduced a new framework called isomorph theory, inspired by density scaling, to study material phase behavior more easily [14]. Isomorphs are lines in phase diagrams where dynamics and structures remain constant. Along an isomorph, no phase transitions occur, making the phase diagrams simpler and one-dimensional. This study focuses on finding isomorphs in the phase diagram of liquid crystals through computer simulations. Finding isomorphs in the phase diagram of an LC would help us to overcome the challenges of studying the LC's phase diagram mentioned earlier. Chapter 2 explains what isomorphs are and how to identify them in a phase diagram. Chapter 4 details the models and techniques used for the simulations. Chapter 5 presents all the results from the computer simulations, and the final chapter 7 provides a brief conclusion.

1.5   Physical aging

As mentioned earlier, this thesis spans two different research topics. In the second part, which is a smaller project, we study physical aging through computer simulation.

In physics, physical aging is a phenomenon observed in certain materials, particularly glasses and polymers, which experience changes in their properties over time, even at a constant temperature [15–17]. This aging process occurs without any external stresses or changes in the material's environment and has been extensively studied in condensed matter physics and materials science.

Physical aging is primarily observed in amorphous materials. When these materials are rapidly cooled from a high-temperature liquid state to a solid state, they retain some of the disordered structure and dynamic properties of the liquid phase. As a result, they exhibit characteristics of both a solid and a liquid.

The aging process arises from the slow relaxation of amorphous materials, which become kinetically trapped in metastable configurations. These trapped states are not in their equilibrium positions, and the material may not fully relax to its stable ground state over time. The relaxation process occurs very slowly, leading to the time-dependent changes observed in the material's properties.

Physical aging is a manifestation of the non-equilibrium nature of amorphous materials. These materials exist in a metastable state, far from their equilibrium configuration, and the aging process is a consequence of their slow approach toward equilibrium.

The kinetics of physical aging depend on various factors, such as the material's composition, structure, and the temperature at which aging occurs. Higher temperatures accelerate the relaxation process, causing faster changes in material properties, while lower temperatures slow down the aging process.

Rejuvenation and overaging are interesting phenomena related to physical aging [18]. Rejuvenation occurs when a material is subjected to elevated temperatures, temporarily erasing the aging effects. However, when the material is cooled back to a lower temperature, the aging process resumes. Overaging, on the other hand, is observed when materials age for an extended period, leading to a more pronounced change in properties than predicted by traditional models.

The concept of material time is a fundamental aspect of physical aging in amorphous materials. It refers to the idea that the relaxation or aging of a material depends not only on the actual time that has passed but also on the material's thermal history, i.e., the temperature and time-temperature history it has experienced since its formation or processing [17, 19–21].

In amorphous materials, when they are rapidly cooled from a high-temperature liquid state to a solid state, they may retain some of the disordered structures and dynamic properties of the liquid phase. These materials are in a metastable state, far from their equilibrium configuration. As a result, the molecules or atoms are kinetically trapped in these metastable configurations.

Over time, these trapped states slowly relax towards their equilibrium configurations, a process known as physical aging. The relaxation of the material depends on how long it has been at its aging temperature (actual time) but is also significantly influenced by the temperature at which aging occurs (thermal history).

To illustrate the concept of material time, consider two samples of the same amorphous material that have been cooled to the same aging temperature but at different rates. Sample A is cooled slowly, allowing enough time for the molecules to find more stable configurations. Sample B is cooled rapidly, trapping the molecules in less stable configurations.

Even though both samples are at the same aging temperature, Sample A, which experienced slower cooling, will have aged more than Sample B, which experienced rapid cooling. This is because Sample A has had higher "material time" at the aging temperature to relax towards its equilibrium configuration.

In practical terms, the concept of material time means that the aging pro-

cess of an amorphous material can be accelerated or decelerated by changing the temperature at which it is aged. Higher temperatures accelerate aging because more molecular rearrangements occur in a shorter time, while lower temperatures slow down the aging process.

The so-called TN formalism is the standard framework for studying aging. Material time is an essential concept for TN formalism. One can say material time is similar to the proper time concept in the theory of relativity. During an aging process, the clock rate (clock rate is a measure of how fast the material time varies over time) also ages, leading to nonlinearity in temperature variation. An important assumption in TN formalism is both the measured quantity and the clock rate are controlled by a single parameter. If single-parameter aging is obeyed, one can predict the relaxation function of one jump in temperature ($T_{start} \to T_{end}$) by knowing the relaxation function of another jump [22, 23].

The primary goal is to validate the single-parameter formalism by simulation. Despite the fact that we studied significantly larger temperature jumps compared to those of simulation studies, our results conform to the single-parameter aging scenario. Chapter 6 first provides a more detailed introduction to physical aging, TN formalism, and single-parameter aging, then presents all the computer simulation results.

In Chapter 7, the thesis provides a brief review of the conclusions of the two topics (isomorphs in LCs, single-parameter aging). Appendix A provides a detailed definition of force and torque calculation of the liquid crystal model under study. Appendix B contains all the consistency checks we made with the literature to ensure our package works appropriately. Appendix C presents the results of extra ismorphs we found in isotropic and nematic phases of both disc-shaped and rod-shaped molecules. Appendix D shows the results of the two isomorphs we found in the smectic phase of rod-shaped molecules, and finally, we gathered all 6 resulting papers of this Ph.D. studies in Appendix E.

Chapter 2

Isomorph Theory

This chapter provides a definition of Roskilde simple systems and a general overview of the isomorph theory. Isomorph theory has been developed in a series of publications from the Glass and time group at Roskilde University (Bailey *et al*. [14, 24], Gnan *et al*. [25], Ingebrigtsen *et al*. [26], Schrøder *et al*. [27, 28], Pedersen *et al*. [29], and Dyre *et al*. [30, 31]).

2.1 Roskilde Simple Liquid

Traditionally, a simple liquid is defined as a many-body system with isotropic pair-interaction. Here "simple" refers to mathematical simplicity rather than to the system's behavior. In 2012, Ingebrigtsen *et al*. established a new definition for simple liquids [26]. In this new definition, simple liquids are identified by strong virial potential energy correlations in the NVT ensemble, i.e., constant number of particles N, volume V, and temperature T. Virial is the configurational contribution to pressure, i.e., $pV = Nk_BT + W$ and is defined by [7]

$$W = -\frac{1}{3}\sum_i \mathbf{r}_i \cdot \nabla_{\mathbf{r}_i}U, \qquad (2.1)$$

where $\mathbf{r}_i$ is the position of ith particle and U is the potential energy. The simplicity in this new definition refers to the system's behavior. To avoid confusion with strongly correlated systems in quantum physics, these systems are referred to as Roskilde simple systems (R-simple systems). [32–34]. Isomorph theory has been developed over the last decade [14, 24, 25, 27, 29, 35–40]. The theory was built based on the strong correlation between the configurational part of the pressure, namely virial, W, and potential energy, U, equilibrium fluctuations in a canonical ensemble of liquids, solids, and
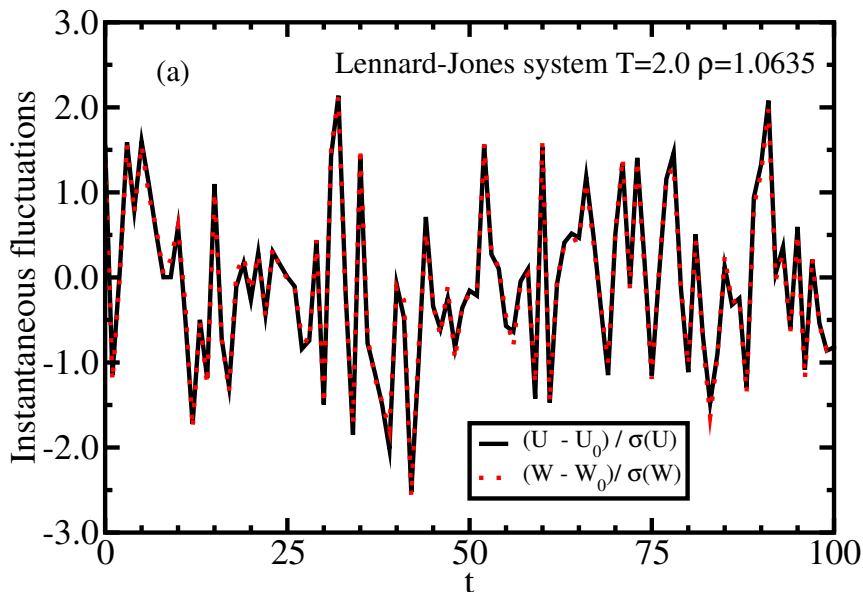
Figure 2.1: Correlation between potential energy and virial of a Lennard-Jones system at $(\rho, T) = (1.0635, 2.0)$. Instantaneous deviations from the mean equilibrium value of the potential energy and virial per particle normalized by their standard deviations. The collapse indicate strong crrolation between U and W. Taken from Ref. [42].

gases [25, 37, 41].

Fig. 2.1 shows how W and U equilibrium fluctuations are strongly correlated for a Lennard-Jones system. This strong correlation leads to identifying the so-called isomorphs in R-simple systems [25].

One can evaluate the degree of correlation of the system under study by calculating the standard Pearson correlation coefficient,

$$R(\rho, T) = \frac{\langle \Delta W \Delta U \rangle}{\sqrt{\langle (\Delta W)^2 \rangle \langle (\Delta U)^2 \rangle}}, \tag{2.2}$$

where angular brackets $\langle \rangle$ denote NVT ensemble average, Δ denotes deviation from equilibrium mean value, ρ and T are density and temperature respectively. A system is R-simple when $R > 0.9$. It has been shown that isomorphs can exist in systems with $R < 0.9$ [36, 41]. Since R has state point dependency, strong correlations only appear in some region of the phase diagram and usually R decreases by getting closer to the critical point [43]. For R-simple systems one can write

$$\Delta U \cong \gamma \Delta W, \tag{2.3}$$
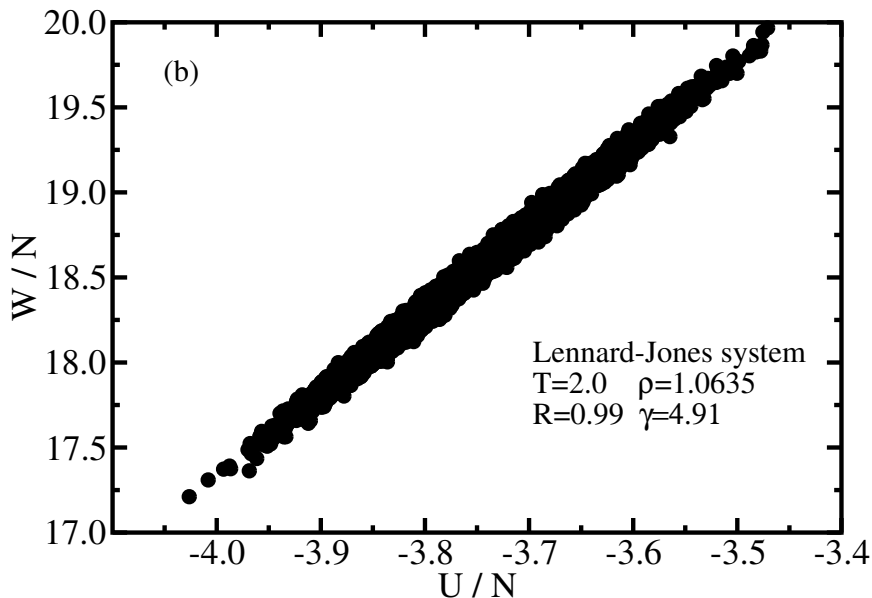
Figure 2.2: Scatter plot $W - U$ correlation for a Lennard-Jones system at $(\rho, T) = (1.0635, 2.0)$. The system is R-simple with $R = 0.99$ and $\gamma = 4.91$. Taken from Ref. [42].

where γ is a state point dependent quantity. γ is the slope of $W - U$ correlation (see Fig. 2.2) and can be evaluated by linear regression [44–46],

$$\gamma(\rho, T) = \frac{\langle \Delta W \Delta U \rangle}{\langle (\Delta U)^2 \rangle}. \tag{2.4}$$

2.2 Isomorph Theory

Consider a system of N particles; the microconfiguration $\mathbf{R}$ denotes the coordinate vectors of all particles, i.e., $\mathbf{R} \equiv (\mathbf{r}_1 \ldots \mathbf{r}_N)$. For any microconfiguration with density ρ, the reduced coordinates are defined by $\tilde{\mathbf{R}} \equiv \rho^{1/3} \mathbf{R}$. The original definition of isomorph theory states that, for a R-simple system if two state points (ρ_1, T_1) and (ρ_2, T_2) have the same reduced coordinates $\tilde{\mathbf{R}} = \rho_1^{1/3} \mathbf{R}_1 = \rho_2^{1/3} \mathbf{R}_2$, their canonical Boltzmann factors are proportional,

$$\exp\left[-U(\mathbf{R}_2)/k_B T_2\right] \cong C \exp\left[-U(\mathbf{R}_1)/k_B T_1\right], \tag{2.5}$$

where C is a constant and k_B is the Boltzmann constant. An IPL (inverse power-law) system with $U(r) \propto r^{-n}$, where r denotes pair distance, obeys Eq. 2.5 with $C = 1$. For other R-simple systems it has been shown that Eq. 2.5 is a good approxiamtion [25].

In 2014, Schrøder and Dyre reformulated isomorph theory in a more general way by referring to the potential function of R-simple systems [28]. For a R-simple system, consider two configurations with potential energies $U(\mathbf{R}_1)$ and $U(\mathbf{R}_2)$. If $U(\mathbf{R}_1) < U(\mathbf{R}_2)$, the ordering of potential energies remains intact through a uniform scaling,

$$U(\mathbf{R}_1) < U(\mathbf{R}_2) \Leftrightarrow U(\lambda\mathbf{R}_1) < U(\lambda\mathbf{R}_2), \tag{2.6}$$

where λ is the scaling factor.

The entropy of any system can be written as the sum of the entropy of ideal gas, S_{id}, at the same density and temperature and an additional term, S_{ex}, associated with the interaction between particles. For an ideal gas $S_{ex} = 0$, and any other systems $S_{ex} < 0$. By considering microconfigurations at the same ρ with the same $U(\mathbf{R})$, one can write

$$S_{ex}(\mathbf{R}) \equiv S_{ex}(\rho, U(\mathbf{R})). \tag{2.7}$$

Now $U(\mathbf{R})$ can be expressed as a function of ρ and S_{ex}

$$U(\mathbf{R}) = U(\rho, S_{ex}(\mathbf{R})). \tag{2.8}$$

Eq. 2.8 is valid for any system, but in the case of R-simple systems it is of particular interest as it used to find curves of invariant structure and dynamics. It has already been shown that for R-simple systems, if two microconfigurations obey Eq. 2.6 they have the same excess entropy, i.e., $S_{ex}(\mathbf{R}_1) = S_{ex}(\mathbf{R}_2)$ [28]. The invariance of excess entropy under uniform scaling implies that S_{ex} for R-simple system only depends on reduced configuration,

$$S_{ex}(\mathbf{R}) = S_{ex}(\tilde{\mathbf{R}}), \tag{2.9}$$

and we can rewrite Eq. 2.8 as

$$U(\mathbf{R}) = U(\rho, S_{ex}(\tilde{\mathbf{R}})). \tag{2.10}$$

Eq. 2.10 establishes the connection between the microconfiguration potential energy and equilibrium averaged potential energy, and it can be use to show the invariance of structure and dynamics in the isomorph theory.

It is important to note that isomorph invariance only occurs in reduced units. In such units, the length l_0 unit is defined by the density $\rho \equiv N/V$, the energy unit e_0 is defined by the temperature, and the time unit t_0 is defined by the density and thermal velocity;

$$l_0 = \rho^{-1/3} \quad, e_0 = k_B T \quad, t_0 = \rho^{-1/3}\sqrt{m/k_B T}.$$

To show the invariance of structure and dynamics along an isomorph, we just need to show that Newton's second law of motion is invariant, in reduced units, along an isomorph. The reduced Newton's second law is

$$\frac{d^2\tilde{\mathbf{R}}}{d\tilde{t}^2} = \tilde{\mathbf{F}}(\mathbf{R}) \equiv \frac{\mathbf{F}(\mathbf{R})\rho^{-\frac{1}{3}}}{k_B T}, \tag{2.11}$$

the vector force, $\mathbf{F}$, contain the force of all particles and can be obtained by $\mathbf{F} = -\nabla U$. For R-simple systems from Eq. 2.10 that U is function of reduced coordinates $\tilde{\mathbf{R}}$. So we can write

$$\mathbf{F} = -\nabla U(\rho, \tilde{\mathbf{R}}) = -\left.\frac{\partial U(\rho, S_{ex})}{\partial S_{ex}}\right|_\rho \nabla S_{ex}(\tilde{\mathbf{R}}), \tag{2.12}$$

by substituting $\nabla = \rho^{1/3}\tilde{\nabla}$ and $\left.\partial U/\partial S_{ex}\right|_\rho = T$, we have

$$\mathbf{F} = -\rho^{\frac{1}{3}}T\tilde{\nabla}S_{ex}(\tilde{\mathbf{R}}). \tag{2.13}$$

Now the reduced force is a function of reduced coordinates, $\tilde{\mathbf{R}}$, and consequently is invariant along an isomorph. This means that structure and dynamics are invariant along an isomorph in reduced units [28].

2.3 Generating Isomorphs

There are different ways to generate isomorphs. The one that we used here in this study is based on invariant excess entropy curves, i.e., configurational adiabats.

Along a configurational adiabat $dS_{ex} = 0$, one can write

$$dS_{ex} = \left(\frac{\partial S_{ex}}{\partial T}\right)_V dT + \left(\frac{\partial S_{ex}}{\partial V}\right)_T dV = 0. \tag{2.14}$$

From Maxwell volume-temperature relation we know,

$$\left(\frac{\partial S_{ex}}{\partial V}\right)_T = \left(\frac{\partial (W/V)}{\partial T}\right)_V,$$

so we rewrite Eq. 2.14 as

$$\left(\frac{\partial S_{ex}}{\partial T}\right)_V T\, d\ln T = \left(\frac{\partial W}{\partial T}\right)_V d\ln \rho. \tag{2.15}$$

Considering $dU = T\, dS_{ex} - (W/V)dV$ we have,

$$\left(\frac{\partial U}{\partial T}\right)_V d\ln T = \left(\frac{\partial W}{\partial T}\right)_V d\ln \rho, \tag{2.16}$$

using fluctuation relation $\left(\frac{\partial W}{\partial T}\right)_V = -\langle \Delta W\, \Delta U \rangle$ and $\left(\frac{\partial U}{\partial T}\right)_V = -\langle (\Delta U)^2 \rangle$ [25], and Eq. 2.14 for γ lead to

$$\gamma = \left(\frac{\partial \ln T}{\partial \ln \rho}\right)_{S_{ex}} = \frac{\langle \Delta W\, \Delta U \rangle}{\langle (\Delta U)^2 \rangle}. \tag{2.17}$$

Eq. 2.17 is general and used to identify configurational adiabats in the phase diagram of any system [25]. If a system has isomorphs, Eq. 2.17 can be use to trace out isomorphs without knowing the equation of state. For a given state point, (ρ_1, T_1), one can calculate γ using Eq. 2.4. Afterward, by scaling the system to a slightly different density, ρ_2, and numerically solving $\gamma = \left(\frac{\partial \ln T}{\partial \ln \rho}\right)_{S_{ex}}$ from Eq. 2.17, one can evaluate T_2 for which (ρ_1, T_1) and (ρ_2, T_2) are on the same isomorph. In this work we use fourth-order Runge-Kutta integration [47] to generate isomorphs with a density step of approximately 1%.

Chapter 3

Introduction to Liquid Crystals

This chapter provides a general overview of what a liquid crystal is. There are two main types of liquid crystals; *thermotropic* and *lyotropic*. This chapter is mainly about the *thermotropic* liquid crystals, its applications, and different phases formed by them where the constituent molecules are rod-shaped or disk-shaped.

3.1 Introduction

The liquid crystal (LC) or mesomorphic is a state of matter that has the properties between conventional liquids and solid crystals [48]. For instance, LCs can exhibit some liquid-like properties such as fluidity, inability to support shear, etc.; on the other hand, they show some crystal-like anisotropy in optical properties. The most well-known application of LCs is in the display technology.

There are two main categories of liquid crystals; "thermotropic" and "lyotropic". For the case of thermotropic, a phase transition occurs as temperature changes. By increasing temperature, the energy will increase and consequently motion of the molecules will induce a phase transition; the LC will become an isotropic liquid. Here the molecules are mainly elongated (ellipsoids, rod, etc.) or disk-shaped. Due to this shape anisotropy, molecules tend to align with each other (not everywhere in the phase diagram). Usually, they are referred to calamitic (for elongated molecules) and discotic (for disk-shaped molecules) mesogens in the literature. Lyotropic

LCs are formed by amphiphile molecules (An amphiphilic molecule refers to any compound that contains two distinct covalently bonded components) in a given solvent under specific conditions of concentration, temperature, and pressure [49, 50]. A soap and water mixture is an everyday example of lyotropic LCs.

LCs are essential materials in applications, especially in the liquid crystal displays (LCDs) technology [51, 52]. They are sensitive to the external field. One can control the orientation of molecules by applying an electric field through LCs. Since LCs do not emit light directly, as illustrated in Fig. 3.1, external light is polarized before entering the twisted-nematic film. The inner surfaces of the film is coated with conductive polymer to apply and control voltage. Due to the applied electric field, molecules are aligned from one spiral surface to the other surface. Through the twisted film, the axis of polarization rotates gradually and continuously. If the final layer of LC's orientation matches the second polariser's angle, the light can pass. We can break the twisted structure, and light can not pass by applying an external field. Although the twisted-nematic LCDs are economical, their view angles and contrast are low. They are preferred in low-cost applications such as digital clocks, energy meters, metering controls, etc. The main advantages of LCDs compare to the others displays are fast response time, high resolution, and energy efficiency.
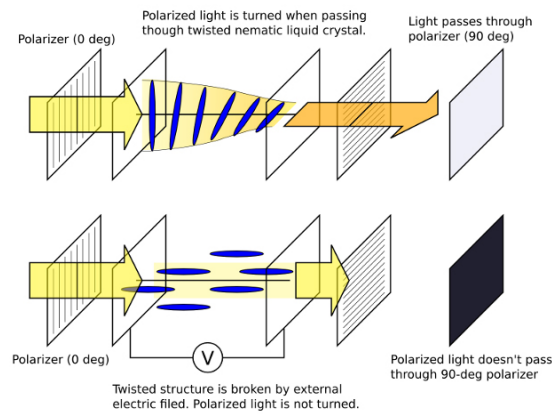
Figure 3.1: schematic working structure of a twisted-nematic liquid crystal display. As shown in the lower panel, by applying a voltage we can brake the twisted structure and block the light. Taken from Ref. [53].

3.2   Liquid Crystal Different Phases

3.2.1   Mesophases Formed by Elongated Molecules

In 1880 the first liquid crystal discovered consisted of rod-shaped molecules [54]. According to the long-range molecular arrangement, the mesophases formed by rod-shaped molecules can be classified into three groups: *nematic*, *chiral nematic*, and *smectic*. By looking at the long-range orientational order, one can easily distinguish all these mesophases from the isotropic phase. The molecules tend to align along a preferred axis called the director. The orientational order parameter, S, measures how much molecules are orientationally ordered.

For the symmetric molecules, S is defined as:

$$S = \langle (3\cos^2\beta - 1)/2 \rangle, \tag{3.1}$$

where β is the angle between the symmetric axis of a molecule and the director, $\mathbf{n}$, and angular bracket, $\langle \rangle$, denotes statistical average. The value $S = 1$ refers to a crystal phase with perfect parallel order, while $S = 0$ means a complete disorder as in the isotropic phase. Moreover, in liquid-crystalline mesophases, S takes intermediate values ($0 < S < 1$), which are strongly temperature-dependent, as they should be in thermotropic liquid crystals.

G. Friedel invented the word nematic, which has a Greek origin "$\nu\eta\mu\alpha =$ thread" and refers to thread-like defects in LCs. Fig.3.2 shows a schematic representation of molecular orientation in the nematic phase of a LC consisting of rod-shaped molecules. As it is clear, there is no long-range order in the centers of mass positions. This implies that the spatial positions of the molecules appear to be uncorrelated with respect to their center of mass, and they are similar to liquids. In fact, nematics do flow like liquid. On the other hand, there are some orientational orders in the nematic phase. The unit vectors, $\hat{\mathbf{e}}$, of molecules tend to be aligned along a preferred axis. The nematic phase occurs only with achiral molecules (achiral objects are superimposable with their mirror images).
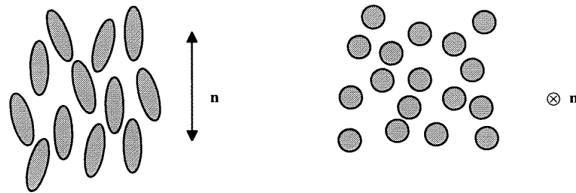
Figure 3.2: schematic orientation of particle in nematic phase from both parallel and perpendicular point of view. Taken from Ref. [55].

The nematic phase is a special case of the chiral nematic phase; a nematic

can be considered as a chiral nematic with an infinite pitch. Here, in this case, a local nematic ordering is observable at any point through the LC. By getting away from the point perpendicular to the director, the local ordering will rotate in a helix way along a preferred axis (see Fig. 3.3), and a long-range helical structure will be formed. The pitch, p, defines as the distance that the director rotates 2π.
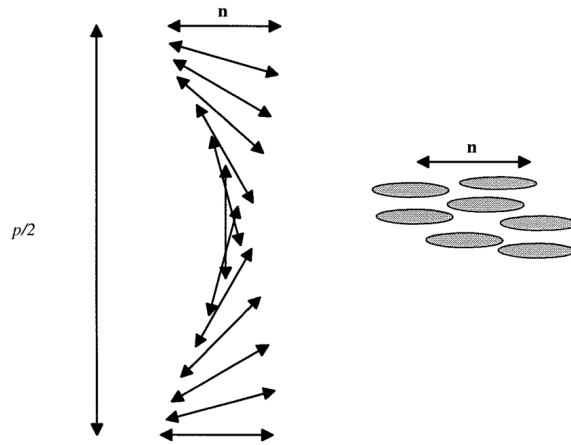
Figure 3.3: schematic of director rotation through a chiral nematic LC. Taken from Ref. [55].

Smectic, was used by Frield to refer to mesophases, from the Greek "$\sigma\nu\eta\gamma\nu\alpha$ = soap", for mesophases which have mechanical properties similar to soap. Many different smectic phases have been identified (SA, SB, SC, ...) [56], and they are classified based on the long-range ordering. All the smectic phases have layer structures with long-range orientational order. Smectic phases generally happen at lower temperatures compared to the nematic and chiral nematic because they have a higher degree of positional ordering. Among all smectics, SA is the one with a less ordered structure; there is only a short-range positional ordering within or in some cases between layers (see Fig. 3.4). Hence, each layer is a two-dimensional liquid, but still, there is a long-range orientational ordering. SB is similar to SA; the molecules here tend to form hexagonal structures within layers. SC is like SA, but the molecules are tilted. Each layer is still a two dimensional liquid.

3.2.2 Mesophases Formed by Disk-shaped Molecules

It was 1923 when Vorländer discovered that disc-shaped molecules could form mesophases [57]. Afterward, Chandrasekhar *et al*. synthesized the very first discotic liquid crystal [58]. Like rod-shaped molecules, discotic molecules align with their symmetry axes (the symmetry axis is normal to the plane of discs) parallel, and the result is the formation of three main
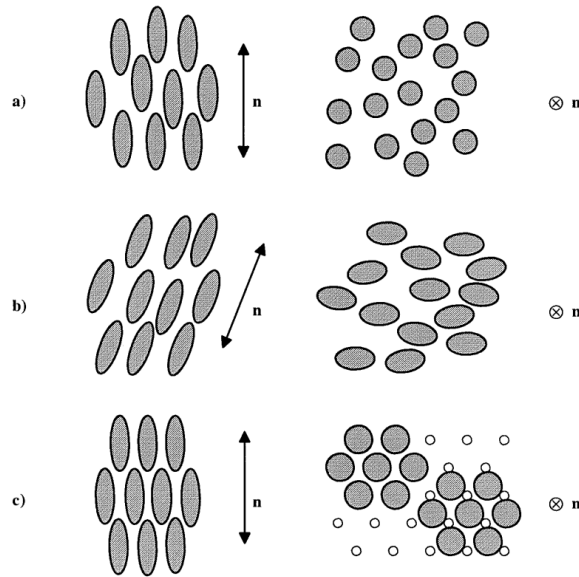
Figure 3.4: schematic of different smectics; a)S_A, b)S_C and c)S_B. Taken from Ref. [55].

phases: *discotic nematic, columnar, and discotic smectic.*
Similar to the standard nematic discussed earlier, discotic nematic is the simplest mesophase formed by disc-shaped molecules. The first example of it was discovered by Tinah *et al.* in 1979 [59]. Although there is a short-range positional correlation, the molecules are translationally disordered, yet the long-range orientational order remains intact.
The columnar phase was the first discotic phase that was discovered [58]. Here the molecules are stacked on columns. The columns have $2D$ long-range translational ordering and long-range orientational ordering. Within each column, molecules can be ordered, C_O, or disordered, C_D, which forms liquid along with the column. The molecules can also be perpendicular or tilted with respect to the column's normal. Moreover, the columns can be parallel or tilted while forming hexagonal or different types of rectangular lattices. In the discotic smectic phase, there is no translational ordering within the layers. The symmetry axis of each molecule can be perpendicular or tilted (similar to smectic C) with respect to the layer's normal [60, 61]. There is also a discotic columnar smectic phase inwhich molecules within each layer form columns (similar to smectic B) [62].

Chapter 4

Method and Models

This chapter gives a basic overview of computer simulation methods and molecular models of liquid crystals. These models divide into two main groups; *Hard Particles*, and *Soft Particles* models. Here we review some of the important and relevant studies in the literature.

4.1 Molecular Dynamics

Computer simulation is an essential and powerful tool to study and investigate liquid crystals. It has been used to study phase transitions [63], viscosities [64–66], elastic constant [67–69], etc. Molecular Dynamics is a computer simulation technique for computing a classical many-body system's equilibrium and transport properties [70].

In general, Molecular Dynamics simulations are very similar to real experiments. In an actual experiment, we prepare a sample of the desired material and connect it to a measuring device, for instance, a thermometer. We monitor the sample over time and measure the properties of interest. We do a time average over the measured properties to overcome the statistical noises. The longer the average, the more accurate the result is.

In Molecular Dynamics simulations, we follow the same procedure. First, we start with a model system consisting of N particles and solve Newton's equation of motion until we reach equilibrium. After equilibration is completed, we perform the actual measurements.

In Molecular Dynamics, we can measure any observables which can be expressed as a function of the position and momenta of particles. For average

kinetic energy per degree of freedom, we have

$$\langle \frac{1}{2}mv_i^2 \rangle = \frac{1}{2}k_B T, \qquad (4.1)$$

where m is the mass, v_i is the velocity vector of particle i, k_B is the Boltzmann constant, and T is the kinetic temperature. In simulations, we can measure the total kinetic energy of the system and divide it by the number of degrees of freedom N_f ($3N - 3$ for a system of N particles with fixed total momentum). The fluctuation of instantaneous temperature can be written as,

$$T(t) = \sum_{i=1}^{N} \frac{m_i v_i^2(t)}{k_B N_f}. \qquad (4.2)$$

Several methods can be applied to reduce the computational time of the simulations. Most molecular dynamics simulations only consider pair interaction and neglect higher orders. For a system consisting of N molecules, the potential energy can be written in terms of individual, pairs, triplets, etc. molecules,

$$U(\mathbf{r}_1, \mathbf{r}_2, \ldots, \mathbf{r}_N) = \sum_i U_1(\mathbf{r}_i) + \sum_i \sum_{j>i} U_2(\mathbf{r}_i, \mathbf{r}_j) + \\ \sum_i \sum_{j>i} \sum_{k>j>i} U_3(\mathbf{r}_i, \mathbf{r}_j, \mathbf{r}_k) + \ldots \quad (4.3)$$

where $\mathbf{r}$ is the positional vector of each particle. The first term in the equation mimics the behavior of an external field, and the rest represent the intermolecular interactions. The second term, $U_2(\mathbf{r}_i, \mathbf{r}_j)$, also known as the pair potential, is the potential interaction between all pairs of molecules and has a significant contribution to the total energy. Since the higher terms are expensive from the computational point of view, they are usually neglected. The force calculation is the most expensive process of Molecular Dynamics simulations. Since most potentials are short-range, we can truncate them at the cut-off distance r_c. Beyond r_c, the potential is set to zero. The smaller the cut-off, the smaller the number of force calculations. The proper value for r_c depends on the system under study. Potentials are often shifted vertically to make the it continuous at the cut-off,

$$U_{cut}(r) = \begin{cases} U(r) - U(r_c) & r \leq r_c, \\ 0 & r > r_c. \end{cases} \qquad (4.4)$$

Moreover, periodic boundary conditions are used for a bulk system to avoid the effects of the edges [70]. According to periodic boundary conditions, if a particle leaves the simulation box from one side, another identical particle with the exact same velocity and momentum enters the box from the other
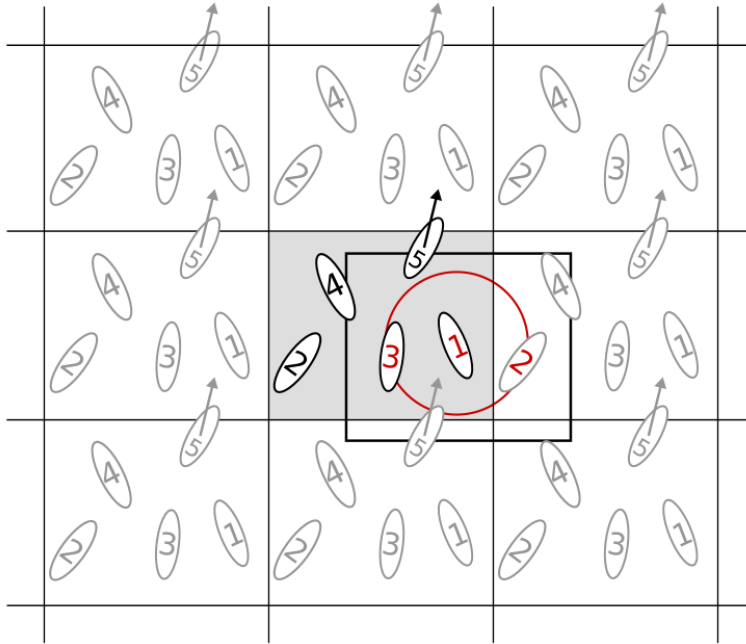
Figure 4.1: Schematic sketch of periodic boundary conditions and minimum image convention. Grey particles are the mirror images of the original particles. The original box colored to grey. Only the particles within the cut-off distance (the red radius) interact with particle 1, i.e. the mirror image of particle 2 and the particle 3 itself. Taken from Ref. [71].

side. So basically, periodic boundary conditions replicate identical simulation boxes around the original one. Fig. 4.1 shows a schematic sketch of periodic boundary conditions in two dimensions. The image particles in the replicate boxes behave the same as the original particles, and the number of particles remains unchanged within each box. The minimum image convention states that only the nearest image of a particle will contribute during the forces calculations. This is like drawing an imaginary simulation box of the same size as the original one with the particles of interest at its center. As it is evident in Fig. 4.1, particle 1 interacts with an image of particle 2, but not the particle itself.

4.2 Translational Leap-Frog

One can numerically solve Newton's equation of motion, i.e. $\mathbf{F} = m\mathbf{a}$, by discretizing the time domain. Newton's second law is expressed as two coupled first-order equations,

$$\frac{d\mathbf{v}_i}{dt} = \frac{\mathbf{f}_i}{m_i} = \mathbf{a}_i(t), \tag{4.5}$$

and

$$\frac{d\mathbf{r}_i}{dt} = \mathbf{v}_i(t). \tag{4.6}$$

Several algorithms evaluate the time evolution of the equation of motion. Here in this work, we use the Leap-Frog algorithm, which is a modification over the Verlet algorithm [72, 73]. Unlike Verlet, Leap-Frog avoids time step squared and can write position and velocity at different times. By discretizing time around t, i.e. $..., t - \Delta, t - \Delta/2, t, t + \Delta/2, t + \Delta, ...$, we can obtain the time evolution of the velocity and position of each particle

$$\mathbf{v}_i(t + \Delta t/2) = \mathbf{v}_i(t - \Delta t/2) + \Delta t \frac{\mathbf{f}_i(t)}{m_i}, \tag{4.7}$$

$$\mathbf{r}_i(t + \Delta t) = \mathbf{r}_i(t) + \Delta t \mathbf{v}_i(t + \Delta t/2). \tag{4.8}$$

Solving Newton's second law using the Leap-Frog algorithm leads to an NVE simulation, i.e., constant number of particles N, constant volume V, and constant total (mechanical) energy E. We often wish to conduct Molecular Dynamics simulations in canonical ensemble (NVT) to compare the model system with the real system. In this thesis, all the simulations are done in the NVT ensemble, i.e., constant number of particles N, constant volume V, and constant temperature T. To keep the temperature constant, we use Nose-Hoover thermostat [70, 74–77].

Nose-Hoover thermostat uses friction to keep the kinetic energy constant, and thereby the temperature via the equipartition theorem. We can rewrite the equation of motion as

$$\frac{d\mathbf{v}_i(t)}{dt} = \frac{\mathbf{f}_i(t)}{m_i} - \eta(t)\,\mathbf{v}_i(t), \tag{4.9}$$

$$\dot{\eta}(t) = \frac{K(t) - K_T}{d\,(N-1)\,T\,\tau_{Th}^2}, \tag{4.10}$$

where $K(t) = 1/2 \sum_N m_i\, v_i^2(t)$ is the kinetic energy at each time, K_T is the kinetic energy of the system in an equilibrium state at temperature T, and d is the dimension of the system. η is typically referred to as the thermostat state, and the thermostat relaxation time τ_{Th} controls its variations. Using the Leap-Frog algorithm to numerically solve Eqs. 4.9 and 4.10 leads to

$$\mathbf{v}_i(t + \Delta t/2) = \frac{(1 - \frac{1}{2}\Delta t\eta(t))\mathbf{v}_i(t - \Delta t/2) + \Delta t \dfrac{\mathbf{f}_i(t)}{m_i}}{1 + \frac{1}{2}\Delta t\eta(t)}, \tag{4.11}$$

$$\mathbf{r}_i(t + \Delta t) = \mathbf{r}_i(t) + \Delta t \mathbf{v}_i(t + \Delta t/2), \tag{4.12}$$

$$\eta(t + \Delta t) = \eta(t) + \Delta t \frac{K(t) - K_T}{d\,(N-1)\,T\,\tau_{Th}^2}. \tag{4.13}$$

Now if we set $\eta(t) = 0$, Eqs. 4.11 and 4.12 reduced to Eqs. 4.7 and 4.8.

4.3   Rotational Leap-Frog for Linear Molecules

To integrate the rotational equation of motion, we use the implicit algorithm (IPM) of Fincham [78]. Although it is not a time reversable algorithm we observe excellent energy conservation. For the rotational motion of a linear molecule, the orientation can be specified by a unit vector, $\hat{\mathbf{e}}$, along the molecule axis. When the molecules are not spherically symmetric, they can rotate while interacting with each other. We can write the equation of motion for a general nonspherical rigid body as

$$\frac{d\mathbf{J}}{dt} = \boldsymbol{\tau}, \tag{4.14}$$

$$\mathbf{J} = \boldsymbol{I}\,\boldsymbol{\omega}, \tag{4.15}$$

$$\frac{d\mathbf{e}}{dt} = \boldsymbol{\omega} \times \mathbf{e}, \tag{4.16}$$

where $\mathbf{J}$ is angular momentum, $\boldsymbol{\tau}$ is torque, $\boldsymbol{\omega}$ is the angular velocity, $\mathbf{I}$ is the moment of inertia (which is a tensor), and $\mathbf{e}$ is the unit vector of each particle along the main axis and indicates the orientation of the particle. For linear particles, the moment of inertia is a scalar. The moment of inertia is, in general a tensor. For an ellipsoidal shaped particle, this tensor has three independent components, which reduce to two in the case of a rotation ellipsoid. In our case, we ignore rotations around the long axis. Therefore the only relevant component of the inertia tensor is the one relative to the rotation around the short axes. For this reason, we treat the moment of inertia as a scalar. So we can write the above equations as two first order equations

$$\frac{d\boldsymbol{\omega}}{dt} = I^{-1}\boldsymbol{\tau}, \tag{4.17}$$

$$\frac{d\mathbf{e}}{dt} = \boldsymbol{\omega} \times \mathbf{e}. \tag{4.18}$$

The time evolution of angular velocity and orientation of particles are

$$\boldsymbol{\omega}(t) = \boldsymbol{\omega}(t - \Delta t/2) + \frac{1}{2}I^{-1}\boldsymbol{\tau}(t)\Delta t, \tag{4.19}$$

$$\boldsymbol{\omega}(t + \Delta t/2) = \boldsymbol{\omega}(t - \Delta t/2) + I^{-1}\boldsymbol{\tau}(t)\Delta t, \tag{4.20}$$

$$\boldsymbol{\omega}(t + \Delta t) = \boldsymbol{\omega}(t) + I^{-1}\boldsymbol{\tau}\Delta t, \tag{4.21}$$

$$\mathbf{e}(t + \Delta t) = \mathbf{e}(t) + \frac{1}{2}\big[\boldsymbol{\omega}(t) \times \mathbf{e}(t) \\ + \boldsymbol{\omega}(t + \Delta t) \times \mathbf{e}(t + \Delta t)\big]\Delta t \tag{4.22}$$

Eq. 4.22 is an implicit expression for $\mathbf{e}(t + \Delta t)$, which can be solved by iteration over

$$\mathbf{e}(t + \Delta t) = \mathbf{e}(t) + \big[\boldsymbol{\omega}(t) \times \mathbf{e}(t)\big]\Delta t, \tag{4.23}$$

as an initial guess [78]. We use 10 iterations in our codes to evaluate $\mathbf{e}(t+\Delta t)$.

By implementing the Toxvaerd's leapfrog version [79] of the Nose-Hoover thermostat [74] as

$$\beta = (1 + \frac{1}{2}\eta(t))^{-1}, \tag{4.24}$$

we can write the thermostatted version of the implicit algorithm as

$$\boldsymbol{\omega}_u(t) = \boldsymbol{\omega}(t - \Delta t/2) + \frac{1}{2}I^{-1}\boldsymbol{\tau}(t)\Delta t, \tag{4.25}$$

$$\boldsymbol{\omega}(t) = \beta\,\boldsymbol{\omega}_u(t), \tag{4.26}$$

$$\boldsymbol{\omega}(t + \Delta t/2) = (2 - \beta^{-1})\,\boldsymbol{\omega}(t) + \frac{1}{2}I^{-1}\boldsymbol{\tau}(t)\Delta t, \tag{4.27}$$

$$\boldsymbol{\omega}(t + \Delta t) = (3 - 2\beta^{-1})\,\boldsymbol{\omega}(t) + \frac{1}{2}I^{-1}\boldsymbol{\tau}(t)\Delta t, \tag{4.28}$$

where $\boldsymbol{\omega}_u$ is the unmodified angular velocity.

Since liquid-crystalline states have the properties of both the solid and liquid phases, modeling and simulating LCs is quite challenging. Moreover, weak phase transitions are common in LCs, and they have long-range order, so large system sizes are required to simulate them. Various models have been introduced so far to study and simulate liquid crystals. These models can be classified into two main groups; hard non-spherical models and soft non-spherical models.

4.4   Hard non-Spherical Models

These models were built based on the fact that short rang repulsive force control the structure of simple liquids [80]. In general, the repulsions between molecules dominate the liquid state. This can be represented by infinitely steep hard-sphere potential,

$$\begin{cases} U_{HS} = 0 & r \geq \sigma, \\ U_{HS} = \infty & r < \sigma. \end{cases} \tag{4.29}$$

In Eq. 4.29, r is the separation between molecules and σ is the contact diameter, the distance at which two particles collide. The problem with the Eq. 4.29 is that the particles are considered to be spheres, but as we know from experimental studies, a deviation from spherical symmetry is crucial for the molecules to form a liquid-crystalline mesophase [81].
One challenge here is to ascertain whether these repulsive forces can be used to model liquid crystals or not. This question had been answered by Onsager theory [82]. According to the second law of thermodynamics, an isolated system tends to maximize its entropy and consequently its disorder

(Entropy is not always equal to order. In some cases, increasing entropy leads to increasing order in a system). Onsager interprets this tendency as an ordering force. Based on Onsager works, at high density, a system of infinitely thin spherocylinders (thin rods) with diameter D and length L could spontaneously order (form an orientationally ordered nematic phase) from an isotropic fluid. So the orientational entropy will decrease, but this compensates by an increase in the translational entropy. The reason is that, the excluded volume (of two rods) in the nematic phase is smaller compare to isotropc phase [83].

Another challenge is to choose the shape of molecules. For non-atomistic potential, several simple anisotropic shapes can be used to model a liquid crystal, yet they must have a certain minimum length-to-breadth ratio to exhibit mesophases. To model rod-shaped mesogens, one can use prolate ellipsoids and spherocylinders. In contrast, oblate ellipsoids and cut spheres are helpful to model disc-shaped molecules. It is worth mentioning that these are only rigid and simplified shapes and do not include characteristics of genuine liquid crystal such as flexibility or attractive forces. Now lets look at some simulation results from literature, corresponding different shapes anisotropy.

Spheroid particles are extensively studied and divided into two groups: ellipsoids of revolution (uniaxial ellipsoid), $a \neq b = c$, and biaxial ellipsoids, $a \neq b \neq c$. Where a, b and c are the symmetry axes of ellipsoid. Frenkel *et al*. conducted a successful simulation of hard ellipsoids of revolutions [84, 85] and constructed the corresponding phase diagram. They found the existence of isotropic, nematic, and solid phases for a system consisting of prolate or oblate ellipsoids. According to the Fig. 4.2, there is a degree of symmetry between oblate and prolate ellipsoids when the length-to-breadth ratio varies from $1/e$ to e. They have been reported that the nematic phase was formed by spontaneous ordering from the isotropic phase.

A system of hard ellipsoids can not form a smectic phase [83]; it is also evident in the Fig. 4.2. To investigate the possibility of forming a smectic phase by a system of hard particles, a tenuous change of shape anisotropy to a *spherocylinder* was suggested. It is a basic three-dimensional geometric shape consisting of a cylinder of length L and diameter D with a hemispherical end of diameter D. The length-to-breadth ratio is $\frac{L+D}{D}$. Sometimes it referred to as an oval, except the sides are parallel. The first study of such a system was conducted by Vieillard-Baron *etal*. [86]. Afterward, more detailed studies were carried out on a system of parallel spherocylinders [87, 88] where the particles are forced to be parallel, and they just have translational degrees of freedom. It was observed that the system formed a close-packed crystal at high enough densities, but at lower densities, it formed a nematic phase because the particles were confined to be parallel. The next step was to study the same system, taking both translational and orientational
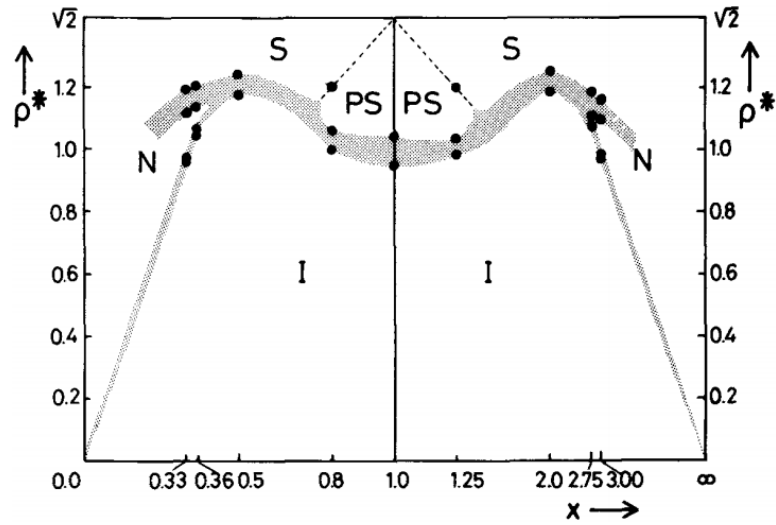
Figure 4.2: Phase diagram of hard ellipsoids of revolution. Vertical axis is density, ρ, horizontal axis is length-to-breadth ratio, x. The shaded areas correspond to coexistence regions. The following phases can be distinguished: I, isotropic fluid; N, nematic fluid; S, orientationally ordered solid; PS, plastic solid. The figure directly taken from Ref. [85].

degrees of freedom into account. For $L/D = 0.5$, increasing density leads to the formation of nematic and smectic A phases [89]. A tentative phase diagram of the system has been introduced [90]. As it is evident in Fig. 4.3, the liquid crystalline mesophases are forming for $L/D > 3.5$ approximately.

Another interesting case of shape anisotropy studied in detail is the cut-sphere. As one can understand from the name, it consists of a standard sphere of diameter D with the top and bottom removed, and the thickness is L. $L/D = 1$ represents a hard-sphere. Fig. 4.4 shows the phase behavior for a range of L/D ratios [91]. At $L/D = 0.1$, increasing density causes a spontaneous phase transition to nematic and columnar phases from an isotropic fluid. At $L/D = 0.2$, a cubic phase was found for a specific density range. In this region, short columnar stacks of particles are packing against each other. Thus, there is a short-range translational order, but overall the columns are orientationally disordered. By increasing the thickness of the particles, as you can see in Fig. 4.4, all liquid-crystalline behavior will vanish.

4.5 Soft non-Spherical Models

The hard models, which only considered the repulsive forces between molecules, were successful in only describing certain LCs mesophases. Hence, the soft models of liquid crystals take both repulsive and attractive forces into account. As we saw earlier, the hard models do not exhibit thermodynamic
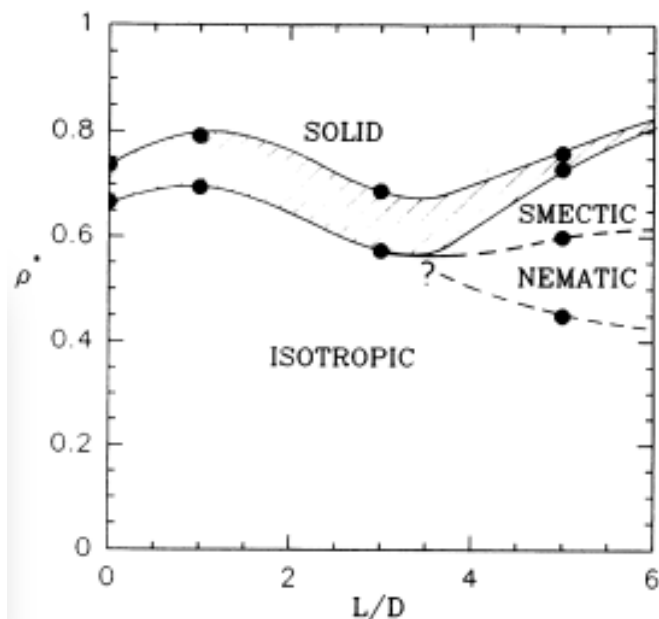
Figure 4.3: Phase diagram of a system of spherocylinders. The filled circles denoted the calculated coexistence points. The shaded area is coexistence region. The figure directly taken from Ref. [90].

phase diagrams (ρ vs T phase diagram). In soft models, one can observe a transition between isotropic phase and liquid-crystalline mesophases by increasing the temperature and not just the density. Here, the interaction potential between molecules depends not only on the separation distance between the center of masses but also on the orientation of the molecules. So basically, these models are anisotropic versions of the well-known Lennard-Jones potential:

$$U(r) = 4\epsilon \left[\left(\frac{\sigma}{r} \right)^{12} - \left(\frac{\sigma}{r} \right)^{6} \right], \tag{4.30}$$

where ϵ and σ are energy and length parameters, respectively, and r is the separation distance between centers of pair particles. The repulsive forces dominate at short distances, while at large separations, the attractive forces take over. Now one can investigate the contribution of attractive and repulsive components to the stability of mesophases formed by liquid crystals. A vast number of continuous potential models for fluids of aspherical molecules have been introduced, such as the Kihara potential [92], the site–site potential [93], the Gaussian overlap model [94], and the Gay–Berne potential [95]. Using site-site potential, one can mimic the structure of real LC molecules, comparable with those of experimental studies [96–102]; this model nevertheless requires tremendous computing power. On the contrary, the Gay-Berne model is computationally cheap and has become a popular system.

27
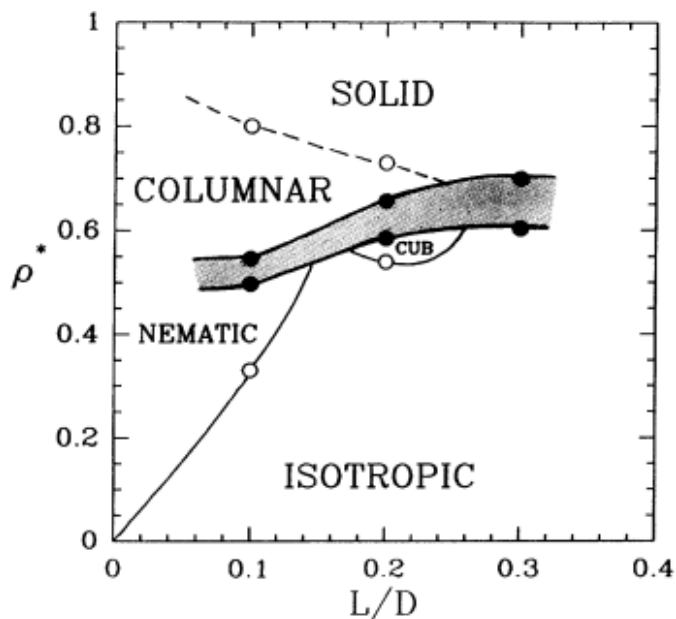
Figure 4.4: Tentative phase diagram of cut spheres with length-to-breadth ratio L/D between 0.1 and 0.3. The high-density solid-columnar phase is separated by a first-order phase transition from the low-density fluid phase. The shaded area indicates the coexistence region. The densities of the coexisting phases are indicated by closed circles. The open circles indicate the approximate location of phase transitions that have been estimated using techniques other than free-energy calculations. The isotropic-nemnatic transition is weakly first order. The same appears to be the case with the isotropic-cubatic transition. The figure is taken from [91].

4.5.1 The Gay-Berne Potential

Gay-Berne (GB) potential considers both attractive and repulsive forces. The initial work was conducted by Corner in 1948 [103]. The idea was to model a linear non-spherical molecule by multiple Lennard-Jones sites located at equal distances along a symmetry axis. To avoid complicated, numerically expensive interactions between many Lennard-Jones particles, Corner proposed a single-site potential consisting of multi-sites potential fitted numerically to a 12-6 Lennard-Jones potential. The potential considered the interaction between two particles as a function of the separation distance between centers and scaled by a range parameter that depends on the molecules' orientations, $\sigma(\Omega)$;

$$U_{Corner} = \epsilon(\Omega) f \left(\frac{r}{\sigma(\Omega)} \right). \tag{4.31}$$

The strength parameter, $\epsilon(\Omega)$, and the range parameter, $\sigma(\Omega)$, both depends on the orientation, Ω, as well as the separation distance r. Later on, Berne and Pechukas [94] proposed new definitions for the strength and range

parameters using the gaussian overlap model. If $\mathbf{x}$ is a three-dimensional vector, then the gaussian function can be defined as:

$$G(\mathbf{x}) = \exp\left(-\mathbf{x}.\gamma^{-1}.\mathbf{x}\right), \tag{4.32a}$$

$$\gamma = (\sigma_e^2 - \sigma_s^2)\hat{\mathbf{e}}\hat{\mathbf{e}} + \sigma_s\mathbf{I}, \tag{4.32b}$$

σ_e and σ_s are long and short diameters of ellipsoid respectively, $\hat{\mathbf{e}}$ is the unit vector indicating the orientation of the molecule or particle and $\mathbf{I}$ is the unity matrix. Berne and Pechukas calimed that the overlap between two ellipsoids of revolution should be:

$$G(\mathbf{r}, \hat{\mathbf{e}}_i, \hat{\mathbf{e}}_j) \approx |\gamma_i|^{-\frac{1}{2}}|\gamma_j|^{-\frac{1}{2}}$$
$$\int d\mathbf{x} \exp\left(-\mathbf{x}.\gamma_i^{-1}.\mathbf{x} - (\mathbf{x}-\mathbf{r}).\gamma_j^{-1}.(\mathbf{x}-\mathbf{r})\right), \tag{4.33}$$

where $|\gamma|$ is the determinant of the matrix. Eq. 4.33 can be simplified to [94]:

$$G(\hat{\mathbf{r}}, \hat{\mathbf{e}}_i, \hat{\mathbf{e}}_j) = \epsilon(\hat{\mathbf{e}}_i, \hat{\mathbf{e}}_j)\exp\left[-\mathbf{r}^2/\sigma^2(\hat{\mathbf{r}}, \hat{\mathbf{e}}_i, \hat{\mathbf{e}}_j)\right], \tag{4.34}$$

where

$$\epsilon(\hat{\mathbf{e}}_i, \hat{\mathbf{e}}_j) = \epsilon_0\left[1 - \chi^2(\hat{\mathbf{e}}_i, \hat{\mathbf{e}}_j)\right]^{-\frac{1}{2}}, \tag{4.35}$$

and

$$\sigma(\hat{\mathbf{r}}, \hat{\mathbf{e}}_i, \hat{\mathbf{e}}_j) = \sigma_s\left[1 - \frac{\chi}{2}\left(\frac{(\hat{\mathbf{e}}_i.\hat{\mathbf{r}} + \hat{\mathbf{e}}_j.\hat{\mathbf{r}})^2}{1 + \chi(\hat{\mathbf{e}}_i.\hat{\mathbf{e}}_j)} + \frac{(\hat{\mathbf{e}}_i.\hat{\mathbf{r}} - \hat{\mathbf{e}}_j.\hat{\mathbf{r}})^2}{1 - \chi(\hat{\mathbf{e}}_i.\hat{\mathbf{e}}_j)}\right)\right]^{-1/2} \tag{4.36a}$$

$$\text{where} \quad \chi = \frac{\kappa^2 - 1}{\kappa^2 + 1}, \quad \text{and} \quad \kappa = \sigma_e/\sigma_s. \tag{4.36b}$$

This overlap model is studied in detail [104, 105]. However, the overlap potential possesses some unrealistic features [95]. According to Eq. 4.35, the well-depth depends on the relative orientation of two particles. In this case, the well-depth of various configurations, for example the side-side and end-end configurations, are identical. In order to overcome this problem, several modifications were proposed [106, 107], yet the most well-known one developed by Gay and Berne as a modification of the overlap model [95]. The first change they implemented was to shift the potential, just like Kihara's model [108], rather than scale it. Thus the potential has a form

$$U^{GB}(\mathbf{r}_{ij}, \hat{\mathbf{e}}_i, \hat{\mathbf{e}}_j) = 4\epsilon(\hat{\mathbf{r}}, \hat{\mathbf{e}}_i, \hat{\mathbf{e}}_j)\left[(\sigma_s/\rho_{ij})^{12} - (\sigma_s/\rho_{ij})^6\right], \tag{4.37a}$$

$$\text{where} \quad \rho_{ij} = r_{ij} - \sigma(\hat{\mathbf{r}}, \hat{\mathbf{e}}_i, \hat{\mathbf{e}}_j) + \sigma_s. \tag{4.37b}$$

The range parameter is the same as in the overlap model, Eq. 4.36a There is a slight modification in the strength parameter

$$\epsilon(\hat{\mathbf{r}}, \hat{\mathbf{e}}_i, \hat{\mathbf{e}}_j) = \epsilon_0\epsilon_1^\nu(\hat{\mathbf{e}}_i, \hat{\mathbf{e}}_j)\epsilon_2^\mu(\hat{\mathbf{r}}, \hat{\mathbf{e}}_i, \hat{\mathbf{e}}_j) \tag{4.38a}$$

where

$$\epsilon_1(\hat{\mathbf{e}}_i, \hat{\mathbf{e}}_j) = \left(1 - \chi^2(\hat{\mathbf{e}}_i, \hat{\mathbf{e}}_j)^2\right)^{-1/2} \tag{4.38b}$$

$$\epsilon_2(\hat{\mathbf{r}}, \hat{\mathbf{e}}_i, \hat{\mathbf{e}}_j) = 1 - \frac{\chi'}{2}\left(\frac{(\hat{\mathbf{e}}_i.\hat{\mathbf{r}} + \hat{\mathbf{e}}_j.\hat{\mathbf{r}})^2}{1 + \chi'(\hat{\mathbf{e}}_i.\hat{\mathbf{e}}_j)} + \frac{(\hat{\mathbf{e}}_i.\hat{\mathbf{r}} - \hat{\mathbf{e}}_j.\hat{\mathbf{r}})^2}{1 - \chi'(\hat{\mathbf{e}}_i.\hat{\mathbf{e}}_j)}\right) \tag{4.38c}$$

and the energy anisotropy parameter is

$$\chi' = \frac{\kappa'^{1/\mu} - 1}{\kappa'^{1/\mu} + 1}, \quad \text{where} \quad \kappa' = \epsilon_{ss}/\epsilon_{ee}. \tag{4.38d}$$

ϵ_{ss} and ϵ_{ee} are the well depth of the potential in side-side and end-end configurations respectively. Fig. 4.5 shows the potential energy as a function of separation distance for different configurations (check the Appendix A for full derivation of force and torque).

Previous studies of the Gay-Berne model have focused on the phase behav-
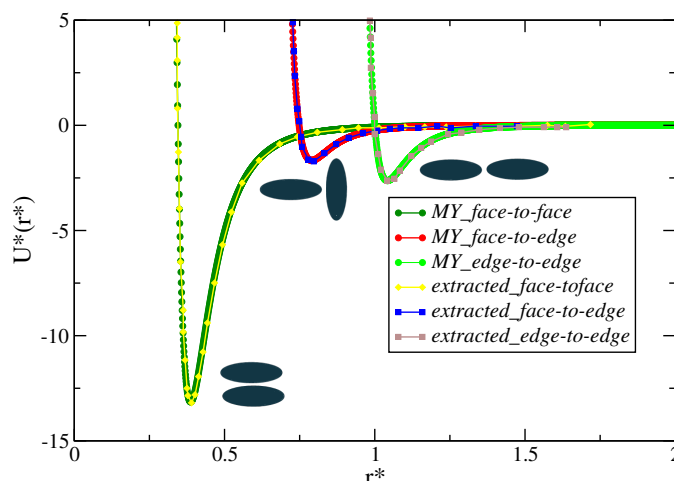
Figure 4.5: The Gay-Berne potential ($U^* = U/\epsilon_0$) as a function of pair distance ($r^* = r/\sigma_0$) for side-side, side-end and end-end configurations. The yellow, brown, and blue curves are extracted from Ref. [109]. The red, light green, and dark green is results of my simulation.

ior [110–117], per-particle translational and orientational dynamics [118], interfacial properties [119], elastic constants [68], thermal conductivity [120, 121], and viscosity coefficients [122, 123]. Different perturbation theories have been applied to explore the phase diagram of various Gay-Berne fluids in detail [124, 125]. Using the Gay-Berne model, one can describe a wide range of shape anisotropy within the system, from elongated ellipsoids to very thin disks. The Gay-Berne potential depends on a set of four parameters, usually written as $GB(\kappa, \kappa', \mu, \nu)$, which control the shape of molecules as well as the strength of the potential between them. The case of $GB(3, 5, 2, 1)$ is the most studied one among all possible sets of parameters.

The $GB(3, 5, 2, 1)$, first introduced by Gay and Berne, inspired by the Gaussian overlap model proposed by Berne and Pechukas [94], in their original paper back in 1981 [95]. The choice of the shape anisotropy parameter, κ, is straightforward. For real liquid crystals, the ratio of length-to-breadth is equal to or greater than 3; this leads to the choice of $\kappa = 3$ by Gay and Berne [95]. To obtain the other parameters, the Gay-Berne potential was
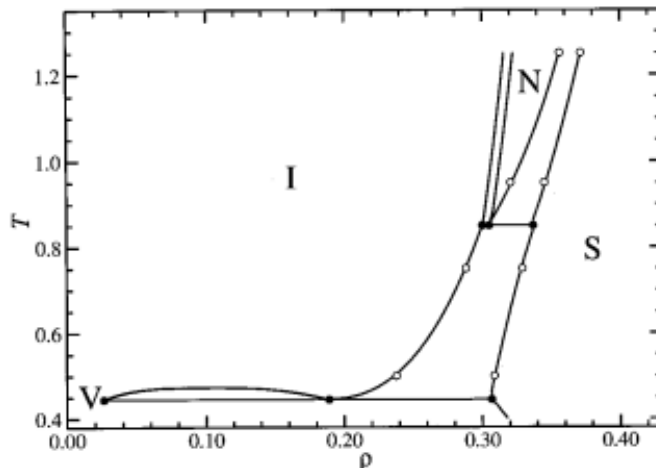
Figure 4.6: Global temperature-density phase diagam of the $GB(3, 5, 2, 1)$ showing the domain of vapor (V), isotropic (I), nematic (N), and solid (S) phases. The figure directly taken from [126].

compared with the case of a pair of linear molecules, each of which consists of four sites LJ particles placed equally within a line such that the length-to-breadth ratio is equal to 3. It resulted to $\kappa' = 5$, $\mu = 2$ and $\nu = 1$ [95]. For this set of parameters, the phase diagram and orientational order parameter are already known [113, 126]. Moreover, the velocity autocorrelation function [118], viscosity [127], elastic constants [69], free energies and enthalpy [128], the isotropic-nematic transitions [112] and the liquid-vapor coexistence [129], stress tensor components [130], and self-diffusion coefficient [131] of $GB(3, 5, 2, 1)$ fluids have been studied in detail. The $GB(3, 5, 2, 1)$ shows a rich phase behavior with isotropic, nematic and smectic B phases [111, 113]. Furthermore, smectic A [111], a tilted smectic B [113] and a rippled smectic B phase [117] have also been observed for the slightly different parameters. Adams et al. [110] investigate the nematic-isotropic transition of rod-shaped mesogens using the Gay-Berne potential. Luckhurst et al. [111] studied the case of $\mu = 2$ and $\nu = 1$, and they found smectic A and smectic B in addition to isotropic, nematic, and solid phases. De Miguel et al. conducted detailed studies of prolated Gay-Berne fluids [112, 113, 115]. Berardi et al. [132] , using $\mu = 1$ and $\nu = 3$, showed how the structure and orientation of molecules depend on the set of the parameter you choose.

The Gay-Berne potential is flexible enough to simulate a wide range of anisotropy in the shape of linear molecules, from a very long ellipsoid to a thin disk-shaped molecule. The first simulation studies of disk-shaped Gay-Berne molecules were performed by Emerson et al. [109]. Using $\kappa = 0.345$, they showed that the system could form discotic nematic and columnar phases. The phase diagram has been obtained in the case of discotic fluids [133] by varying both κ and κ' [134–136]. The most studied set of parameters here is $GB(0.345, 0.2, 1, 2)$ [137], which resulted in an improvement in the angle of view in liquid crystals displays [138]. The Gay-Berne potential was also used to model systems other than liquid crystals such as benzene [139, 140] and naphthalene [141, 142].
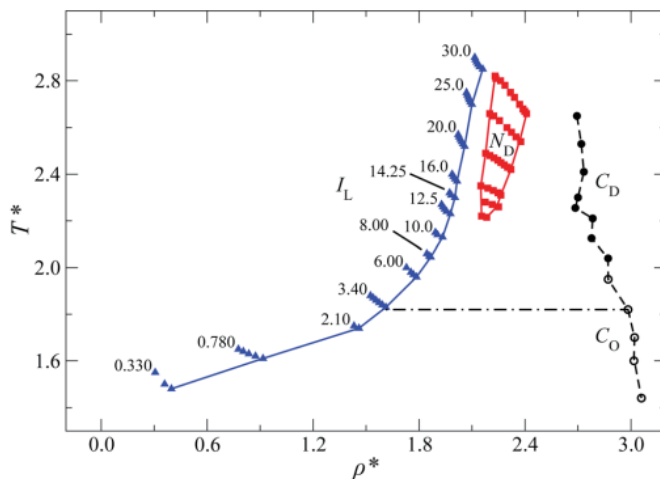
Figure 4.7: Thermodynamic phase diagram of discotic fluids of $GB(0.345, 0.2, 1, 2)$ showing isotropic liquid (I_L, triangles), nematic (N_D, squares), disordered columnar (C_D, filled circles), and ordered columnar (C_O, open circles). The figure directly taken from [137].

In this study, we mainly focus on $GB(3, 5, 2, 1)$ and $GB(0.345, 0.2, 1, 2)$ because their phase diagram is already known. Fig. 4.7 shows the phase diagram of $GB(0.345, 0.2, 1, 2)$.

4.6 Structural, Orientational and Dynamic Properties

As mentioned earlier, all simulations in this study are done in an NVT ensemble. We start with a random initial configuration and equilibrate it at a certain density, ρ, and temperature, T. Once the system has been equilibrated, the production begins. Some properties such as temperature and per-particle energy are calculated during the simulation. Other properties like mean square displacement and auto-correlation functions are usually

calculated after simulations have been finished.

4.6.1 Orientational Order Parameter

An order parameter is a physical quantity that distinguishes between two phases. It measures how the molecules are orientationally ordered in the system. The second rank order parameter, S_2, takes values between 0 and 1. For a perfectly aligned system, S_2 is equal to 1, whereas $S_2 = 0$ indicates an isotropic state. For a uniaxial phase, S_2 can be defined as

$$S_2 = \left\langle \frac{1}{N} \sum_i^N P_2(\hat{\mathbf{e}}_i(t) \cdot \mathbf{n}(t)) \right\rangle, \tag{4.39}$$

where P_2 is the second Legendre polynomial, $\mathbf{n}$ is the director of the phase, and the angular brackets denote the time average. However, in simulation $\mathbf{n}$ is unknown. The order parameter can be evaluated by maximizing S_2 with respect to $\mathbf{n}$, so we can rewrite Eq. 4.39 as

$$S_2 = \langle \mathbf{n} \cdot \mathbf{Q} \cdot \mathbf{n} \rangle, \tag{4.40}$$

where

$$\mathbf{Q} = \frac{1}{2N} \sum_i^N (3\hat{\mathbf{e}}_i \otimes \hat{\mathbf{e}}_i - \mathbf{I}). \tag{4.41}$$

$\mathbf{Q}$ is the orientational tensor, $\otimes$ denotes the tensor product, $\mathbf{I}$ is the unity matrix, and N is the total number of molecules in the system. S_2 is equal to the largest eigenvalue, λ_{max}, obtained by diagonalizing the $\mathbf{Q}$ tensor [69, 143].

4.6.2 Structural Properties

4.6.2.1 Radial Distribution Function

The radial distribution function, $g(r)$, is used to investigate the translational order in the system, where r is the distance between the particle centers. It describes how the density locally varies in the system as a function of distance from a reference particle. $g(r)$ gives the probability of finding pair of particles with distance r apart (see Fig. 4.8). In the simulation, first, we calculate the distance between all pairs and bin them with the width of dr, into a histogram. To calculate $g(r)$, we divide each histogram interval by the number of particles in the ideal gas at the same density. The position of peaks gives us information about the shells of neighbors, and the area beneath each peak gives us the number of neighboring particles. Fig. 4.9 shows $g(r)$ for the $GB(3, 5, 2, 1)$ at $(\rho, T) = (0.32, 1.2)$ which is in the nematic phase.
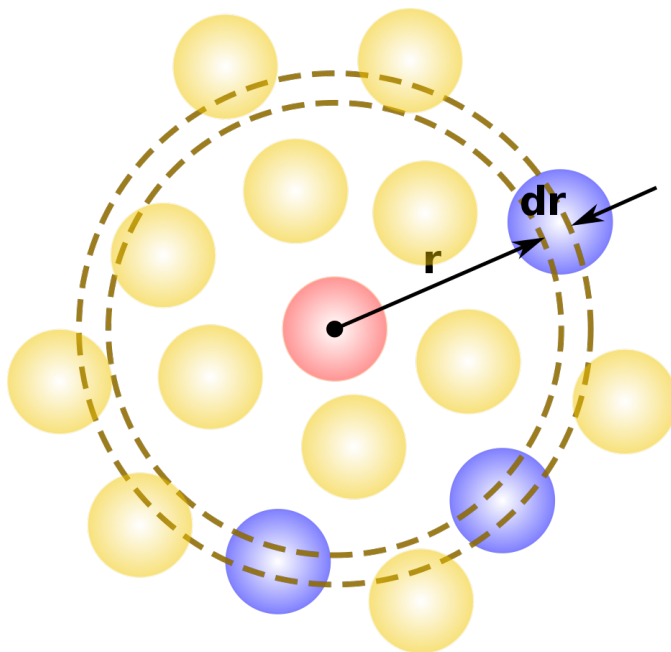
Figure 4.8: Schematic binning for calculating $g(r)$. Taken from Ref. [144].
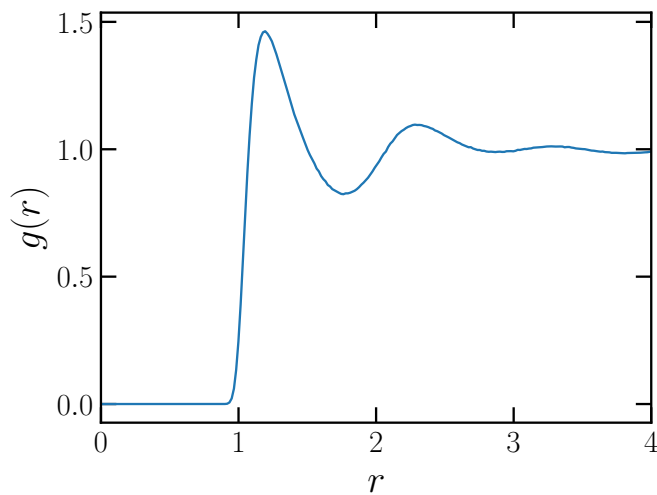
Figure 4.9: $g(r)$ corresponds to $GB(3,5,2,1)$ at $(\rho, T) = (0.32, 1.2)$.

4.6.2.2 Second Rank Orientational Pair-correlation Function

The second rank orientational pair-correlation function defines as follows

$$G_2(r) = \langle P_2(\hat{\mathbf{e}}_i \cdot \hat{\mathbf{e}}_j)\rangle, \tag{4.42}$$

where P_2 is the second order Legendre polynomial. $G_2(r)$ measures how the molecules are orientationally correlated as a function of r. We follow the

same procedure as $g(r)$ to make a histogram of all the pair distances. Fig. 4.10 shows $G_2(r)$ for $GB(3, 5, 2, 1)$ in the nematic phase. As it is clear in the figure, the tail maintains a value around 0.2 at long distances, which means there is a long-range orientational ordering in the system.
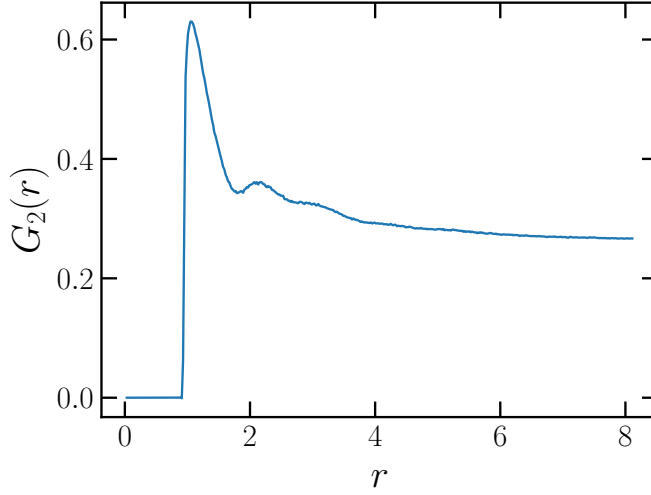
Figure 4.10: $G_2(r)$ corresponds to $GB(3, 5, 2, 1)$ at $(\rho, T) = (0.32, 1.2)$.

4.6.3   Dynamic Properties

4.6.3.1   Auto-correlation Functions

The auto-correlation function tells us how a property correlated with itself at different times and gives valuable information on the dynamical evolution. The normalized auto-correlation function of property $\mathbf{A}(t)$ is defined by

$$\phi_A(t) = \frac{\langle \mathbf{A}(t_0) \cdot \mathbf{A}(t_0 + t) \rangle}{\langle \mathbf{A}(t_0) \cdot \mathbf{A}(t_0) \rangle}. \tag{4.43}$$

When there is no correlation, $\phi_A(t)$ decays to zero, while $\phi_A(t) = 1$ at $t = 0$.

4.6.3.2   Mean Square Displacement

Mean square displacement, $m(t)$, measures the squared traveled distance of a particle with respect to its initial position. The $m(t)$ tells us how diffusive the dynamics are at each time and is defined as

$$m(t) = \langle |\mathbf{r}_i(t) - \mathbf{r}_i(0)|^2 \rangle. \tag{4.44}$$

The behavior of the $m(t)$ varies from one system to another, but it retains some important features. In many liquids it consists of two main regimes.

The early regime represents ballistic motion, a collision-free regime where particles move freely. $m(t)$ in the ballistic regime is proportional to t^2. In the long-time regime, which represents the diffusion mode, the motion is dominated by collisions, and $m(t)$ is proportional to t. At a very long time, $m(t)$ becomes linear (see Fig. 4.11), and we can calculate the diffusion coefficient, D, from

$$D = \lim_{t \to \infty} \frac{1}{6t} m(t). \tag{4.45}$$
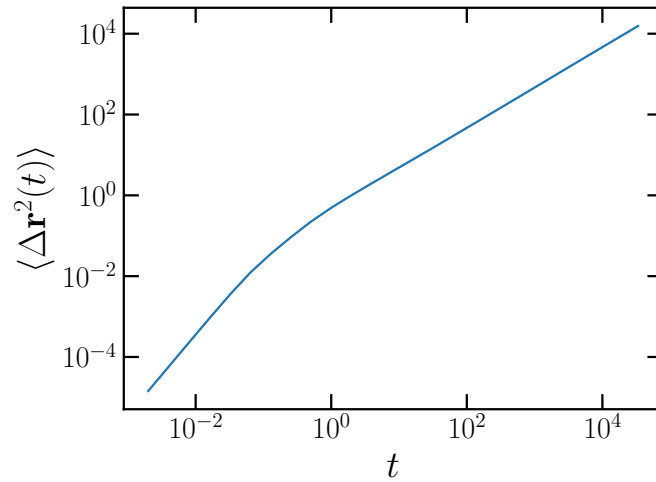
Figure 4.11: $m(t)$ corresponds to $GB(3, 5, 2, 1)$ at $(\rho, T) = (0.32, 1.2)$.

Chapter 5

Isomorphs in the GB Model

This chapter provides results for generating isomorph in the phase diagram of the Gay-Berne systems. Among all possible sets of parameters, we choose $GB(3, 5, 2, 1)$ and $GB(0.345, 0.2, 1, 2)$. These two sets have been extensively studied, and their phase diagrams, dynamics, and structures are already known. First, we present how the orientational and rotational dynamics and structure of the disc-shaped Gay-Berne system are invariant along isomorphs. Afterward, we apply the constant-exponent density scaling and discuss the results. Finally, we trace isomorphs in the isotropic and nematic phases of the rod-shaped Gay-Berne system.

5.1 Isomorph in Discotic Liquid Crystal

We study the Gay-Berne model for the set of parameters, $GB(0.345, 0.2, 1, 2)$, which leads to discotic liquid crystal phases at low temperatures. Many studies have considered this parametrization, and its corresponding thermodynamic phase diagram is already known [137]. We investigate the possibility of finding isomorphs in the high-temperature isotropic phase. We are inspired by previous studies reported that at the high-temperature isotropic phase, the system under study has strong virial potential-energy correlation [14, 25, 26, 28]. To study and simulate a discotic liquid using the Gay-Berne potential, one may replace σ_s by σ_e in Eq. 4.37a and Eq. 4.37a and keep everything else the same. By doing these changes, we can avoid unphysical effects [109, 137]. Here the parameter σ_e defines the thickness of the discs.

The system under study consists of $N = 2048$ discogens. The potential is truncated but not shifted at the cut-off distance $r_c = 1.6$ [137]. Units are defined by choosing $\sigma_s = 1$ and $\epsilon_0 = 1$. The moment of inertia for all discs

is set to $I = 1$. The equilibration and production simulations consist of 5×10^6 steps with $\Delta t = 5 \times 10^{-4}$. The Gay-Berne code first was compared with literature, and complete agreement was observed for radial distribution function [113, 145], second rank orientational pair-correlation function [110, 112, 113], orientational order parameter [112, 113, 146], and various auto-correlation functions [118, 147], etc. We present some of these consistency checks in the Appendix B.

We use the so-called configurational adiabat method to generate the isomorphs. In this method, an isomorph defines as a curve of constant excess entropy, S_{ex}, in the thermodynamic phase diagram. Let us recall the equation for γ again:

$$\gamma \equiv \left(\frac{\partial \ln T}{\partial \ln \rho} \right) = \frac{\langle \Delta U \Delta W \rangle}{\langle (\Delta U)^2 \rangle}, \tag{5.1}$$

where ρ is the density, T is the temperature, U is the potential energy, and W is the virial. We can clarify the generating process of isomorph with a simple example. From an NVT simulation at a given state point, one can calculate the right-hand side of the Eq. 5.1 from fluctuations of U and W. If it results in $\gamma = 3$, and if we increase the density by 1%, according to Eq. 5.1, the temperature will increase by 3% to keep the excess entropy constant. We use fourth-order Runge-Kutta algorithm ($RK4$) to numerically solve Eq. 5.1. We increase density by 1% at each step, leading to an overall 20% density increment.

5.1.1 Phase Diagram of GB(0.345,0.2,1,2)

We investigate the model's thermodynamic phase diagram and calculate the order parameter, S_2, and virial potential energy correlation coefficient (see Fig. 5.1). The regions of the phase diagram with $R > 0.9$ are expected to have isomorphs. In Fig. 5.1, "I", "N", and "C" correspond to isotropic, nematic, and columnar phases, respectively. The dark green triangles are directly extracted from Ref. [137] indicating the phase boundaries. The color coding reflects the value of R. Fig. 5.1 reveals that for higher densities (approximately $\rho > 2.4$) and sufficiently high enough temperature, $T > 5.0$, The system is R-simple.

Fig. 5.2 is a snapshot of the system at equilibrium from NVT simulations in the isotropic, nematic, and columnar phases. Each simulation starts from a perfect crystal, then we scale the system to the state point of interest and equilibrate them there.
The isomorph, the white line, was generated as described earlier starting from the reference state point $(\rho_{ref}, T_{ref}) = (2.3, 5.0)$.
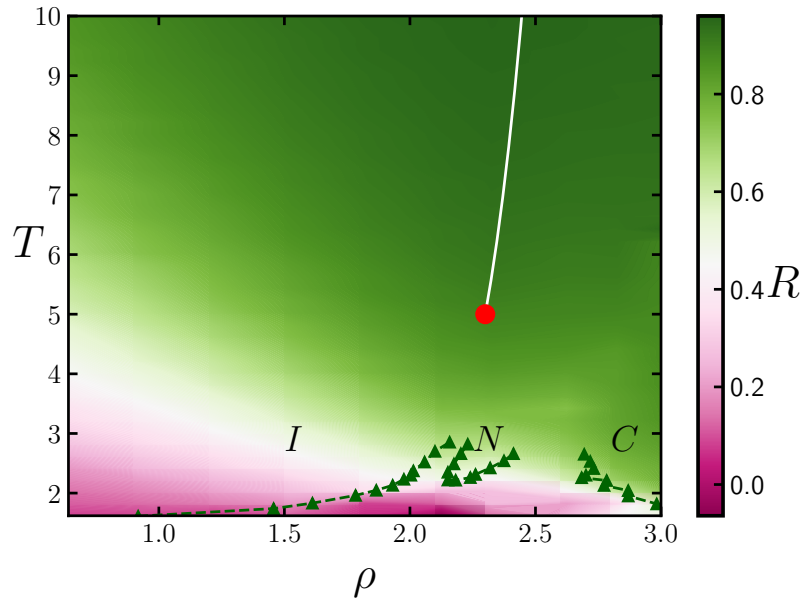
(a)
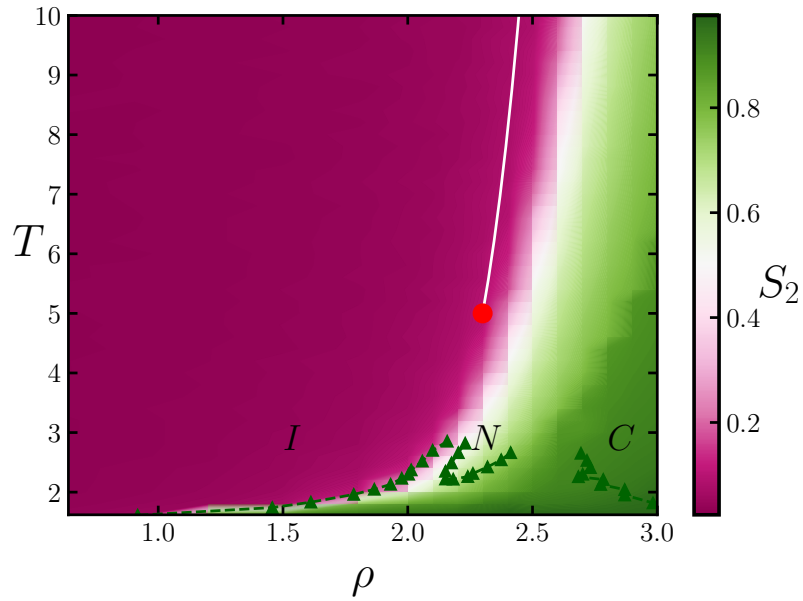
(b)

Figure 5.1: The phase diagram of the discotic GB(0.345,0.2,1,2) model with (a) correlation coefficient, R, values; and (b) order parameter, S_2 values given by the color code to the right. The triangular symbols delimit the phase boundaries [137]. I stands for the isotropic, N for the nematic, and C for the columnar phases. The red filled circle is the isomorph reference state point $(\rho, T) = (2.3, 5.0)$, the white curve is the isomorph (which is studied up to $T = 43$).
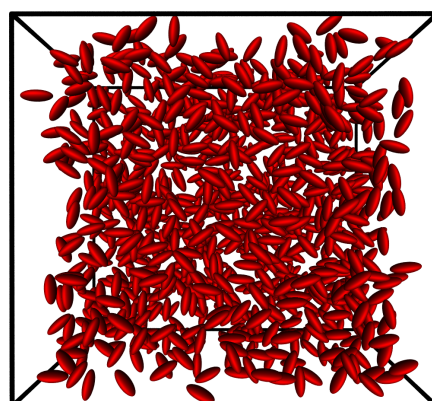
(a)
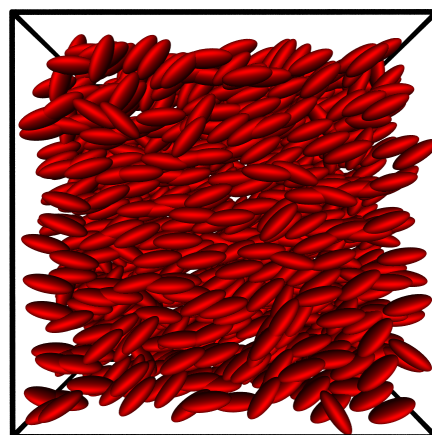
(b)
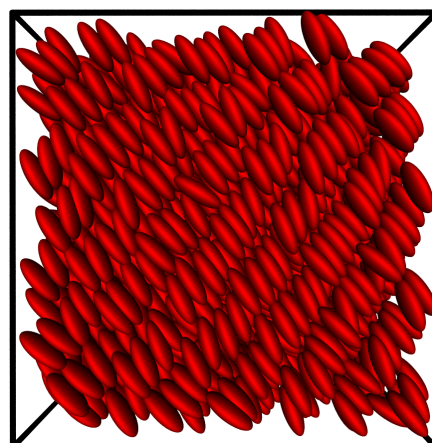
(c)

Figure 5.2: Snapshots of the discotic Gay-Berne model in thermal equilibrium at three state points. (a) shows the isotropic liquid phase at $(\rho, T) = (0.6, 2.6)$; (b) shows the nematic phase at $(\rho, T) = (2.3, 2.6)$; (c) shows the columnar phase at $(\rho, T) = (3.0, 2.6)$

5.1.2 Comparing the Isomorph to the $\rho = 2.3$ Isochore

Here we will look at the level of invariance in dynamics and structure along the isomorph, i.e., the white line in Fig. 5.1. All quantities are presented in reduced units. We compare the variation of these quantities along the isomorph to the $\rho = 2.3$ isochore with the same temperature range ($5 < T < 43$). Table 5.1 provides the variation of density, temperature, correlation coefficient, and γ along the isomorph.

In the rest, we investigate how the different structural and dynamic properties vary along this isomorph. Another isomorph has been generated starting at $(\rho_{ref}, T_{ref}) = (2.3, 4.0)$, and we report the result in Appendix C.

ρ	T	R	γ
2.3	5.0	0.8919	10.7172
2.323	5.5695	0.9087	10.9915
2.3462	6.2222	0.9236	11.2484
2.3697	6.9642	0.9354	11.4076
2.3934	7.8054	0.9449	11.5265
2.4173	8.7532	0.9511	11.5605
2.4415	9.8206	0.9567	11.5761
2.4659	11.0182	0.9598	11.5705
2.4906	12.3614	0.9626	11.5618
2.5155	13.8658	0.9646	11.5344
2.5406	15.5487	0.9657	11.4808
2.566	17.4288	0.9672	11.4648
2.5917	19.5313	0.9676	11.4252
2.6176	21.8793	0.9678	11.4113
2.6438	24.5037	0.9677	11.372
2.6702	27.4346	0.9673	11.3317
2.6969	30.7086	0.9673	11.3163
2.7239	34.3641	0.9673	11.3023
2.7511	38.4498	0.9668	11.2795
2.7787	43.0139	0.9662	11.2634

Table 5.1: Variation of density, temperature, correlation coefficient and γ for isomorph. At each step we increased density by 1%. For the case of isochore the density is constants and we use same temperatures presented here.

5.1.2.1 Dynamics

The comparison of mean square displacement along the isochore and the isomorph is shown in Fig. 5.3. At short times good data collapses happen in both cases. However, only along the isomorph dynamics is invariant for long times. Along an isomorph, one can say that all the physics relating to the position and motion of particles are the same. This means if you

make a movie of particle movements at different isomorphic state points, the same film will play except for the scaling of time and space. It is worth mentioning again that the isomorph theory is an approximation, and it is only exact for IPL potentials with $R = 1$.

In Fig. 5.4, the center of mass velocity (upper row) and the angular ve-
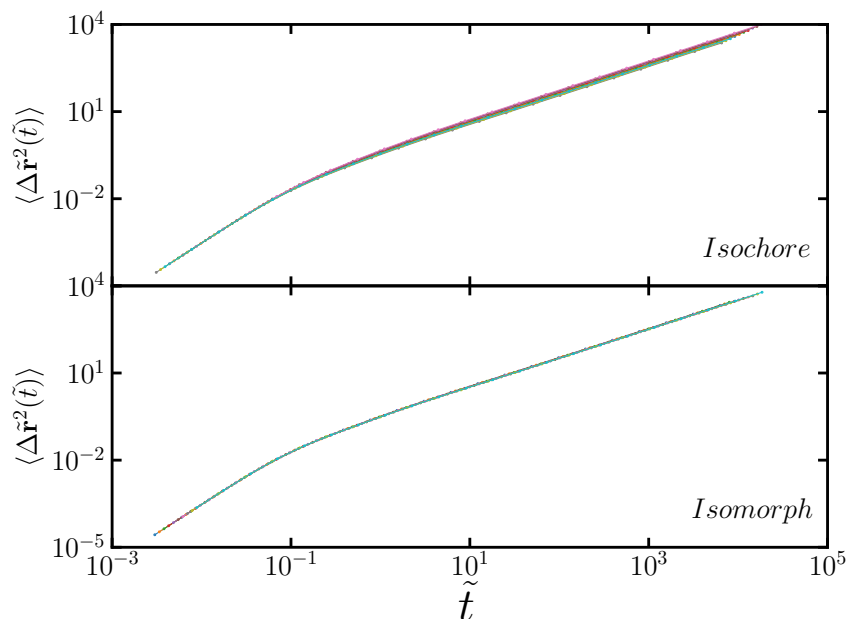
Figure 5.3: Comparing the reduced-unit mean square displacement along the isochore (upper panel) and the isomorph (lower panel). In the short times, they show ballistic regime, while they exhibit diffusive regime at long times. Only along the isomorph do the data collapse in both regimes. Data indicated with varying colors correspond to 20 state points with $2.30 < \rho < 2.78$ and $5 < T < 43$ as reported in table 5.1

.

locity (lower row) auto-correlation functions are plotted along the isochore (left column) and the isomorph (right column). A pronounced data collapse occurs along the isomorph compared to the isochore. This is not surprising as the velocity auto-correlation function is equivalent to the second derivative of the mean square displacement.

The force and the torque auto-correlation functions are plotted in Fig. 5.5. The two functions are invariant only along the isomorph.

Fig. 5.6 gives data for first- and second-order orientational auto-correlation functions. The function starts from unity and decays to zero in all cases. This indicates that the system is in the isotropic phase; thus, there is no orientational ordering. Here again, only along the isomorph is this decay invariant.
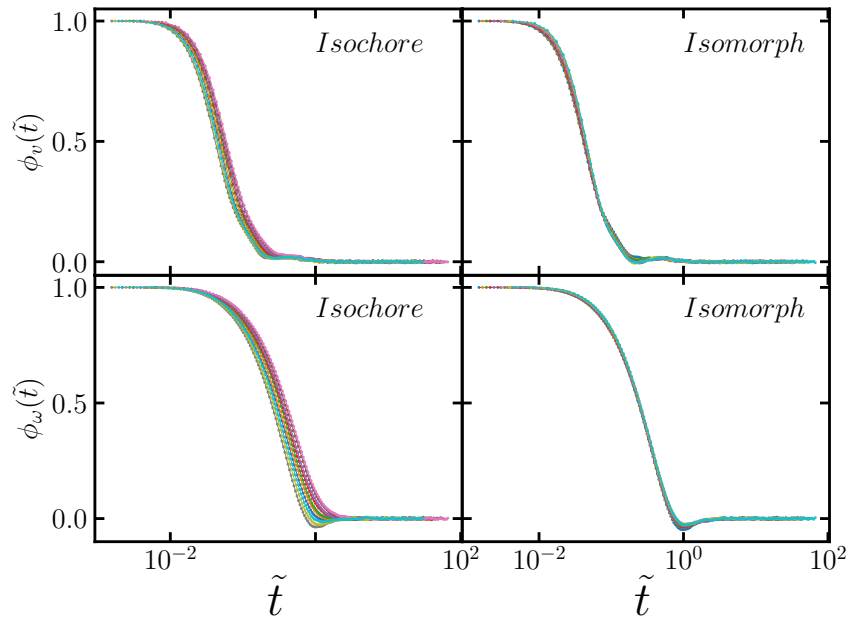
Figure 5.4: Upper panel: center-of-mass velocity auto-correlation function as a function of the reduced time. Lower panel: angular velocity auto-correlation function.
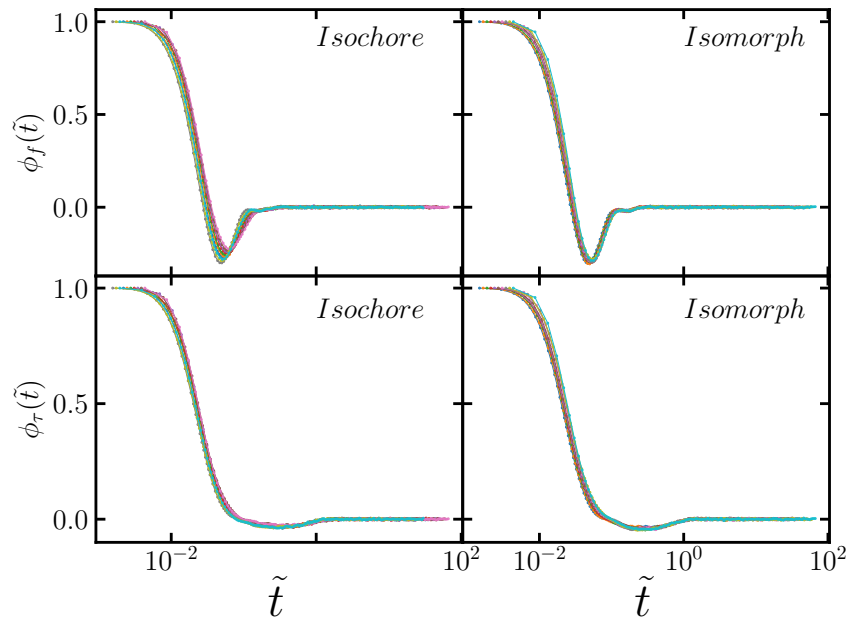
Figure 5.5: Upper panel: force auto-correlation function as a function of the reduced time. Lower panel: torque auto-correlation function.
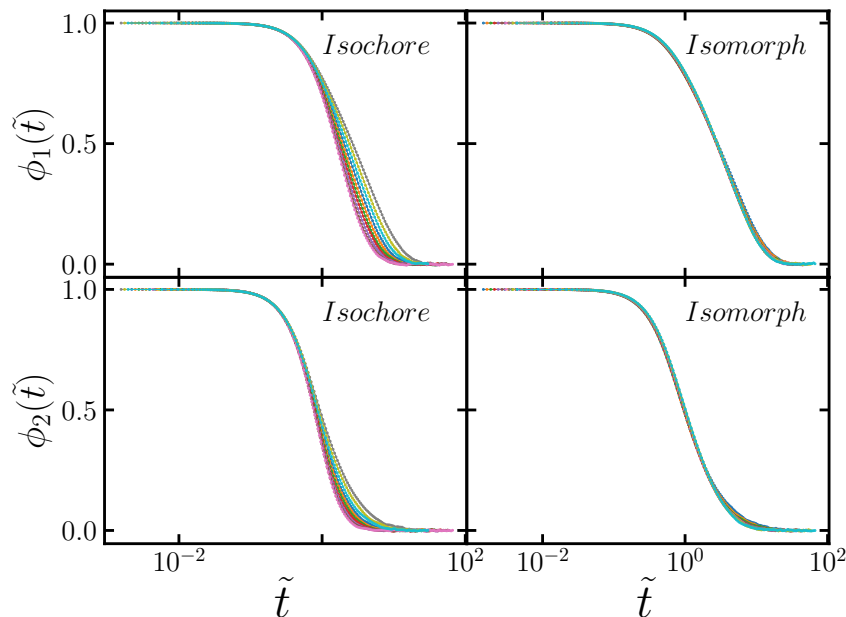
Figure 5.6: First order (upper panel) and second order (lower panel) orientational auto-correlation function.

We have observed that the dynamic characteristics of the $GB(0.345, 0.2, 1, 2)$ is only invariant along the isomorph but not the isochore, which is consistent with the isomorph theory prediction.

5.1.2.2 Structure

In this part, we are going to look at the structure in the reduced unit. In Fig. 5.7, we show the radial distribution function (upper row), $g(r)$, and the second rank orientational pair-correlation function (lower row), $G_2(r)$, along the isochore and the isomorph as a function of distance. Although there is not a big difference between the two, the data are more invariant along the isomorph.

Based on the observations so far, we can conclude that the isomorph invariant of the isotropic phase of the discotic Gay-Berne model is more evident in dynamics than the structure. Bacher *et al.* [37] reported a similar finding for the EXP pair potential system.

5.1.3 Constant-Exponent Density-Scaling

According to density scaling, which is often known as the thermodynamic scaling concept, various dynamic quantities, such as relaxation time, diffusion coefficient, etc., can be scaled onto a master curve. This master curve
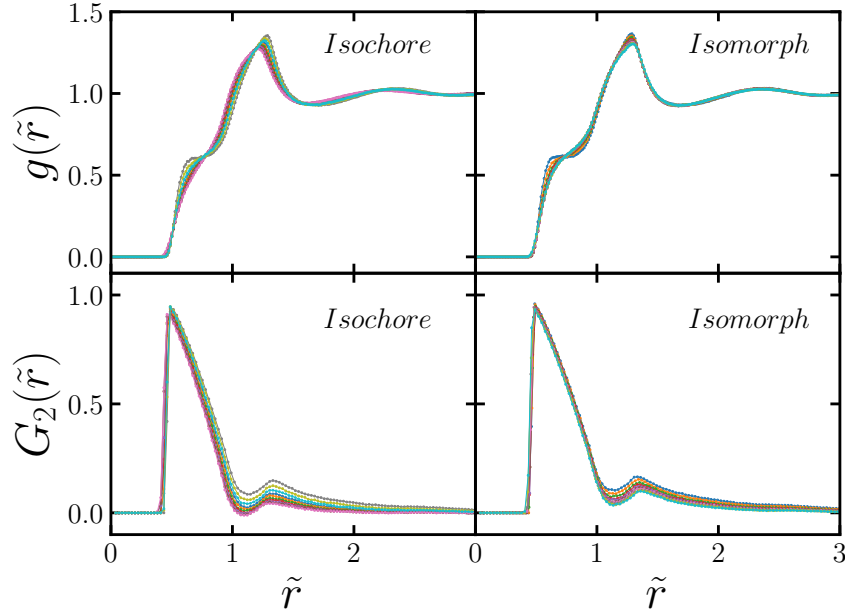
Figure 5.7: Radial distribution function and orientational correlation function plotted as functions of the reduced distance along the isochore and the isomorph.

is defined as a function $f(\Gamma)$ of a single scaling variable

$$\Gamma = \frac{\rho^{\gamma_{ds}}}{T},$$

(5.2)

where ρ is the density, T is the temperature, and γ_{ds} is the scaling exponent. In the classical version of density scaling, γ_{ds} is assumed to be a material constant independent of the thermodynamic conditions, i.e., not varying through the phase diagram [8, 148], and obtained by fitting.

However, in the isomorph theory, γ is not a material constant; it is a state point-related quantity. According to the isomorph theory, whenever there is a strong correlation between the potential energy and the virial; the density scaling exponent is equal to the average value of γ, i.e., $\gamma_{ds} = \bar{\gamma}$. Variation of γ and R along the isomorph shown in Fig. 5.8. The correlation coefficient increases by density and temperature. Meanwhile, γ also increases and reaches a maximum value close to $\gamma = 11.6$ and then levels off.

We calculate the average value of γ along four different isochores $\rho_1 = 2.2$, $\rho_2 = 2.3$, $\rho_3 = 2.4$, and $\rho_4 = 2.5$ with temperature range $T_1 \in [5, 43]$, $T_2 \in [4, 32]$, $T_3 \in [10, 32]$, and $T_1 \in [11, 43]$, which resulted in $\gamma = 11.5$. Compare to different Lennard-Jones models, where γ is close to 6, γ value for discotic Gay-Berne is much larger [14, 24, 25].

Fig. 5.9 shows the average angular relaxation time, i.e., the average relaxation time of the angular auto-correlation function $\phi_1(t)$, both in regular

and reduced units. We identified the $\tau_{angular}$ as the time at which $\phi_1(t)$ has decayed to the value 0.2. Fig. 5.9a corresponds to the regular unit, while in Fig. 5.9b, we test the constant-exponent density-scaling with the average value of γ. A good collapse occurs for most data with some deviations at longer relaxation times which correspond to the low-temperature simulation. The γ values deviate most from their average value in this region.

The same thing happens in Fig. 5.10, which shows the center of mass diffusion coefficient D. Fig. 5.10a shows the variation of diffusion coefficient as temperature varies. Fig. 5.10b shows the reduced diffusion coefficient as a function of $\rho^{11.5}/T$. A good data collapse occurs here.

So far, we have demonstrated the existence of isomorphs in the high-temperature isotropic phase of the discotic Gay-Berne model with the choice of parameters $GB(0.345, 0.3, 1, 2)$. This means that the model has hidden-scale-invariance symmetry [30], making the thermodynamic phase diagram one-dimensional. We also show that the constant-exponent density-scaling with $\gamma = 11.5$ applies for the model, and good collapses have been observed when $\tilde{D}$ and $\tilde{\tau}_{angular}$ plotted as functions of $\rho^{11.5}/T$.
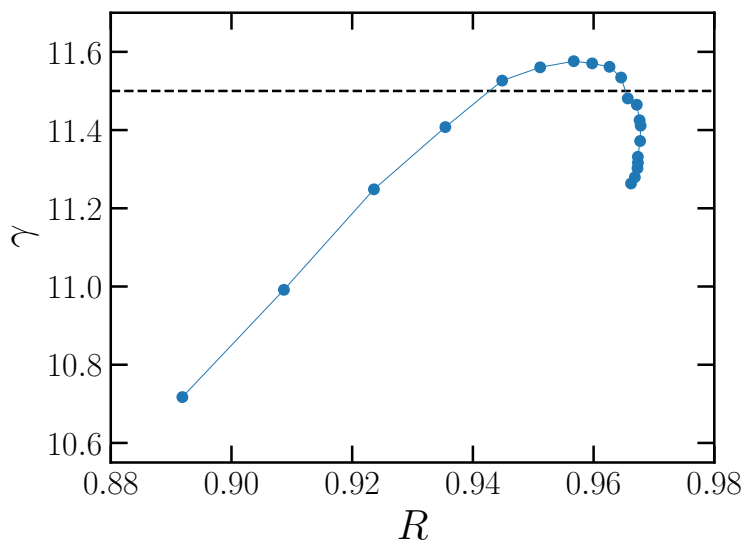
Figure 5.8: Variation of R and γ along the isomorph. The lower left corner data point correspond to the starting point $(\rho_{ref}, T_{ref}) = (2.3, 5.0)$.
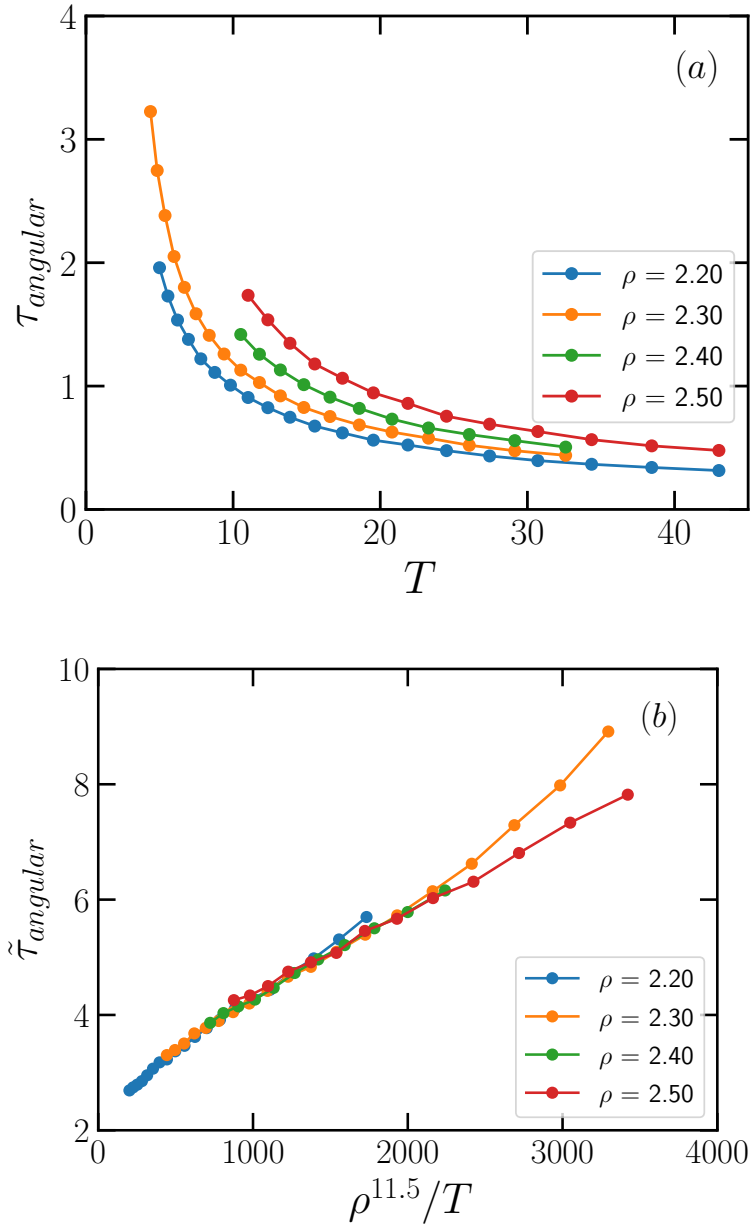
Figure 5.9: (a) Average angular relaxation time as a function of temperature along four isochores with density varying from $\rho = 2.2$ to $\rho = 2.5$. (b) The same data for the average angular relaxation time plotted in reduced units as a function of the density-scaling variable ρ^{γ}/T with $\gamma = 11.5$.
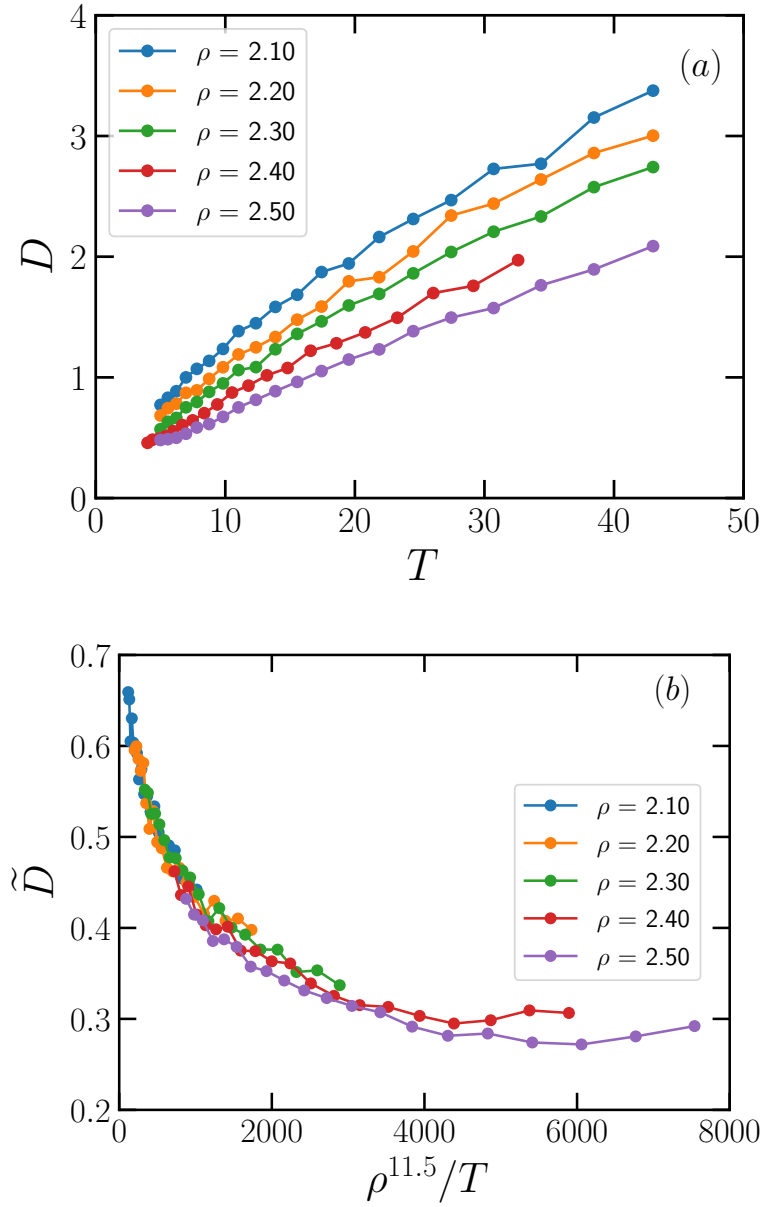
Figure 5.10: (a) Diffusion coefficient as a function of temperature along five isochores with density varying from $\rho = 2.1$ to $\rho = 2.5$. (b) The same data for the diffusion coefficient plotted in reduced units as a function of the density-scaling variable ρ^γ / T with $\gamma = 11.5$.

5.2 Isomorphs in Calamitic Liquid Crystal

In this section, we study the case of $GB(3, 5, 2, 1)$, which leads to calamitic liquid crystal phases. This set of parameters had been initially introduced by Gay and Berne [95]. We investigate the possibility of finding isomorphs in the isotropic and nematic phases of the model. We were inspired by the works of Satoh *et al.*, which show that the density scaling method works quite well for the Gay-Berne potential with the choice of parameters that form calamitic liquid crystal (rod-shaped particles) [12, 13]. Unlike discotic Gay-Berne, no extra modification is needed here, and we use the same potential introduced in Chapter 4 (see Eqs. 4.37a - 4.38c).

We simulate a system consisting of $N = 1372$ mesogens. The potential is truncated and shifted at $r_c = 4.0$. Units are defined by fixing σ_s and ϵ_0 to unity. The moment of inertia for all rods is chosen to be $I = 1$. The equilibration and production simulation consist of 19×10^6 and 67×10^6 respectively with $\delta t = 0.001$. We use the same method explained earlier in the previous section to generate isomorphs, i.e., configurational adiabat.

5.2.1 Phase Diagram of GB(3,5,2,1)

Fig. 5.11 shows the heat-map phase diagram of the model with respect to the correlation coefficient and the orientational order parameter. The regions with $R > 0.9$ are expected to show isomorphic behaviors. In Fig. 5.11 "I" stands for isotropic, "N" for nematic, and "S" for smectic phases. The dark green triangles are extracted from Ref [126]. The isomorphs, solid lines, are starting from the reference points $(\rho_{ref}, T_{ref}) = (0.25, 1.2)$, $(\rho_{ref}, T_{ref}) = (0.27, 1.2)$, $(\rho_{ref}, T_{ref}) = (0.30, 1.2)$, $(\rho_{ref}, T_{ref}) = (0.32, 1.2)$, $(\rho_{ref}, T_{ref}) = (0.33, 1.1)$, $(\rho_{ref}, T_{ref}) = (0.33, 1.2)$, and $(\rho_{ref}, T_{ref}) = (0.35, 1.2)$. We will present the results for $(\rho_{ref}, T_{ref}) = (0.27, 1.2)$ and $(\rho_{ref}, T_{ref}) = (0.33, 1.2)$, the two solid black curves, and bring the rest in the Appendix C. The light blue triangles are approximate prediction of the isotropic-nematic phase boundary based on $(\rho_{ref}, T_{ref}) = (0.32, 1.2)$ isomorph. Smectic investigation is still in progress and you can find some preliminary results in Appendix D.

In Fig. 5.12, we present a snapshot of the system at equilibrium in isotropic, nematic, and smectic phases. It is clear that there is no positional and orientational ordering in the isotropic phase. In the nematic phase still, there is no positional ordering, but there is some long-range orientational ordering. In the smectic phase, particles form parallel layers, and there is a robust orientational ordering within the layers.
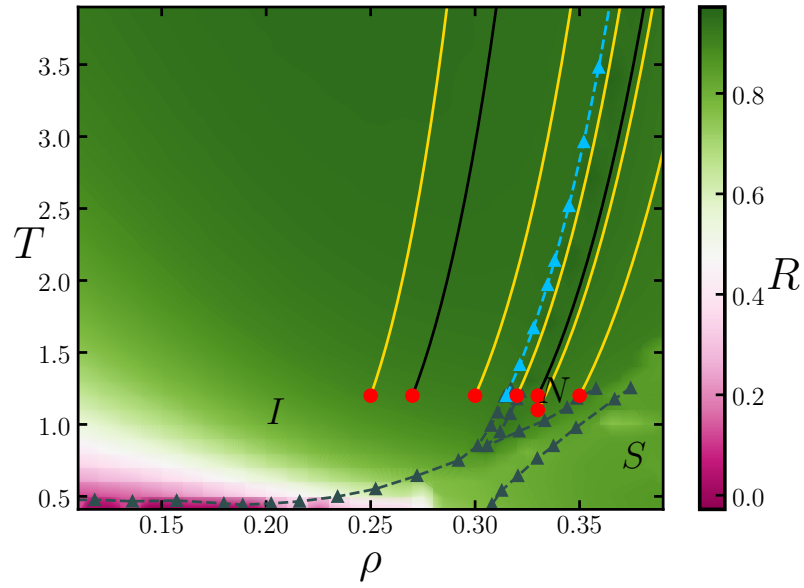
(a)
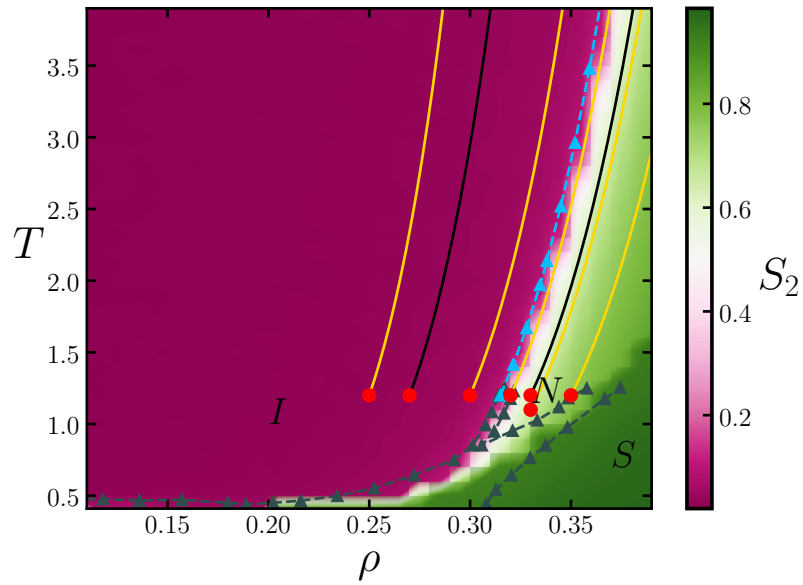
(b)

Figure 5.11: The phase diagram of the calmitic $GB(3,5,2,1)$ model with (a) correlation coefficient, R, values; and (b) order parameter, S_2 values given by the color code to the right. The dark green triangular symbols delimit the phase boundaries[126]. I stands for the isotropic, N for the nematic, and S for the smectic phases. The red filled circles are the isomorph reference state points and the solid curves are the isomorphs. The two black curves are correspond to the two isomorph we presenting here.
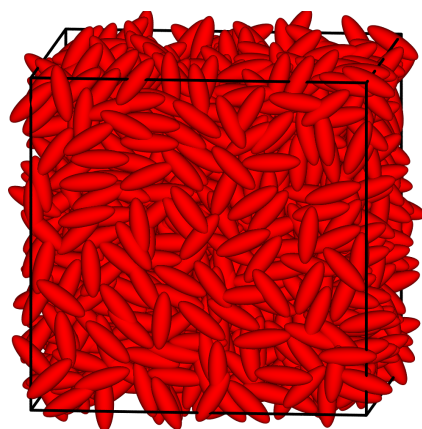
(a)
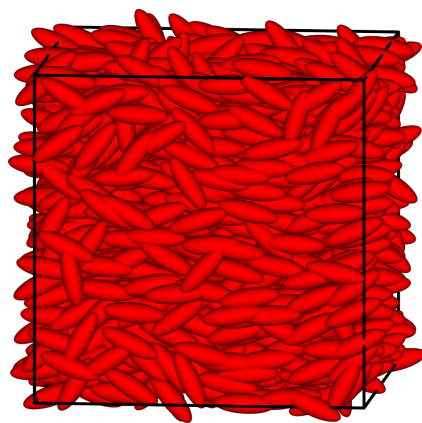
(b)
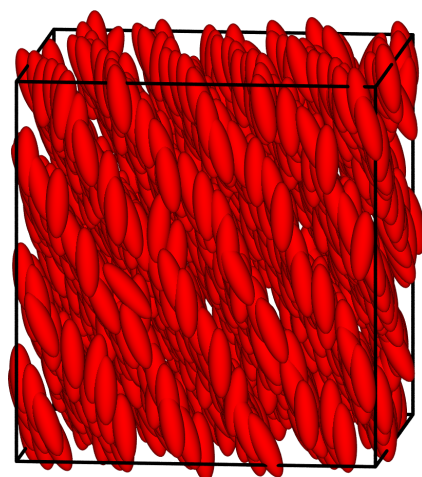
(c)

Figure 5.12: Snapshots of the calamitic Gay-Berne model in thermal equilibrium at three state points (schematic drawings). (a) shows the isotropic liquid phase at $(\rho, T) = (0.27, 1.2)$; (b) shows the nematic phase at $(\rho, T) = (3.3, 1.2)$; (c) shows the smectic phase at $(\rho, T) = (3.9, 1.2)$

51

5.2.2 Isomorph in Isotropic Phase

Here we will compare the level of invariance in dynamics and structure along the isomorph starting at $(\rho_{ref}, T_{ref}) = (0.27, 1.2)$ with $\rho = 0.27$ isochore. We use the same temperature range $(1.2 < T < 27)$ for both. Table. 5.2 shows how the density, temperature, correlation coefficient, and γ vary along the isomorph.

5.2.2.1 Dynamics

Fig. 5.13 provides data for mean square displacement along the isomorph and the isochore. Like what we observed in discotic liquid crystal, the center of mass dynamics is invariant for longer times along the isomorph.
A comparison of the center of mass velocity (upper row) and the angular velocity (lower row) auto-correlation functions along the isochore (left column) and the isomorph (right column) is shown in Fig. 5.14. A pronounced data collapse occurs along the latter.
The force and torque auto-correlation functions are shown in Fig. 5.15. The two functions are invariant only along the isomorph.
Fig. 5.16 gives data for first- and second-order orientational auto-correlation functions. The function goes to zero in all cases, which means there is no orientational ordering in the system.
So far, we have seen that the dynamics of $GB(3,5,2,1)$ in the isotropic phase are only invariant along the isomorph but not the isochore. For the next step, we are going to check the structure.

5.2.2.2 Structure

This section aims to look at the structure in reduced units. Fig. 5.17 shows the radial distribution function, $g(r)$, and the second-rank orientational pair correlation function, $G_2(r)$, as a function of pair distance along the isochore and the isomorph. The data are more invariant along the isomorph.

ρ	T	R	γ
0.27	1.2	0.9077	8.4553
0.2727	1.3057	0.9158	8.5107
0.2754	1.4215	0.9231	8.5535
0.2782	1.548	0.9285	8.5737
0.281	1.6859	0.933	8.5795
0.2838	1.8361	0.9367	8.5756
0.2866	1.9995	0.9396	8.5615
0.2895	2.177	0.9416	8.5383
0.2924	2.3697	0.9433	8.5126
0.2953	2.5788	0.9445	8.482
0.2982	2.8056	0.9457	8.4555
0.3012	3.0514	0.9461	8.4252
0.3042	3.3177	0.9467	8.3962
0.3073	3.6062	0.9469	8.3646
0.3104	3.9186	0.9468	8.3364
0.3135	4.257	0.9469	8.3084
0.3166	4.6231	0.9465	8.2815
0.3198	5.0194	0.9463	8.2542
0.323	5.4483	0.946	8.2276
0.3262	5.9125	0.9456	8.2032
0.3295	6.4148	0.945	8.1802
0.3327	6.9583	0.9446	8.1647
0.3361	7.5463	0.9442	8.1479
0.3394	8.1827	0.9436	8.1289
0.3428	8.8712	0.9428	8.1121
0.3463	9.6164	0.9423	8.0987
0.3497	10.4226	0.9416	8.0867
0.3532	11.2953	0.941	8.0735
0.3567	12.2396	0.9403	8.0628
0.3603	13.2616	0.9396	8.0562
0.3639	14.368	0.939	8.0462
0.3676	15.5657	0.9383	8.0443
0.3712	16.8622	0.9376	8.0396
0.3749	18.266	0.937	8.0345
0.3787	19.7859	0.9362	8.0315
0.3825	21.4318	0.9356	8.0285
0.3863	23.2145	0.935	8.0295
0.3902	25.1457	0.9342	8.0295
0.3941	27.2379	0.9335	8.0343

Table 5.2: Variation of density, temperature, correlation coefficient and γ for the isomorph starting at $(\rho_{ref}, T_{ref}) = (0.27, 1.2)$. At each step we increased density by 1% up to 40% overall.

Isotropic phase
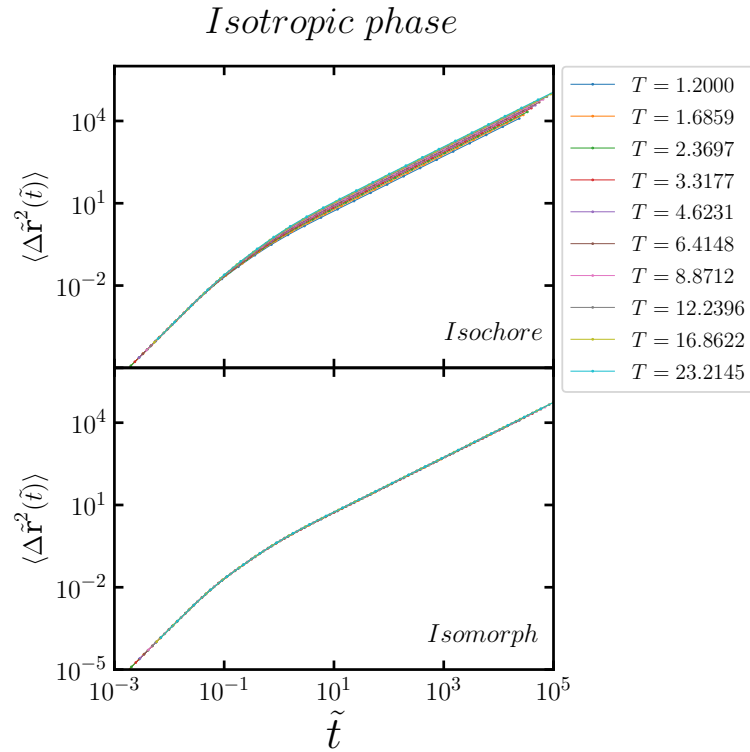
Figure 5.13: Comparing the mean square displacement along the isochore and the isomorph in reduced units. The data collapse is better along the isomorph. Data correspond to around 40% variation in density as reported in table 5.2.

Isotropic phase
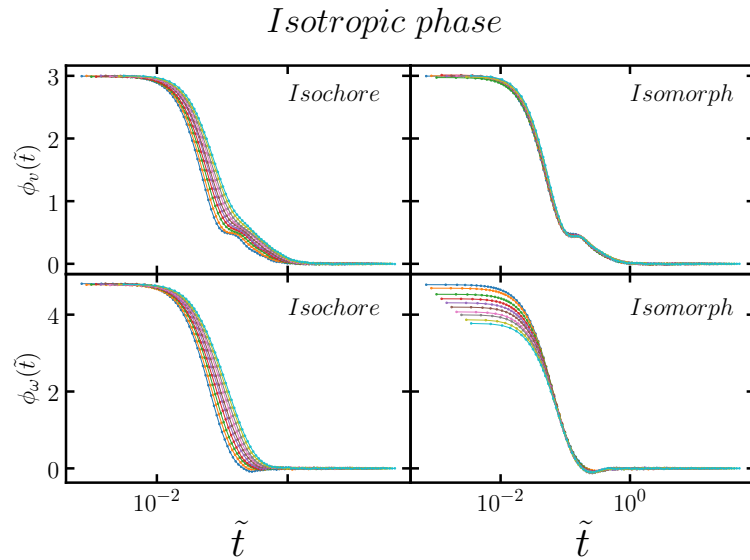
Figure 5.14: Upper: center-of-mass velocity auto-correlation function, lower: angular velocity auto-correlation function both as a function of reduced time.

Isotropic phase
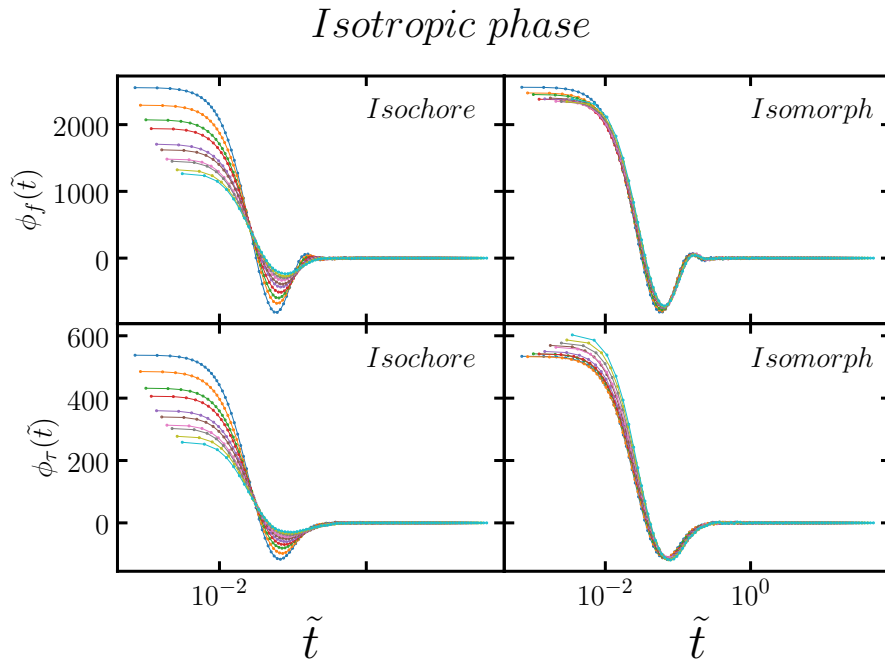
Figure 5.15: Upper: force auto-correlation function, lower: torque auto-correlation function both as a function of reduced time.

Isotropic phase
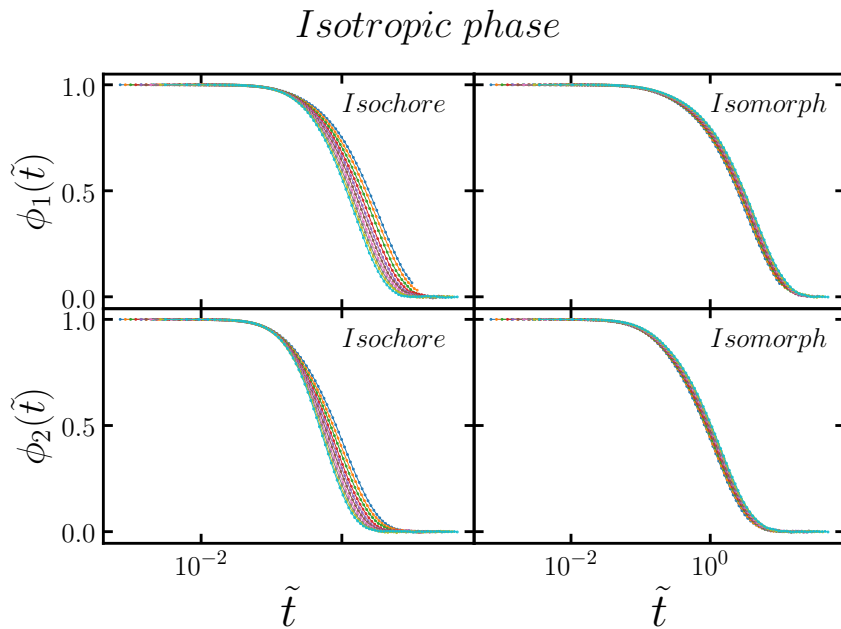
Figure 5.16: Upper: first-order and, lower: second-order orientational auto-correlation function both as a function of reduced time.
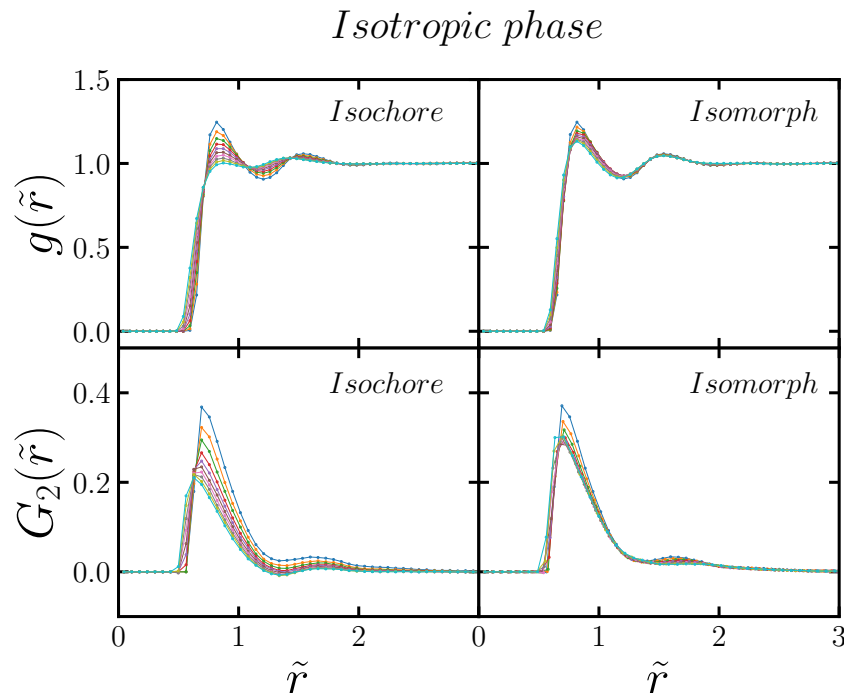
Figure 5.17: Radial distribution function and orientational correlation function plotted as functions of reduced distance along the isochore and the isomorph.

5.2.3 Isomorph in Nematic Phase

Up to now, we have seen that isomorphs exist in the isotropic phase of the Gay-Berne model for both discotic and calamitic cases. Here we will investigate the existence of isomorphs in the nematic phase of $GB(3, 5, 2, 1)$. As explained earlier, there is no positional ordering in the nematic phase. It looks like liquid if you look at the center of mass positions. But there is a long-range orientational ordering, and unit vectors are almost aligned along a preferred direction.

We generate isomorph starting at $(\rho_{ref}, T_{ref}) = (0.33, 1.2)$. Table. 5.3 provides the variation of ρ, T, R, and γ along the isomorph. We plot isomorph result together with the $\rho = 0.33$ isochore using the same temeprature range $(1.2 < T < 16)$ to make visual comparison.

5.2.3.1 Dynamics and Structure

In Fig. 5.18, we plot the mean square displacement along the isomorph and the isochore. As we have already observed earlier, the center-of-mass dynamics are only invariant along the isomorph.

56

ρ	T	R	γ
0.33	1.2	0.9169	8.2217
0.3333	1.3027	0.923	8.2809
0.3366	1.4149	0.9274	8.3187
0.34	1.5371	0.9315	8.3349
0.3434	1.67	0.9342	8.3301
0.3468	1.8142	0.9359	8.3183
0.3503	1.9705	0.9375	8.2957
0.3538	2.1398	0.9385	8.2664
0.3573	2.3229	0.9389	8.2333
0.3609	2.5209	0.9393	8.2066
0.3645	2.7349	0.9394	8.1697
0.3682	2.966	0.9392	8.1395
0.3719	3.2156	0.9393	8.1057
0.3756	3.4851	0.9387	8.0731
0.3793	3.7759	0.9384	8.0433
0.3831	4.0898	0.9375	8.0058
0.387	4.4283	0.9367	7.9788
0.3908	4.7934	0.9362	7.9487
0.3947	5.1873	0.9354	7.9212
0.3987	5.6119	0.9345	7.8922
0.4027	6.0697	0.9337	7.8677
0.4067	6.5632	0.9321	7.8438
0.4108	7.0953	0.9315	7.8229
0.4149	7.6689	0.9306	7.7996
0.419	8.287	0.9296	7.7791
0.4232	8.9533	0.9286	7.762
0.4274	9.6715	0.9277	7.7464
0.4317	10.4455	0.9264	7.7286
0.436	11.2797	0.9258	7.7155
0.4404	12.1786	0.9244	7.6942
0.4448	13.1473	0.9232	7.6844
0.4492	14.1912	0.9223	7.6712
0.4537	15.316	0.9209	7.6535
0.4583	16.5277	0.9197	7.6442

Table 5.3: Variation of density, temperature, correlation coefficient and γ for the isomorph starting at $(\rho_{ref}, T_{ref}) = (0.33, 1.2)$. At each step we increased density by 1%.
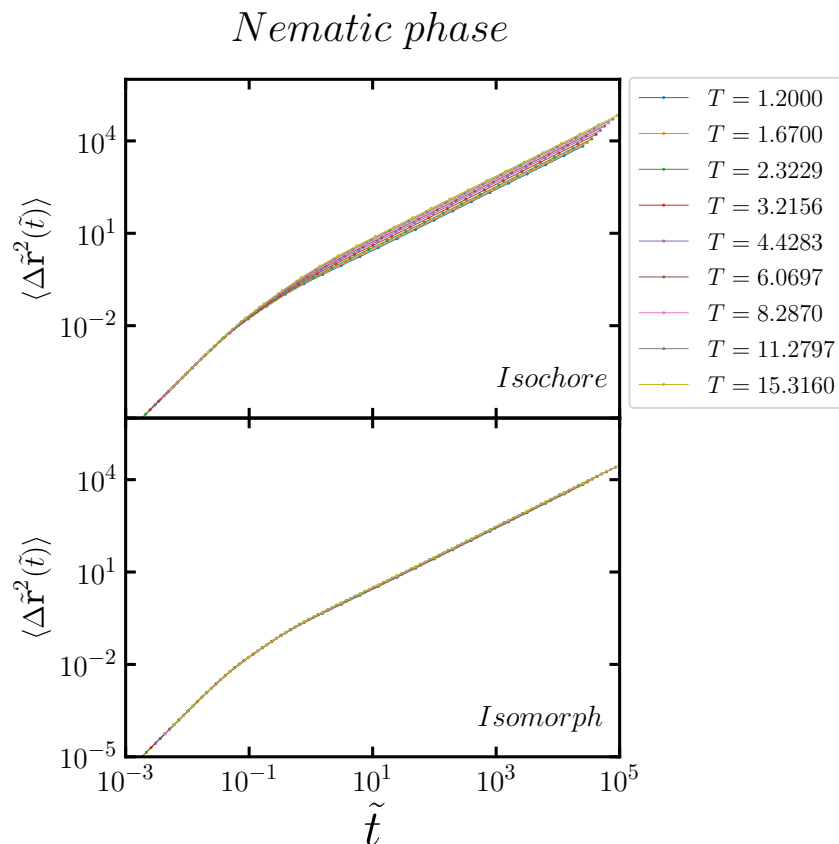
Figure 5.18: Comparing the mean square displacement along the isochore and the isomorph in reduced units. The data collapse is better along the isomorph. Data correspond to around 35% variation in density as reported in table 5.3.

Fig. 5.19 compares the velocity and angular velocity auto-correlation functions along the isomorph and the isochore. A pronounced data collapse can be observed only along the isomorph.

The force and torque auto-correlation functions are shown in Fig. 5.20. The two functions are invariant only along the isomorph. The first- and second-rank orientational auto-correlation functions are plotted in Fig. 5.21 along both isomorph and isochore. In the case of isochore, for temperature higher than $T_{ref} = 1.2$, the function goes to zero, which means that a nematic to isotropic phase transition is happening. On the other hand, the function maintains its value for longer time along the isomorph. We can claim that no phase transition occurs if you go along the isomorph.

In Fig. 5.22, we examine the validity of the isomorph theory in the structure of the $GB(3, 5, 2, 1)$ model. The $g(r)$ and $G_2(r)$ are plotted as functions of pair distance along the isochore and the isomorph. Both functions are

Nematic phase
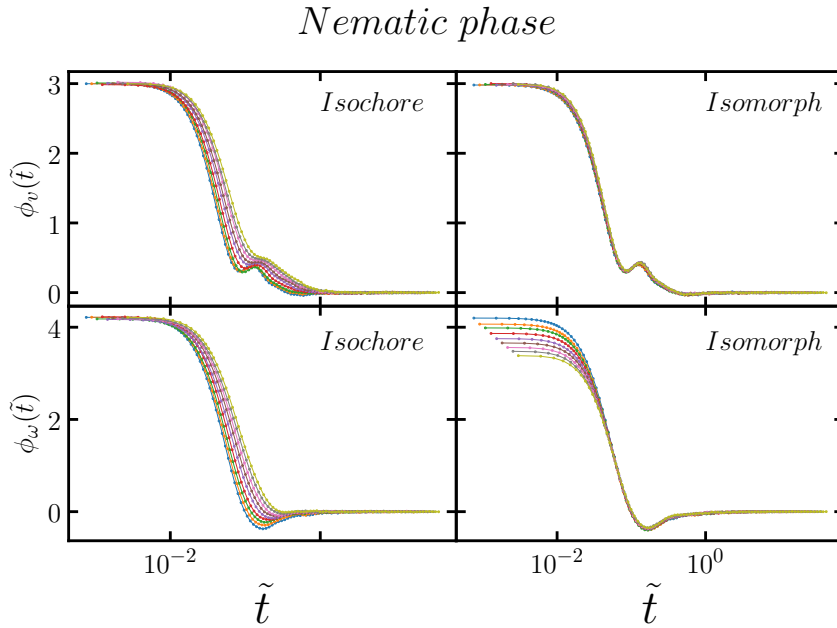
Figure 5.19: Upper: center-of-mass velocity auto-correlation function, lower: angular velocity auto-correlation function both as a function of reduced time.

invariant only along the latter. In the case of the isochore, the average tail value of $G_2(r)$ decreases and goes to zero as the temperature increases. One can interpret that as a nematic to isotropic phase transition. The average value of the tail remains intact along the isomorph as we increase the density and temperature, which is not surprising because dynamics and structure are invariant along the isomorph.

This chapter demonstrates the existence of isomorphs in the phase diagram of the Gay-Berne model. To show that, we investigated two set of parameters, i.e., $GB(0.345, 0.2, 1, 2)$ and $GB(3, 5, 2, 1)$ which are the most studied sets of parameters in the literature. We have shown that isomorphs exist at high temperatures in the phase diagram of discotic Gay-Berne. We also showed that the constant exponent density scaling works quite well for the model. Finally, we proved the existence of isomorphs in the nematic and isotropic phases of the calamitic Gay-Berne model.

Nematic phase
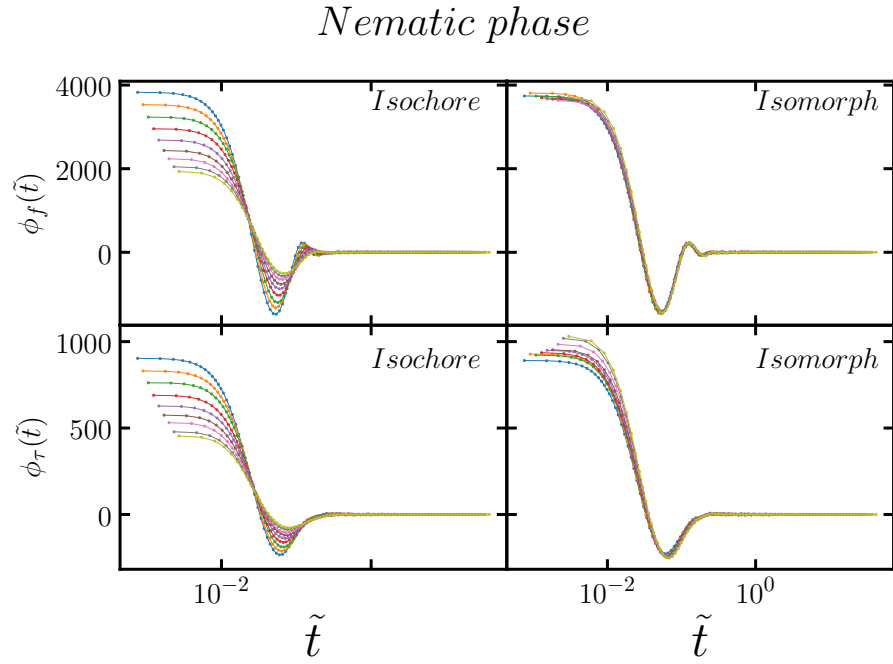
Figure 5.20: Upper: force auto-correlation function, lower: torque auto-correlation function both as a function of reduced time.

Nematic phase
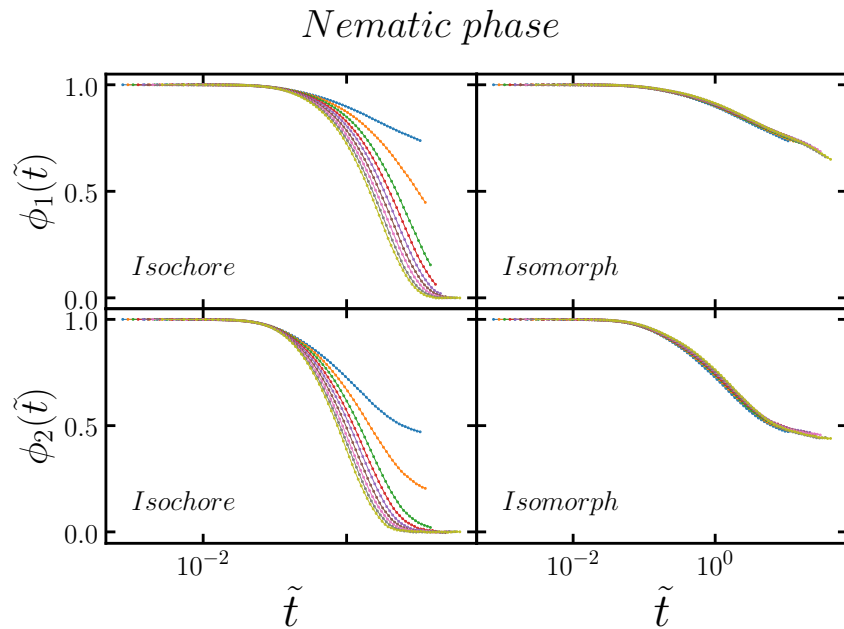
Figure 5.21: Upper: first-order and, lower: second-order orientational auto-correlation function both as a function of reduced time.

Nematic phase
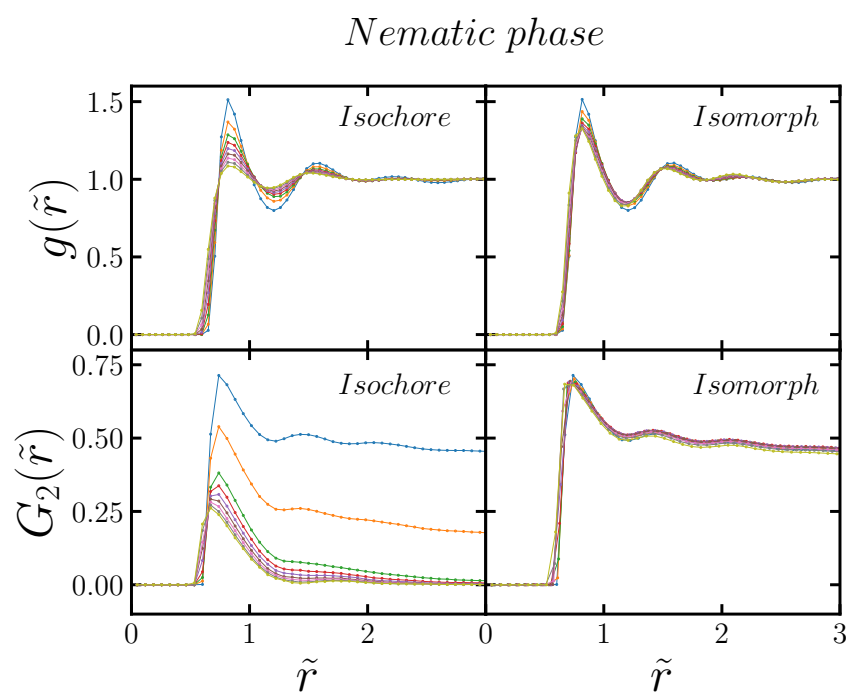
Figure 5.22: Radial distribution function and orientational correlation function plotted as functions of reduced distance along the isochore and the isomorph.

Chapter 6

Single-Paramter Aging

This chapter investigates physical aging of the 2:1 Kob-Andersen binary Lennard-Jones mixture through computer simulation. It has been shown that this system shows remarkable resilience against crystalization compared to the standard 4:1 concentration. All the aging simulations reported in this chapter started from thermal equilibrium at T_{start} and eventually reached equilibrium at the new T_{end}. Meanwhile, the following four quantities have been monitored during aging: 1) virial, 2) potential energy, 3) average squared force, and 4) Laplacian of the potential energy. Although we initiated larger temperature jumps compared to experimental studies, the results show good agreement with single parameter aging predictions.

6.1 Introduction

Understanding and predicting how fast a material property changes over time is of a great interest [149]. A gradual change in a material property is called aging; weathering and corrosion are good examples. Physical aging refers to changes in properties that result from changes in molecular arrangements due to, e.g., a different equilibrium temperature. [15–17]. A vast number of theoretical studies of aging have been conducted [15–17, 23, 150–159]. Physical aging has also been investigated in experimental studies under different circumstances dealing with oxide, metallic, and spin glasses [16, 17, 160–163]. To probe physical aging density [164, 165], enthalpy [16, 151], Young's modulus [164], and some frequency-dependent responses [23, 152, 166–172] have been monitored.

Far away from the glass transition temperature, the thermal cycling is reversible. Cooling and reheating fall on the same path. In the vicinity of the glass transition region, when a material is cooled or reheated, the same

path is not followed. The hysteresis effect is a consequence of physical aging. Physical aging is non-linear and non-exponential. The non-linearity of aging implies that the system's response to a small perturbation, in our case, an up or down temperature jump, depends on the sign of the input and its magnitude. More often, experimental studies of aging start from thermal equilibrium at T_{start} and end in equilibrium at T_{end}. Aging indicates that the two responses, the up and down temperature jumps, are not mirror-symmetric even if they have the same magnitude and target temperature.

As illustrated in Fig. 6.1, the down jump is flat at the beginning but slows down by getting closer to equilibrium at T_{end} ("self-retarding"). On the other hand, the up jump appears to be slower at the beginning and shows a steeper approach toward equilibrium ("self-acceleration"). This is the fictive temperature effect, also known as "asymmetry of approach" [173–175], an effect that comes from the fact that the relaxation rate is not constant and varies through time [17, 150, 151, 176–180].

6.2   TN Material Time Concept

At a temperature higher than the melting point, a liquid has a low viscosity. In the lower temperature range, the liquid becomes supercooled. By further cooling, a supercooled liquid behaves more like a "flowing solid" than a liquid [181]. In both regimes, the liquid and glassy phase, physical properties are highly temperature-dependent. At the glass transition region, a different behavior has been observed. The molecular arrangement changes gradually as temperature varies, and a significant delay is observed before reaching the equilibrium state. In this case, physical properties mainly depend on the thermal history of the system.

The standard formalism of physical aging was established by Narayanaswamy in 1971. The primary purpose was to predict how the thermal history affects the frozen-in stress in a windshield. Based on Tool's studies [15], Narayanaswamy introduced a single parameter aging assumption that considers the non-linearity of aging. This framework is now referred to as the Tool-Narayanaswamy (TN) formalism.

An essential concept of TN formalism is the material time ξ. One can interpret ξ as the time measured with a clock whose clock rate changes through the aging process. In simple terms, the material time is the time that the system experiences through the aging process and is proportional to laboratory time t as equilibrium approaches. This is similar to the proper time of relativity.

Since the clock rate measures how fast ξ changes over time, one can write

$$d\xi = \gamma(t)dt, \tag{6.1}$$

where $\gamma(t)$ is the clock rate.

According to the experimental data reported by Narayanaswamy, by switching from the actual time to the material time, the aging response becomes linear. In other words, the non-linearity nature of aging can be described by a linear convolution integral with respect to the material time [16, 17]. This implies that jumps with the same target temperature are symmetric if one considers them as functions of the material time.

6.3 Simulation Details And Initial Aging Results

All simulations reported here were performed in NVT ensemble with a Nose-Hoover thermostat using the $RUMD$ package (http://rumd.org). The system under study consists of $N = 10002$ particles of two different Lennard-Jones (LJ) spheres, A and B. The LJ interaction potential between particle types A and B is

$$U_{AB} = \epsilon_{AB}\left(\left(\frac{r}{\sigma_{AB}}\right)^{-12} - \left(\frac{r}{\sigma_{AB}}\right)^{-6}\right), \tag{6.2}$$

with $\sigma_{AA} = 1.0$, $\sigma_{AB} = \sigma_{BA} = 0.8$, $\sigma_{BB} = 0.88$, $\epsilon_{AA} = 1.0$, $\epsilon_{AB} = \epsilon_{BA} = 1.5$, and $\epsilon_{BB} = 0.5$. We use shifted potential model with $r_{cut} = 2.5\sigma_{\alpha\beta}$, where $\alpha, \beta \in \{A, B\}$ are particle types corresponding to interactions particle i and j, and $\Delta t = 0.0025$ in units defined by the A particle parameters. The potential parameters we use here are the same as those of the well-known Kob-Andersen mixture [182]. We choose the 2:1 ratio for A and B particles concentration instead of the standard 4:1 because the chosen ratio is more resistant to crystallization [183–185]. The mode-coupling temperature is approximately 0.55 for the 2:1 ratio, while the standard mixture's value is around 0.44. Mode-coupling temperature is a key concept in mode coupling theory (MCT) which predicts the onset of glassy behavior in a fluid or a disordered system.

MCT assumes that the dynamics of a fluid can be described in terms of a set of collective modes that become increasingly coupled to each other as the density or concentration of the system increases. At a certain value, the MCT predicts that the coupling between these modes becomes so strong that the system is no longer able to relax into its equilibrium state, resulting in a glassy or jammed state.

The mode coupling temperature, T_m, is defined as the temperature at which the dynamics of the system begin to deviate from those of a simple liquid, and the non-linear coupling of the collective modes becomes dominant. Above the mode coupling temperature, the system behaves as a simple liquid with exponential relaxation, while below T_m, the relaxation becomes non-exponential and glassy behavior emerges.

The following results correspond to $\rho = 1.4$ in the A particles units and averaged over 100 simulations. The system was carefully equilibrated at each starting temperature T_{start} before initiating any temperature jump. To equilibrate the lowest temperature, $T = 0.50$, we performed a rather long simulation consisting of 2.4×10^{11} time steps. Afterward, we obtained 100 equilibrium configurations by writing a configuration every 1.678×10^8 time step, which is of the same order of magnitude as the relaxation time τ to ensure statistically independent configurations.

Along with each aging simulation, we probe five different quantities; the potential energy, the virial, the configurational temperature defined as follow,

$$k_B T_{conf} = \frac{\langle (\nabla U)^2 \rangle}{\nabla^2 U}, \tag{6.3}$$

its numerator (the average squared force), and its denominator (the Laplacian of the potential energy). Eq 6.3 is valid in thermal equilibrium, it is interesting to see if it is still valid out of equilibrium. Fig. 6.1 and Fig. 6.2 present temperature jumps to the same and different temperatures, respectively. Each curve is a result of averaging over 100 simulations. We find that the configurational temperature, T_{conf}, does not age and equilibrate instantaneously (see Fig. 6.1c), consistent with previous results reported by Powles *et al.* [186]. Most likely there is a simple explanation for it, but we do not know it. In the rest, we focus on the other four quantities. These quantities are easy to calculate and probe along with an aging simulation. After the equilibration process at each starting temperature, T_{start}, we initiate a temperature jump by changing the thermostat temperature to desired target temperature T_{end}. The system eventually reaches equilibrium at T_{end} after a certain number of time steps which varies for each jump. The equilibrium value of the measured quantity χ at T_{end} is denoted by χ_{eq}. $\chi(0)$ denotes the equilibrium value of χ at T_{start}, just before aging simulation starts.
For each temperature jump we can define a normalized relaxation function $R(t)$ by subtracting χ_{eq} from the value at each time, $\chi(t)$, and divide it by overall changes, i.e.,

$$R(t) \equiv \frac{\Delta \chi(t)}{\Delta \chi(0)} = \frac{\chi(t) - \chi_{eq}}{\chi(0) - \chi_{eq}} \tag{6.4}$$

at $t = 0$, just before initiating a temperature jump, $R(0) = 1$ and for longer time as equilibrium approaches $R(t) \rightarrow 0$.
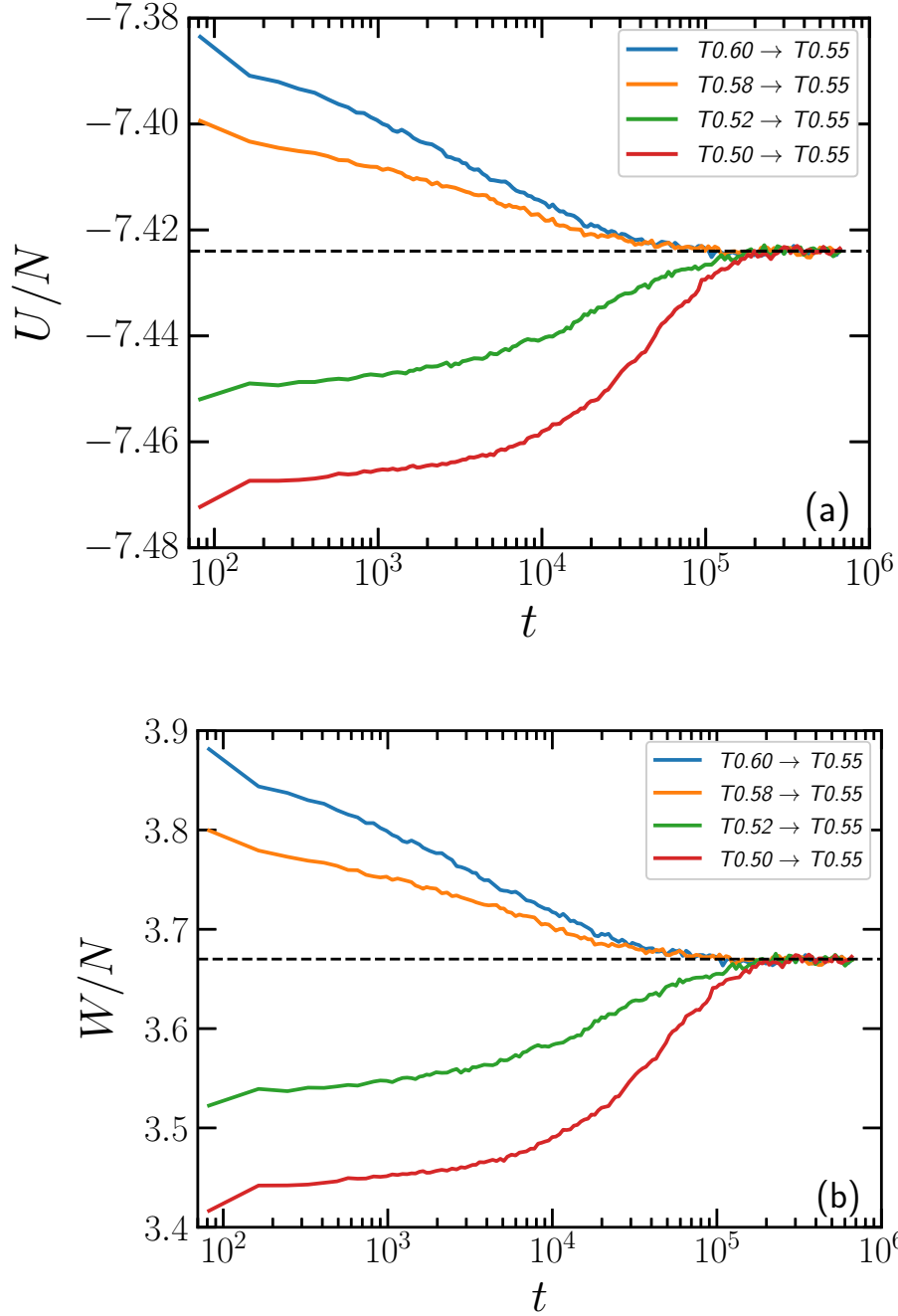
Figure 6.1: Aging data for jumps to the same target temperature $T = 0.55$. Each panel contains four jumps with $\Delta T = \pm 0.03$ and $\Delta T = \pm 0.05$. Red and green curves are correspond to up jumps, while those for down jumps are shown in blue and orange. (a) potential energy; (b) virial;

67
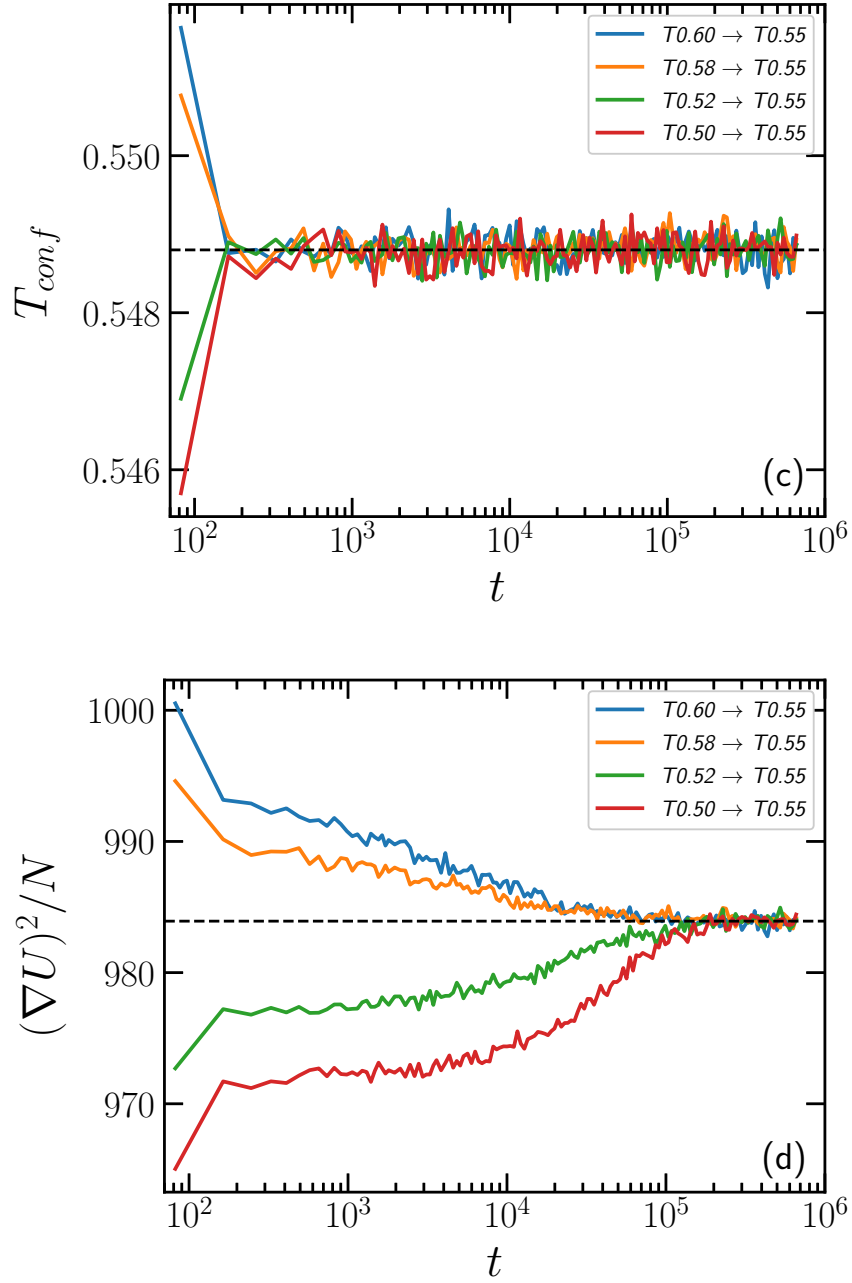
Figure 6.1: (c) configurational temperature, which does not age; (d) average squared force, which is the numerator of configurational temperature Eq. 6.3;
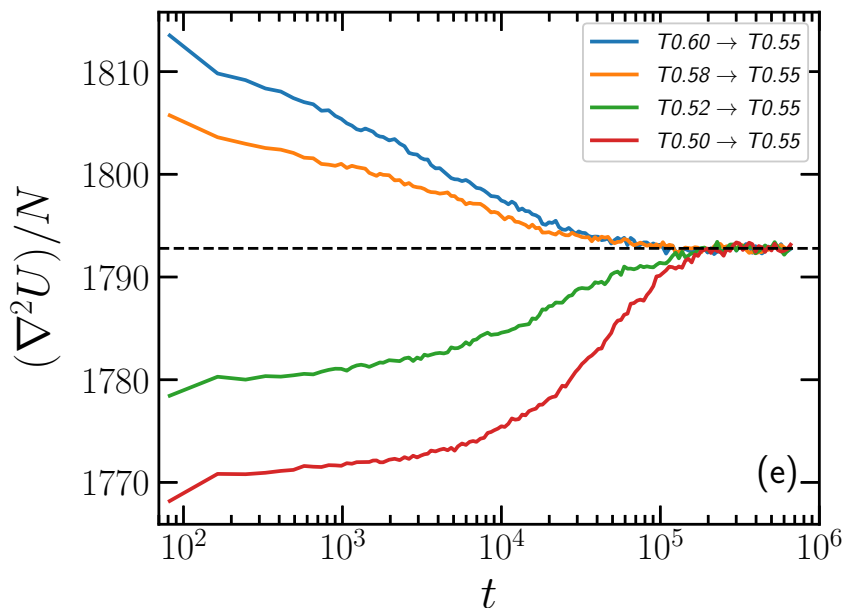
Figure 6.1: (e) the Laplacian of the potential energy, which is the denominator of configurational temperature, Eq. 6.3.

6.4 Single Parameter Aging

In experimental aging studies, the temperature is controlled and monitored on a thermometer. Hecksher *et al*. [23] and Roed *et al*. [22] recently studied physical aging of glass-forming liquids close to the glass transition temperature and probed the dielectric loss at 1 Hz, shear mechanical resonance frequency, the loss-peak frequency of the dielectric beta process, and the real part of the dielectric constant at 10 kHz. Hecksher *et al*. developed a single parameter aging (SPA) formalism based on Narayanaswamy's idea that the material time controls aging [16]. By using SPA, one can predict the normalized relaxation function of any desired temperature from the data of a single jump. SPA was first tested for jumps end at the same temperature for three different van der Waals liquids [23] and later on generalized by Roed *et al*. to deal with jumps ending at different temperatures [22].

The main assumption of SPA is that the clock rate, $\gamma(t)$, can be determined from the probe quantity $\chi(t)$. On other assumption is that temperature jumps are small enough to use a first-order Taylor expansion of the logarithm of the aging rate in term of χ. According to SPA, there is a single parameter $Q(t)$ controlling both the measured quantity $\chi(t)$ and the clock rate $\gamma(t)$. For small temperature changes one can Taylor expand $\chi(t)$ to the first-order in $Q(t)$: $\Delta\chi(t) \cong c_1 \Delta Q(t)$. The same is valid for the clock rate $\Delta \ln \gamma(t) \cong c_2 \Delta Q(t)$. c_1 and c_2 are constants and $\Delta Q(t)$, $\Delta\chi(t)$
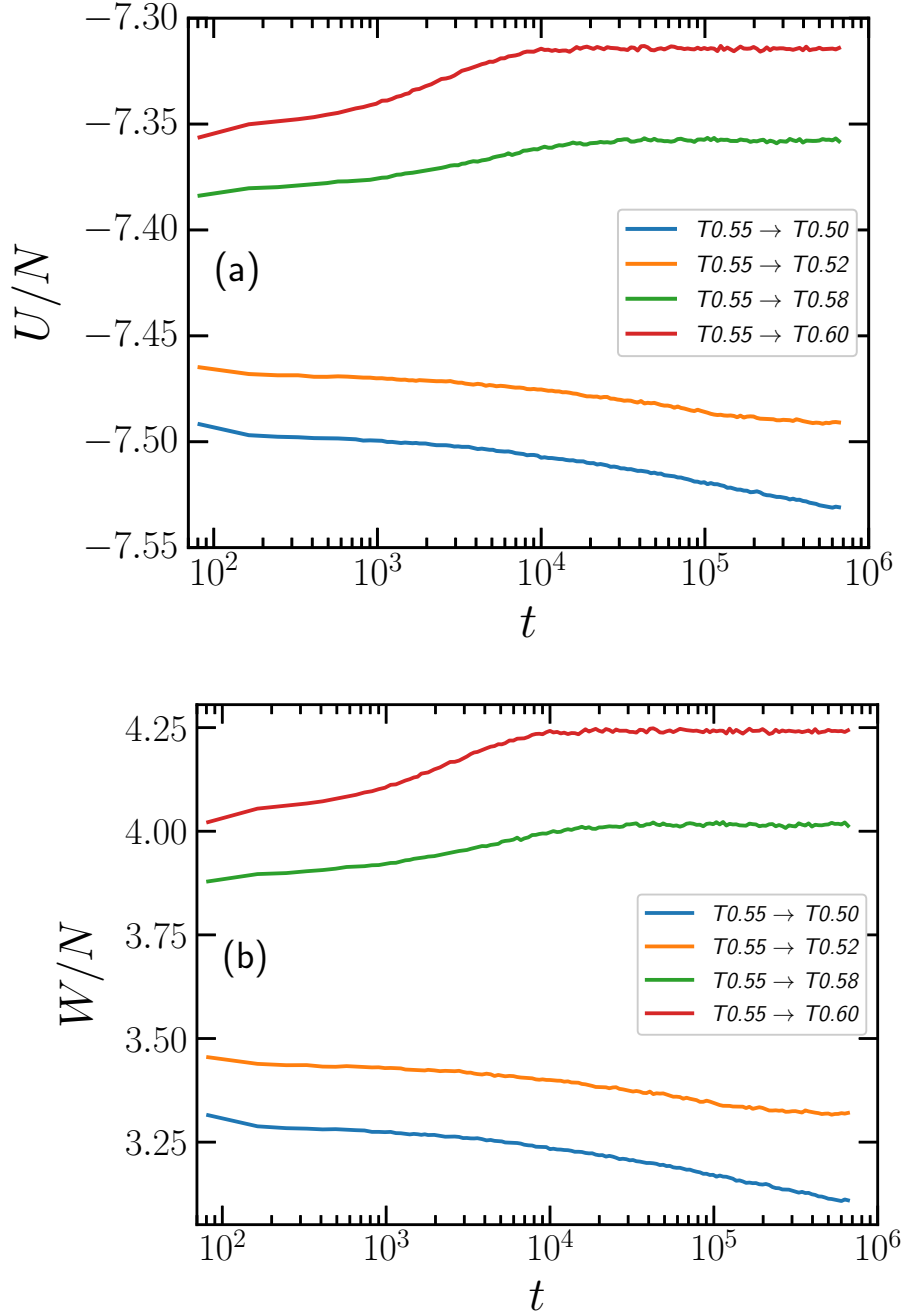
Figure 6.2: Aging data for jumps from the same initial temperature $T = 0.55$. Each panel contains four jumps with $\Delta T = \pm 0.03$ and $\Delta T = \pm 0.05$. Red and green curve are up jumps, while those for down jumps are shown in blue and orange. Note that the scale on the y axis is different from Fig. 6.1a potential energy; (b) virial;
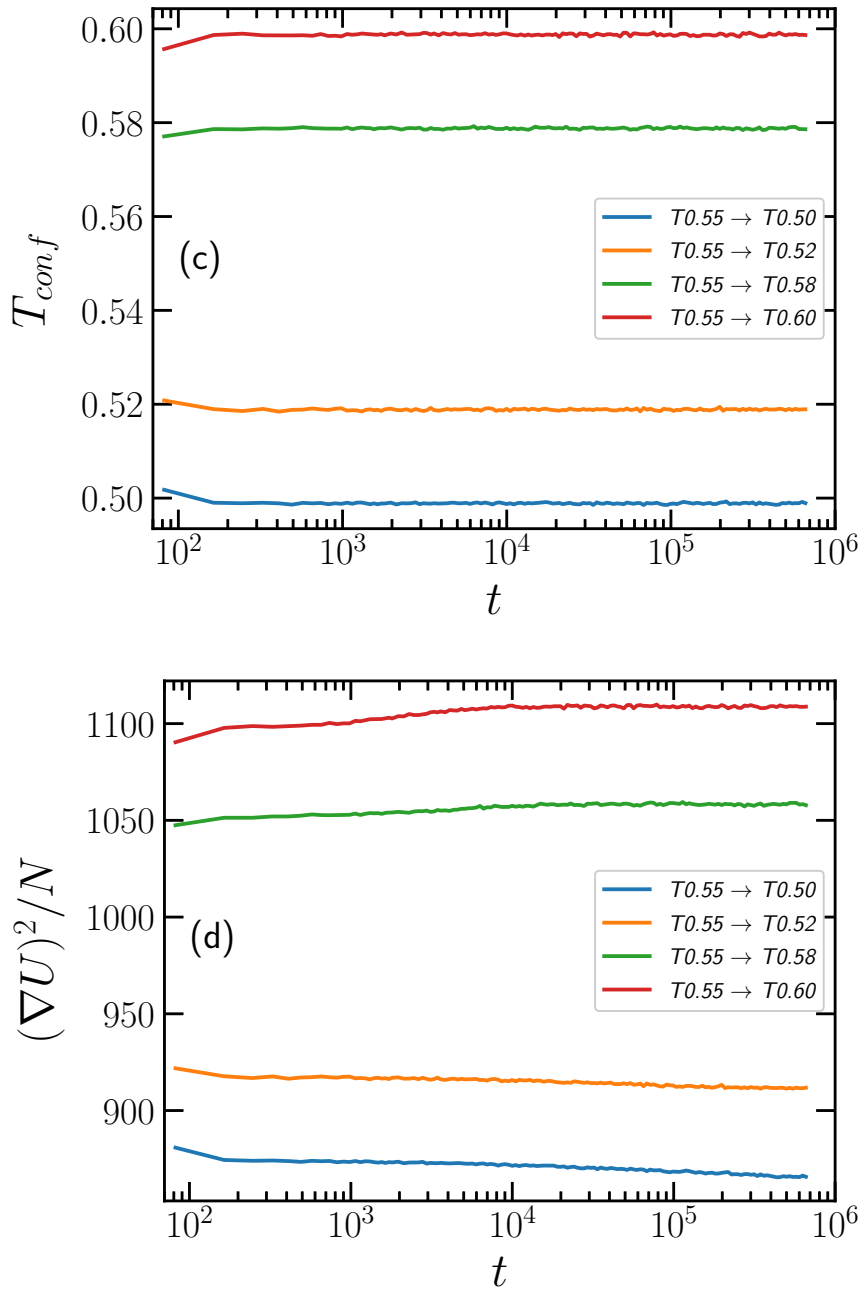
Figure 6.2: (c) configurational temperature, which does not age; (d) average squared force, which is the numerator of configurational temperature, Eq. 6.3;
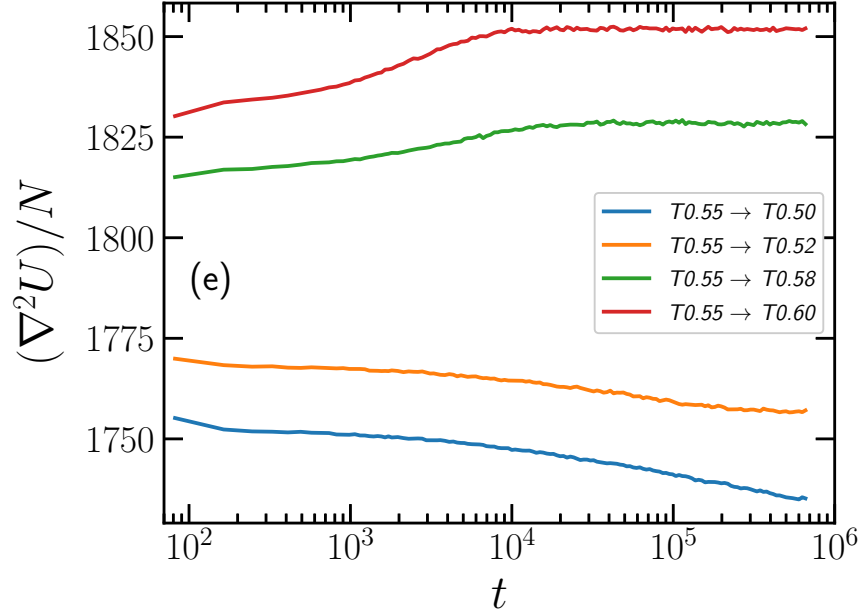
Figure 6.2: (e) the Laplacian of the potential energy, which is the denominator of configurational temperature Eq. 6.3.

and $\Delta \ln \gamma(t)$ are distances taken relative to equilibrium at each time for $Q(t)$, $\chi(t)$ and $\ln \gamma(t)$. By eliminating $\Delta Q(t)$ we have

$$\ln \gamma(t) = \ln \gamma_{eq} + \frac{\Delta \chi(t)}{\chi_{const}}, \tag{6.5}$$

where $\ln \gamma_{eq}$ is the equilibrium clock rate at the target temperature $\mathrm{T_{end}}$ and $\chi_{const} = c_1/c_2$. Based on the definition of $R(t)$, we can substitute $\Delta \chi(t)$ by $\Delta \chi(0) R(t)$

$$\ln \gamma(t) = \ln \gamma_{eq} + \frac{\Delta \chi(0)}{\chi_{const}} R(t), \tag{6.6}$$

so

$$\gamma(t) = \gamma_{eq} \exp\left(\frac{\Delta \chi(0)}{\chi_{const}} R(t)\right). \tag{6.7}$$

As t goes to infinity, $R(t)$ becomes zero so $\gamma(t) = \gamma_{eq}$.
The normalized relaxation function is a unique function of material time and is given by [16, 17, 23]

$$R(t) = \Phi(\xi). \tag{6.8}$$

According to the TN formalism, the function $\Phi(\xi)$ should be the same for all the temperature jumps. On the other hand, the time dependency of the material time, $\xi(t)$, is not universal. This is understandable as the clock

rate varies as the system ages. By considering equations 6.1 and 6.8, we can write

$$\dot{R}(t) = \Phi'(\xi)d\xi/dt,$$
$$= \Phi'(\xi)\gamma(t). \tag{6.9}$$

Since $R(t)$ is a unique function of ξ, we can conclude that for all jumps ξ is the same function of R. By $F(R) \equiv -\Phi'(\xi(R))$, we have [8]

$$\dot{R}(t) = -F(R)\gamma(t). \tag{6.10}$$

The negative sign arises from the normalized relaxation function being a monotonically decreasing function. Now by substituting $\gamma(t)$ from Eq. 6.7 to Eq. 6.10 one can write

$$-\frac{\dot{R}}{\gamma_{eq}}\exp\left(-\frac{\Delta\chi(0)}{\chi_{const}}R(t)\right) = F(R). \tag{6.11}$$

For a given $R(t)$, the right-hand side of the equation is independent of the magnitude and the sign (up or down jump) of the jump; this is also valid for the left-hand side. Eq. 6.11 enables us to predict the relaxation function of one jump from the relaxation function of another jump. To determine χ_{const}, two jumps are needed. For the rest, we refer to the known relaxation function as "jump 1". "jump 2" refers to the relaxation function we compared to the prediction based on jump 1. The primary purpose of SPA is to use the relaxation function of jump 1, $R_1(t)$ and its inverse function $t_1(R)$, to evaluate $t_2(R)$ for the relaxation function of jump 2.
At time $t_1^*(R)$ and $t_2^*(R)$ where the two jumps have the same relaxation function, $R_1 = R_2 = R$, Eq. 6.11 implies

$$-\frac{dR_1}{dt_1^*} \cdot \frac{1}{\gamma_{eq,1}} \cdot \exp\left(-\frac{\Delta\chi(0)_1}{\chi_{const}}R(t_1^*)\right)$$
$$= -\frac{dR_2}{dt_2^*} \cdot \frac{1}{\gamma_{eq,2}} \cdot \exp\left(-\frac{\Delta\chi(0)_2}{\chi_{const}}R(t_2^*)\right). \tag{6.12}$$

We can choose dt_1^* and dt_2^* in a way that $dR_1 = dR_2$, and by doing some simple math one can write

$$dt_2^* = \frac{\gamma_{eq,1}}{\gamma_{eq,2}}\exp\left(\frac{\Delta\chi(0)_1 - \Delta\chi(0)_2}{\chi_{const}}R(t_1^*)\right)dt_1^*, \tag{6.13}$$

and by integrating this

$$t_2 = \int_0^{t_2} dt_2^* = \frac{\gamma_{eq,1}}{\gamma_{eq,2}} \int_0^{t_1} \exp\left(\frac{\Delta\chi(0)_1 - \Delta\chi(0)_2}{\chi_{const}} R(t_1^*)\right) dt_1^*. \tag{6.14}$$

Eq. 6.14 transports a discrete set of time vector $\mathbf{t}_1 = (t_1^1, t_1^2, \ldots, t_1^n)$ and its corresponding relaxation vector $\mathbf{R}_1 = (R_1^1, R_1^2, \ldots, R_1^n)$ to a new set of time vector $\mathbf{t}_2 = (t_2^1, t_2^2, \ldots, t_2^n)$ corresponding to $\mathbf{R}_1$. Now if one plot $(\mathbf{t}_2, \mathbf{R}_1)$ it should coincides with R_2. For jumps ending at the same temperature Eq. 6.14 reduces to

$$t_2 = \int_0^{t_1} \exp\left(\frac{\Delta\chi(0)_1 - \Delta\chi(0)_2}{\chi_{const}} R(t_1^*)\right) dt_1^*. \tag{6.15}$$

In this study we define $\gamma_{eq} \equiv 1/\tau$, where τ is the relaxation time and can be identified from the intermediate scattering function. τ is the time at which intermediate scattering function decayed to 0.2.
The final step is to determine χ_{const}. For simplicity, let us consider the case of jumps ending at the same temperature; Eq. 6.15 implies

$$t_2 - t_1 = \int_0^{t_1} \left[\exp\left(\frac{\Delta\chi(0)_1 - \Delta\chi(0)_2}{\chi_{const}} R(t_1^*)\right) - 1\right] dt_1^*. \tag{6.16}$$

We can write similar expression for $t_1 - t_2$. Considering the long limits of the two expressions leads to the following self consistency requirement [23],

$$\int_0^\infty \left[\exp\left(\frac{\Delta\chi(0)_1 - \Delta\chi(0)_2}{\chi_{const}} R(t_1^*)\right) - 1\right] dt_1^* +$$
$$\int_0^\infty \left[\exp\left(\frac{\Delta\chi(0)_2 - \Delta\chi(0)_1}{\chi_{const}} R(t_2^*)\right) - 1\right] dt_2^* = 0 \tag{6.17}$$

By numerically solving Eq. 6.17 one can obtain χ_{const} for each quantity (see Fig. 6.3). Table 6.1 provides the values of χ_{const} for all studied quantities.

Quantity	U	W	$(\nabla U)^2$	$\nabla^2 U$
χ_{const}	0.01857	0.09944	5.117	10.04

Table 6.1: Different values of χ_{const} for all four measured quantities.
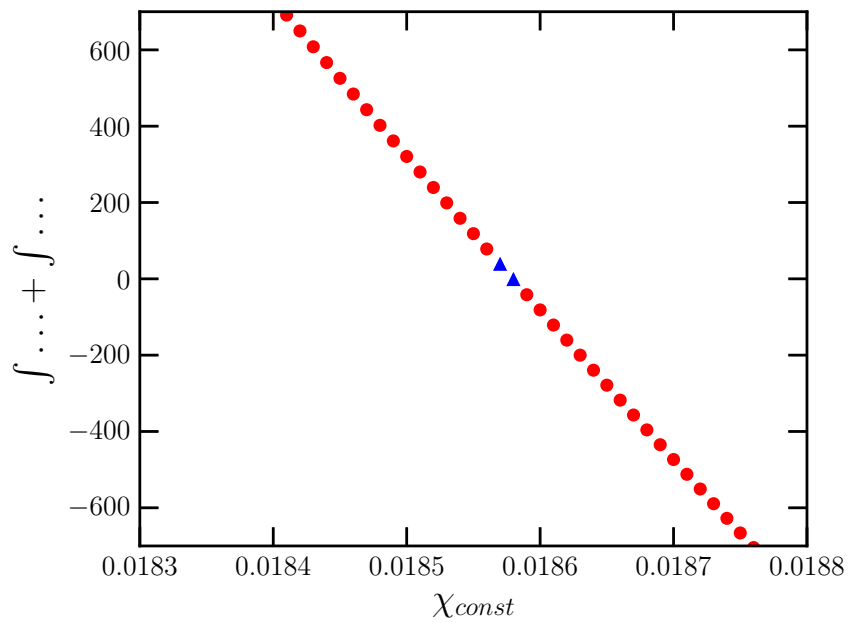
Figure 6.3: Determining the χ_{const} value for the potential energy by numerically solving Eq. 6.17. We used the two closet values to zero (one in negative and one other in positive side), the two blue triangles, to interpolate and calculate for which χ_{const}, Eq. 6.17 becomes zero.

6.5   Results

Fig. 6.4 validates SPA for jumps ending at the same target temperature, $T_{end} = 0.55$. Upper panels use down jumps (green curves) to predict up jumps (blue curves), and lower panels use up jumps to predict down jumps. All the relaxations start lower than unity because of the instantaneous relaxation at the early stage of the aging simulation. We investigate the case of jumps ending at different target temperatures in Fig. 6.5. The upper panels correspond to predictions based on up jumps, while in the lower panels, down jumps were used to predict up jumps. Although there are some small deviations initially, we can conclude that the results validate SPA in computer simulations.

In Fig. 6.6 and 6.7, we plot the four relaxation curves. They have been empirically scaled by multiplying $R(t)$ by a number to make the curves more comparable. It can be seen that the four quantities age in the same manner and control by the same material time.

It has been already discussed earlier in chapter 2 that there is a strong correlation between virial and potential energy equilibrium fluctuations for this system. The same is valid for out-of-equilibrium situations [27]. Therefore, except for the scaling constant, we expect W and U to have the same relaxation curves.

We have already seen that the configurational temperature does not age and equilibrate instantaneously after jumps. This implies that its numerator and denominator should have the same relaxation curves.
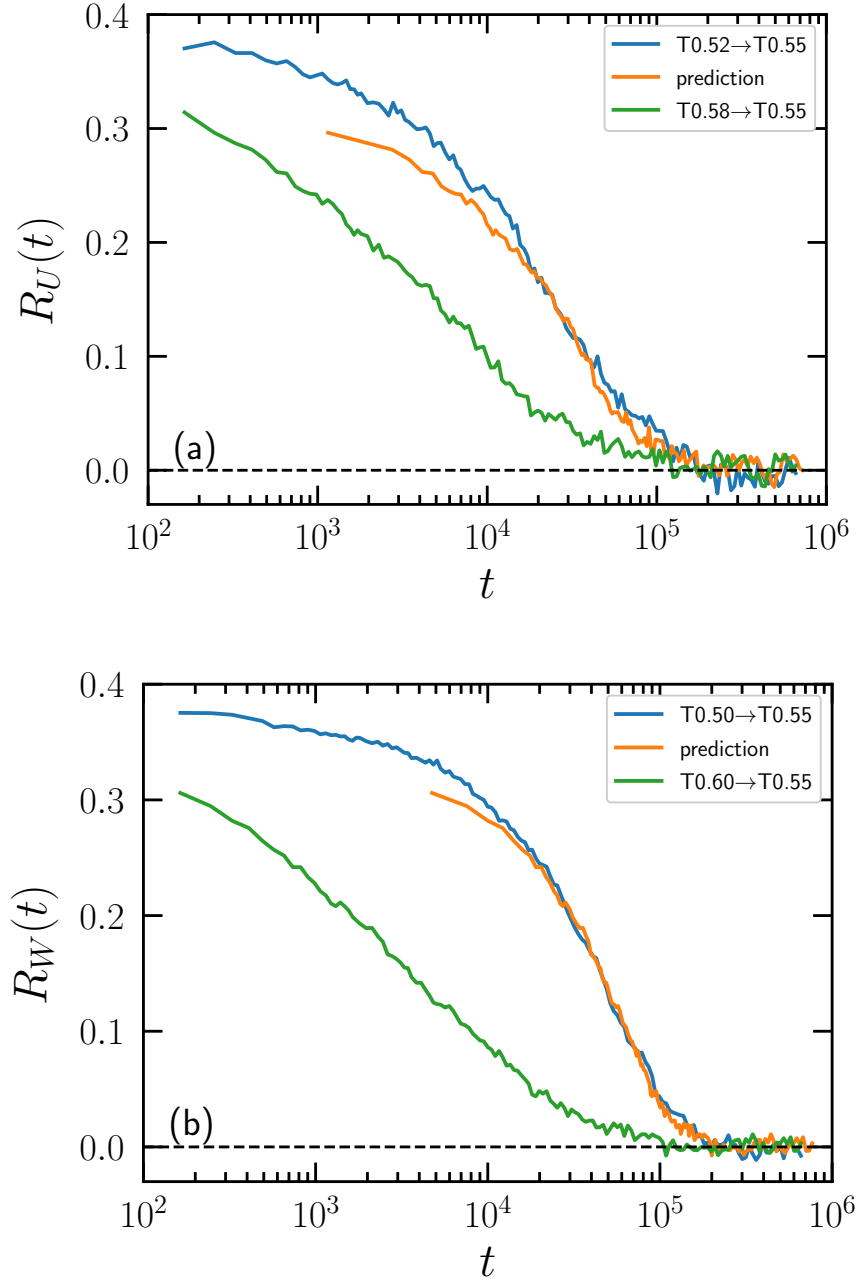
Figure 6.4: Single-parameter aging predictions for jumps to the same target temperature $T = 0.55$. The green curve in each panel is normalized relation function $R(t)$ for the "jump1". The predictions based on jump1 according to Eq. 6.14 are shown in orange. These are to be compared to the "jump2" data (blue curves). (a) and (b) give the predictions of up jumps based on down jumps for the potential energy and the virial, respectively.
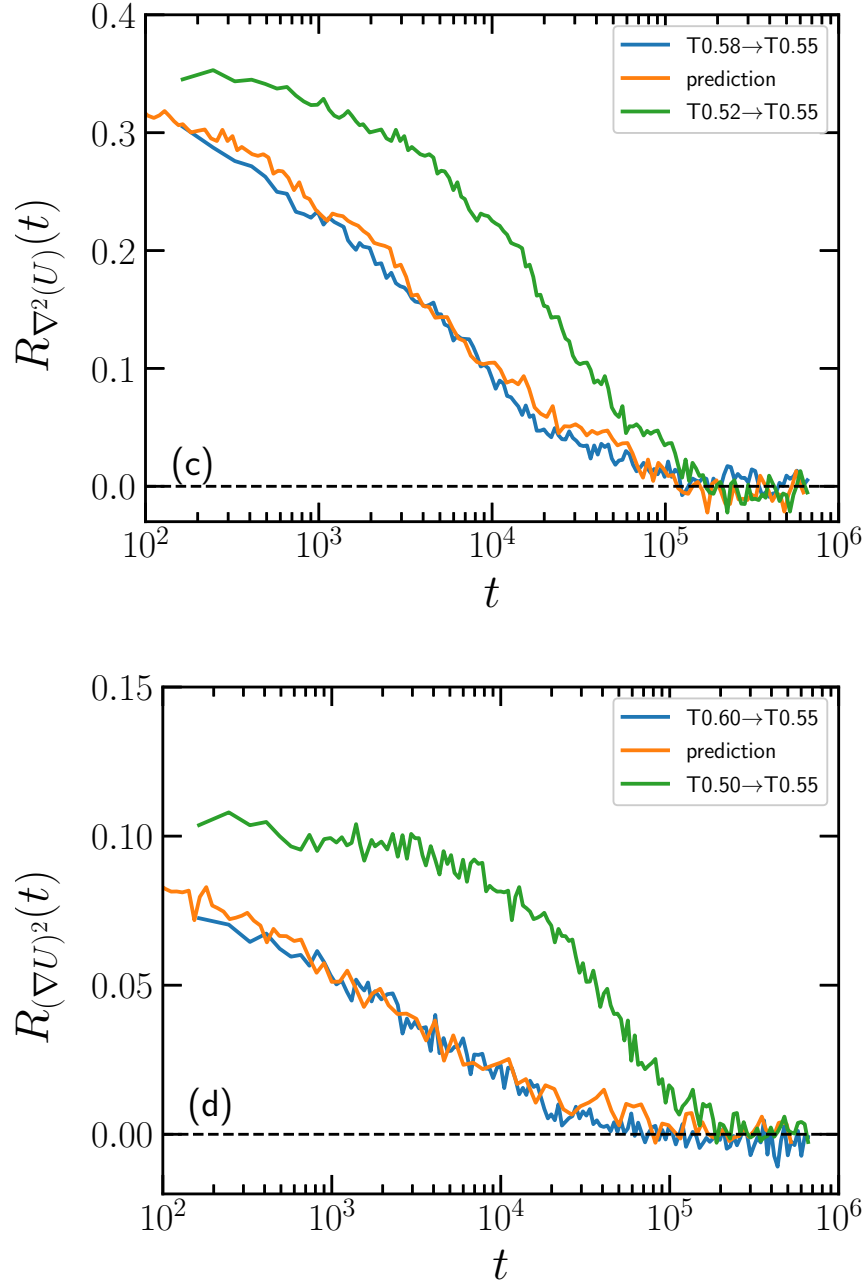
Figure 6.4: (c) and (d) predict down jumps based on up jumps for the Laplacian of the potential energy and the average squared force, respectively.
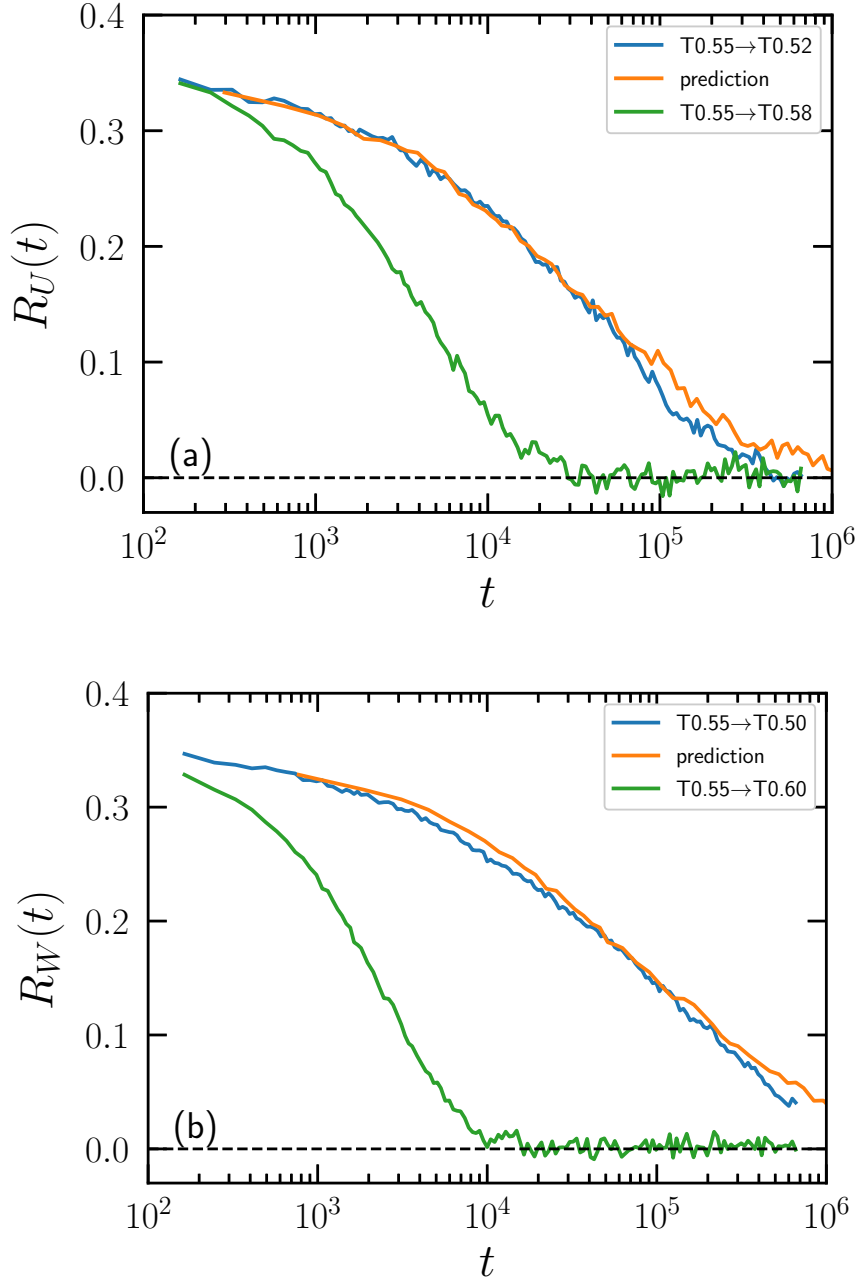
Figure 6.5: Single-parameter aging predictions for jumps initiated from the same temperature $T = 0.55$ and ended at different target temperatures. The green curve in each panel is normalized relation function $R(t)$ for the "jump1". The predictions based on jump1 according to Eq. 6.14 are shown in orange. These are to be compared to the "jump2" data (blue curves). (a) and (b) predict down jumps based on up jumps for the potential energy and the virial, respectively
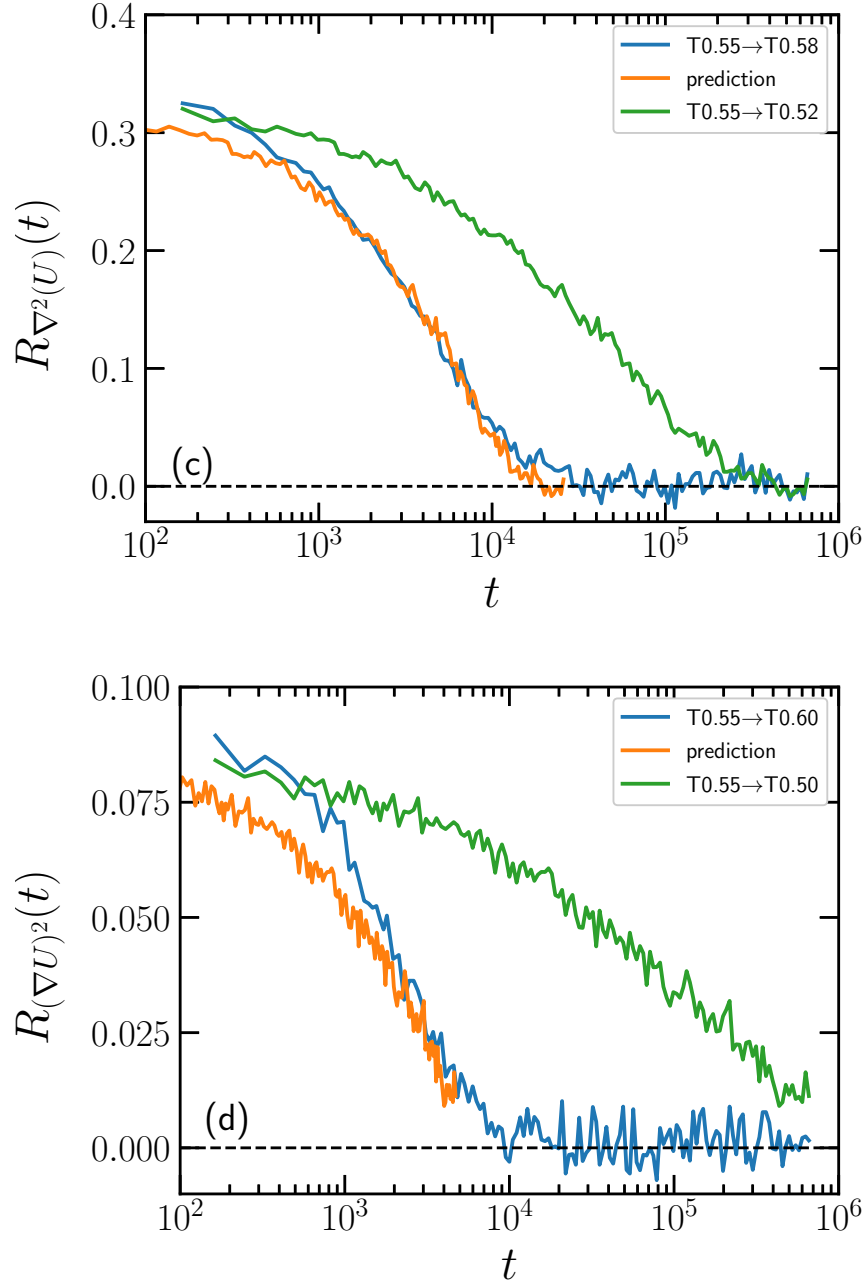
Figure 6.5: (c) and (d) are the predictions of up jumps based on down jumps for the Laplacian of the potential energy and the average squared force, respectively.
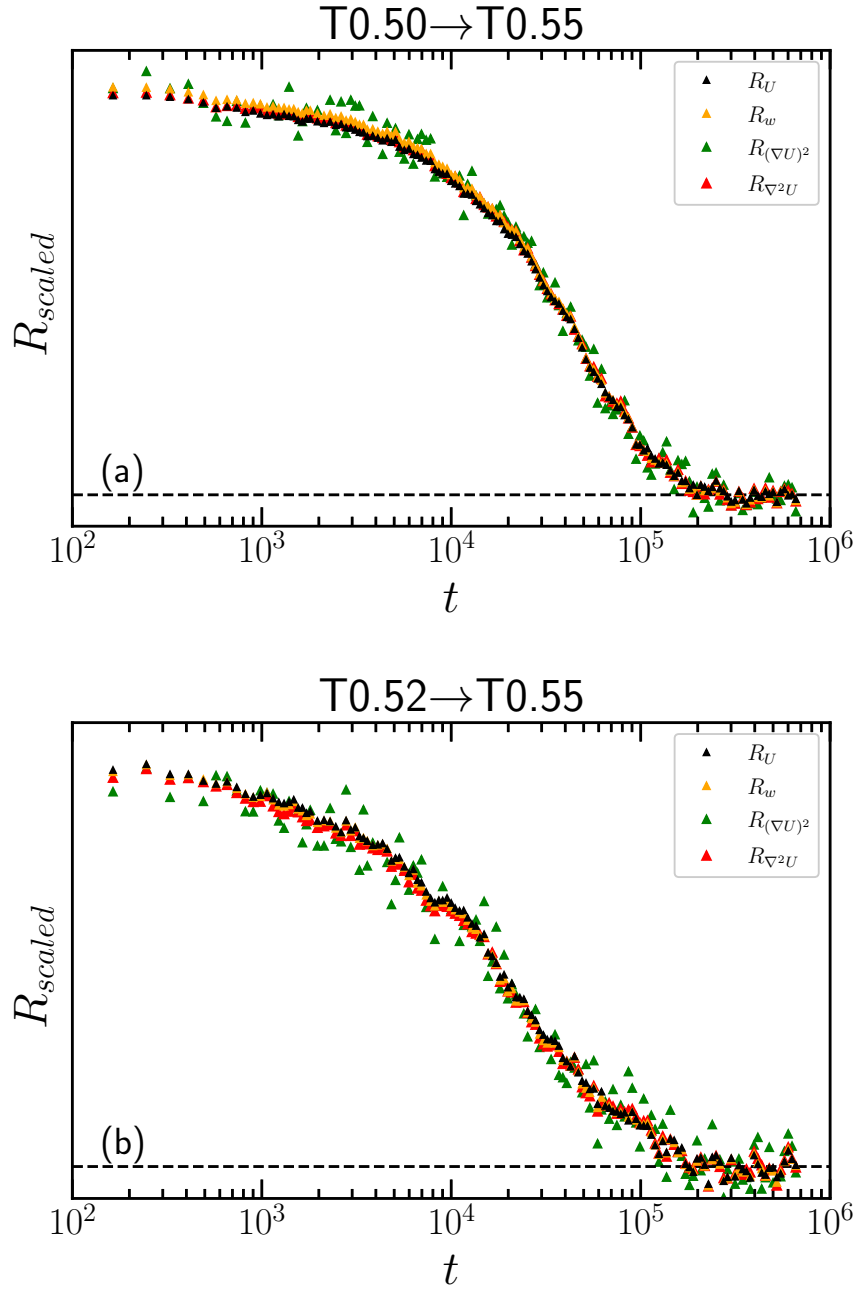
Figure 6.6: Empirically scaled relaxation curves of the all four measured quantities, plotted for jumps to the same target temperature $T = 0.55$. The black points represent the potential energy, yellow points represent the virial, green points represent the average squared force, and red points represent the Laplacian of the potential energy. The dashed lines mark zero. The (c) and (d) panels are presented in next page.
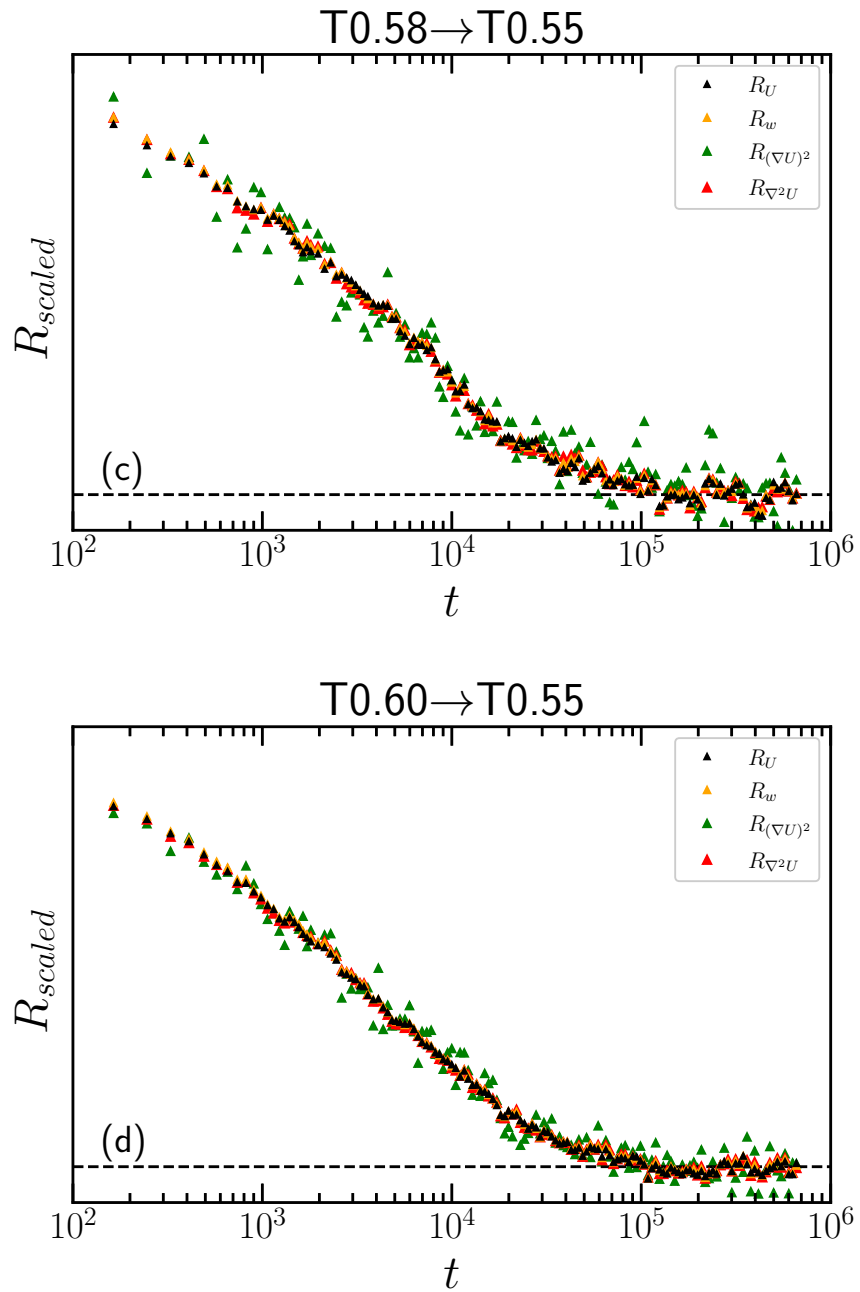
Figure 6.6
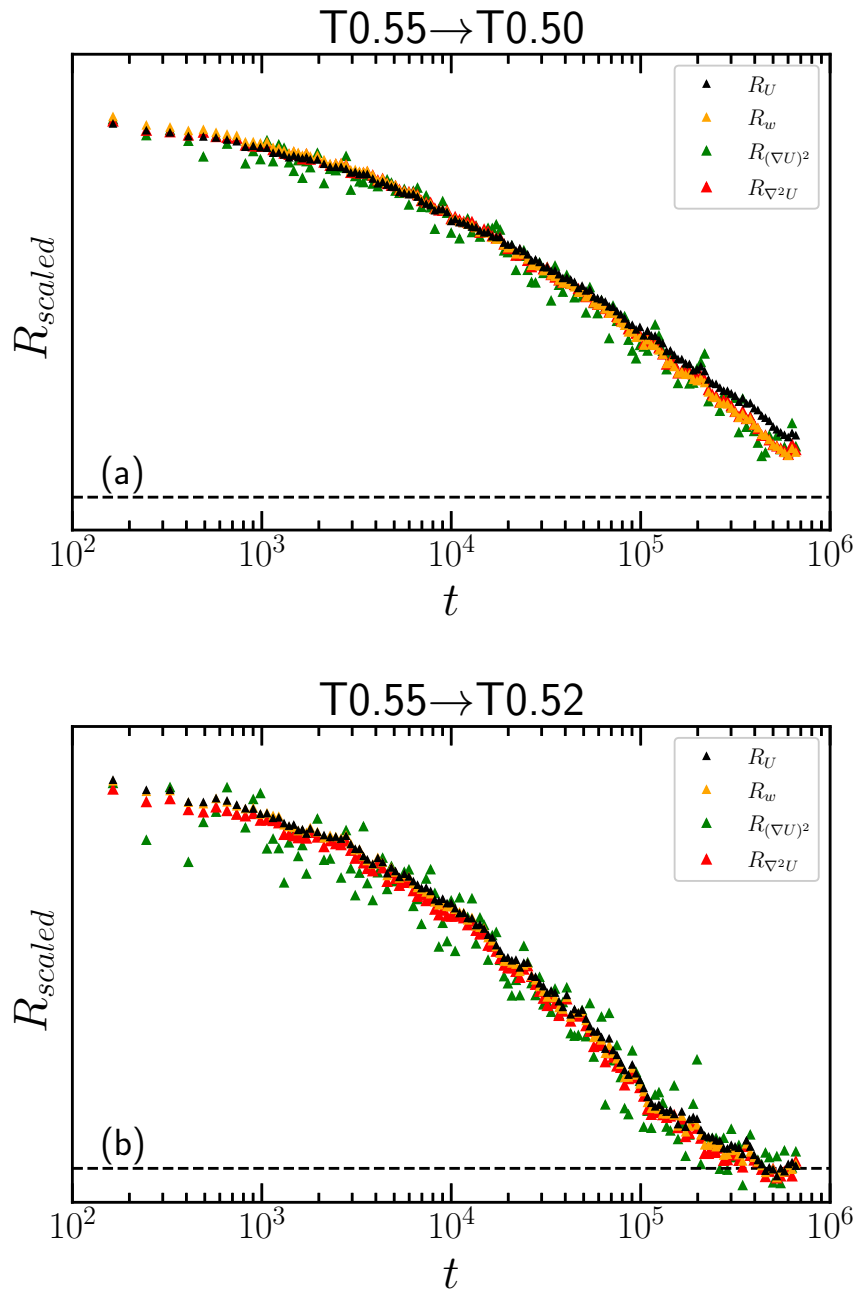
Figure 6.7: Empirically scaled relaxation curves of the four quantities for jumps from the same temperature $T = 0.55$. The same color codes are used here as in Fig. 6.6. The (c) and (d) panels are presented in next page.
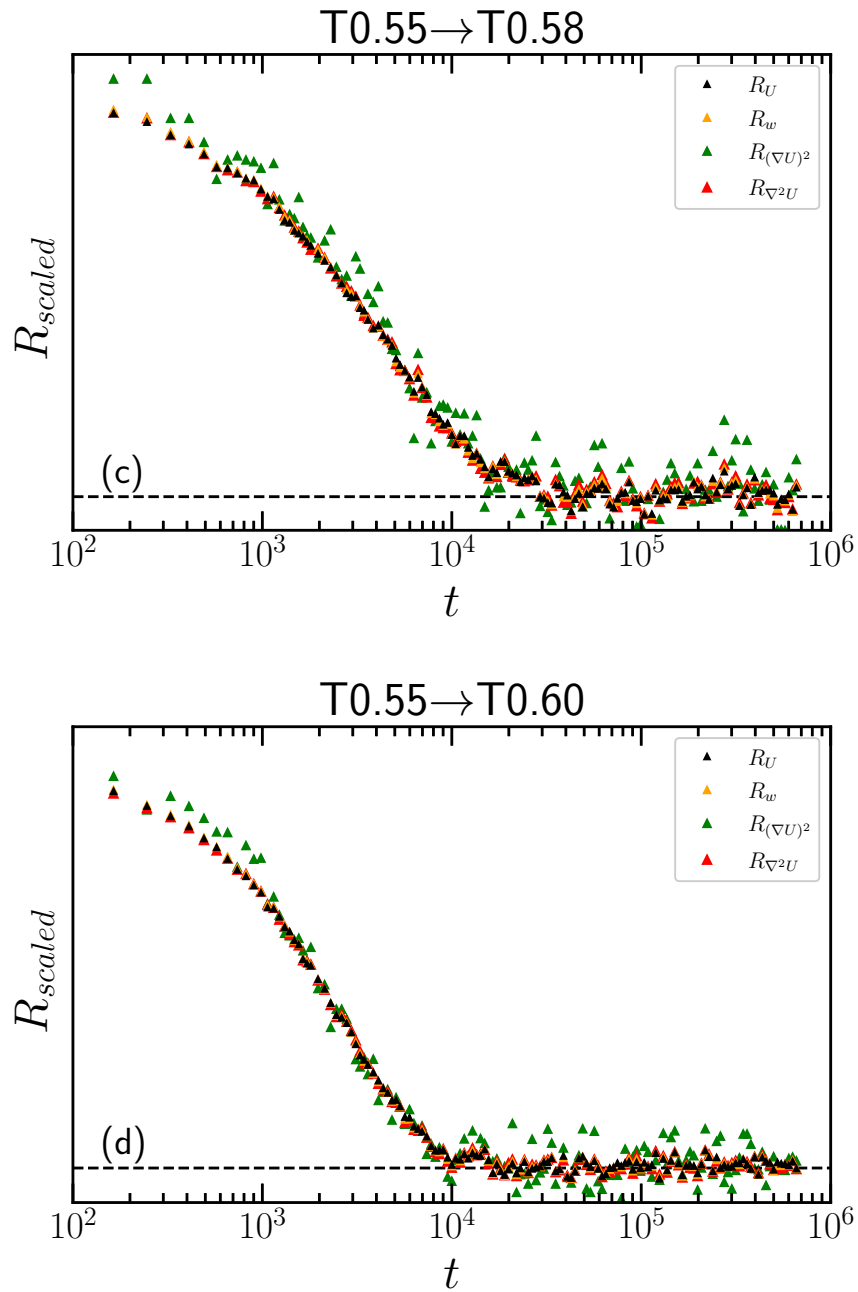
Figure 6.7

6.6 Predict Aging Curves From Equilibrium Fluctuations

According to the fluctuation-dissipation theorem, one can determine the linear response to any small perturbation (in our case, temperature jumps) from equilibrium potential energy autocorrelation function $\langle U(0)U(t)\rangle$ [187]. This section investigates if one can predict relaxation curves of different jumps end at the same target temperature, $T_{end} = 0.60$, from equilibrium potential energy autocorrelation function at $T_{end} = 0.60$.

The system under study is Kob-Andersen 4:1 binary LJ mixture [182]. The simulations were performed in an NVT ensemble using GPU-optimized software RUMD [188]. The system consists of $N = 8000$ particles. We used the shifted-potential method with $r_{cut} = 2.5\sigma_{\alpha\beta}$, where $\alpha, \beta \in \{A, B\}$ are particle types corresponding to interactions particle i and j, and $\Delta t = 0.0025$. We first equilibrated the system at the $T_{end} = 0.60$ using 10^7 time steps; afterward fast Fourier transforms technique was used to calculate the potential energy autocorrelation function. We first equilibrated the system for all the aging simulations at the given starting temperatures using 5×10^8 steps. After that, longer simulations were performed with 5×10^8 steps for production runs. All the presented data in this section are averaged over 1000 simulations starting from independent configurations. We did the averaging to get rid of noises.

Fig. 6.8a presents potential energy data for jumps that end at the same target temperature $T_{end} = 0.60$. The nonlinearity of aging is evident, although the jumps are larger than in the previous section. In Fig. 6.8b, SPA predicted nonlinear temperature jumps from the linear response. Now $\Delta\chi(0)_1 = 0$, and instead of $R(t_1^*)$ we should use potential energy autocorrelation function in Eq. 6.15. We identified χ_{const} to be 0.0404 from the two smallest jumps. The colored dashed lines in Fig. 6.8b are predictions based on the energy autocorrelation at $T_{end} = 0.60$ (solid black line). Filled circles are normalized relaxation curves of potential energy. Predictions work very well, except minor deviations for the two largest jumps. For these two jumps, temperature changes are more than 15%, where SPA is likely not to be accurate.

In this chapter, we investigated the validity of SPA through a computer simulation study. Although we studied bigger temperature jumps than experimental studies, the results were consistent. We validate SPA for both cases of jumps ending at the same target temperature and jumps ending at different temperatures, i.e., general jumps.
We also showed that the nonlinear aging could be predicted from linear

fluctuations at the equilibrium state.
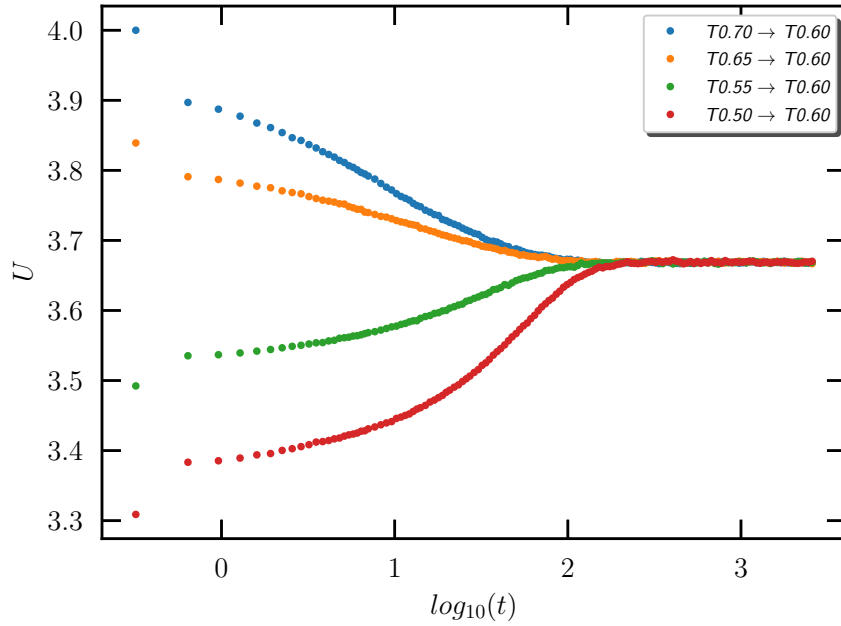
(a)
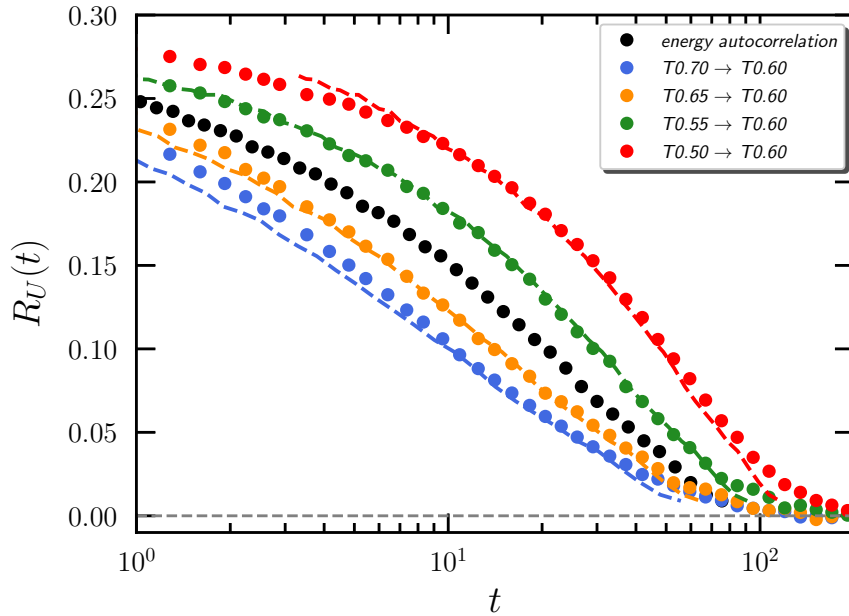
(b)

Figure 6.8: (a) Data for four jumps ending at the same temperature, $T_{end} = 0.60$. (b) The thermal equilibrium potential energy autocorrelation function at this temperature (black line) and the predictions based on this for the temperature jumps (colored dashed curves). The data for the normalized relaxation functions are colored filled circles. The nonlinearity parameter was determined from the two smallest jumps.

Chapter 7

Conclusions and outlooks

This chapter summarizes a brief conclusion of the thesis. In the first part, we investigate the possibility of finding isomorphs in the phase diagram of LCs. We chose the so-called GB model to simulate the phase behavior of LCs. The model is flexible enough to simulate very thin disks up to long rods. Among all the possible sets of parameters, we chose $GB(0.345, 0.2, 1, 2)$ and $GB(3, 5, 2, 1)$.

In the case of $GB(0.345, 0.2, 1, 2)$, we found isomorph at high-temperature isotropic phase using the configurational adiabat method. We start by investigating the phase diagram. At high temperatures and densities ($T > 6.0$, $\rho > 1.5$), we found the virial potential-energy correlation coefficient is higher than 0.9. These are the regions of our interest. Calculating the order parameter showed no phase transition happening along the isomorph (see Fig 5.1).

Then by plotting some dynamic properties, such as mean square displacement and various auto-correlation functions in reduced units, we showed that the dynamics are invariant along the isomorph. We conclude that the center of mass and orientational structures are both invariant along isomorph by looking at $g(r)$ and $G_2(r)$, respectively. It is worth mentioning that there is no significant difference between isomorph and isochore in this case. One reason could be that there is no positional and orientational ordering in the isotropic phase and the isomorph and isochore are entirely in the isotropic phase, so their structures are very similar.

We also tested the constant density scaling for the case of angular relaxation time and diffusion coefficient. Traditionally the density scaling exponent, γ, is considered as a material constant. We showed that γ is state point dependent and varies as temperature and density vary. For the average value of $\gamma = 11.5$, we have shown that a good data collapse happens if we plot D and $\tau_{angular}$ as functions of $\rho^{11.5}/T$.

In the case of $GB(3, 5, 2, 1)$, which leads to calamitic liquid crystals, we investigate the possibility of finding isomorphs in the isotropic and nematic

phases. We followed the same procedure as in the discotic study and found that the dynamics and structure of the GB model are only invariant along the isomorph.

The second part of the thesis aimed to check the validity f single-parameter formalism (SPA) through a computer simulation study. Along each aging simulation, we monitored five different quantities: the potential energy, the virial, the configurational temperature, its numerator (mean-squared force), and its denominator (the Laplacian of the potential energy). We considered both cases of temperature jump ends to the same final temperature and general jumps. In both cases, the configurational temperature did not age at all equilibrated instantaneously. By using SPA, we showed that one could predict the normalized relaxation function of any desired temperature from the data of a single jump. As the jump's magnitude increased, the accuracy of the prediction decreased.
In the final step, we predict aging curves from equilibrium fluctuation (instead of another aging curve). We considered only the case of jumps ending at the same temperature. We showed that by calculating the potential energy auto-correlation function, one can predict different aging curves.

Future study

Isomorphs in plastic crystals

At the beginning of my Ph.D., we tried to find isomorphs in plastic crystals using the so-called Shintani model, and we failed. With a more accurate study, one can find isomorphs at least at high temperatures in the isotropic phase of the model, just like what we saw in the discotic GB model.

Aging of LCs

The novelty of SPA formalism is that it is independent of the interaction potential between the particles. As a small project, one can validate this assumption by aging the LCs.

Finding isomorphs using machine learning techniques

Isomorph theory is an approximation, and we have shown that it is a challenging task to find isomorph while the potential is complicated. It would be great if one could develop a machine learning algorithm and feed it with all the data we have to find isomorphs for different pair-potentials.

Appendix A

Force and Torque Derivations

A.1 Deriving Force

For simplicity one can write $c_i = \hat{\mathbf{e}}_i.\hat{\mathbf{r}}_{ij}$, $c_j = \hat{\mathbf{e}}_j.\hat{\mathbf{r}}_{ij}$, and $c_{ij} = \hat{\mathbf{e}}_i.\hat{\mathbf{e}}_j$. By using this new notation and considering the case of $\sigma_s = 1$, we can rewrite the equation for potential energy

$$U^{GB}(r_{ij}, c_i, c_j, c_{ij}) = 4\epsilon(c_i, c_j, c_{ij}) \left[\rho_{ij}^{-12} - \rho_{ij}^{-6} \right], \tag{A.1a}$$

$$\text{where} \quad \rho_{ij} = r_{ij} - \sigma(\hat{\mathbf{r}}, \hat{\mathbf{e}}_i, \hat{\mathbf{e}}_j) + \sigma_s \tag{A.1b}$$

$$\sigma = \sigma_s \left[1 - \frac{\chi}{2} \left(\frac{(c_i + c_j)^2}{1 + \chi c_{ij}} + \frac{(c_i - c_j)^2}{1 - \chi c_{ij}} \right) \right]^{-1/2}, \tag{A.1c}$$

$$\epsilon = \epsilon_0 \epsilon_1^{\nu}(c_{ij}) \epsilon_2^{\mu}(c_i, c_j, c_{ij}), \tag{A.1d}$$

where

$$\epsilon_1(c_{ij}) = \left(1 - \chi^2 c_{ij}^2 \right)^{-1/2}, \tag{A.1e}$$

$$\epsilon_2(c_i, c_j, c_{ij}) = 1 - \frac{\chi'}{2} \left(\frac{(c_i + c_j)^2}{1 + \chi' c_{ij}} + \frac{(c_i - c_j)^2}{1 - \chi' c_{ij}} \right). \tag{A.1f}$$

The General equation for force is:

$$\mathbf{f}_{ij} = -\nabla_{\mathbf{r}_{ij}} U^{GB} \tag{A.2}$$

Using the chain rule

$$\nabla_{\mathbf{r}_{ij}} U_{ij} = \left(\frac{\partial U_{ij}}{\partial r_{ij}} \right) \nabla_{\mathbf{r}_{ij}} r_{ij} + \left(\frac{\partial U_{ij}}{\partial c_i} \right) \nabla_{\mathbf{r}_{ij}} c_i + \left(\frac{\partial U_{ij}}{\partial c_j} \right) \nabla_{\mathbf{r}_{ij}} c_j + \left(\frac{\partial U_{ij}}{\partial c_{ij}} \right) \nabla_{\mathbf{r}_{ij}} c_{ij} \tag{A.3}$$

91

The c_{ij} is independent of $\mathbf{r}_{ij}$, so the last term vanishes. From the definition of c_i and c_j we can obtain

$$\nabla_{\mathbf{r}_{ij}} c_i = \nabla_{\mathbf{r}_{ij}} \frac{\hat{\mathbf{e}}_i . \mathbf{r}_{ij}}{r_{ij}} = \frac{\hat{\mathbf{e}}_i}{r_{ij}} + c_i \nabla_{\mathbf{r}_{ij}} \left(\frac{1}{r_{ij}} \right)$$

$$\text{where} \quad \nabla_{\mathbf{r}_{ij}} \left(\frac{1}{r_{ij}} \right) = -\frac{\mathbf{r}_{ij}}{r_{ij}^2}$$

$$\text{so} \quad \nabla_{\mathbf{r}_{ij}} c_i = \frac{\hat{\mathbf{e}}_i - c_i \hat{\mathbf{r}}_{ij}}{r_{ij}}$$

Same expression is true for $\nabla_{\mathbf{r}_{ij}} c_j$. Finally for calculating the force we can use

$$\mathbf{f}_{ij} = -\left(\frac{\partial U^{GB}}{\partial r_{ij}} \right) \hat{\mathbf{r}}_{ij} - \sum_{\mathbf{e}} \frac{\partial U^{GB}}{\partial (\mathbf{e}.\hat{\mathbf{r}}_{ij})} \frac{\mathbf{e} - (\mathbf{e}.\hat{\mathbf{r}}_{ij})\hat{\mathbf{r}}_{ij}}{r_{ij}} \quad \text{(A.4)}$$

Now lets go back to Eq(A.3) and derive it term by term. The First term is easy and straight forward, because ϵ is independent of r_{ij} and the dependency of σ is linear with a negative sign. Thus

$$\frac{\partial U^{GB}}{\partial r_{ij}} = -24\epsilon(c_i, c_j, c_{ij})[2\rho_{ij}^{-13} - \rho_{ij}^{-7}]. \quad \text{(A.5)}$$

The second and the third terms are function of c_i and c_j.
The second term of Eq(A.3):

$$\left(\frac{\partial U^{GB}}{\partial c_i} \right) = 4 \left\{ \left(\frac{\partial \epsilon(c_i, c_j, c_{ij})}{\partial c_i} \right) \left[\rho_{ij}^{-12} - \rho_{ij}^{-6} \right] \right.$$
$$\left. + 6\epsilon(c_i, c_j, c_{ij}) \left[2\rho_{ij}^{-13} - \rho_{ij}^{-7} \right] \left(\frac{\partial \sigma(c_i, c_j, c_{ij})}{\partial c_i} \right) \right\} \quad \text{(A.6)}$$

Now we just need to calculate $\left(\frac{\partial \epsilon}{\partial c_i} \right)$ and $\left(\frac{\partial \sigma}{\partial c_i} \right)$.

$$\frac{\partial \epsilon}{\partial c_i} = \mu \epsilon_0 \epsilon_1^{\nu} \epsilon_2^{\mu-1} \left(\frac{\partial \epsilon_2}{\partial c_i} \right)$$

$$\left(\frac{\partial \epsilon_2}{\partial c_i} \right) = -\frac{\chi'}{2} \left(\frac{2(c_i + c_j)}{1 + \chi' c_{ij}} + \frac{2(c_i - c_j)}{1 - \chi' c_{ij}} \right)$$

$$= -\chi'(c'_+ + c'_-)$$

$$\text{where} \quad c'_{\pm} = \frac{c_i \pm c_j}{1 \pm \chi' c_{ij}}$$

so

$$\left(\frac{\partial \epsilon}{\partial c_i}\right) = -\epsilon_0 \mu \epsilon_1^{\nu} \epsilon_2^{\mu-1} \left(\chi'(c_+' + c_-')\right)$$

now for σ

$$\left(\frac{\partial \sigma}{\partial c_i}\right) = -\frac{1}{2}\left[-\frac{\chi}{2}\left(\frac{2(c_i + c_j)}{1 + \chi c_{ij}} + \frac{2(c_i - c_j)}{1 - \chi c_{ij}}\right)\right]\sigma^3$$

$$= \frac{1}{2}\chi\sigma^3(c_+ + c_-)$$

and finally:

$$\left(\frac{\partial U^{GB}}{\partial c_i}\right) = -4\mu\epsilon_0\epsilon_1^{\nu}\epsilon_2^{\mu-1}\left[\rho_{ij}^{-12} - \rho_{ij}^{-6}\right]\left\{\chi'(c_+' + c_-')\right\}$$

$$+ 12\epsilon\chi\sigma^3(c_+ + c_-)\left[2\rho_{ij}^{-13} - \rho_{ij}^{-7}\right]$$

The third term of Eq(A.3):

$$\left(\frac{\partial U^{GB}}{\partial c_j}\right) = 4\left\{\left(\frac{\partial \epsilon(c_i, c_j, c_{ij})}{\partial c_j}\right)\left[\rho_{ij}^{-12} - \rho_{ij}^{-6}\right]\right.$$

$$\left. + 6\epsilon(c_i, c_j, c_{ij})\left[2\rho_{ij}^{-13} - \rho_{ij}^{-7}\right]\left(\frac{\partial \sigma(c_i, c_j, c_{ij})}{\partial c_j}\right)\right\} \tag{A.8}$$

Now we need to calculate the partial differentiate σ and ϵ with respect to c_j.

$$\left(\frac{\partial \epsilon}{\partial c_j}\right) = \epsilon_0 \mu \epsilon_1^{\nu} \epsilon_2^{\mu-1}\left(\frac{\partial \epsilon_2}{\partial c_j}\right)$$

$$\left(\frac{\partial \epsilon_2}{\partial c_j}\right) = -\frac{\chi'}{2}\left[\frac{2(c_i + c_j)}{1 + \chi' c_{ij}} - \frac{2(c_i - c_j)}{1 - \chi' c_{ij}}\right]$$

$$= -\chi'(c_+' - c_-')$$

$$\left(\frac{\partial \epsilon}{\partial c_j}\right) = -\epsilon_0 \mu \epsilon_1^{\nu} \epsilon_2^{\mu-1}\left(\chi'(c_+' - c_-')\right)$$

and for σ

$$\left(\frac{\partial \sigma}{\partial c_j}\right) = \frac{1}{2}\chi\sigma^3(c_+ - c_-)$$

and finally:

$$\left(\frac{\partial U^{GB}}{\partial c_j}\right) = -4\mu\epsilon_0\epsilon_1^{\nu}\epsilon_2^{\mu-1}\left[\rho_{ij}^{-12} - \rho_{ij}^{-6}\right]\left\{\chi'(c_+' - c_-')\right\}$$

$$+ 12\epsilon\chi\sigma^3(c_+ - c_-)\left[2\rho_{ij}^{-13} - \rho_{ij}^{-7}\right]$$

These are the exact expressions which I used in our code.

A.2 Deriving Torque

The torque on molecule i due to molecule j is define by

$$\tau_{ij} = -\hat{\mathbf{e}}_i \times \nabla_{\mathbf{e}_i} U_{ij} \tag{A.10}$$

again applying the chain rule

$$\nabla_{\mathbf{e}_i} U_{ij} = \left(\frac{\partial U_{ij}}{\partial r_{ij}}\right)\nabla_{\mathbf{e}_i} r_{ij} + \left(\frac{\partial U_{ij}}{\partial c_i}\right)\nabla_{\mathbf{e}_i} c_i + \left(\frac{\partial U_{ij}}{\partial c_j}\right)\nabla_{\mathbf{e}_i} c_j + \left(\frac{\partial U_{ij}}{\partial c_{ij}}\right)\nabla_{\mathbf{e}_i} c_{ij} \tag{A.11}$$

The first and third terms vanish, and

$$\nabla_{\mathbf{e}_i} c_i = \nabla_{\mathbf{e}_i}(\hat{\mathbf{e}}_i.\hat{\mathbf{r}}_{ij}) = \hat{\mathbf{r}}_{ij},$$
$$\nabla_{\mathbf{e}_i} c_{ij} = \nabla_{\mathbf{e}_i}(\hat{\mathbf{e}}_i.\hat{\mathbf{e}}_j) = \hat{\mathbf{e}}_j.$$

Now finally we can right Eq(A.10) as

$$\tau_{ij} = -\hat{\mathbf{e}}_i \times \left[\left(\frac{\partial U_{ij}}{\partial c_i}\right)\hat{\mathbf{r}}_{ij} + \left(\frac{\partial U_{ij}}{\partial c_{ij}}\right)\hat{\mathbf{e}}_j\right] \tag{A.12}$$

We have already calculated the first term of this equation and for second term we have

$$\left(\frac{\partial U^{GB}}{\partial c_{ij}}\right) = 4\left\{\left(\frac{\partial \epsilon(c_i, c_j, c_{ij})}{\partial c_{ij}}\right)\left[\rho_{ij}^{-12} - \rho_{ij}^{-6}\right]\right.$$
$$\left. + 6\epsilon(c_i, c_j, c_{ij})\left[2\rho_{ij}^{-13} - \rho_{ij}^{-7}\right]\left(\frac{\partial \sigma(c_i, c_j, c_{ij})}{\partial c_{ij}}\right)\right\} \tag{A.13}$$

where

$$\left(\frac{\partial \epsilon}{\partial c_{ij}}\right) = \epsilon_0 \nu \epsilon_1^{\nu-1} \epsilon_2^{\mu}\left(\frac{\partial \epsilon_1}{\partial c_{ij}}\right) + \epsilon_0 \mu \epsilon_1^{\nu} \epsilon_2^{\mu-1}\left(\frac{\partial \epsilon_2}{\partial c_{ij}}\right)$$

$$\left(\frac{\partial \epsilon_1}{\partial c_{ij}}\right) = c_{ij}\chi^2 \epsilon_1^3$$

$$\left(\frac{\partial \epsilon_2}{\partial c_{ij}}\right) = -\frac{\chi'}{2}\left[\frac{-\chi'(c_i + c_j)^2}{(1 + \chi' c_{ij})^2} + \frac{\chi'(c_i - c_j)^2}{(1 - \chi' c_{ij})^2}\right]$$
$$= \frac{\chi'^2}{2}(c_+'^2 - c_-'^2)$$

and for σ

$$\left(\frac{\partial \sigma}{\partial c_{ij}}\right) = -\left(\frac{1}{2}\chi\right)^2 \sigma^3(c_+^2 - c_-^2)$$

finally:

$$\left(\frac{\partial \epsilon}{\partial c_{ij}}\right) = \epsilon_0 \mu c_{ij} \chi^2 \epsilon_1^{\nu+2} \epsilon_2^{\mu}$$
$$+ \frac{1}{2}\epsilon_0 \mu \chi'^2 \epsilon_1^{\nu} \epsilon_2^{\mu-1}(c_+'^2 - c_-'^2).$$

Note that by interchanging the labels and changing the signs of c_i and c_j, the force and torque on molecule j due to i can be obtained. From Eq(A.4) we can see that $\mathbf{f}_{ij} = -\mathbf{f}_{ji}$. Following the same procedure for Eq(A.12) leads to

$$\tau_{ij} = -\hat{\mathbf{e}}_j \times \left[\left(\frac{\partial U_{ij}}{\partial c_i}\right)\hat{\mathbf{r}}_{ij} + \left(\frac{\partial U_{ij}}{\partial c_{ij}}\right)\hat{\mathbf{e}}_i\right], \qquad (A.15)$$

and we should note that $\tau_{ij} \neq -\tau_{ji}$.

Appendix B

Consistency Check

Here I am going to show some of our consistency check with literature.

Fig. B.1 shows $g(r)$ corresponding to three different state points. In all panels, the blue (my results) and orange (extracted form Ref. [113]) curves are on top of each other. We did this as a consistency check with literature results.

Fig. B.2 shows that our simulation results are consistent with the one from literature for orientational order parameter. Here we extract data form Ref. [112].

Fig. B.3 shows that there is a good agreement between our results and Ref. [113].

As a final consistency check we compare our results with Ref. [118] for the case of different auto-correlation functions. In all cases we found good agreements between our data and literature (see Fig. B.4), Our main purpose was to make sure that our codes work properly then start our main study.

(a)

(b)

(c)
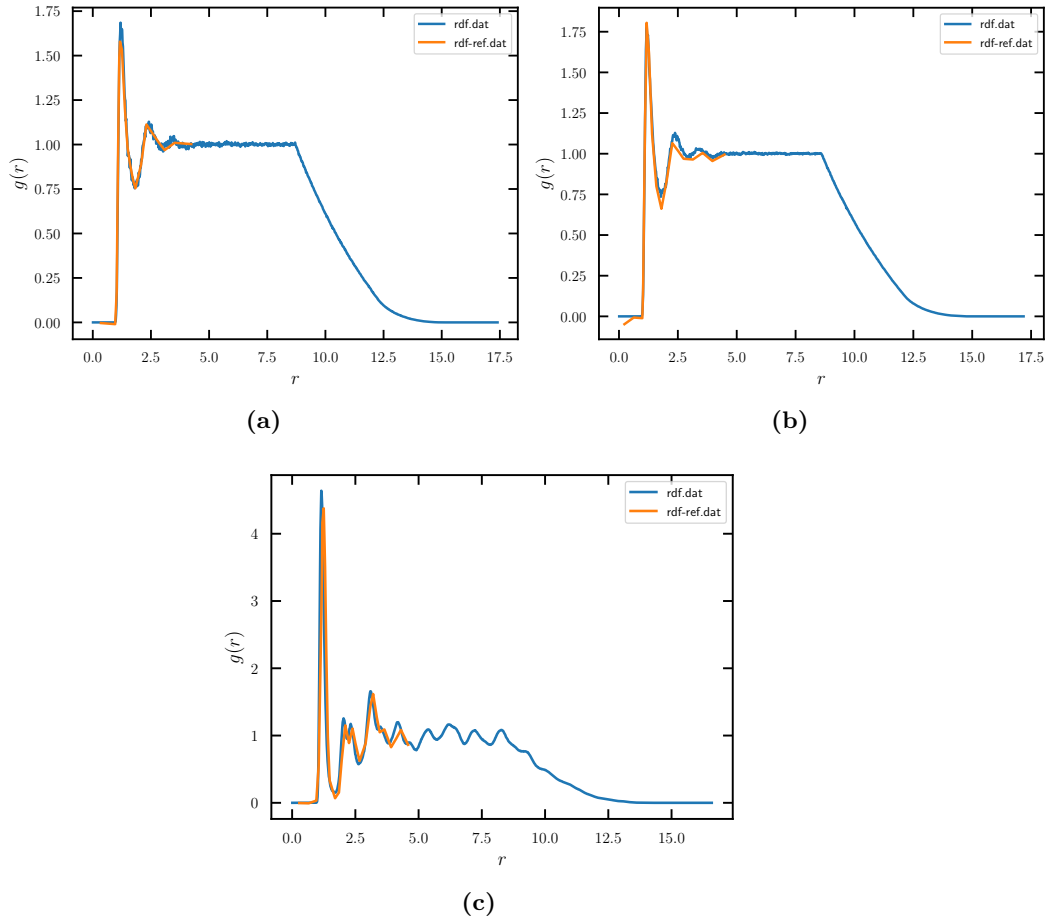
Figure B.1: Radial distribution function plotted against distance at $T = 0.5$ for different densities for the case **GB(3,5,2,1)**. The blue curves are outputs of my simulations and the orange curves extracted from the Ref. [113]. Panel (a) $\rho = 0.26$ (b) corresponds to $\rho = 0.27$ and (c) $\rho = 0.30$.
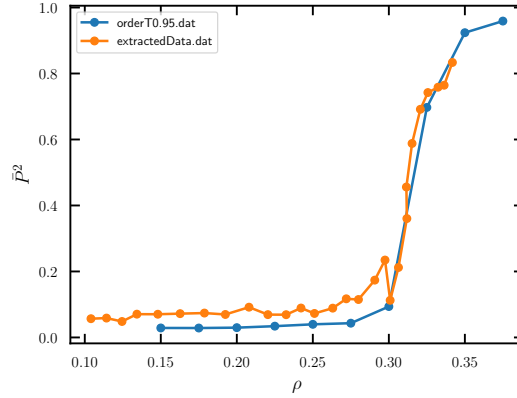
(a)
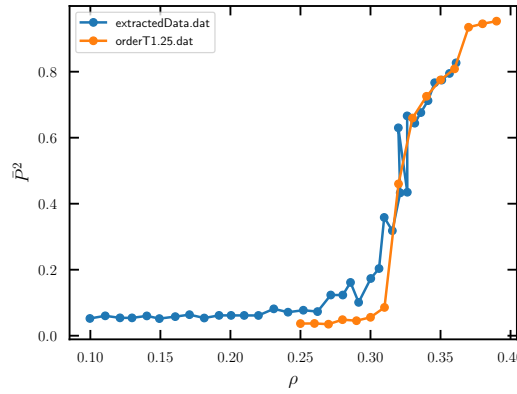
(b)

Figure B.2: Order parameter plotted against density at various temperature for the case $GB(3, 5, 2, 1)$ and $r_c = 4.0$. $\bar{P}_2$ and S_2 are the main two notations (we use S_2 in chapter 4) for the orientational order parameter. (a) $T = 0.95$ the orange curve corresponds to data extracted from Ref. [112] and blue curves is result of our simulation. (b) $T = 1.25$, here the color coding is the other way around.
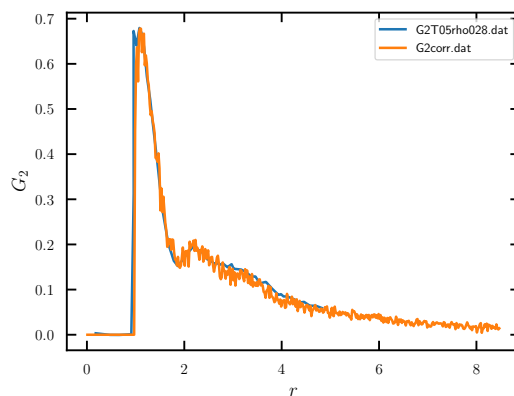
(a)
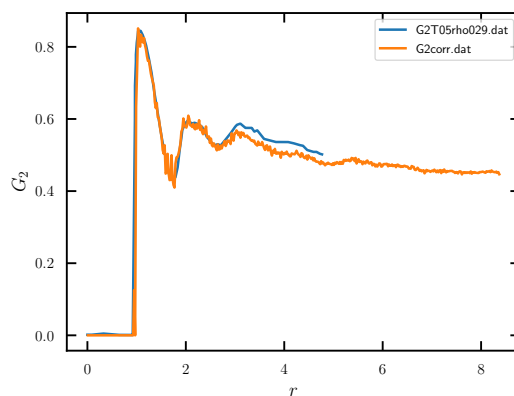
(b)

Figure B.3: Orientational pair-correlation function as a function of pair-distances. (a) $\rho = 2.8$, $T = 0.5$ and (b) $\rho = 2.9$, $T = 0.5$. In both panels, the orange curves is resulted from our simulations and the blue curves are extracted from Ref. [113].
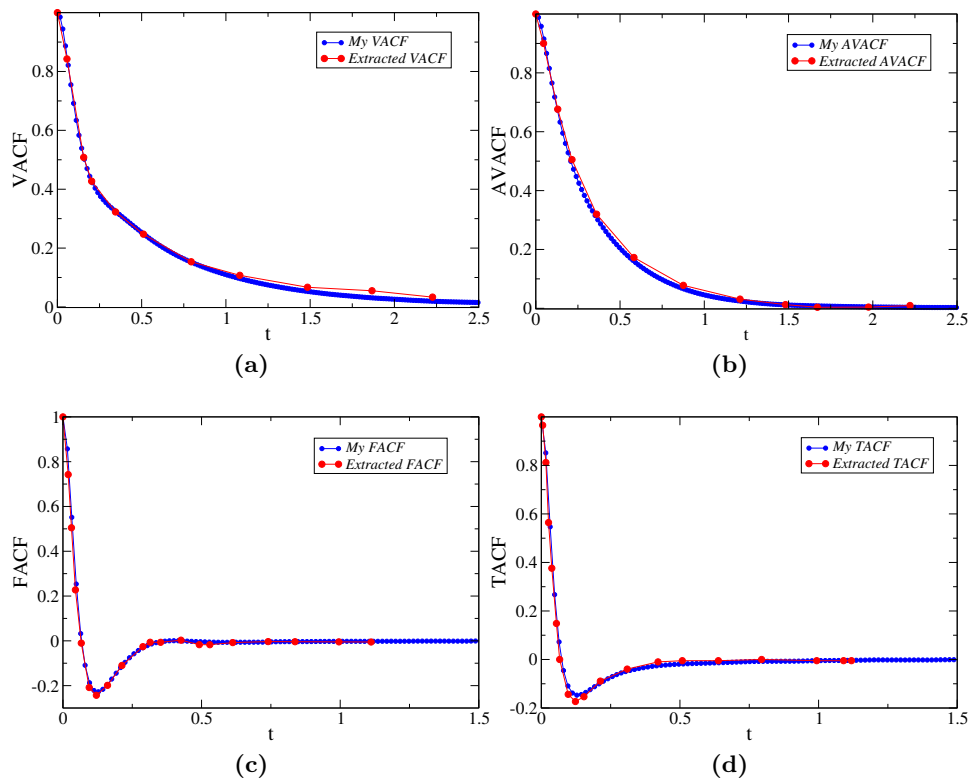
Figure B.4: Various auto-correlation functions plotted as functions of time. (a) Velocity, (b) angular velocity, (c) force, (d) torque, the blue curves are results of our simulations and the red curves extracted from Ref. [118].
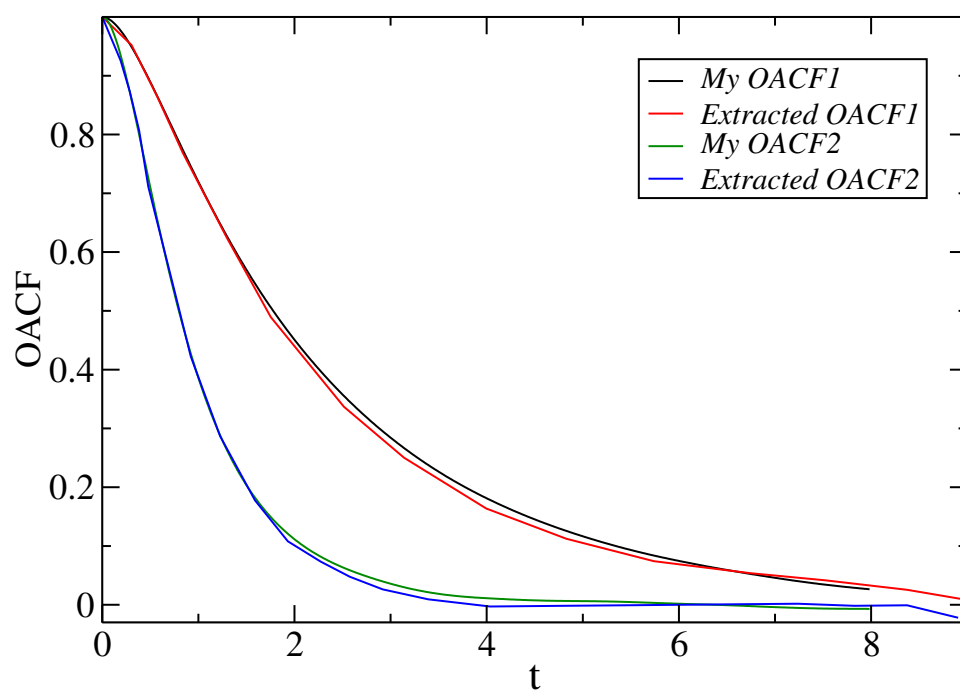
Figure B.5: First- and second rank orientational auto-correlation function, the black and the green curves are results of our simulations and the red and the blue curves extracted fron Ref. [118].

Appendix C

Extra Isomorphs

C.1 Discotic Gay-Berne

ρ	T	R	γ
2.3	4.0	0.8311	8.723
2.323	4.3848	0.8597	9.6485
2.3462	4.8418	0.8842	10.2574
2.3697	5.3744	0.9047	10.6867
2.3934	5.9873	0.9212	11.0441
2.4173	6.6876	0.9327	11.2204
2.4415	7.4807	0.9416	11.3315
2.4659	8.3765	0.9491	11.4292
2.4906	9.3859	0.9538	11.441
2.5155	10.5189	0.958	11.4596
2.5406	11.7895	0.9614	11.4587
2.566	13.2131	0.9633	11.4484
2.5917	14.8063	0.9645	11.4162
2.6176	16.5863	0.9659	11.3968
2.6438	18.576	0.9662	11.3484
2.6702	20.798	0.9665	11.3435
2.6969	23.2783	0.9667	11.3165
2.7239	26.0491	0.967	11.3032
2.7511	29.1443	0.9661	11.268
2.7787	32.5986	0.9659	11.2347

Table C.1: Variation of density, temperature, correlation coefficient and γ for isomorph corresponding to $GB(0.345, 0.2, 1, 2)$. At each step we increased density by 1%. Isomorph starts at $(\rho_{ref}, T_{ref}) = (2.3, 4.0)$ in isotropic phase.

C.2 Calamitic Gay-Bern

ρ	T	R	γ
0.25	1.2	0.8989	8.5505
0.2525	1.3071	0.9093	8.6337
0.255	1.4247	0.9176	8.6758
0.2576	1.5535	0.9246	8.7082
0.2602	1.6943	0.9303	8.7246
0.2628	1.8479	0.935	8.7203
0.2654	2.0153	0.9384	8.7076
0.268	2.1975	0.9413	8.6822
0.2707	2.3955	0.9435	8.6565
0.2734	2.6106	0.9452	8.6279
0.2762	2.8442	0.9467	8.5939
0.2789	3.0976	0.9475	8.5582
0.2817	3.3725	0.9484	8.5281
0.2845	3.6705	0.9488	8.4929
0.2874	3.9936	0.949	8.4605
0.2902	4.3436	0.9491	8.4298
0.2931	4.7229	0.9492	8.3995
0.2961	5.1339	0.9489	8.3704
0.299	5.5789	0.9488	8.3418
0.302	6.061	0.9484	8.3158
0.305	6.583	0.9481	8.2898
0.3081	7.1482	0.9477	8.2673
0.3112	7.7603	0.9472	8.2476
0.3143	8.4232	0.9468	8.228
0.3174	9.1412	0.9462	8.2112
0.3206	9.9185	0.9457	8.1944
0.3238	10.7605	0.945	8.1796
0.3271	11.6722	0.9446	8.1691
0.3303	12.6596	0.9439	8.1559
0.3336	13.7292	0.9434	8.1448
0.337	14.8878	0.9427	8.1387
0.3403	16.1429	0.9422	8.1317
0.3437	17.5028	0.9416	8.1258
0.3472	18.9763	0.9408	8.1208
0.3506	20.5732	0.9404	8.1184
0.3542	22.3039	0.9398	8.1175
0.3577	24.1799	0.9392	8.1174
0.3613	26.2136	0.9385	8.117
0.3649	28.419	0.938	8.1184
0.3685	30.8103	0.9373	8.1195

Table C.2: Variation of density, temperature, correlation coefficient and γ for isomorph corresponding to $GB(3, 5, 2, 1)$. At each step we increased density by 1%. Isomorph starts at $(\rho_{ref}, T_{ref}) = (0.25, 1.2)$ in isotropic phase.

ρ	T	R	γ
0.3	1.2	0.9166	8.2792
0.303	1.3033	0.9222	8.3223
0.306	1.416	0.9276	8.3471
0.3091	1.5387	0.9314	8.3584
0.3122	1.6722	0.9349	8.366
0.3153	1.8172	0.9371	8.353
0.3185	1.9745	0.939	8.3394
0.3216	2.1451	0.9404	8.3212
0.3249	2.33	0.9413	8.2941
0.3281	2.5303	0.9422	8.279
0.3314	2.7472	0.9426	8.2503
0.3347	2.9819	0.9429	8.2239
0.338	3.2358	0.9431	8.203
0.3414	3.5105	0.943	8.1736
0.3448	3.8075	0.9427	8.1539
0.3483	4.1287	0.9423	8.128
0.3518	4.476	0.942	8.1045
0.3553	4.8514	0.9414	8.081
0.3588	5.2571	0.9411	8.0664
0.3624	5.6958	0.9403	8.042
0.3661	6.1699	0.9396	8.0217
0.3697	6.6821	0.939	8.0091
0.3734	7.2357	0.9384	7.9917
0.3771	7.8342	0.9377	7.9798
0.3809	8.481	0.9369	7.9644
0.3847	9.18	0.936	7.9534
0.3886	9.9356	0.9354	7.9419
0.3925	10.7522	0.9345	7.9339
0.3964	11.6349	0.9337	7.9219
0.4004	12.5889	0.933	7.9171
0.4044	13.6203	0.9321	7.9109
0.4084	14.7353	0.9313	7.9057

Table C.3: Variation of density, temperature, correlation coefficient and γ for isomorph corresponding to $GB(3, 5, 2, 1)$. At each step we increased density by 1%. Isomorph starts at $(\rho_{ref}, T_{ref}) = (0.30, 1.2)$ in isotropic phase.

ρ	T	R	γ
0.32	1.2	0.9329	8.2558
0.3232	1.303	0.9375	8.2985
0.3264	1.4154	0.9421	8.3254
0.3297	1.5376	0.9449	8.3279
0.333	1.6704	0.9475	8.3145
0.3363	1.8143	0.9487	8.2963
0.3397	1.9703	0.9507	8.2723
0.3431	2.1391	0.9512	8.2489
0.3465	2.3218	0.9516	8.2184
0.35	2.5193	0.9531	8.1846
0.3535	2.7327	0.9533	8.1552
0.357	2.9633	0.9535	8.1233
0.3606	3.2121	0.9535	8.0878
0.3642	3.4809	0.9532	8.0605
0.3678	3.7709	0.9539	8.0259
0.3715	4.0838	0.953	7.9957
0.3752	4.4213	0.9535	7.9669
0.379	4.7853	0.9526	7.9379
0.3828	5.1779	0.9524	7.9116
0.3866	5.601	0.9525	7.882
0.3905	6.0571	0.9517	7.8567
0.3944	6.5488	0.9518	7.8242
0.3983	7.0784	0.9519	7.8016
0.4023	7.6492	0.9513	7.7826
0.4063	8.2644	0.9505	7.7576
0.4104	8.927	0.9498	7.7426
0.4145	9.6408	0.9503	7.7207
0.4186	10.4095	0.95	7.6977
0.4228	11.2374	0.9479	7.6857
0.427	12.1288	0.9486	7.6611
0.4313	13.088	0.9483	7.6448
0.4356	14.1209	0.9479	7.6245
0.44	15.2324	0.9469	7.6112
0.4444	16.4281	0.9502	7.5744

Table C.4: Variation of density, temperature, correlation coefficient and γ for isomorph corresponding to $GB(3,5,2,1)$. At each step we increased density by 1%. Isomorph starts at $(\rho_{ref}, T_{ref}) = (0.32, 1.2)$ in nematic phase.

ρ	T	R	γ
0.33	1.1	0.9036	8.0511
0.3333	1.1926	0.9126	8.185
0.3366	1.2942	0.9195	8.2552
0.34	1.4053	0.9245	8.2996
0.3434	1.5264	0.9284	8.3145
0.3468	1.6581	0.9311	8.3065
0.3503	1.801	0.9331	8.3037
0.3538	1.956	0.9349	8.2852
0.3573	2.1238	0.9357	8.2611
0.3609	2.3053	0.9363	8.2278
0.3645	2.5016	0.9368	8.1994
0.3682	2.7137	0.9367	8.1619
0.3719	2.9429	0.9365	8.1338
0.3756	3.1904	0.936	8.0968
0.3793	3.4574	0.9358	8.0625
0.3831	3.7458	0.9349	8.03
0.387	4.0568	0.9346	7.9985
0.3908	4.3923	0.934	7.9744
0.3947	4.7543	0.933	7.9412
0.3987	5.1446	0.9322	7.9121
0.4027	5.5653	0.9312	7.8896
0.4067	6.019	0.9302	7.8636
0.4108	6.5081	0.9293	7.8395
0.4149	7.0354	0.9282	7.8189
0.419	7.6035	0.9273	7.8003
0.4232	8.2161	0.9263	7.7753
0.4274	8.8764	0.925	7.7568
0.4317	9.5879	0.924	7.7423
0.436	10.3547	0.9226	7.7261

Table C.5: Variation of density, temperature, correlation coefficient and γ for isomorph corresponding to $GB(3, 5, 2, 1)$. At each step we increased density by 1%. Isomorph starts at $(\rho_{ref}, T_{ref}) = (0.33, 1.1)$ in nematic phase.

ρ	T	R	γ
0.35	1.2	0.8981	7.9431
0.3535	1.2998	0.9079	8.0952
0.357	1.4094	0.9149	8.1762
0.3606	1.529	0.9192	8.2075
0.3642	1.6592	0.9221	8.2221
0.3679	1.8007	0.9244	8.2174
0.3715	1.954	0.926	8.2029
0.3752	2.12	0.927	8.1851
0.379	2.2996	0.9275	8.1607
0.3828	2.4938	0.9276	8.1315
0.3866	2.7035	0.9274	8.1003
0.3905	2.9299	0.9271	8.0699
0.3944	3.1744	0.9267	8.0394
0.3983	3.4381	0.926	8.0066
0.4023	3.7227	0.9253	7.9742
0.4063	4.0296	0.9244	7.9486
0.4104	4.3606	0.9234	7.9194
0.4145	4.7174	0.9222	7.8895
0.4187	5.1019	0.9213	7.8678
0.4228	5.5165	0.9201	7.8393
0.4271	5.9634	0.9189	7.8179
0.4313	6.445	0.9174	7.7942
0.4357	6.964	0.9164	7.7708
0.44	7.5231	0.915	7.7514
0.4444	8.1256	0.9135	7.7314
0.4489	8.7749	0.9121	7.7138
0.4533	9.4744	0.9107	7.702

Table C.6: Variation of density, temperature, correlation coefficient and γ for isomorph corresponding to $GB(3, 5, 2, 1)$. At each step we increased density by 1%. Isomorph starts at $(\rho_{ref}, T_{ref}) = (0.35, 1.2)$ in nematic phase.

Appendix D

Isomorphs in Smectic Phase

The smectic phase investigation of $GB(3, 5, 2, 1)$ is still ongoing, and we are working on it. I would like to quote Demiguel [113]: "Our results appear to indicate that the The smectic B phase undergoes a further transition which implies a tilt of the average molecular orientation with respect to the smectic layers. We should point out that the mere fact that this tilted phase appears in our simulations does not necessarily imply that it is thermodynamically stable: it could be preempted by a more stable phase (for instance, a molecular solid-like phase). Moreover, it remains unresolved to what extent this phase is a consequence of compressing a constant-volume cubic box. A constant pressure technique in which both the volume and the shape of the simulation box are allowed to change would be more suitable for studying these highly condensed phases." We also observed similar things. A slight change of structure happening at some reference point, Figs. D.1 and D.5 illustrate this. We still do not entirely understand the reason, yet acceptable collapses happen in auto-correlation functions (see Figs. D.2, D.3, and D.4) along the isomorph. We have studied two different isomorphs, $(\rho, T) = (0.4, 0.4)$ and $(\rho, T) = (0.4, 0.9)$, in the smectic phase. In the rest, I only present the results corresponding to $(\rho, T) = (0.4, 0.4)$. Tables. D.1 and D.2 provide detailed information about the two isomorphs.
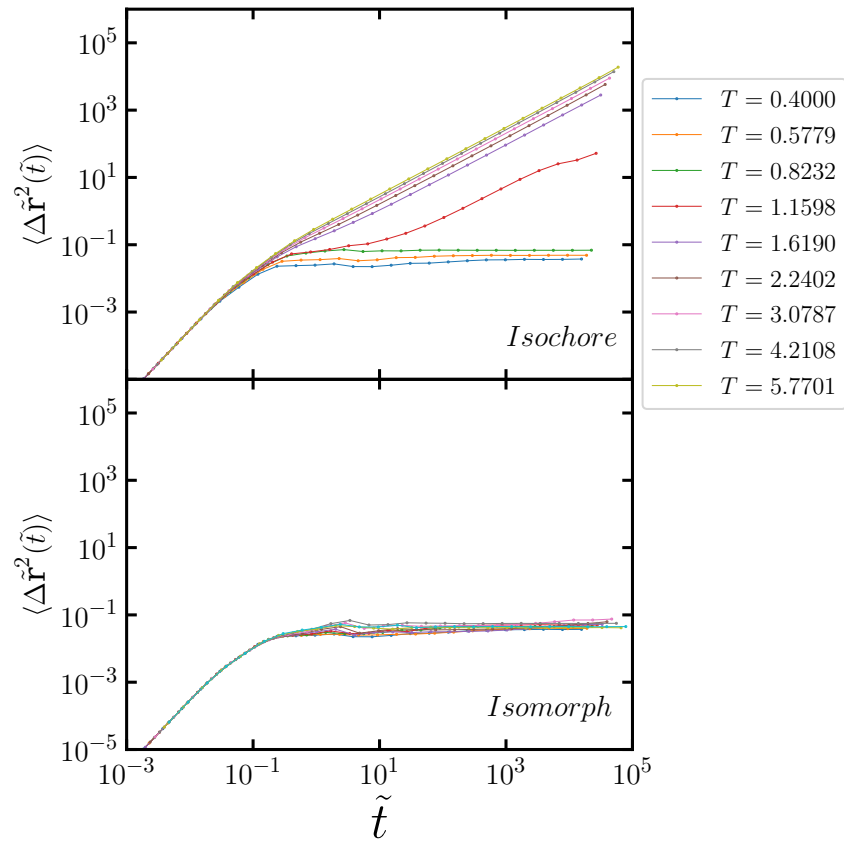
Figure D.1: Comparing the mean square displacement along the isochore and the isomorph in reduced unites. The data collapse is better along the isomorph. Data correspond to around 35% variation in density as reported in table D.1.
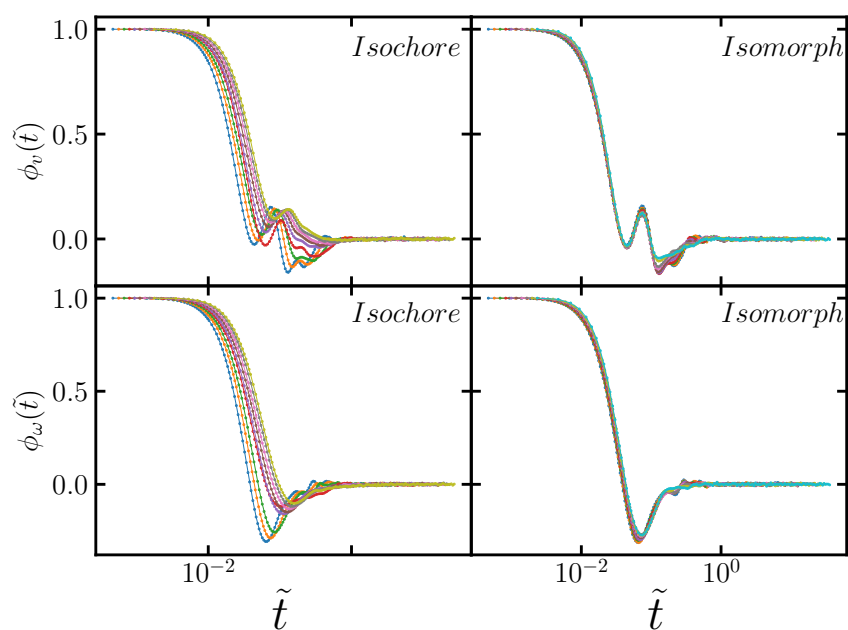
Figure D.2: Upper: center-of-mass velocity auto-correlation function, lower: angular velocity auto-correlation function both as a function of reduced time.
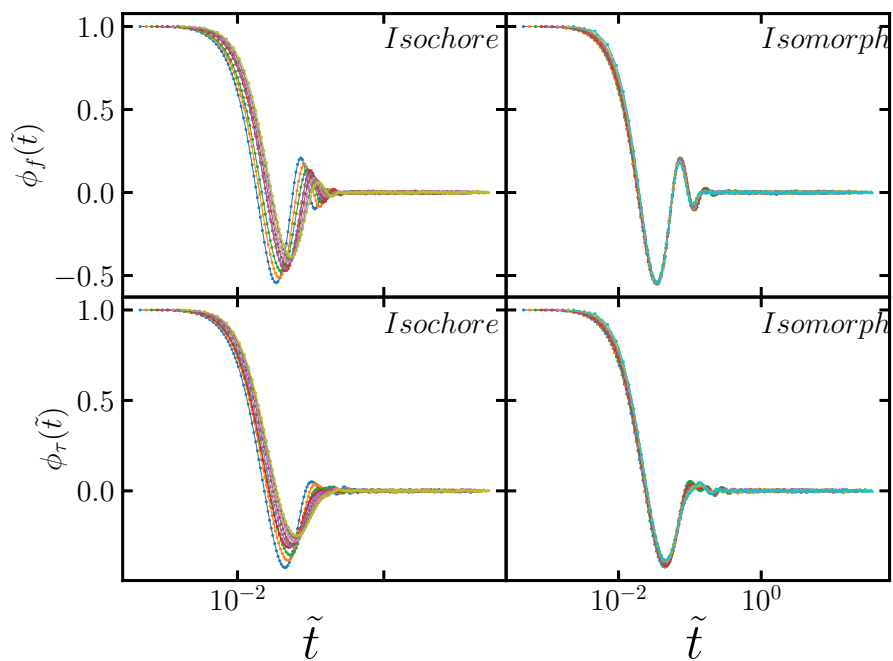
Figure D.3: Upper: force auto-correlation function, lower: torque auto-correlation function both as a function of reduced time.
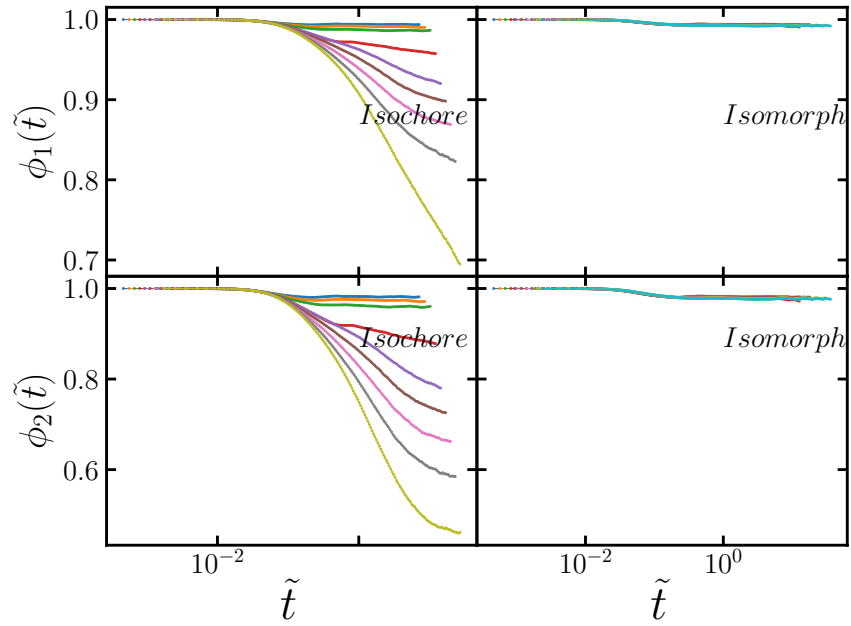
Figure D.4: Upper: first-order and, lower: second-order orientational auto-correlation function both as a function of reduced time.
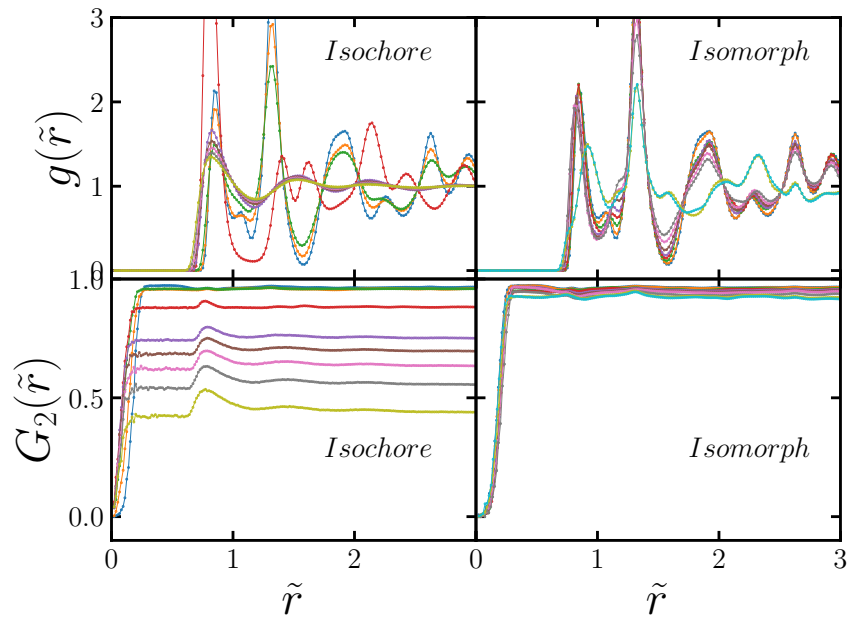
Figure D.5: Radial distribution function and orientational correlation function plotted as functions of reduced distance along the isochore and the isomorph.

ρ	T	R	γ
0.4	0.4	0.956	9.4561
0.404	0.4392	0.9539	9.3492
0.408	0.4818	0.9514	9.2432
0.4121	0.5279	0.9486	9.1396
0.4162	0.5779	0.9458	9.0439
0.4204	0.632	0.9443	8.9681
0.4246	0.6908	0.9421	8.8847
0.4289	0.7543	0.9394	8.8123
0.4331	0.8232	0.9359	8.7446
0.4375	0.8976	0.9337	8.6793
0.4418	0.9783	0.9305	8.6215
0.4463	1.0656	0.9266	8.5481
0.4507	1.1598	0.9245	8.4987
0.4552	1.2618	0.9204	8.44
0.4598	1.372	0.9163	8.3922
0.4644	1.491	0.9082	8.3095
0.469	1.619	0.9052	8.2758
0.4737	1.7573	0.9015	8.2207
0.4785	1.9064	0.896	8.1537
0.4832	2.067	0.8908	8.1013
0.4881	2.2402	0.8873	8.0615
0.493	2.427	0.8822	8.0374
0.4979	2.6281	0.8785	8.0069
0.5029	2.8451	0.8709	7.9258
0.5079	3.0787	0.8676	7.9055
0.513	3.3306	0.8623	7.8758
0.5181	3.602	0.8577	7.8463
0.5233	3.8947	0.8523	7.8168
0.5285	4.2108	0.854	7.8451
0.5338	4.55	0.8336	7.7719
0.5391	4.9171	0.8083	7.9098
0.5445	5.3281	0.8575	8.0181
0.55	5.7701	0.8542	7.9963
0.5555	6.2481	0.8507	7.9868
0.561	6.7649	0.8486	7.9885
0.5666	7.3245	0.8424	7.9914
0.5723	7.9304	0.8397	7.9524

Table D.1: Variation of density, temperature, correlation coefficient and γ for the isomorph starting at $(\rho_{ref}, T_{ref}) = (0.4, 0.4)$. At each step we increased density by 1%.

ρ	T	R	γ
0.4	0.9	0.9524	9.2144
0.404	0.9861	0.9502	9.167
0.408	1.0807	0.947	9.2859
0.4121	1.1868	0.944	9.5727
0.4162	1.3056	0.9419	9.4825
0.4204	1.4309	0.9418	8.964
0.4246	1.5626	0.9404	8.7475
0.4289	1.7035	0.9383	8.6268
0.4331	1.8555	0.9361	8.5398
0.4375	2.0194	0.9335	8.4613
0.4418	2.1965	0.9305	8.4155
0.4463	2.3874	0.928	8.3218
0.4507	2.5933	0.9256	8.2644
0.4552	2.8151	0.9221	8.2157
0.4598	3.0541	0.9205	8.1504
0.4644	3.3108	0.9174	8.0744
0.469	3.5875	0.9154	8.0751
0.4737	3.8857	0.9131	7.9967
0.4785	4.2063	0.9086	7.9369
0.4832	4.5507	0.9054	7.8931
0.4881	4.9215	0.9025	7.8532
0.493	5.3211	0.9012	7.8212
0.4979	5.7506	0.8984	7.7878
0.5029	6.2128	0.889	7.7568
0.5079	6.7026	0.8811	7.5906
0.513	7.2277	0.8793	7.5639
0.5181	7.792	0.8757	7.544
0.5233	8.4164	0.9012	8.2261
0.5285	9.1338	0.8987	8.1691
0.5338	9.9127	0.8952	8.1572
0.5391	10.7494	0.896	8.1361
0.5445	11.6467	0.8954	8.0925
0.55	12.7586	0.9052	8.7326
0.5555	13.9398	0.9053	8.5871
0.561	15.1705	0.9041	8.412
0.5666	16.4842	0.9038	8.2758

Table D.2: Variation of density, temperature, correlation coefficient and γ for the isomorph starting at $(\rho_{ref}, T_{ref}) = (0.4, 0.9)$. At each step we increased density by 1%.

Appendix E

Reprints of Articles

Single-parameter aging in a binary Lennard-Jones system

View Online   Export Citation   CrossMark

Saeed Mehri,[a)] (iD) Trond S. Ingebrigtsen, (iD) and Jeppe C. Dyre[b)] (iD)

AFFILIATIONS

Glass and Time, IMFUFA, Department of Science and Environment, Roskilde University, P.O. Box 260,
DK-4000 Roskilde, Denmark

[a)] Author to whom correspondence should be addressed: mehri@ruc.dk
[b)] dyre@ruc.dk

ABSTRACT

This paper studies physical aging by computer simulations of a 2:1 Kob–Andersen binary Lennard-Jones mixture, a system that is less prone to crystallization than the standard 4:1 composition. Starting from thermal-equilibrium states, the time evolution of the following four quantities is monitored by following up and down jumps in temperature: potential energy, virial, average squared force, and the Laplacian of the potential energy. Despite the fact that significantly larger temperature jumps are studied here than in typical similar experiments, to a good approximation, all four quantities conform to the single-parameter-aging scenario derived and validated for small jumps in experiments [T. Hecksher, N. B. Olsen, and J. C. Dyre, J. Chem. Phys. **142**, 241103 (2015)]. As a further confirmation of single-parameter aging with a common material time for the four different quantities monitored, their relaxing parts are found to be almost identical for all temperature jumps.

Published under license by AIP Publishing. https://doi.org/10.1063/5.0039250

I. INTRODUCTION

It is of great interest to be able to predict how much and how fast material properties change over time.[1] Such gradual property changes are referred to as aging. Corrosion and weathering, in general, give rise to aging. The term "physical aging" refers to changes in material properties that result exclusively from molecular rearrangements, i.e., involve no chemical changes.[2–4] A number of theories of physical aging have been developed,[2–15] and physical aging has been the subject of experimental studies in different contexts dealing with, e.g., oxide glasses,[3,4] polymers,[5,16–20] metallic glasses,[21,22] colloids,[22] and spin glasses.[23,24] Examples of quantities monitored in order to probe physical aging are density,[19,25] enthalpy,[3,6] Young's modulus,[19] and various frequency-dependent responses.[7,8,26–32]

Physical aging is generally both non-exponential and non-linear. The latter property is reflected in the fact that the system's response to a small perturbation depends on both the sign and the magnitude of the input. Ideally, an aging experiment consists of an up or a down jump in temperature starting from a state of thermal equilibrium, eventually ending in equilibrium at the "target" (annealing) temperature. The hallmark of aging is that these two responses, even if they go to the same temperature, are *not* mirror symmetric. A down jump is fast at the beginning but slows down gradually as equilibrium is approached ("self-retarding"). An up jump—while slower in the beginning—will, after an initial delay, show a steeper approach to equilibrium ("self-accelerating").[4,9,19] This is the fictive-temperature effect, also referred to as "asymmetry of approach,"[33–35] an effect that is well understood as a consequence of the fact that the relaxation rate itself ages.[4–6,16,36–39]

In experimental studies of physical aging, the temperature T is externally controlled and identified as the phonon "bath" temperature measured on a thermometer. Recently, Hecksher *et al.*[8] and Roed *et al.*[40] studied the physical aging of glass-forming liquids around the glass transition temperature by probing the shear-mechanical resonance frequency (~360 kHz), the dielectric loss at 1 Hz, the real part of the dielectric constant at 10 kHz, and the loss-peak frequency of the dielectric beta process (~10 kHz). These authors developed a "single-parameter aging" (SPA) formalism as a simple realization of Narayanaswamy's idea that a material time

controls aging.[3] SPA basically allows one to predict the normalized relaxation functions of an arbitrary temperature jump from the data of a single jump. SPA was first demonstrated for jumps to the same temperature for three different van der Waals liquids[8] and subsequently generalized to deal with jumps ending at different temperatures in a study of glycerol.[40]

The motivation of this study is to illuminate how general SPA is by investigating whether SPA applies also in computer simulations. The advantage of simulations is that one can probe well-defined microscopic quantities and, for instance, easily study the aging of several different quantities under identical circumstances. We report below data for the physical aging of a binary Lennard-Jones mixture upon a temperature jump. The following four quantities were monitored: virial, potential energy, average squared force, and the Laplacian of the potential energy. We find that all four quantities conform to SPA to a good approximation, even for temperature jumps as large as 10%.

II. THE TOOL-NARAYANASWAMY MATERIAL-TIME CONCEPT

Above the melting temperature, a liquid is rarely particularly viscous. At lower temperatures, the liquid becomes supercooled, and because of the extraordinary large viscosities reached upon further cooling, the liquid gradually behaves more like a "solid that flows" than like an ordinary liquid.[41] For both the ordinary liquid phase and the glass phase, under ambient pressure conditions, physical properties are found to depend only on the temperature. At temperatures in the vicinity of the glass transition temperature (defined by the applied cooling and heating rates), however, the behavior is different. In this temperature range, the molecular structure changes gradually with temperature, and following an external perturbation, a noticeable delay is observed before equilibrium is reached. In this case, the physical properties depend not just on the actual temperature, but on the entire thermal history of the system.

In 1971, Narayanaswamy established what has become the standard formalism for physical aging. It was developed for predicting how the frozen-in stresses in a wind shield depend on the glass's thermal history during production. The theoretical framework, which turned out to be generally applicable for physical aging involving moderate temperature changes,[3,4] is now referred to as the Tool-Narayanaswamy (TN) formalism. This framework systematically addresses the non-exponential and non-linear nature of aging. The TN formalism reproduces all observed qualitative features of physical aging, and it is also in quantitative agreement with experiments.[2–4,42,43]

The crucial concept of TN is that of a *material time*, denoted by ξ. The material time may be thought of as the time measured on a clock with a clock rate, $\gamma(t)$, that changes as the material ages. Simply put, the material time is the time that a substance "experiences," which in equilibrium is proportional to the actual time. In this physical picture, one expects the existence of a single material time controlling the physical aging of different quantities.

Since the clock rate by definition measures how fast the material time changes,[3,43] one has

$$d\xi = \gamma(t)dt. \tag{1}$$

Narayanaswamy showed from experimental data that if one switches from time to material time the aging response becomes linear. In other words, a non-linear aging response is described by a *linear* convolution integral over the material time.[3,4] This was an important and highly nontrivial finding. For instance, it implies that the "asymmetry of approach" becomes a "symmetry of approach" when jumps of equal magnitude to the same temperature are considered as functions of the material time.

III. SIMULATION DETAILS

The simulations were performed in the *NVT* ensemble with the Nosé–Hoover thermostat using the RUMD (Roskilde University Molecular Dynamics) GPU open-source code (http://rumd.org). We simulated a system of 10 002 particles consisting of two different Lennard-Jones (LJ) spheres, A and B. Writing the LJ pair potential between particles of type α and β as $v_{\alpha\beta}(r) = \varepsilon_{\alpha\beta}((r/\sigma_{\alpha\beta})^{-12} - (r/\sigma_{\alpha\beta})^{-6})$ ($\alpha, \beta = A, B$), the parameters used are $\sigma_{AA} = 1.0$, $\sigma_{AB} = \sigma_{BA} = 0.8$, $\sigma_{BB} = 0.88$, $\varepsilon_{AA} = 1.0$, $\varepsilon_{AB} = \varepsilon_{BA} = 1.5$, and $\varepsilon_{BB} = 0.5$. All simulations employed a MD time step of 0.0025 (in the units defined by the A particle parameters) and a shifted-potential cutoff of $v_{\alpha\beta}(r)$ at $r_{\text{cut}} = 2.5\sigma_{\alpha\beta}$. The pair-potential parameters are the same as those of the well-known Kob–Andersen (KA) mixture,[44] which has previously been used for numerical studies of physical aging and other glass-transition related non-equilibrium phenomena.[45–49] We use a ratio of A and B particles that is 2:1 instead of the standard 4:1 ratio, however, because the 2:1 mixture is much more resistant toward crystallization than the 4:1 composition[50–52] (an alternative option for avoiding crystallization of KA mixtures is to keep the 4:1 composition and employ a short-distance shifted-force cutoff for the AA and BB interactions[53]). To facilitate a comparison of results for the two different compositions, we note that the mode-coupling temperature is around 0.55 for the 2:1 KA system, whereas it is around 0.44 for the standard mixture.

All results reported below were obtained at density 1.4 (in A particle units) and represent averaging over 100 simulations. Each data point was obtained by averaging in time every 2048 time steps for an interval of 32 768 time steps. Before performing a temperature jump, the system was carefully equilibrated. To reach equilibrium at the lowest temperature ($T = 0.50$) and ensure that there is no crystallization issue, we first simulated the system by performing 2.4×10^{11} time steps. After this, 100 equilibrium configurations were obtained by dumping a configuration every 1.678×10^8 time steps, which is of the same order of magnitude as the average relaxation time. At higher temperatures, equilibrium is reached much faster, of course.

Initially, the following five quantities were probed: the potential energy, the virial, the configurational temperature defined by

$$k_B T_{\text{conf}} = \frac{\langle (\nabla U)^2 \rangle}{\langle \nabla^2 U \rangle}, \tag{2}$$

its numerator (the average squared force), and its denominator (the Laplacian of the potential energy). In equilibrium in the thermodynamic limit, the configurational temperature is equal to the temperature T. The data of this study, obtained after averaging over 100 simulations, are presented in Figs. 1 and 2. We find that the configurational temperature does not age but equilibrates almost instantaneously [Fig. 1(c)], confirming previous results by
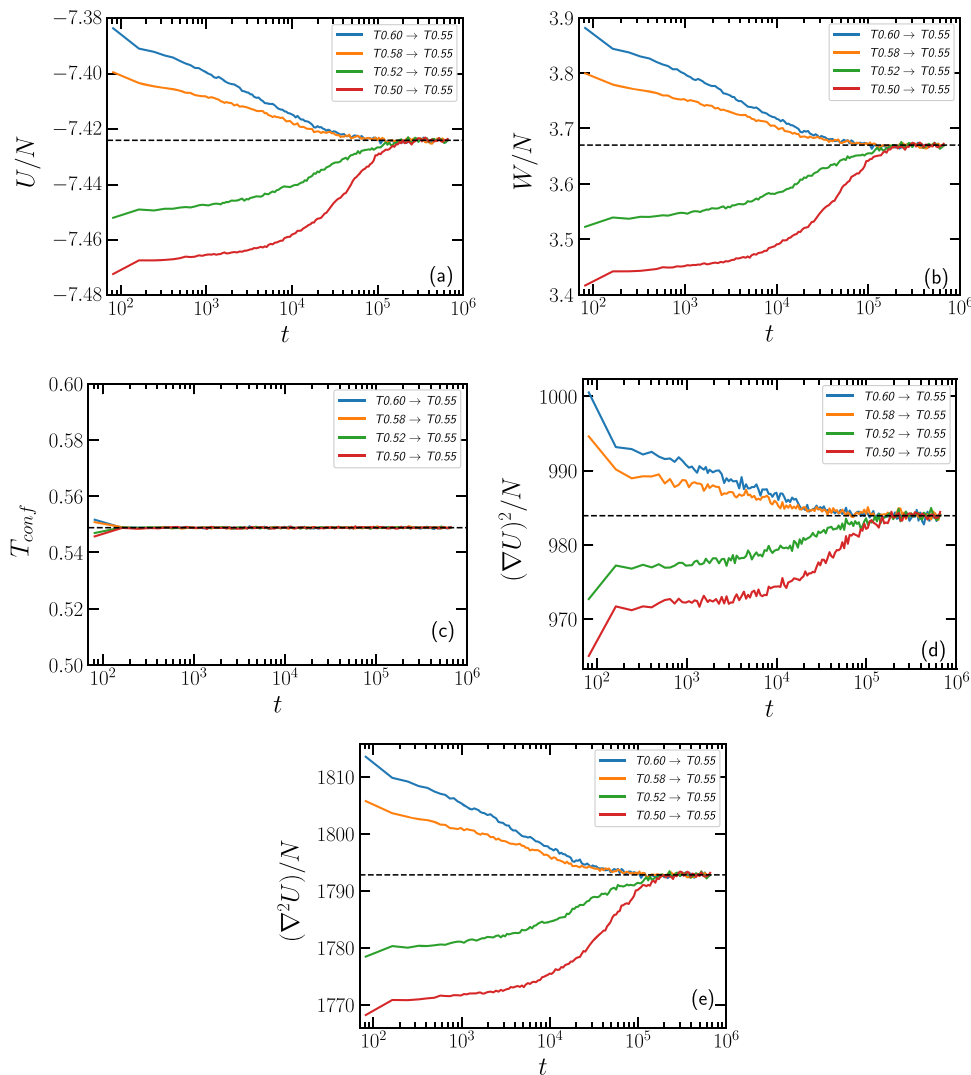
FIG. 1. Aging data for jumps to the same target temperature. Each panel shows four jumps from $T_{start} = T_0 + \Delta T$ to $T_0 = 0.55$ with $\Delta T = \pm 0.03$ and $\Delta T = \pm 0.05$. Results for temperature up jumps are shown in red and green, while those for down jumps are shown in blue and orange. The fictive-temperature effect (asymmetry of approach) is clearly observed, with down jumps being faster and more stretched than up jumps: (a) potential energy; (b) virial; (c) configurational temperature [Eq. (2)], which does not age; (d) average squared force; and (e) the Laplacian of the potential energy.

Powles et al.[54] We have no simple explanation of this observation. The remainder of the paper focuses on the aging of the four other quantities. These quantities are easily probed and obvious choices for testing SPA in a computer simulation.

After equilibration at each starting temperature $T_{start} = T_0 + \Delta T$, we initiate an aging simulation at $t = 0$ by changing the thermostat temperature to the "target" temperature T_0. The system eventually reaches the thermal equilibrium at T_0. We denote the quantity probed by $\chi(t)$. The equilibrium value of χ at T_0 is denoted by χ_{eq}, while $\chi(0)$ is the equilibrium value of χ at T_{start}, i.e., just before the jump is initiated at $t = 0$.

From $\chi(t)$, we define for each temperature jump the normalized relaxation function $R(t)$ by subtracting the value of χ at T_0 from the value at each time, subsequently dividing by the overall change, i.e.,

$$R(t) \equiv \frac{\chi(t) - \chi_{eq}}{\chi(0) - \chi_{eq}}. \quad (3)$$

Note that while $R(0) = 1$ just before the jump is initiated, within a few time steps after $t = 0$ there is a significant "instantaneous" drop in $R(t)$. Aging descriptions conventionally focus only on the subsequent, relaxing part of the temperature response, but it is convenient to use instead the above defined $R(t)$ because this quantity can be determined directly from the data without having to estimate the magnitude of the initial "instantaneous" change of χ.

IV. SINGLE-PARAMETER AGING

We briefly review here the derivation of SPA, which is based on two assumptions within the TN formalism.[8,40] The first assumption is that the clock rate, $\gamma(t)$, is determined by the monitored parameter $\chi(t)$ itself. The second assumption is that temperature changes are so small that a first-order Taylor expansion of the logarithm of the aging rate in terms of χ applies. If $\Delta\chi(t) \equiv \chi(t) - \chi_{eq}$ is the variation of
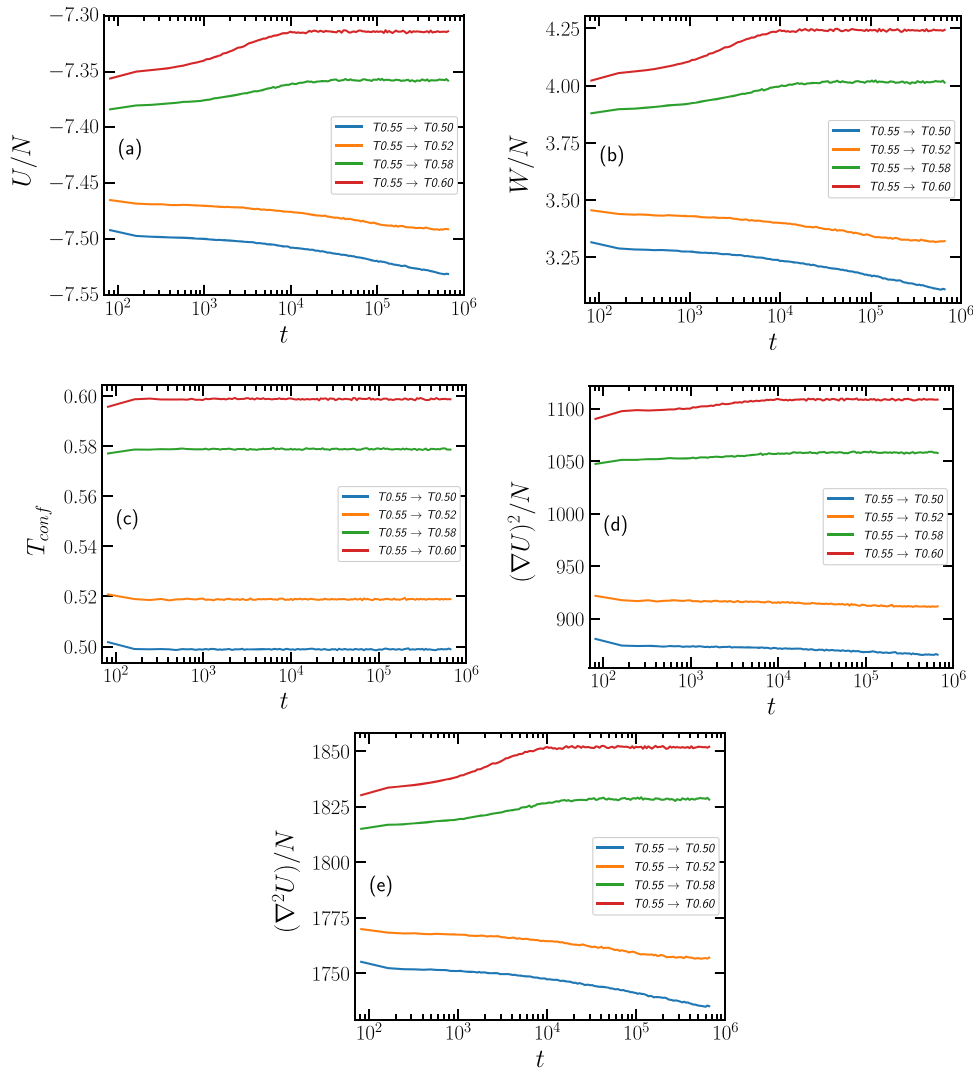
FIG. 2. Aging data for jumps from the same temperature. Each panel shows four jumps from $T_0 = 0.55$ to $0.55 + \Delta T$ with $\Delta T = \pm 0.03$ and $\Delta T = \pm 0.05$. Results for temperature up jumps are shown in red and green, while those for down jumps are shown in blue and orange. Note that the scale on the y axis is different from that of Fig. 1. (a) Potential energy, (b) virial, (c) configurational temperature, (d) average squared force, and (e) the Laplacian of the potential energy.

χ from its equilibrium value at the target temperature T_0 [implying that $\Delta\chi(t) \to 0$ as $t \to \infty$], the first-order Taylor expansion leads to[8]

$$\ln \gamma(t) = \ln \gamma_{\text{eq}} + \Delta\chi(t)/\chi_{\text{const}}, \qquad (4)$$

in which γ_{eq} is the equilibrium relaxation rate at the target temperature T_0 and χ_{const} is a constant of the same dimension as χ. This expression summarizes the general SPA framework. In conjunction with the TN basic assumption that physical aging is a linear response in the temperature variation when formulated in terms of the material time, SPA may be applied to any relatively small temperature variation, no matter whether it is continuous or discontinuous. We henceforth consider the simplest case with that of a (discontinuous) temperature jump.

Since $\Delta\chi(t) = \Delta\chi(0)R(t)$ by the definition of $R(t)$, Eq. (4) implies[8]

$$\gamma(t) = \gamma_{\text{eq}} \exp\left(\frac{\Delta\chi(0)}{\chi_{\text{const}}} R(t)\right). \qquad (5)$$

The normalized relaxation function $R(t)$ is given by[3,4,8]

$$R(t) = \Phi(\xi). \qquad (6)$$

The point of the TN formalism is that the function $\Phi(\xi)$ is the same for all temperature jumps. In contrast, the time dependence of the material time, $\xi(t)$, is not universal because the aging rate changes as the system ages. In conjunction with the definition of the aging rate in terms of the material time [Eq. (1)], Eq. (6) implies $\dot{R}(t) = \Phi'(\xi)\gamma(t)$. Since Eq. (6) means that ξ is the same function of R for all jumps, by defining $F(R) \equiv -\Phi'(\xi(R))$, one gets[8]

$$\dot{R}(t) = -F(R)\gamma(t). \qquad (7)$$

The negative sign in Eq. (7) is convenient because $R(t)$ is (usually) a monotonically decreasing function of time, thus making $F(R)$ positive.

Equations (5) and (7) lead to

$$-\frac{\dot{R}(t)}{\gamma_{eq}} \exp\left(-\frac{\Delta\chi(0)}{\chi_{const}}R(t)\right) = F(R(t)). \tag{8}$$

Since the right-hand side for a given value of $R(t)$ is independent of the jump sign and magnitude, this applies also for the left-hand side. This prediction was validated in 2015 in experiments monitoring four different quantities.[8] From Eq. (8), one can basically predict the relaxation function of one jump from the relaxation function of another jump since a single jump is enough to determine the function $F(R)$. In order to determine the constant χ_{const}, however, two jumps are needed (see below); alternatively, a determination of the equilibrium relaxation rate at two different temperatures can also be used to find χ_{const}. We refer below to the "known" relaxation function as "jump1," while the relaxation function to be compared to the prediction based on jump1 is referred to as "jump2."

For the times $t_1^*(R)$ and $t_2^*(R)$ at which two jumps have the same normalized relaxation function, i.e., $R_1 = R_2 = R$, since $F(R_1) = F(R_2)$, Eq. (8) implies that

$$-\frac{dR_1}{dt_1^*} \cdot \frac{1}{\gamma_{eq,1}} \cdot \exp\left(-\frac{\Delta\chi(0)_1}{\chi_{const}}R(t_1^*)\right)$$
$$= -\frac{dR_2}{dt_2^*} \cdot \frac{1}{\gamma_{eq,2}} \cdot \exp\left(-\frac{\Delta\chi(0)_2}{\chi_{const}}R(t_2^*)\right). \tag{9}$$

If we choose dt_1^* and dt_2^* such that $dR_1 = dR_2$ and use $R_1(t_1^*) = R_2(t_2^*)$, Eq. (9) leads to

$$dt_2^* = \frac{\gamma_{eq,1}}{\gamma_{eq,2}} \exp\left(\frac{\Delta\chi(0)_1 - \Delta\chi(0)_2}{\chi_{const}}R(t_1^*)\right)dt_1^*. \tag{10}$$

By integrating this, one gets

$$t_2 = \int_0^{t_2} dt_2^* = \frac{\gamma_{eq,1}}{\gamma_{eq,2}} \int_0^{t_1} \exp\left(\frac{\Delta\chi(0)_1 - \Delta\chi(0)_2}{\chi_{const}}R(t_1^*)\right)dt_1^*. \tag{11}$$

Equation (11) states that for predicting jump2, one just needs to "transport" the discrete time vector $\mathbf{t}_1 = (t_1^1, t_1^2, \ldots, t_1^n)$ and its corresponding relaxation vector $\mathbf{R}_1 = (R_1^1, R_1^2, \ldots, R_1^n)$ to a new time vector $\mathbf{t}_2 = (t_2^1, t_2^2, \ldots, t_2^n)$, corresponding to the same $\mathbf{R}$ vector $\mathbf{R}_1$.[40] Thus, by plotting $(\mathbf{t}_2, \mathbf{R}_1)$ and $(\mathbf{t}_2, \mathbf{R}_2)$, data are predicted to collapse if SPA applies. For jumps to the same target temperature, Eq. (11) reduces to[8]

$$t_2 = \int_0^{t_1} \exp\left(\frac{\Delta\chi(0)_1 - \Delta\chi(0)_2}{\chi_{const}}R(t_1^*)\right)dt_1^*. \tag{12}$$

The more general SPA version developed by Roed *et al.*[40] allows one to predict all jumps from the knowledge of a single jump and

TABLE I. Different values of χ_{const}—derived using Eq. (14) for jumps from 0.60 and 0.50 to the target temperature 0.55.

Quantity	U	W	$(\nabla U)^2$	$\nabla^2 U$
χ_{const}	0.018 57	0.099 44	5.117	10.04

χ_{const} [still assuming that ΔT is small enough to justify the first-order Taylor expansion given in Eq. (4)]. In contrast to the first SPA derivation considering only jumps to the same target temperature,[8] however, one needs to know the equilibrium clock rate, γ_{eq}, at the target temperature T_0. In this paper, we identified this quantity from $\gamma_{eq} \equiv 1/\tau$, in which the relaxation time τ is determined from the intermediate scattering function evaluated at the wave vector corresponding to the first-peak maximum of the AA particle radial distribution function (τ is the time at which this quantity has decayed to 0.2).

From two jumps to the same target temperature, by means of Eq. (12), χ_{const} can be determined and subsequently used to predict all the other jumps. Thus, Eq. (12) implies that

$$t_2(R) - t_1(R) = \int_0^{t_1(R)}\left[\exp\left(\frac{\Delta\chi(0)_1 - \Delta\chi(0)_2}{\chi_{const}}R(t_1^*)\right) - 1\right]dt_1^*. \tag{13}$$

A similar expression applies for $t_1(R) - t_2(R)$. Taking the long-time limits of these expressions for the two normalized relaxation functions in question leads to the self-consistency requirement,[8]

$$\int_0^\infty\left[\exp\left(\frac{\Delta\chi(0)_1 - \Delta\chi(0)_2}{\chi_{const}}R(t_1^*)\right) - 1\right]dt_1^*$$
$$+ \int_0^\infty\left[\exp\left(\frac{\Delta\chi(0)_2 - \Delta\chi(0)_1}{\chi_{const}}R(t_2^*)\right) - 1\right]dt_2^* = 0. \tag{14}$$

Equation (14) is an equation for χ_{const} that is easily solved numerically. The value of χ_{const} depends on the quantity probed, of course. Table I provides the values of χ_{const} for the four different quantities monitored.

V. TEMPERATURE-JUMP RESULTS

Figure 3 investigates SPA for jumps to the same target temperature ($T_0 = 0.55$). In the upper panels, down jumps (green) were used to predict up jumps (blue), and in the lower panels, up jumps were used to predict down jumps. The relaxation curves do not start at unity because of the already mentioned "instantaneous" jump that occurs within the first few time steps of an aging simulation. The relative magnitude of this jump depends on the quantity in question. Jumps to different target temperatures were also investigated (Fig. 4). The predictions in the upper panels are based on up jumps, while the predictions in the lower panels are based on down jumps. There are small deviations at the beginning, and the predictions do not fit data as well for larger jumps as for smaller ones. Despite these
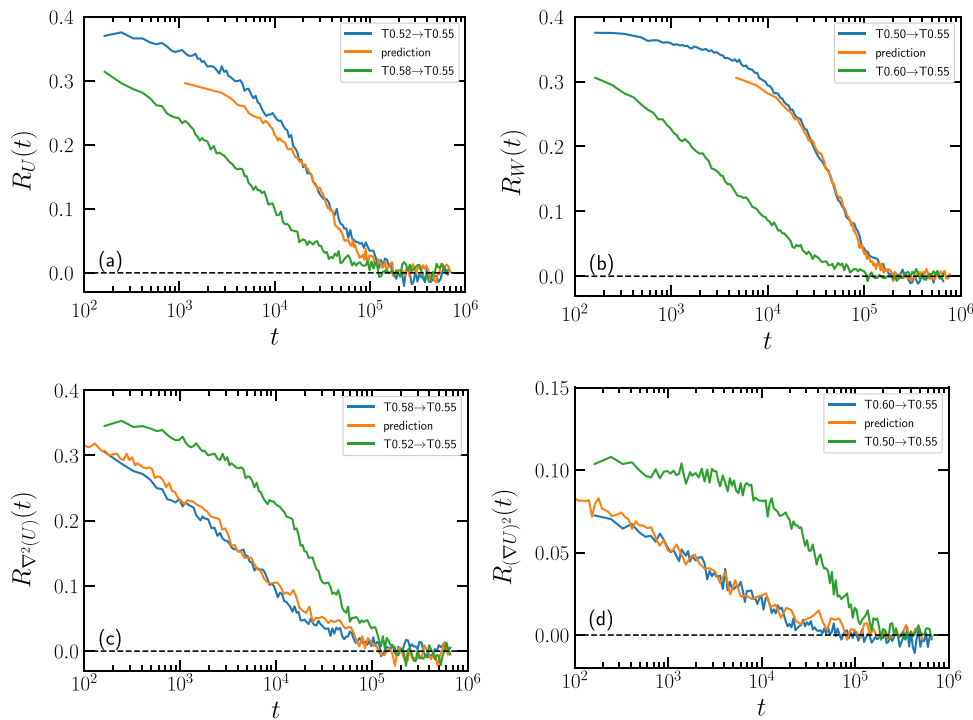
FIG. 3. Test of the SPA predictions for jumps to the same target temperature $T_0 = 0.55$. The data for the "jump1" normalized relaxation functions $R(t)$ are represented by the green curves. The predictions based on jump1 according to Eq. (12) are represented by the orange curves. These are to be compared to the "jump2" data (blue curves). (a) and (b) give the predictions of up jumps based on down jumps for the potential energy and the virial, respectively. (c) and (d) give the predictions of down jumps based on up jumps for the Laplacian of the potential energy and the average squared force, respectively.

minor deviations, we conclude that, overall, the results validate SPA for computer simulations.

Figures 5 and 6 plot for each temperature jump all four relaxation curves. The curves have here been scaled empirically by multiplying $R(t)$ by a constant in order to be able to compare the relaxing parts of the aging signals. We see that the four quantities relax almost identically. This demonstrates a physically appealing version of SPA according to which all four quantities' age in
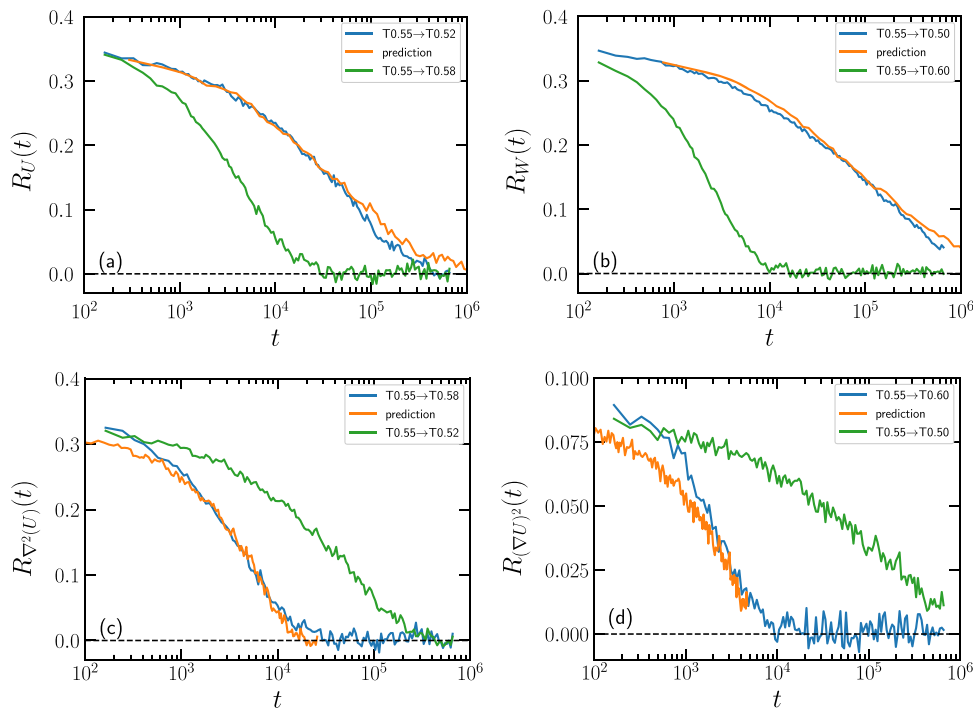
FIG. 4. SPA tested for jumps starting at the same temperature (0.55) and ending at different target temperatures. Jump1 data are represented by the green curves. The predictions based on jump1 according to Eq. (12) are represented by orange, while the jump2 simulation results are represented by blue. (a) and (b) give the predictions of down jumps based on up jumps for the potential energy and the virial, respectively. (c) and (d) give the predictions of up jumps based on down jumps for the Laplacian of the potential energy and the average squared force, respectively.
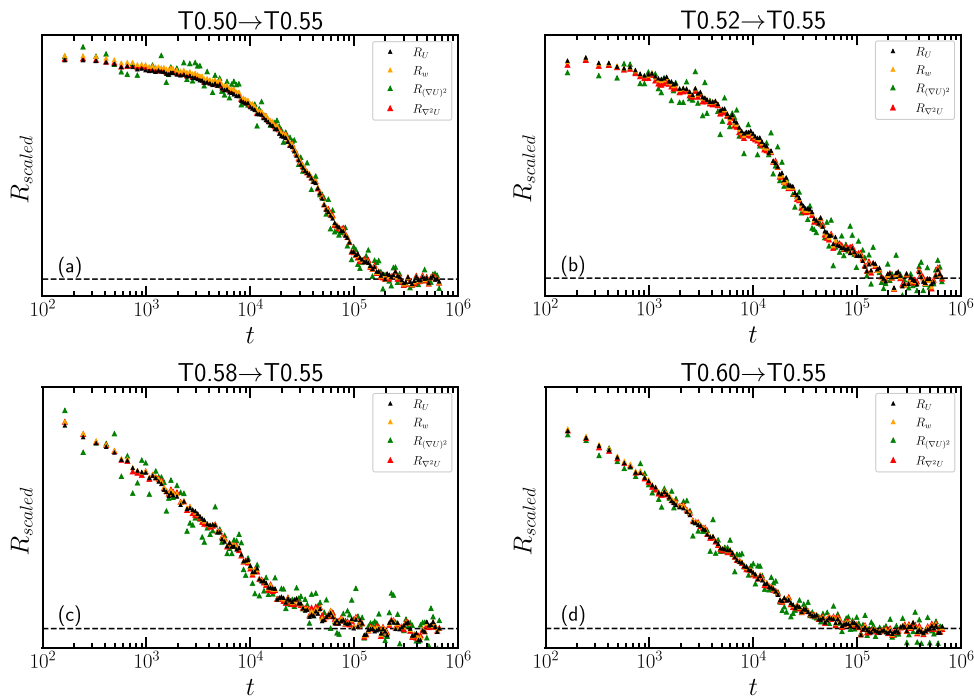
FIG. 5. Empirically scaled relaxation curves of the four quantities, plotted for each of the four jumps to the target temperature 0.55. The black points represent the potential energy, yellow points represent the virial, green points represent the average squared force, and red points represent the Laplacian of the potential energy. The dashed lines mark zero.
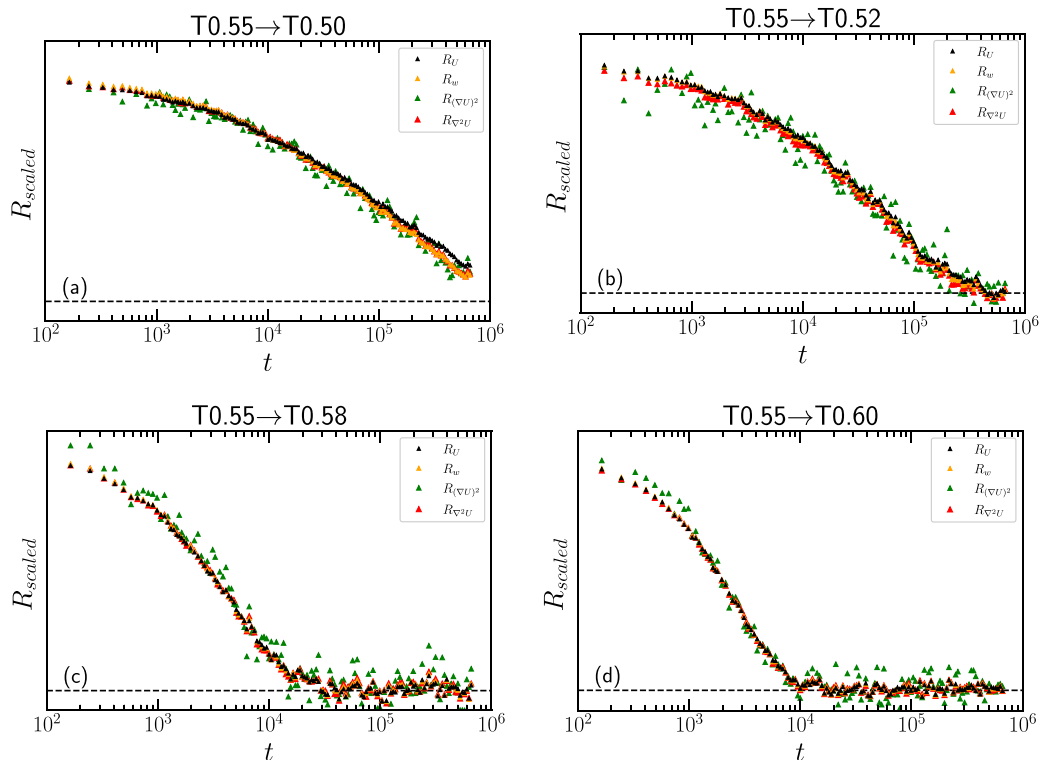
FIG. 6. Empirically scaled relaxation curves of the four quantities, plotted for each of the four jumps away from the target temperature 0.55. The same color codes are used here as in Fig. 5.

the same way and controlled by the same material time. This is consistent with a material time thought of physically as reflecting the time on an "internal clock" of the aging system. In the present context, we note, however, that part of the scaled relaxing curves being virtually identical is not surprising. Thus, it is known that binary Lennard-Jones systems have strong virial potential-energy correlations, implying that in equilibrium, the virial is a linear function of the potential energy.[55–57] This extends to out-of-equilibrium situations.[58] Thus, one expects the virial and the potential energy to have the same relaxation functions, except for scaling constants. Likewise, the observation that the configurational temperature equilibrates almost instantaneously implies that its numerator (the average squared force) and its denominator (the Laplacian of the potential energy) must have the same relaxation functions.

VI. DISCUSSION

While physical aging is usually studied experimentally, computer simulations provide an alternative means for systematically investigating aging. For instance, it is much easier to control and rapidly change temperature in a computer simulation. It should be noted, though, that it is only with the presently available strong computing powers that it is possible to obtain the simulation results of a quality approaching that of the best aging experiments.

We find that SPA works well in computer simulations, albeit with an accuracy that decreases somewhat as the jump size increases. This is not surprising since a first-order Taylor expansion was used to derive SPA. It is important to note, however, that the largest temperature jumps considered here are, relatively, almost ten times larger than those of the experimental validations of the SPA formalism[8,40] (10% vs 1%). Not surprisingly, the larger the deviations observed in some of the predictions at the beginning are, the larger the jumps are. Confirming the previous findings by Powles and co-workers,[54] we find that the configurational temperature, $k_B T_{conf}$, does not age; on the other hand, both its numerator and denominator age following SPA. We recommend using data from up and down jumps with the same magnitude to the same target temperature when identifying χ_{const} by use of Eq. (14). In this way, one avoids the need to model the temperature dependence of γ_{eq}.

The above-mentioned computer simulations were performed at constant volume. We have not attempted to test SPA in constant-pressure simulations but expect that SPA applies equally well here. Thus, the experiments confirming SPA were all performed at ambient pressure;[8,40] moreover, the SPA derivation does not assume constant-volume conditions.

SPA is the simplest aging scenario consistent with the TN concept of a material time. This is because SPA is derived by assuming just a single relevant parameter and because first-order Taylor expansions are used.[8] Our finding that all four quantities conform to SPA and relax in the same way shows that they are controlled by the same material time. This is not trivial. Whether all quantities of the binary LJ system age controlled by this clock is an interesting question for future work. It would also be interesting to investigate whether the agreement with simulations may be improved by Taylor expanding to higher order, without making the SPA formalism highly involved or introducing a wealth of adjustable parameters.

DATA AVAILABILITY

The data that support the findings of this study are available from the corresponding author upon reasonable request. We thank Lorenzo Costigliola and Thomas Schrøder for technical assistance.

REFERENCES

[1] D. Cangialosi, "Dynamics and thermodynamics of polymer glasses," J. Phys.: Condens. Matter **26**, 153101 (2014).

[2] A. Q. Tool, "Relation between inelastic deformability and thermal expansion of glass in its annealing range," J. Am. Ceram. Soc. **29**, 240–253 (1946).

[3] O. S. Narayanaswamy, "A model of structural relaxation in glass," J. Am. Ceram. Soc. **54**, 491–498 (1971).

[4] G. W. Scherer, *Relaxation in Glass and Composites* (Wiley, New York, 1986).

[5] I. M. Hodge, "Physical aging in polymer glasses," Science **267**, 1945–1947 (1995).

[6] C. T. Moynihan, A. J. Easteal, M. A. De Bolt, and J. Tucker, "Dependence of the fictive temperature of glass on cooling rate," J. Am. Ceram. Soc. **59**, 12–16 (1976).

[7] N. B. Olsen, J. C. Dyre, and T. Christensen, "Structural relaxation monitored by instantaneous shear modulus," Phys. Rev. Lett. **81**, 1031 (1998).

[8] T. Hecksher, N. B. Olsen, and J. C. Dyre, "Communication: Direct tests of single-parameter aging," J. Chem. Phys. **142**, 241103 (2015).

[9] J. C. Mauro, R. J. Loucks, and P. K. Gupta, "Fictive temperature and the glassy state," J. Am. Ceram. Soc. **92**, 75–86 (2009).

[10] L. F. Cugliandolo and J. Kurchan, "On the out-of-equilibrium relaxation of the Sherrington-Kirkpatrick model," J. Phys. A: Math. Gen. **27**, 5749 (1994).

[11] W. Kob and J.-L. Barrat, "Fluctuations, response and aging dynamics in a simple glass-forming liquid out of equilibrium," Eur. Phys. J. B **13**, 319–333 (2000).

[12] D. B. Adolf, R. S. Chambers, J. Flemming, J. Budzien, and J. McCoy, "Potential energy clock model: Justification and challenging predictions," J. Rheol. **51**, 517–540 (2007).

[13] H. E. Castillo and A. Parsaeian, "Local fluctuations in the ageing of a simple structural glass," Nat. Phys. **3**, 26–28 (2007).

[14] A. Parsaeian and H. E. Castillo, "Equilibrium and nonequilibrium fluctuations in a glass-forming liquid," Phys. Rev. Lett. **102**, 055704 (2009).

[15] I. Kolvin and E. Bouchbinder, "Simple nonlinear equation for structural relaxation in glasses," Phys. Rev. E **86**, 010501 (2012).

[16] L. C. E. Struik, *Physical Aging in Amorphous Polymers and Other Materials* (Elsevier, Amsterdam, 1978).

[17] J. M. Hutchinson, "Physical aging of polymers," Prog. Polym. Sci. **20**, 703–760 (1995).

[18] G. M. Odegard and A. Bandyopadhyay, "Physical aging of epoxy polymers and their composites," J. Polym. Sci., Part B: Polym. Phys. **49**, 1695–1716 (2011).

[19] D. Cangialosi and V. M. Boucher, A. Alegría, and J. Colmenero, "Physical aging in polymers and polymer nanocomposites: Recent results and open questions," Soft Matter **9**, 8619–8630 (2013).

[20] L. Grassia and S. L. Simon, "Modeling volume relaxation of amorphous polymers: Modification of the equation for the relaxation time in the KAHR model," Polymer **53**, 3613–3620 (2012).

[21] J. C. Qiao and J.-M. Pelletier, "Dynamic mechanical relaxation in bulk metallic glasses: A review," J. Mater. Sci. Technol. **30**, 523–545 (2014).

[22] L. Song, W. Xu, J. Huo, F. Li, L.-M. Wang, M. D. Ediger, and J.-Q. Wang, "Activation entropy as a key factor controlling the memory effect in glasses," Phys. Rev. Lett. **125**, 135501 (2020).

[23] L. Lundgren, P. Svedlindh, P. Nordblad, and O. Beckman, "Dynamics of the relaxation-time spectrum in a CuMn spin-glass," Phys. Rev. Lett. **51**, 911 (1983).

[24] L. Berthier and J.-P. Bouchaud, "Geometrical aspects of aging and rejuvenation in the Ising spin glass: A numerical study," Phys. Rev. B **66**, 054404 (2002).

[25] S. Spinner and A. Napolitano, "Further studies in the annealing of a borosilicate glass," J. Res. Natl. Bur. Stand., Sect. A **70A**, 147 (1966).

[26] E. Schlosser and A. Schönhals, "Dielectric relaxation during physical ageing," Polymer **32**, 2135–2140 (1991).

[27] R. L. Leheny and S. R. Nagel, "Frequency-domain study of physical aging in a simple liquid," Phys. Rev. B **57**, 5154 (1998).

[28] P. Lunkenheimer, R. Wehn, U. Schneider, and A. Loidl, "Glassy aging dynamics," Phys. Rev. Lett. **95**, 055702 (2005).

[29] R. Richert, "Supercooled liquids and glasses by dielectric relaxation spectroscopy," Adv. Chem. Phys. **156**, 101–195 (2015).

[30] T. Hecksher, N. B. Olsen, K. Niss, and J. C. Dyre, "Physical aging of molecular glasses studied by a device allowing for rapid thermal equilibration," J. Chem. Phys. **133**, 174514 (2010).

[31] R. Wehn, P. Lunkenheimer, and A. Loidl, "Broadband dielectric spectroscopy and aging of glass formers," J. Non-Cryst. Solids **353**, 3862–3870 (2007).

[32] J. C. Dyre and N. B. Olsen, "Minimal model for beta relaxation in viscous liquids," Phys. Rev. Lett. **91**, 155703 (2003).

[33] A. J. Kovacs, "Transition vitreuse dans les polymeres amorphes. Etude phenomenologique," Fortschr. Hochpolym.-Forsch. **3**, 394–507 (1963).

[34] X. Di, K. Z. Win, G. B. McKenna, T. Narita, F. Lequeux, S. R. Pullela, and Z. Cheng, "Signatures of structural recovery in colloidal glasses," Phys. Rev. Lett. **106**, 095701 (2011).

[35] G. B. McKenna and S. L. Simon, "50th anniversary perspective: Challenges in the dynamics and kinetics of glass-forming polymers," Macromolecules **50**, 6333–6361 (2017).

[36] O. V. Mazurin, "Relaxation phenomena in glass," J. Non-Cryst. Solids **25**, 129–169 (1977).

[37] G. B. McKenna, "On the physics required for prediction of long term performance of polymers and their composites," J. Res. Natl. Inst. Stand. Technol. **99**, 169 (1994).

[38] I. M. Hodge, "Enthalpy relaxation and recovery in amorphous materials," J. Non-Cryst. Solids **169**, 211–266 (1994).

[39] I. Avramov, "Kinetics of structural relaxation of glass-forming melts," Thermochim. Acta **280-281**, 363–382 (1996).

[40] L. A. Roed, T. Hecksher, J. C. Dyre, and K. Niss, "Generalized single-parameter aging tests and their application to glycerol," J. Chem. Phys. **150**, 044501 (2019).

[41] J. C. Dyre, "The glass transition and elastic models of glass-forming liquids," Rev. Mod. Phys. **78**, 953–972 (2006).

[42] H. N. Ritland, "Limitations of the fictive temperature concept," J. Am. Ceram. Soc. **39**, 403–406 (1956).

[43] J. C. Dyre, "Narayanaswamy's 1971 aging theory and material time," J. Chem. Phys. **143**, 114507 (2015).

[44] W. Kob and H. C. Andersen, "Testing mode-coupling theory for a supercooled binary Lennard-Jones mixture I: The van Hove correlation function," Phys. Rev. E **51**, 4626–4641 (1995).

[45] K. Vollmayr, W. Kob, and K. Binder, "How do the properties of a glass depend on the cooling rate? A computer simulation study of a Lennard-Jones system," J. Chem. Phys. **105**, 4714–4728 (1996).

[46] A. Parsaeian and H. E. Castillo, "Growth of spatial correlations in the aging of a simple structural glass," Phys. Rev. E **78**, 060105 (2008).

[47] C. Rehwald, N. Gnan, A. Heuer, T. Schrøder, J. C. Dyre, and G. Diezemann, "Aging effects manifested in the potential-energy landscape of a model glass former," Phys. Rev. E **82**, 021503 (2010).

[48] N. Gnan, C. Maggi, G. Parisi, and F. Sciortino, "Generalized fluctuation-dissipation relation and effective temperature upon heating a deeply supercooled liquid," Phys. Rev. Lett. **110**, 035701 (2013).

[49] N. V. Priezjev, "Slow relaxation dynamics in binary glasses during stress-controlled, tension-compression cyclic loading," Comput. Mater. Sci. **153**, 235–240 (2018).

[50] T. S. Ingebrigtsen, J. C. Dyre, T. B. Schrøder, and C. Patrick Royall, "Crystallization instability in glass-forming mixtures," Phys. Rev. X **9**, 031016 (2019).

[51] U. R. Pedersen, T. B. Schrøder, and J. C. Dyre, "Phase diagram of Kob-Andersen-type binary Lennard-Jones mixtures," Phys. Rev. Lett. **120**, 165501 (2018).

[52] I. H. Bell, J. C. Dyre, and T. S. Ingebrigtsen, "Excess-entropy scaling in supercooled binary mixtures," Nat. Commun. **11**, 4300 (2020).

[53] T. B. Schrøder and J. C. Dyre, "Solid-like mean-square displacement in glass-forming liquids," J. Chem. Phys. **152**, 141101 (2020).

[54] J. G. Powles, G. Rickayzen, and D. M. Heyes, "Temperatures: Old, new and middle aged," Mol. Phys. **103**, 1361–1373 (2005).

[55] N. Gnan, T. B. Schrøder, U. R. Pedersen, N. P. Bailey, and J. C. Dyre, "Pressure-energy correlations in liquids. IV. 'Isomorphs' in liquid phase diagrams," J. Chem. Phys. **131**, 234504 (2009).

[56] L. Bøhling, T. S. Ingebrigtsen, A. Grzybowski, M. Paluch, J. C. Dyre, and T. B. Schrøder, "Scaling of viscous dynamics in simple liquids: Theory, simulation and experiment," New J. Phys. **14**, 113035 (2012).

[57] T. S. Ingebrigtsen and H. Tanaka, "Effect of size polydispersity on the nature of Lennard-Jones liquids," J. Phys. Chem. B **119**, 11052–11062 (2015).

[58] T. B. Schrøder, N. P. Bailey, U. R. Pedersen, N. Gnan, and J. C. Dyre, "Pressure-energy correlations in liquids. III. Statistical mechanics and thermodynamics of liquids with hidden scale invariance," J. Chem. Phys. **131**, 234503 (2009).

PHYSICS

Predicting nonlinear physical aging of glasses from equilibrium relaxation via the material time

Birte Riechers†, Lisa A. Roed, Saeed Mehri, Trond S. Ingebrigtsen, Tina Hecksher, Jeppe C. Dyre*, Kristine Niss*

The noncrystalline glassy state of matter plays a role in virtually all fields of materials science and offers complementary properties to those of the crystalline counterpart. The caveat of the glassy state is that it is out of equilibrium and therefore exhibits physical aging, i.e., material properties change over time. For half a century, the physical aging of glasses has been known to be described well by the material-time concept, although the existence of a material time has never been directly validated. We do this here by successfully predicting the aging of the molecular glass 4-vinyl-1,3-dioxolan-2-one from its linear relaxation behavior. This establishes the defining property of the material time. Via the fluctuation-dissipation theorem, our results imply that physical aging can be predicted from thermal-equilibrium fluctuation data, which is confirmed by computer simulations of a binary liquid mixture.

INTRODUCTION

Physical aging deals with small property changes resulting from molecular rearrangements (1–5). While the aging of a material is, in practice, often due to chemical degradation, physical aging does not involve any chemical change. Understanding this type of aging is crucial for applications of noncrystalline materials such as oxide glasses (4, 6–8), polymers (2, 5, 9–13), metallic glasses (14–18), amorphous pharmaceuticals (19), colloidal suspensions (20), etc. For instance, the performance of a smartphone display glass substrate is controlled by details of the physical aging during production (21), and some plastics eventually become brittle as a result of physical aging (22). Noncrystalline or partly noncrystalline states play a role in modern materials science, e.g., in connection with metal-organic frameworks (23) and high-entropy alloys (24), and physical aging is also important in connection with active matter (25–27). Last, it should be mentioned that aging under nano-confined conditions differs from that of bulk materials (28). The lack of a fundamental understanding of the glassy state and its aging with time influences all branches of materials science, which explains the continued interest in the field from a theoretical point of view (17, 27, 29–32).

Describing and predicting physical aging has been a focus of glass science for many years, yet the subject still presents important challenges (13, 31). In this work, we address the concept of a material ("reduced") time controlling aging, which was proposed by Narayanaswamy in 1971 in a paper dealing with the physical aging of oxide glasses (6). A closely related formalism describing polymer aging was developed a few years later by Kovacs and co-workers (3) and, in the 1990s, in the entirely different context of spin glasses by Cugliandolo and Kurchan (29). The material-time concept rationalizes several notable aging phenomena (4, 6, 33–35). It is used routinely in both basic research and applications. The material-time formalism is generally recognized to describe well the

physical aging of systems subjected to relatively small temperature variations, but the existence of a material time has never been validated in direct experiments. We do this here in long-time experiments on a glass-forming molecular liquid by demonstrating the fundamental prediction that linear response aging data determine the nonlinear aging behavior in the intermediate regime involving temperature variations of a few percent.

Physical aging is a complex phenomenon as it is both nonexponential and nonlinear. The simplest and best controlled aging experiment is based on the temperature jump protocol: The sample is initially in a state of thermal equilibrium, then its temperature is changed instantaneously, i.e., rapidly compared to the response time of the material, and the full approach to equilibrium at the new temperature is monitored as a function of time (36). This procedure requires a setup that allows for fast temperature changes and has a precise temperature control with a minimal long-time drift. Moreover, accurate measurements are needed because the long time tail of physical aging, as well as the entire aging response to a small temperature step, involves only minute changes of material properties.

Our experimental setup is based on a Peltier element in direct contact with a plane-plate capacitor. The setup keeps temperature constant over months with less than 1 mK variation, and the samples are so thin (50 μm) that the temperature may be changed within a few seconds to a new, constant value. Dielectric properties are monitored using an ultraprecision Andeen-Hagerling capacitance bridge. More details on the setup are provided in Materials and Methods and in (36–40).

RESULTS

We performed several temperature jump experiments around a reference temperature on the glass-forming liquid 4-vinyl-1,3-dioxolan-2-one (VEC) and monitored, after each jump, both the real and the imaginary part of the capacitance at 10 kHz as the system gradually equilibrates (41, 42). The real part of the VEC data is presented in Fig. 1; the imaginary part of the data can be found in the Supplementary Materials in which we also give analogous data for N-methyl-ε-caprolactam (NMEC). Capacitance can be measured very precisely and is an excellent probe in aging experiments

"Glass and Time", IMFUFA, Department of Science and Environment, Roskilde University, P.O. Box 260, DK-4000 Roskilde, Denmark.
*Corresponding author. Email: dyre@ruc.dk (J.C.D.); kniss@ruc.dk (K.N.)
†Present address: Federal Institute of Materials Research and Testing (BAM), Unter den Eichen 87, 12205 Berlin, Germany.
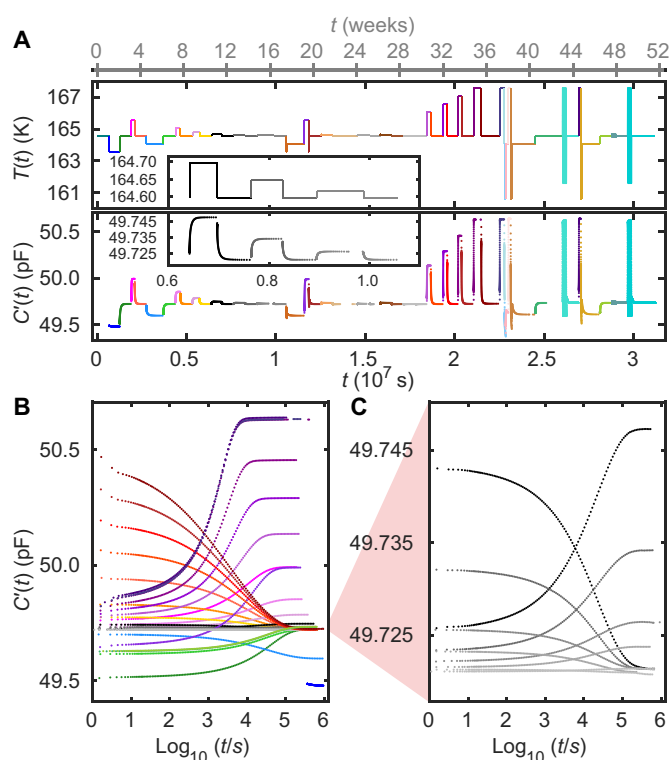
Fig. 1. Overview of the temperature protocol and the raw data of the full experiment on VEC. (**A**) The experimental protocol realized by temperature modulations around the reference temperature 164.6 K (top) and the real part of the measured capacitance C'(10 kHz) (bottom), both plotted as functions of time on a linear scale. Jumps larger than 100 mK are colored, while jumps of 100 mK or less are depicted on a gray scale; a selection of the latter is shown in the inset. The sinusoidal temperature modulations that are also studied (see below) are not resolved in this figure, where they appear as turquoise thick vertical lines. (**B**) The capacitance C'(10 kHz) data plotted as functions of the logarithm of the time t that has passed after each jump. (**C**) Magnification of the jumps of magnitude 100 mK or less.

Fig. 2. The real part of the capacitance from small-amplitude temperature modulation experiments on VEC along with predictions demonstrating that the response is linear. (**A**) Normalized relaxation function (Eq. 3) of single temperature jumps of amplitude 10 to 100 mK around the reference temperature $T_0 = 164.6$ K. All data collapse as predicted for linear relaxation. (**B**) Data from a small-amplitude temperature double jump starting at $T_0 = 164.6$ K and jumping first by −100 mK and then by +50 mK (colored curves) along with the prediction according to Eq. 4 (black dashed lines). The top panel shows the full experiment on a linear time scale; the bottom panel shows the data on a logarithmic time scale that sets the time of the beginning of each temperature jump to zero. The inset illustrates the temperature protocol. (**C**) Sinusoidal small-amplitude temperature protocol (red points) and data (turquoise points behind the black points). The prediction based on the linear response formalism (Eq. 5) is shown as black points. The deviations between prediction and data that can barely be discerned in the main figure can be seen in the magnified panels.

(36, 43, 44). For samples of molecules with a low dipole moment, the real part of the capacitance provides a direct measure of the density (38). The VEC and NMEC molecules have large dipole moments, which implies that rotational polarizations contribute substantially to the capacitance even at high frequencies (38, 45). Although this means that the simple connection to density is lost, the capacitance still provides a precise probe of the state of the sample during aging.

The reference temperature for the VEC experiment is 164.6 K at which the main (alpha) relaxation time is roughly 12 hours (see the Supplementary Materials). This is large enough for the setup to thermalize after a temperature jump before any notable relaxation has taken place in the sample. Figure 1A shows our temperature protocol with the 10 kHz real part of the capacitance measured as a function of time. The first 36 weeks of the experiment were devoted to single temperature jumps with size varying from 10 mK to 3 K, carefully equilibrating the sample after each jump before the next one was initiated. The last 15 weeks were spent on temperature variations involving double jumps and sinusoidal modulations. The latter are not resolved in this figure, where they appear as thick turquoise vertical lines; we return to these protocols later (Figs. 2

and 3). Figure 1B shows the data for the single jumps plotted as a function of the logarithm of the time that has passed after each jump was initiated. Note that these curves have very different shapes, demonstrating that even fairly small temperature jumps lead to a notable nonlinear response. This is a hallmark of physical aging, reflecting the "asymmetry of approach" that jumping to the same final temperature from a higher temperature results in a faster and more stretched response than the same size jump coming from below (4, 6, 13, 46). Figure 1C focuses on the smaller jumps that are not resolved in Fig. 1B.

The response to a temperature variation is usually highly nonlinear. Nevertheless, any response is expected to have a small-amplitude limit at which the measured quantity, $X(t)$, depends linearly on the external perturbation. Even in this limit, the measured signal, in general, depends on the temperature history. This means that $X(t)$ in the linear limit is given by a convolution of the change in temperature with the normalized linear time-domain response function $R_{lin}(t)$ in the following manner
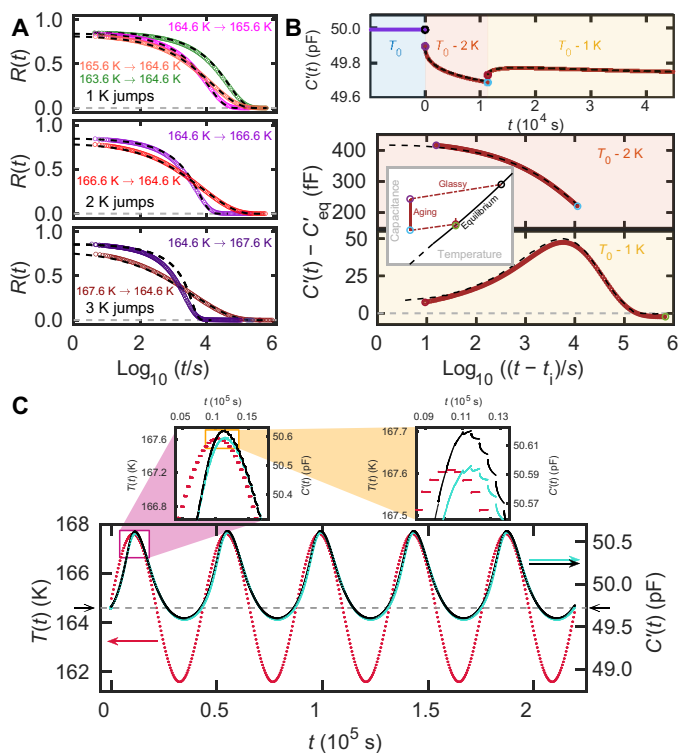
Fig. 3. The real part of the capacitance from large-amplitude temperature modulation experiments on VEC along with predictions based on the measured linear response $R_{lin}(t)$. The prediction is calculated using Eq. 6 in combination with Eqs. 7 and 8. Colored curves are the data, and black dashed lines are predictions. (**A**) Normalized relaxation functions (Eq. 3) of single temperature jumps with amplitudes ranging from 1 to 3 K. (**B**) Data from a double jump starting at $T_0 = 167.6$ K and jumping by $−2$ K and $+1$ K (colored curves). The top panel shows the full experiment on a linear time scale; the bottom panel shows the data on a logarithmic time scale, setting the time of the beginning of each temperature jump to zero. The inset illustrates the temperature protocol. (**C**) Sinusoidal temperature protocol (red points) and data (turquoise points) shown together. The horizontal dashed line marks the equilibrium capacitance at the starting temperature 164.6 K. The prediction of the material-time formalism is shown as black points. The response is highly nonlinear, resulting in a nonsinusoidal curve that is far from symmetric around the horizontal dashed line. The deviations between prediction and data that can barely be discerned in the main panel are visible in the magnified panels.

$$X(t) - X_{eq}(T) = -\alpha_X \int_{-\infty}^{t} R_{lin}(t - t') \frac{dT}{dt'} dt' \quad (1)$$

Here, the temperature T is, in general, a function of the time t, $X_{eq}(T)$ is the equilibrium value of the measured property at temperature T, and $\alpha_X = dX_{eq}/dT$ quantifies its temperature dependence. This linear description is also known as the Boltzmann superposition principle. In the case of a temperature jump at time zero from the initial temperature T_i to the "bath" temperature T_b, one has $dT/dt' = -\Delta T\delta(t')$ in which (following the convention in the field) $\Delta T = T_i - T_b$ and $\delta(t')$ is the Dirac delta function. Equation 1 implies that the time-dependent response is $\alpha_X \Delta T R_{lin}(t)$. Defining $\Delta X = X_{eq}(T_i) - X_{eq}(T_b)$ and noting that $\Delta X = \alpha_X \Delta T$, the response is given by

$$X(t) - X_{eq}(T_b) = \Delta X R_{lin}(t) \quad (2)$$

We have previously worked with this linear limit for temperature jumps down to 100 mK (*38–40, 47*); the data of the present paper take this a step further by involving temperature jumps as small as 10 mK, as well as by optimizing the protocol to make it possible to properly resolve both the long- and the short-time plateaus of the linear aging curve.

Linearity is investigated, in general, by considering the normalized relaxation function of the quantity X, denoted by $R(t)$, which for a jump to temperature T_b at $t = 0$ is defined by

$$R(t) = \frac{X(t) - X_{eq}(T_b)}{\Delta X} \quad (3)$$

We note that $R(0) = 1$ and that $R(t)$ goes to zero as the system equilibrates at T_b at long times. Whenever the data are in the linear regime, the relaxation function is the response function of Eq. 1, $R(t) = R_{lin}(t)$, i.e., relaxations following all temperature jumps have the same time-dependent normalized relaxation function in the linear limit.

Figure 2 shows $R(t)$ for temperature jumps of magnitude 10 to 100 mK to and from the reference temperature, where $X = C'(10$ kHz$)$ is the real part of the capacitance at 10 kHz of VEC. Similar data are shown for the imaginary part and for NMEC in the Supplementary Materials. The short-time plateau of $R(t)$ is below the theoretical value $R(0) = 1$. This is because there is a fast response that cannot be resolved by our setup, a common finding in studies of physical aging that was discussed in detail in previous works (*39, 47*). We believe that the fast response mainly happens on the phonon time scale due to vibrational and librational equilibration. In addition, one or more beta relaxations may take place at times shorter than the experimental cutoff of about 4 s (the time it takes to change temperature and equilibrate the setup at the new temperature). However, in the dielectric spectra (Fig. S1), the beta relaxation is only seen as a small shoulder, which indicates that it probably only accounts for a few percent of the initial decay in $R(t)$.

All the normalized relaxation functions observed for these small temperature jumps around the reference temperature collapse within the experimental uncertainty, as predicted for a linear response. True linearity is a theoretical limit, which means that higher precision and better resolution would reveal tiny differences between the relaxation curves. For the data of Fig. 2, the uncertainty is of the same order of magnitude as the symbol size and no differences are resolved, meaning that the measured curves for all practical purposes represent the linear response function $R_{lin}(t)$. In the following, we demonstrate how the linear response function can be used to predict the response for different temperature protocols resulting in linear (Fig. 2) and nonlinear (Fig. 3) aging responses.

A simple generalization of the temperature jump experiment is to introduce a second jump before the system has equilibrated fully in response to the first one, a so-called double-jump experiment. If the temperature changes are both small enough to be within the linear range, then the measured value of $X(t)$ after the second jump is a sum of the responses to the individual jumps. For two temperature jumps corresponding to changes in the measured property X by ΔX_1 and ΔX_2 performed at times t_1 and t_2 ($t_1 < t_2$), respectively, one has

$$X(t) = \Delta X_1 R_{lin}(t - t_1) + \Delta X_2 R_{lin}(t - t_2) + X_{eq}(T_2) \text{ for } t > t_2 \quad (4)$$

where T_2 is final temperature after the second jump.

We test Eq. 4 for the Ritland-Kovacs crossover protocol (*4, 46, 48, 49*) consisting of two consecutive temperature jumps with an opposite sign determined such that the observable X has its equilibrium value right after the second jump. Figure 2B illustrates this protocol and shows the observations after a −100 mK jump followed by a +50 mK jump for VEC. The data reproduce the crossover effect that $X(t)$ exhibits a peak after the second jump (*4, 46*). This bump is a manifestation of the memory present for any nonexponential linear response (*4*). Along with the data, the predictions based on Eq. 4 and the measured $R_{\mathrm{lin}}(t)$ from the 50 mK jump in Fig. 2A are also shown. The prediction collapses almost exactly with the double-jump data. These small-amplitude double jump results provide an extra confirmation that we have reached the linear limit of physical aging. Similar data are presented for NMEC in the Supplementary Materials, which also provides data for more VEC small (linear) jumps.

Moving on from the double temperature jump, we note that Eq. 1 predicts the response to any temperature perturbation small enough to be linear. Because we do not have an analytic expression for $R_{\mathrm{lin}}(t)$, the integral is calculated by generalizing the sum in Eq. 4

$$X(t) = \sum_{i=1}^{N} \Delta X_i R_{\mathrm{lin}}(t - t_i) + X_{\mathrm{eq}}(T_N) \text{ for } t > t_N \quad (5)$$

where T_N is the final temperature after N jumps. In Fig. 2C, we show how Eq. 5 predicts the output of a small sinusoidal temperature perturbation. The frequency of the perturbation is 2.3×10^{-5} Hz, which is the inverse of the estimated equilibrium relaxation time of the sample at the reference temperature 164.6 K. The amplitude is 100 mK, i.e., within the linear regime of single jumps. The prediction follows the data with a high accuracy, including both the transient behavior (seen, e.g., in a first peak that is higher than the second) and the phase shift. Tiny deviations between prediction and data can be seen in the inset, which also shows how the temperature protocol is composed of 2-mK temperature steps.

After establishing the linear aging limit and showing how linear temperature jump data can be used to predict the response of other linear temperature protocols, we now turn to the main result of this paper, a proof of the existence of a material time for VEC. The radically new idea in the 1970s (*3, 6*) was that aging becomes linear when it is described in terms of the material time $\xi(t)$ instead of the laboratory time t. One assumes the so-called time aging-time superposition, meaning that the spectral shape of R_{lin} is independent of the state of the sample. As a consequence of these assumptions, Eqs. 1, 4, and 5 describe also nonlinear experiments by replacing the laboratory time with the material time, i.e.,

$$X(\xi) = \sum_{i=1}^{N} \Delta X_i R_{\mathrm{lin}}(\xi - \xi_i) + X_{\mathrm{eq}}(T_N) \text{ for } \xi > \xi_N \quad (6)$$

The material time is "measured" by a clock with a rate that reflects the state of the sample, and the nonlinearity of physical aging is a consequence of this fact (*3, 6, 29, 50*). The material time may be thought of as analogous to the proper time in the theory of relativity, which is the time recorded on a clock following the observer. Although a microscopic definition of the material time remains elusive, this concept is generally recognized to form the basis of a good description of physical aging involving relatively small temperature variations (*4*). The very fundamental assumption of the formalism,

however, that nonlinear aging phenomena can be predicted from the linear aging limit has never been validated. In the following, we do so by showing how the measured linear response determines the response to nonlinear temperature protocols for VEC and, in the Supplementary Materials, for NMEC.

Using Eq. 6 requires a connection between the laboratory time t and the material time ξ. This is obtained by introducing the time-dependent aging rate $\gamma(t)$ defined (*3, 6, 8, 11, 51*) by

$$\gamma(t) = d\xi(t)/dt \quad (7)$$

In equilibrium, the aging rate equals the relaxation rate γ_{eq} defined as the inverse of the equilibrium relaxation time. Thus, a linear experiment is the limiting case for which the aging rate is constant and the material time is proportional to the laboratory time, $\xi_{\mathrm{lin}}(t) = \gamma_{\mathrm{eq}} t$.

Different strategies have been used to estimate $\gamma(t)$ during aging, often via the so-called fictive temperature (*4, 33, 35, 48*). We here adopt the single-parameter aging ansatz (*4, 6, 52, 53, 69*) according to which the aging rate is controlled by the measured quantity $X(t)$ itself. In the simplest realization, single-parameter aging is characterized by (*53*)

$$\log(\gamma(t)) - \log(\gamma_{\mathrm{eq}}(T)) = \Lambda(X(t) - X_{\mathrm{eq}}(T)) \quad (8)$$

Here, $\gamma_{\mathrm{eq}}(T)$ and $X_{\mathrm{eq}}(T)$ are the equilibrium values of γ and X at the temperature T, and Λ is a constant that depends only on the substance and the monitored property X. It should be noted that Eq. 8 is arrived at by first-order Taylor expansions and, for this reason, can only be expected to apply for relatively small temperature variations.

The material-time description in Eq. 6, combined with Eqs. 7 and 8, gives a unique prediction for $X(t)$ for any temperature protocol. Equation 6 predicts the value of $X(\xi)$, while Eqs. 7 and 8 connect the material and laboratory times by stretching or compressing the time scale axis. The input needed for the prediction is $R_{\mathrm{lin}}(t)$ as determined in Fig. 2A, the equilibrium values of the rate $\gamma_{\mathrm{eq}}(T)$ and of the measured property $X_{\mathrm{eq}}(T)$, and the parameter Λ. We have equilibrium measurements of $X_{\mathrm{eq}}(T)$ down to 163.6 K and have extrapolated values to lower temperatures (see the Supplementary Materials). The values used for $\gamma_{\mathrm{eq}}(T)$ are extrapolations from a fit of relaxation times derived from dielectric spectra, which, down to 163.6 K, are proportional to the aging rates (see the Supplementary Materials).

The parameter Λ is determined by the method described in (*53*) from the two temperature jump experiments of magnitude ±1 K to the reference temperature 164.6 K (see the Supplementary Materials). This Λ value was used for predicting all other nonlinear responses. Figure 3A shows $R(t)$ data from the nonlinear single-temperature jumps. It is seen that the short-time plateaus of $R(t)$ for the different jumps do not coincide. This is due to a difference in the short-time relaxation deriving from the response on the phonon time scale and, possibly, also from one or more beta relaxations. To predict the aging, we have adjusted for this difference in a manner where the short-time decay of $R(t)$ depends on both the initial and final temperatures (see the Supplementary Materials).

Figure 3 reports the main results of the paper: data from nonlinear temperature protocols along with predictions based on the linear temperature jump data. The nonlinear protocols mirror the linear protocols

of Fig. 2. Figure 3A shows single temperature jumps, Fig. 3B shows a −2 K and +1 K double jump, and Fig. 3C shows a sinusoidal temperature modulation with amplitude 3 K and the same frequency as the linear sinusoidal protocol of Fig. 2.

The single jumps in Fig. 3A exhibit the asymmetry of approach characteristic of nonlinear aging (13, 46): "self-acceleration" of up jumps where the relaxation rate speeds up as equilibrium is approached and "self-retardation" of down jumps (11). The material-time formalism captures well this asymmetry (black dashed lines), and the measured data are predicted with a high accuracy for all down jumps and for up jumps up to 2 K. However, there is a clearly visible deviation for the largest (3 K) up jump, and in the Supplementary Materials it is documented that deviations in fact emerge already for a 2.5 K up jump. Thus, the formalism breaks down for large-amplitude up jumps. This may be related to only going to first order in the Taylor expansion in Eq. 8, but it could also be caused by the sample reaching equilibrium by other mechanisms than the one involved in smaller jumps. This may be similar to what is seen in the case of very large up jumps (30 to 70 K) performed on ultrastable vapor-deposited glasses where it has been shown that equilibrium is reached by heterogeneous growth of mobile domains (54). Alternatively, the deviations between data and predictions could be caused by beta processes playing a role in aging, as has been seen for polymers deep in the glass state (55, 56).

The predictions agree well with the data of the nonlinear double jumps shown in Fig. 3B. This demonstrates that the material-time formalism works well also in this situation; we note that (41) presents an alternative approach for predicting the nonlinear aging response from linear data. The data shown in Fig. 3B are all from measurements in the temperature range where we have access to measured values of X_{eq} and to the fast contribution of $R(t)$, while γ_{eq} used for the prediction is derived from an extrapolation of higher-temperature dielectric relaxation times. The parameter Λ is the same as for the single jumps, and the test of the nonlinear double-jump prediction is therefore performed with no free parameters. In contrast, in the classical Ritland-Kovacs crossover experiment (46, 48, 49), the first down jump goes deep into the glass state where the properties of the equilibrium liquid are not known. In the Supplementary Materials, we show data for a large down jump (7 K); the predictions using extrapolated parameters demonstrate qualitatively good results, although the formalism is not able to predict the time scale of aging in the temperature regime where equilibrium cannot be reached.

Last, Fig. 3C shows the response of the nonlinear sinusoidal temperature modulation along with the predictions. The lowest temperatures in the modulation are in a range where the parameters are extrapolated. Again, there are no free parameters in the prediction. The nonlinearity is seen as a sizable asymmetry in the peak shape: When the temperature is high, there is a substantial response, whereas the liquid responds much less to a decreased temperature. The gray horizontal dashed line corresponds to the equilibrium capacitance at the starting temperature 164.6 K. The asymmetry of the response is very well captured by the prediction. Because a large part of a sinusoidal is close to linear in time, and thus similar to a temperature ramp over several Kelvin, the aging in connection with a standard differential scanning calorimetry cooling or heating protocol is likewise expected to be predicted accurately. Deviations between prediction and data can be seen in the magnified panel of Fig. 3C and are most likely related to the first-order nature of Eq. 8.

The results in Fig. 3 demonstrate that nonlinear physical aging phenomena in the intermediate regime may be predicted from a knowledge of the linear limit of aging. Previous works have come close to this limit (39, 57). While the linear limit is challenging to probe experimentally, it is conceptually important. First, it validates the central assumption of the material-time formalism. Second, linear response theory is well established via the fluctuation-dissipation (FD) theorem that predicts the response from thermal equilibrium fluctuations quantified via a time correlation function (58). Our results therefore imply that intermediate nonlinear physical aging can now, at least in principle and for relatively small jumps, be predicted from measurements of the equilibrium fluctuations, i.e., without perturbing the system at all. We end the paper by illustrating this possibility by presenting results from a computer simulation where thermal fluctuations are much easier to monitor than in experiments.

The system studied is the binary Lennard-Jones (LJ) mixture of Kob and Andersen (59), which, for more than 20 years, has been the standard model for computer simulations of glass-forming liquids. We simulated a system of 8000 particles. The quantity monitored is the potential energy U. Temperature jump data were averaged over 1000 simulations to reduce the noise. Figure 4A shows results for jumps from four different temperatures to $T = 0.60$ (in simulation units), plotted as a function of the logarithm of the time passed after each jump was initiated. The curves are quite different, showing that the jumps are large enough to be notably nonlinear.

The FD theorem implies that the linear response to any small temperature variation is uniquely determined by the thermal equilibrium potential energy time autocorrelation function $\langle U(0)U(t)\rangle$ (60). We evaluated this quantity at $T = 0.60$. Using the single-parameter material-time formalism as above, we then predict nonlinear temperature jump results (Fig. 4B). The only free parameter is the Λ of Eq. 8, which is determined from the two smallest jumps (53). The colored dashed curves in Fig. 4B are the predictions for the normalized relaxation functions based on the black line in the middle that gives the thermal equilibrium normalized time autocorrelation function of the potential energy; the full circles are the normalized data from Fig. 4A. Overall, the predictions work well, demonstrating that intermediate nonlinear aging can be predicted from equilibrium fluctuations. The minor deviations for the two largest jumps are not unexpected, given that these involve temperature changes of more
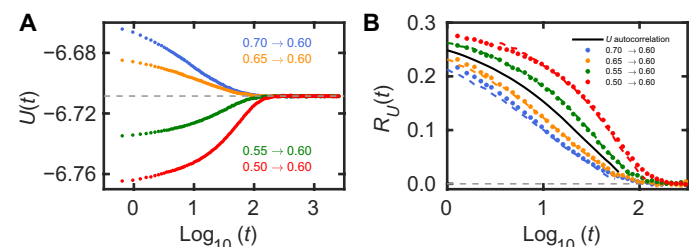
Fig. 4. Results from computer simulations of a binary model liquid monitoring the potential energy. (**A**) Data for four temperature jumps to the same temperature ($T = 0.60$ in units based on the pair potential parameters). (**B**) The normalized relaxation function, $R_U(t)$, of the thermal equilibrium potential energy time autocorrelation function at this temperature (black line) and the predictions based on this for the temperature jumps (colored dashed curves). The data for the normalized relaxation functions based on (A) are shown as colored dots. The nonlinearity parameter was determined from the two smallest jumps in the same way as for the experimental data (see the Supplementary Materials).

than 15% for which the single-parameter ansatz in Eq. 8 is likely not to be accurate.

DISCUSSION

We have shown how physical aging involving temperature changes of a few percent can be predicted from the linear aging response, i.e., from the response to a very small temperature variation. This validates the central assumption of the material-time formalism. At the same time, it is clear that this formalism has limitations. Thus, the largest up jump (3 K) is not well predicted (Fig. 3A, bottom). This suggests that there are two regimes of nonlinear aging: an intermediate regime where the relaxation time varies for, at most, a few decades and the material-time concept describes the situation well, and a strongly nonlinear regime where the formalism breaks down and a new theoretical approach is needed. We speculate that even very large temperature down jumps may fall into the intermediate regime because the system here thermalizes gradually. This is in contrast to large up jumps, which are known to result in heterogeneous states very far from equilibrium (54). Aging far below the glass transition is also likely to deviate from the predictions because processes faster than the alpha relaxation may play a role here, particularly for polymers (55, 56). Along this line of thinking, it is important to note that the standard glass transition resulting from a continuous cooling is likely to be described well by the material-time formalism, i.e., is intermediately nonlinear because vitrification for a constant cooling rate takes place over a narrow range of temperatures.

In regard to the intermediate aging regime, the implications of our findings are important both for the understanding of aging in application and for the theoretical interpretation of the aging dynamics. By reference to the FD theorem, the consequence is that the properties governing the intermediate nonlinear physical aging of a system far from equilibrium are embedded in the thermal equilibrium fluctuations and can be predicted from these. This means that there is no fundamental difference between the intermediate nonlinear and the linear aging responses. Understanding physical aging is therefore intimately linked to characterizing and understanding the spectral shapes of linear responses and autocorrelation functions, a classical field where there has been important recent progress both experimentally (61, 62) and theoretically (63). The approach presented in this paper could prove useful for understanding the nonlinear response to electric fields. This is an active field (64–66) in which concepts from physical aging have been used successfully (65).

For future work, it would also be interesting to see how far the description of physical aging in terms of linear response can be extended by including higher-order terms in the Taylor expansion of Eq. 8. This can hopefully lead to a complete picture of which samples and protocols exhibit aging governed by the same processes as those responsible of the linear alpha relaxation and which situations involve other processes and mechanisms (54–56).

MATERIALS AND METHODS

The study involves the glass-forming liquids VEC (99% purity) from Sigma-Aldrich for which data are shown in the main paper and NMEC (96% purity) from VWR for which data are shown in the Supplementary Materials. Both liquids were stored in a refrigerator at temperatures between 2° and 8°C and used as received.

For each liquid, a single sample was prepared for all the presented experiments. The sample cell was a plane-plate capacitor with a plate distance of 50 μm and a geometric capacitance of $C_{geo} = 16$ pF. The cell was filled under ambient conditions and immediately mounted into a precooled cryostat. VEC was quenched to $T_{cryo} = 163$ K, and NMEC was quenched to $T_{cryo} = 167$ K, at which the samples were kept to equilibrate for a couple of days. The temperature of the main cryostat was constant at $T_{cryo} = 164$ K for VEC and $T_{cryo} = 167$ K for NMEC during the experiments that lasted almost 1 year for each sample.

The temperature control of the experiments was obtained by a microregulator integrated with the capacitor sample cell. The regulation was achieved by controlling a Peltier element in contact with a capacitor plate. Temperature was monitored with a negative temperature coefficient resistor placed inside one of the capacitor plates. A figure showing the sample cell with a microregulator can be found in the Supplementary Materials. Further details on the microregulator and the main cryostat are given in (37). The microregulator can change temperature by steps of a few millikelvin up to several kelvin within seconds and keep the temperature constant with variations of less than 1 mK over weeks. All the temperature protocols shown, including the sinusoidal protocol, were achieved by making jumps in temperature with the microregulator.

The real and the imaginary part of the capacitance at 10 kHz was monitored during the entire experiment with a sampling rate of approximately one measurement per second. The measurements were performed using an AH2700A Andeen Hagerling ultraprecision capacitance bridge. It is the combination of the fast and precise temperature control with the high precision of the bridge that makes it possible to measure aging in the linear limit.

The simulations used the Kob-Andersen 80/20 binary LJ mixture (59), which was simulated by means of standard NVT Nosé-Hoover dynamics (67) using the GPU-optimized software RUMD (68). A system of 8000 particles was simulated. In LJ units, the time step was 0.0025. All pair potentials were cut and shifted at 2.5 times the length parameter σ_{ij} of the relevant LJ pair potential ($i, j = A, B$). At the reference temperature $T = 0.60$, the potential energy time autocorrelation function was calculated as follows: First, 10^7 time steps of simulations were carried out for equilibration. After that, the time autocorrelation function was calculated using the fast Fourier transform. The temperature jump simulations were carried out by the following procedure applied for all starting temperatures. First, 5×10^5 time steps were spent on equilibration at the given starting temperature. After that, a total of 5×10^8 time steps were spent on the production runs from which 1000 independent configurations were selected to serve as starting configurations for a temperature jump to $T = 0.60$. The Fig. 4 data represent averages over these 1000 jumps.

SUPPLEMENTARY MATERIALS

Supplementary material for this article is available at https://science.org/doi/10.1126/sciadv.abl9809

REFERENCES AND NOTES

1. O. Mazurin, Relaxation phenomena in glass. *J. Non Cryst. Solids* **25**, 129–169 (1977).
2. L. C. E. Struik, *Physical Aging in Amorphous Polymers and Other Materials* (Elsevier, 1978).
3. A. J. Kovacs, J. J. Aklonis, J. M. Hutchinson, A. R. Ramos, Isobaric volume and enthalpy recovery of glasses. II. A transparent multiparameter theory. *J. Polym. Sci. B Polym. Phys.* **17**, 1097–1162 (1979).
4. G. W. Scherer, *Relaxation in Glass and Composites* (Wiley, 1986).

5. I. M. Hodge, Physical aging in polymer glasses. *Science* **267**, 1945–1947 (1995).

6. O. S. Narayanaswamy, A model of structural relaxation in glass. *J. Am. Ceram. Soc.* **54**, 491–498 (1971).

7. J. C. Mauro, A. Tandia, K. D. Vargheese, Y. Z. Mauro, M. M. Smedskjaer, Accelerating the design of functional glasses through modeling. *Chem. Mater.* **28**, 4267–4277 (2016).

8. M. Micoulaut, Relaxation and physical aging in network glasses: A review. *Rep. Prog. Phys.* **79**, 066504 (2016).

9. K. Chen, K. S. Schweizer, Molecular theory of physical aging in polymer glasses. *Phys. Rev. Lett.* **98**, 167802 (2007).

10. L. Grassia, S. L. Simon, Modeling volume relaxation of amorphous polymers: Modification of the equation for the relaxation time in the KAHR model. *Polymer* **53**, 3613–3620 (2012).

11. D. Cangialosi, V. M. Boucher, A. Alegria, J. Colmenero, Physical aging in polymers and polymer nanocomposites: Recent results and open questions. *Soft Matter* **9**, 8619–8630 (2013).

12. C. B. Roth, Ed., *Polymer Glasses* (CRC Press, 2017).

13. G. B. McKenna, S. L. Simon, 50th anniversary perspective: Challenges in the dynamics and kinetics of glass-forming polymers. *Macromolecules* **50**, 6333–6361 (2017).

14. S. V. Ketov, Y. H. Sun, S. Nachum, Z. Lu, A. Checchi, A. R. Beraldin, H. Y. Bai, W. H. Wang, D. V. Louzguine-Luzgin, M. A. Carpenter, A. L. Greer, Rejuvenation of metallic glasses by non-affine thermal strain. *Nature* **524**, 200–203 (2015).

15. B. Ruta, E. Pineda, Z. Evenson, Relaxation processes and physical aging in metallic glasses. *J. Phys. Condens. Mat.* **29**, 503002 (2017).

16. S. Küchemann, C. Liu, E. M. Dufresne, J. Shin, R. Maaß, Shear banding leads to accelerated aging dynamics in a metallic glass. *Phys. Rev. B* **97**, 014204 (2018).

17. M. Lüttich, V. M. Giordano, S. Le Floch, E. Pineda, F. Zontone, Y. Luo, K. Samwer, B. Ruta, Anti-aging in ultrastable metallic glasses. *Phys. Rev. Lett.* **120**, 135504 (2018).

18. J. Ketkaew, R. Yamada, H. Wang, D. Kuldinow, B. S. Schroers, W. Dmowski, T. Egami, J. Schroers, The effect of thermal cycling on the fracture toughness of metallic glasses. *Acta Mater.* **184**, 100–108 (2020).

19. S. Vyazovkin, I. Dranca, Effect of physical aging on nucleation of amorphous indomethacin. *J. Phys. Chem. B* **111**, 7283–7287 (2007).

20. F. Bonacci, X. Chateau, E. M. Furst, J. Fusier, J. Goyon, A. Lemaitre, Contact and macroscopic ageing in colloidal suspensions. *Nat. Mater.* **19**, 775–780 (2020).

21. J. C. Mauro, *Materials Kinetics: Transport and Rate Phenomena* (Elsevier, 2021).

22. E. Andersen, R. Mikkelsen, S. Kristiansen, M. Hinge, Accelerated physical ageing of poly(1,4-cyclohexylenedimethylene-co-2,2,4,4-tetramethyl-1,3-cyclobutanediol terephthalate). *RSC Adv.* **9**, 14209–14219 (2019).

23. J. Fonseca, T. Gong, L. Jiao, H.-L. Jiang, Metal-organic frameworks (MOFs) beyond crystallinity: Amorphous MOFs, MOF liquids and MOF glasses. *J. Mater. Chem. A* **9**, 10562–10611 (2021).

24. S. Zhao, Z. Li, C. Zhu, W. Yang, Z. Zhang, D. E. J. Armstrong, P. S. Grant, R. O. Ritchie, M. A. Meyers, Amorphization in extreme deformation of the CrMnFeCoNi high-entropy alloy. *Sci. Adv.* **7**, eabb3108 (2021).

25. S. M. Fielding, P. Sollich, M. E. Cates, Aging and rheology in soft materials. *J. Rheol.* **44**, 323–369 (2000).

26. R. Mandal, P. Sollich, Multiple types of aging in active glasses. *Phys. Rev. Lett.* **125**, 218001 (2020).

27. G. Janzen, L. Janssen, Aging in thermal active glasses. arXiv:2105.05705 [cond-mat. stat-mech] (12 May 2021).

28. R. D. Priestley, Physical aging of confined glasses. *Soft Matter* **5**, 919–926 (2009).

29. L. F. Cugliandolo, J. Kurchan, On the out-of-equilibrium relaxation of the Sherrington-Kirkpatrick model. *J. Phys. A: Math. Gen.* **27**, 5749–5772 (1994).

30. A. P. Holt, D. Fragiadakis, C. M. Roland, Pressure densified 1,3,5-tri(1-naphthyl)benzene glass. I. Volume recovery and physical aging. *J. Chem. Phys.* **151**, 184502 (2019).

31. F. Arceri, F. P. Landes, L. Berthier, G. Biroli, Glasses and aging: A statistical mechanics perspective. arXiv:2006.09725 [cond-mat.stat-mech] (17 June 2020).

32. M. Lulli, C.-S. Lee, H.-Y. Deng, C.-T. Yip, C.-H. Lam, Spatial heterogeneities in structural temperature cause Kovacs' expansion gap paradox in aging of glasses. *Phys. Rev. Lett.* **124**, 095501 (2020).

33. A. Q. Tool, Relation between inelastic deformability and thermal expansion of glass in its annealing range. *J. Am. Ceram. Soc.* **29**, 240–253 (1946).

34. J. C. Dyre, Narayanaswamy's 1971 aging theory and material time. *J. Chem. Phys.* **143**, 114507 (2015).

35. G. B. McKenna, Looking at the glass transition: Challenges of extreme time scales and other interesting problems. *Rubber Chem. Technol.* **93**, 79–120 (2020).

36. T. Hecksher, N. B. Olsen, K. Niss, J. C. Dyre, Physical aging of molecular glasses studied by a device allowing for rapid thermal equilibration. *J. Chem. Phys.* **133**, 174514 (2010).

37. B. Igarashi, T. Christensen, E. H. Larsen, N. B. Olsen, I. H. Pedersen, T. Rasmussen, J. C. Dyre, A cryostat and temperature control system optimized for measuring relaxations of glass-forming liquids. *Rev. Sci. Instrum.* **79**, 045105 (2008a).

38. K. Niss, D. Gundermann, T. Christensen, J. C. Dyre, Dynamic thermal expansivity of liquids near the glass transition. *Phys. Rev. E* **85**, 041501 (2012).

39. K. Niss, Mapping isobaric aging onto the equilibrium phase diagram. *Phys. Rev. Lett.* **119**, 115703 (2017).

40. K. Niss, J. C. Dyre, T. Hecksher, Long-time structural relaxation of glass-forming liquids: Simple or stretched exponential? *J. Chem. Phys.* **152**, 041103 (2020).

41. P. Lunkenheimer, R. Wehn, U. Schneider, A. Loidl, Glassy aging dynamics. *Phys. Rev. Lett.* **95**, 055702 (2005).

42. R. Richert, Supercooled liquids and glasses by dielectric relaxation spectroscopy. *Adv. Chem. Phys.* **156**, 101–195 (2015).

43. P. Lunkenheimer, S. Kastner, M. Köhler, A. Loidl, Temperature development of glassy α-relaxation dynamics determined by broadband dielectric spectroscopy. *Phys. Rev. E* **81**, 051504 (2010).

44. M. Paluch, Z. Wojnarowska, S. Hensel-Bielowka, Heterogeneous dynamics of prototypical ionic glass CKN monitored by physical aging. *Phys. Rev. Lett.* **110**, 015702 (2013).

45. B. Jakobsen, K. Niss, N. B. Olsen, Dielectric and shear mechanical alpha and beta relaxations in seven glass-forming liquids. *J. Chem. Phys.* **123**, 234511 (2005).

46. A. J. Kovacs, Transition vitreuse dans les polymères amorphes. Etude phénoménologique, in *Fortschritte Der Hochpolymeren-Forschung* (Springer, 1964), vol. 3/3, pp. 394–507.

47. T. Hecksher, N. B. Olsen, J. C. Dyre, Fast contribution to the activation energy of a glass-forming liquid. *Proc. Natl. Acad. Sci. U.S.A.* **116**, 16736–16741 (2019).

48. H. N. Ritland, Limitations of the fictive temperature concept. *J. Am. Ceram. Soc.* **39**, 403–406 (1956).

49. L. Song, W. Xu, J. Huo, F. Li, L.-M. Wang, M. D. Ediger, J.-Q. Wang, Activation entropy as a key factor controlling the memory effect in glasses. *Phys. Rev. Lett.* **125**, 135501 (2020).

50. C. Chamon, M. P. Kennett, H. E. Castillo, L. F. Cugliandolo, Separation of time scales and reparametrization invariance for aging systems. *Phys. Rev. Lett.* **89**, 217201 (2002).

51. R. Svoboda, J. Malek, Description of enthalpy relaxation dynamics in terms of TNM model. *J. Non Cryst. Solids* **378**, 186–195 (2013).

52. L. Grassia, D. D'Amore, Constitutive law describing the phenomenology of subyield mechanically stimulated glasses. *Phys. Rev. E* **74**, 021504 (2006).

53. T. Hecksher, N. B. Olsen, J. C. Dyre, Communication: Direct tests of single-parameter aging. *J. Chem. Phys.* **142**, 241103 (2015).

54. A. Sepúlveda, M. Tylinski, A. Guiseppi-Elie, R. Richert, M. D. Ediger, Role of fragility in the formation of highly stable organic glasses. *Phys. Rev. Lett.* **113**, 045901 (2014).

55. D. Cangialosi, V. M. Boucher, A. Alegría, J. Colmenero, Direct evidence of two equilibration mechanisms in glassy polymers. *Phys. Rev. Lett.* **111**, 095701 (2013).

56. X. Monnier, S. Marina, X. Lopez de Pariza, H. Sardon, J. Martin, D. Cangialosi, Physical aging behavior of a glassy polyether. *Polymers* **13**, 954 (2021).

57. S. M. Rekhson, O. V. Mazurin, Stress and structural relaxations in Na_2O-CaO-SiO_2 glass. *J. Am. Ceram. Soc.* **57**, 327–328 (1974).

58. L. E. Reichl, *A Modern Course in Statistical Physics* (Wiley-VCH, ed. 4, 2016).

59. W. Kob, H. C. Andersen, Testing mode-coupling theory for a supercooled binary Lennard-Jones mixture I: The van Hove correlation function. *Phys. Rev. E* **51**, 4626–4641 (1995).

60. J. K. Nielsen, J. C. Dyre, Fluctuation-dissipation theorem for frequency-dependent specific heat. *Phys. Rev. B* **54**, 15754–15761 (1996).

61. T. Körber, R. Stäglich, C. Gainaru, R. Böhmer, E. A. Rössler, Systematic differences in the relaxation stretching of polar molecular liquids probed by dielectric vs magnetic resonance and photon correlation spectroscopy. *J. Chem. Phys.* **153**, 124510 (2020).

62. F. Pabst, J. P. Gabriel, T. Böhmer, P. Weigl, A. Helbling, P. Richter, T. Zourchang, T. Walther, T. Blochowicz, Generic structural relaxation in supercooled liquids. *J. Phys. Chem. Lett.* **12**, 3685–3690 (2021).

63. B. Guiselin, C. Scalliet, L. Berthier, Microscopic origin of excess wings in relaxation spectra of deeply supercooled liquids. arXiv:2103.01569 [cond-mat.soft] (2 March 2021).

64. S. Albert, T. Bauer, M. Michl, G. Biroli, J.-P. Bouchaud, A. Loidl, P. Lunkenheimer, R. Tourbot, C. Wiertel-Gasquet, F. Ladieu, Fifth-order susceptibility unveils growth of thermodynamic amorphous order in glass-formers. *Science* **352**, 1308–1311 (2016).

65. P. Kim, A. R. Young-Gonzales, R. Richert, Dynamics of glass-forming liquids. XX. Third harmonic experiments of non-linear dielectric effects versus a phenomenological model. *J. Chem. Phys.* **145**, 064510 (2016).

66. J. P. Gabriel, E. Thoms, R. Richert, High electric fields elucidate the hydrogen-bonded structures in 1-phenyl-1-propanol. *J. Mol. Liq.* **330**, 115626 (2021).

67. S. Nosé, A unified formulation of the constant temperature molecular dynamics methods. *J. Chem. Phys.* **81**, 511–519 (1984).

68. N. P. Bailey, T. S. Ingebrigtsen, J. S. Hansen, A. A. Veldhorst, L. Bøhling, C. A. Lemarchand, A. E. Olsen, A. K. Bacher, L. Costigliola, U. R. Pedersen, H. Larsen, J. C. Dyre, T. B. Schrøder, RUMD: A general purpose molecular dynamics package optimized to utilize GPU hardware down to a few thousand particles. *SciPost Phys.* **3**, 038 (2017).

69. L. A. Roed, T. Hecksher, J. C. Dyre, K. Niss, Generalized single-parameter aging tests and their application to glycerol. *J. Chem. Phys.* **150**, 044501 (2019).

70. B. Igarashi, T. Christensen, E. H. Larsen, N. B. Olsen, I. H. Pedersen, T. Rasmussen, J. C. Dyre, An impedance-measurement setup optimized for measuring relaxations of glass-forming liquids. *Rev. Sci. Instrum.* **79**, 045106 (2008).

Lines of invariant physics in the isotropic phase of the discotic Gay-Berne model

Saeed Mehri [a], Mohamed A. Kolmangadi [b], Jeppe C. Dyre [a],[*], Trond S. Ingebrigtsen [a]

[a] *"Glass and Time", IMFUFA, Dept. of Science and Environment, Roskilde University, P. O. Box 260, DK-4000 Roskilde, Denmark*
[b] *Bundesanstalt für Materialforschung und -Prüfung, Unter den Eichen 87, 12205 Berlin, Germany*

ABSTRACT

The Gay-Berne model is studied numerically with a choice of parameters allowing for the formation of a discotic liquid crystal at low temperatures. We show that the model has strong virial potential-energy correlations in the isotropic phase at high temperatures, i.e., it obeys the criterion for the existence of isomorphs, which are curves of approximately invariant structure and dynamics. These properties are demonstrated to be approximately invariant in reduced units along the isomorph studied. The isomorph is described well by the constant density-scaling exponent 11.5, a number that is significantly larger than the density-scaling exponents of various Lennard-Jones models that are always below 6.

1. Introduction

Liquid crystals constitute an intriguing family of materials with properties in-between the standard liquid and crystalline phases [1–3]. When the molecules are rod shaped, three main phases are typically found: isotropic, nematic, and smectic. The *isotropic* phase mimics the ordinary fluid phase with no long-range positional or orientational ordering. The *nematic* phase is characterized by long-range orientational order, but only short-range translational order. This phase is liquid in the sense of being able to flow freely, described by a viscosity that is not simply a scalar quantity. Optical properties of the nematic phase are likewise anisotropic, which is the basis for the use of this phase for applications in displays, etc. The *smectic* phase involves additional ordering by forming distinct layers, i.e., a partial positional order is introduced. There are different smectic phases, the most important ones being the *smectic A phase* in which the molecules are directionally ordered perpendicular to the layers and the *smectic C phase* involving molecules that are tilted relative to the layers. Both of these phases are positionally disordered in the layers. Other phases that may be encountered – depending on the molecule in question – are the *cholesteric* phase found only for chiral molecules and the so-called *blue* phase consisting of cubic structures of defects. As for any other first-order phase transition, it is possible to supercool the isotropic phase by cooling it fast below the transition temperatures of the partially ordered phases.

When the molecules instead of being rod-like are disc shaped, the system is termed a discotic liquid crystal [4–9]. Discotic liquid crystals can display various mesophases, the most common being the discotic columnar and nematic phases. The discotic nematic phase is similar to the standard nematic phase; here the short axes of the discs are aligned in one preferred direction. In the columnar phase the discs stack on top of each other into columns that organize into hexagonal or rectangular order. This phase is of interest for optoelectronic applications.

A standard model for numerical studies of rod-like liquid crystals is the Gay-Berne (GB) model [10–15]. This model has also been studied in other contexts than those relevant for liquid-crystal formation. Thus Angell and coworkers [16] in 2013 used the GB model to elucidate the possible existence of ideal glassformers, which are systems that vitrify upon cooling before becoming metastable with respect to crystal formation. This would imply that glasses may also form in the equilibrium liquid phase, contradicting the prevailing opinion that glasses always form from liquids that are supercooled with respect to the freezing transition. While the paper by Angell et al. [16] did not *prove* that this is possible, it presented a convincing case by reporting "that in the aspect range of maximum ellipsoid packing efficiency, various GB crystalline states that cannot be obtained directly from the liquid disorder spontaneously near 0 K and transform to liquids without any detectable enthalpy of fusion." This definitely suggests that the GB model (for certain aspect ratios) may be an ideal glassformer.

This paper presents a GB-model study which, like the 2013 paper by Angell et al., does not focus on liquid-crystal properties. We study the GB model for a set of parameters that allows for the formation of a discotic liquid-crystal phase at low temperatures. The focus is on the model's high-temperature isotropic phase with a view to investigate the possible

---

existence of isomorphs. The motivation is the finding reported below that the high-temperature isotropic phase has strong virial potential-energy correlations, the condition for the existence of isomorphs, which are lines in the thermodynamic phase diagram of approximately invariant reduced-unit structure and dynamics [17–20].

2. Simulation methodology

2.1. The Gay-Berne potential

The GB potential was proposed as a simple model for rod-like molecules [10]. The potential takes the form of a Lennard-Jones interaction with characteristic length and energy scales that depend on the two molecules' orientations relative to one another. The pair potential is given by

$$v(\widehat{\mathbf{r}}_{ij}, \widehat{\mathbf{e}}_i, \widehat{\mathbf{e}}_j) = 4\varepsilon(\widehat{\mathbf{r}}_{ij}, \widehat{\mathbf{e}}_i, \widehat{\mathbf{e}}_j)\left[\left(\frac{\sigma_s}{\rho_{ij}}\right)^{12} - \left(\frac{\sigma_s}{\rho_{ij}}\right)^{6}\right], \tag{1a}$$

$$\rho_{ij} = r_{ij} - \sigma(\widehat{\mathbf{r}}_{ij}, \widehat{\mathbf{e}}_i, \widehat{\mathbf{e}}_j) + \sigma_s. \tag{1b}$$

Here r_{ij} is the distance between the centers of the molecules i and j, $\widehat{\mathbf{r}}_{ij}$ is the unit vector along $\mathbf{r}_{ij} = \mathbf{r}_i - \mathbf{r}_j$, and $\widehat{\mathbf{e}}_i$ and $\widehat{\mathbf{e}}_j$ are unit vectors along the major axes of each molecule. The GB model is characterized by

$$\sigma(\widehat{\mathbf{r}}_{ij}, \widehat{\mathbf{e}}_i, \widehat{\mathbf{e}}_j) = \sigma_s\left[1 - \frac{\chi}{2}\left(\frac{(\widehat{\mathbf{e}}_i\cdot\widehat{\mathbf{r}}_{ij} + \widehat{\mathbf{e}}_j\cdot\widehat{\mathbf{r}}_{ij})^2}{1 + \chi(\widehat{\mathbf{e}}_i\cdot\widehat{\mathbf{e}}_j)} + \frac{(\widehat{\mathbf{e}}_i\cdot\widehat{\mathbf{r}}_{ij} - \widehat{\mathbf{e}}_j\cdot\widehat{\mathbf{r}}_{ij})^2}{1 - \chi(\widehat{\mathbf{e}}_i\cdot\widehat{\mathbf{e}}_j)}\right)\right]^{-1/2}, \tag{2a}$$

with

$$\chi = \frac{\kappa^2 - 1}{\kappa^2 + 1} \quad \text{and} \quad \kappa = \sigma_e / \sigma_s. \tag{2b}$$

Here χ is a shape-anisotropy parameter and κ quantifies the elongation of the molecule. The case $\kappa = 1, \chi = 0$ corresponds to spherical particles, $\kappa \to \infty, \chi \to 1$ corresponds to very long rods, and $\kappa \to 0, \chi \to -1$ corresponds to very thin disks.

The energy term appearing in the GB potential is given by

$$\epsilon(\widehat{\mathbf{r}}_{ij}, \widehat{\mathbf{e}}_i, \widehat{\mathbf{e}}_j) = \epsilon_0 \epsilon_1^\nu(\widehat{\mathbf{e}}_i, \widehat{\mathbf{e}}_j) \epsilon_2^\mu(\widehat{\mathbf{r}}_{ij}, \widehat{\mathbf{e}}_i, \widehat{\mathbf{e}}_j), \tag{3a}$$

in which

$$\epsilon_1(\widehat{\mathbf{e}}_i, \widehat{\mathbf{e}}_j) = \left(1 - \chi^2(\widehat{\mathbf{e}}_i\cdot\widehat{\mathbf{e}}_j)^2\right)^{-1/2} \tag{3b}$$

$$\epsilon_2(\widehat{\mathbf{r}}_{ij}, \widehat{\mathbf{e}}_i, \widehat{\mathbf{e}}_j) = 1 - \frac{\chi'}{2}\left(\frac{(\widehat{\mathbf{e}}_i\cdot\widehat{\mathbf{r}}_{ij} + \widehat{\mathbf{e}}_i\cdot\widehat{\mathbf{r}}_{ij})^2}{1 + \chi'(\widehat{\mathbf{e}}_i\cdot\widehat{\mathbf{e}}_j)} + \frac{(\widehat{\mathbf{e}}_i\cdot\widehat{\mathbf{r}}_{ij} - \widehat{\mathbf{e}}_j\cdot\widehat{\mathbf{r}}_{ij})^2}{1 - \chi'(\widehat{\mathbf{e}}_i\cdot\widehat{\mathbf{e}}_j)}\right). \tag{3c}$$

Here the "energy anisotropy parameter" χ' is defined by

$$\chi' = \frac{\kappa'^{1/\mu} - 1}{\kappa'^{1/\mu} + 1}, \quad \text{with} \quad \kappa' = \epsilon_{ss} / \epsilon_{ee} \tag{3d}$$

The parameters ϵ_{ss} and ϵ_{ee} are the well depth of the potential in the side-to-side and end-to-end configurations, respectively, while ν and μ are exponents. In the original GB paper, rod-like molecules were simulated with parameters in the notation GB($\kappa, \kappa', \mu, \nu$) = GB(3,5,2,1).

2.2. The discotic GB model

To mimic a discotic liquid-crystal using the GB potential one replaces σ_s by σ_e:

$$v(\widehat{\mathbf{r}}_{ij}, \widehat{\mathbf{e}}_i, \widehat{\mathbf{e}}_j) = 4\epsilon(\widehat{\mathbf{r}}_{ij}, \widehat{\mathbf{e}}_i, \widehat{\mathbf{e}}_j)\left[\left(\frac{\sigma_e}{\rho_{ij}}\right)^{12} - \left(\frac{\sigma_e}{\rho_{ij}}\right)^{6}\right] \tag{4a}$$

$$\rho_{ij} = r_{ij} - \sigma(\widehat{\mathbf{r}}_{ij}, \widehat{\mathbf{e}}_i, \widehat{\mathbf{e}}_j) + \sigma_e, \tag{4b}$$

keeping everything else the same. This choice avoids the unphysical

effects [21] previously described by Bates and Luckhurst [12] and used by Cienega-Cacerez et al. [22] to obtain a discogen phase diagram for GB (0.345,0.2,1,2). The parameter σ_e defines the thickness of the discogen.

2.3. Simulation details

The system studied consists of $N = 2048$ disks. The potential is truncated, but not shifted, at $r_c = 1.6\sigma_s$ following the above-mentioned paper. Units are defined by putting $\sigma_s = 1$ and $\varepsilon_0 = 1$. We use the standard Nosé-Hoover *NVT* algorithm for the center-of-mass motion [23] and the IMP algorithm of Fincham for the rotational motion [24] with 10 iterations per step. We find that the latter algorithm, although not rigorously time reversible, conserves the energy very well. *NVT* simulations for the rotational motion follow the "Toxvaerd" version of the Finchham algorithm [25] (not the Berendsen version outlined in Ref. [24]). Two independent thermostats were applied for translation and rotational motion (using a single thermostat did not give noticeable differences). The moment of inertia of the discs was $I = 1$. Equilibration and production runs consisted of 5×10^6 time steps each with $\Delta t = 0.0005$. The GB implementation was compared to the literature comprising also, e.g., quaternion algorithms for the standard GB model; full agreement was established for time-correlation functions, etc.

2.4. Isomorphs

We study in this paper an isomorph in the high-temperature isotropic phase. Isomorphs are defined as curves of constant excess entropy S_{ex}. They can be generated numerically by utilizing the following general statistical-mechanical identity in which ρ is the particle density and T is the temperature [18].

$$\gamma \equiv \left(\frac{\partial \ln T}{\partial \ln \rho}\right)_{S_{\text{ex}}} = \frac{\langle \Delta U \Delta W \rangle}{\langle (\Delta U)^2 \rangle} \tag{5}$$

Here U is the potential energy and W is the virial. This equation is used as follows. At a given state point (ρ, T) one calculates the fluctuation average on the right hand side from an *NVT* simulation. If, for instance, this results in $\gamma = 3$, Eq. (5) implies that if density is increased by 1%, temperature should be increased by 3% to keep the excess entropy constant. In this way one can step-by-step trace out an isomorph in the thermodynamic phase diagram. We used the fourth-order Runge-Kutta algorithm to do this numerically, which is more accurate than the simple Euler algorithm [26]. We increased the density by 1% at each step and covered an overall density variation of 20%.

The dynamical behavior along the isomorph is analyzed in terms of time-autocorrelation functions defined by

$$\phi_A\left(t\right) = \frac{\langle \mathbf{A}(t_0)\cdot\mathbf{A}(t_0 + t)\rangle}{\langle \mathbf{A}(t_0)\cdot\mathbf{A}(t_0)\rangle} \tag{6}$$

where $\mathbf{A}(t)$ is a vector dynamical property referring to a given molecule at time t. We evaluate below $\phi_A(t)$ for $\mathbf{A}$ being the velocity of the molecule's center-of-mass, as well as the angular velocity. To study the orientational motion we calculate the self-particle orientational correlation functions,

$$\phi_l(t) = \langle P_l(\widehat{\mathbf{e}}_i(t_0)\cdot\widehat{\mathbf{e}}_i(t_0 + t))\rangle \tag{7}$$

where P_l is a Legendre polynomial ($l = 1$ and 2) and i is a particle index. In the above expressions, the angular brackets imply an average over particles and time origins. The spatial orientational correlation function is defined as follows

$$G_2(r) \equiv \langle P_2(\widehat{\mathbf{e}}_i\cdot\widehat{\mathbf{e}}_j)\rangle \tag{8}$$

in which the average involves the pairs of particles i and j that are the distance r apart.
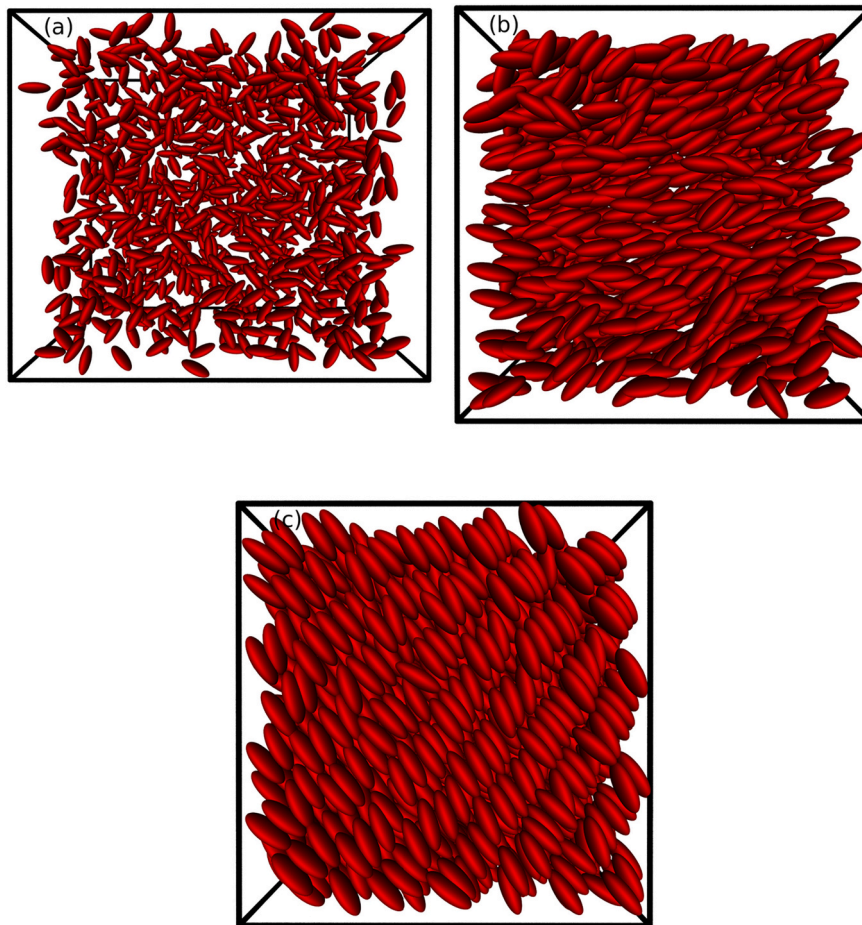
Fig. 1. Snapshots of the discotic GB model in thermal equilibrium at three state points (schematic drawings). (a) shows the isotropic liquid phase at $(\rho, T) = (0.6, 2.6)$; (b) shows the nematic phase at $(\rho, T) = (2.3, 2.6)$; (c) shows the columnar phase at $(\rho, T) = (3.0, 2.6)$.
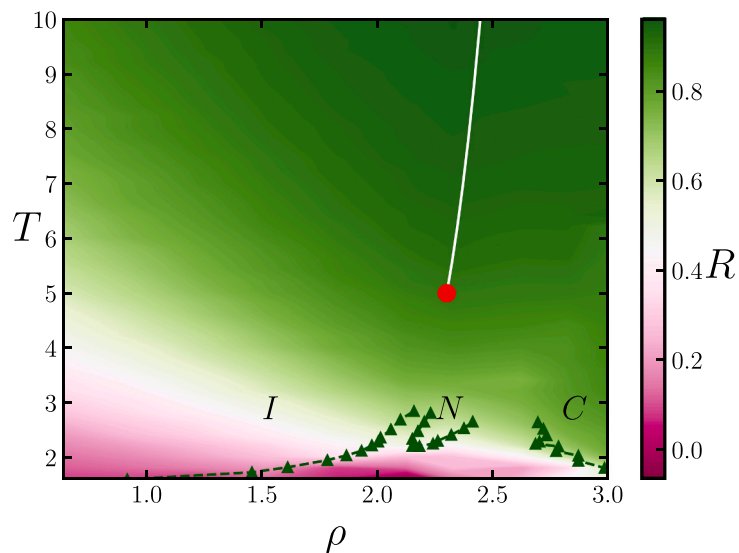
Fig. 2. The phase diagram of the discotic GB(0.345,0.2,1,2) model with R values (Eq. (9)) given by the color code to the right. The triangular symbols delimit the phase boundaries [22]. *I* stands for the isotropic, *N* for the nematic, and *C* for the columnar phase. The red filled circle is the isomorph reference state point $(\rho, T) = (2.3, 5.0)$, the white curve is the isomorph (which is studied up to $T=43$).

Table 1

The density ρ, temperature T, correlation coefficient R (Eq. (9)), and density-scaling exponent γ (Eq. (5)) of the state points studied along the isomorph. At each step density was increased by 1%. For the ρ=2.3 isochore we used same temperatures as in the table.

ρ	T	R	γ
2.300	5.000	0.8919	10.72
2.323	5.569	0.9087	10.99
2.346	6.222	0.9236	11.25
2.370	6.964	0.9354	11.41
2.393	7.805	0.9449	11.53
2.417	8.753	0.9511	11.56
2.441	9.821	0.9567	11.58
2.466	11.02	0.9598	11.57
2.491	12.36	0.9626	11.56
2.515	13.87	0.9646	11.53
2.541	15.55	0.9657	11.48
2.566	17.43	0.9672	11.46
2.592	19.53	0.9676	11.43
2.618	21.88	0.9678	11.41
2.644	24.50	0.9677	11.37
2.670	27.43	0.9673	11.33
2.697	30.71	0.9673	11.32
2.724	34.36	0.9673	11.30
2.751	38.45	0.9668	11.28
2.779	43.01	0.9662	11.26

2.5. Units

As mentioned, quantities are reported using the length unit σ_s and the energy unit ε_0 (MD units). We apply, however, also the "macroscopic" unit system based on the length unit $\rho^{-1/3}$ and the energy unit $k_B T$. Note that these so-called reduced units vary with state point. Isomorph invariance of structure and dynamics applies only when the quantities in question are given in reduced units [18], which is marked below by a tilde.

3. Phase diagram of the discotic GB model

Fig. 1 shows snapshots from simulations of the discotic GB model in the isotropic, nematic, and columnar phases, respectively. The pictures represent typical thermal equilibrium configurations. Each simulation was started from a perfect crystal at unit density after which density and temperature were changed to gradually reach the required values. To ensure that the system at the density and temperature aimed for is in equilibrium, similar simulations were performed starting from a high density and temperature and gradually decreasing those to the desired values.

The thermodynamic phase diagram of the model is investigated in Fig. 2 reporting the virial potential-energy correlation coefficient R defined [17] by

$$R = \frac{\langle \Delta U \Delta W \rangle}{\sqrt{\langle (\Delta U)^2 \rangle \langle (\Delta W)^2 \rangle}} \qquad (9)$$

Here Δ denotes the deviation from the thermal average and the sharp brackets denote equilibrium canonical constant-volume (*NVT*) averages. The condition defining "strong *UW* correlations" is R>0.9. This is the pragmatic criterion used for identifying regions of the phase diagram in which a given system is expected to have isomorphs, implying approximately invariant reduced-unit structure and dynamics [18].

In the figure, the letters "I", "N", and "C" denote the isotropic, nematic, and columnar phases, delimited by the triangular symbols (data taken from Ref. 22). The color coding reflects the value of R. We see that for temperatures above 5 and densities above about 2.4, i.e., well into the high-temperature isotropic phase, R is large enough to qualify for strong virial potential-energy correlation. The isomorph studied in this paper (white line) was generated as described in Sec. 2.3
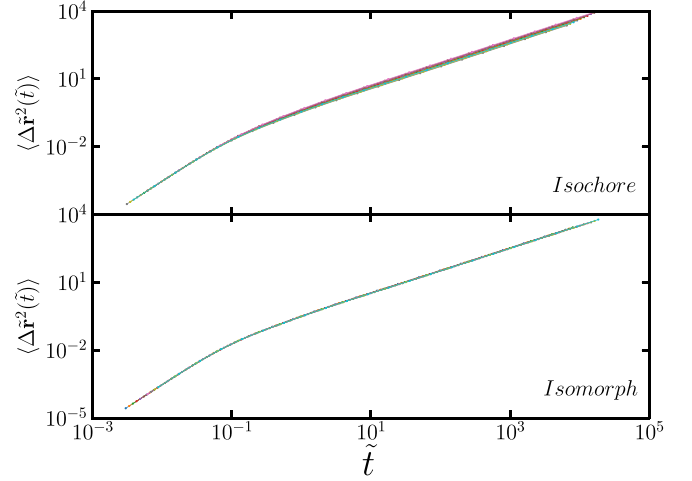
Fig. 3. Comparing the reduced-unit MSD along the isochore and the isomorph. At short times both figures exhibit a ballistic regime where the MSD is proportional to t^2; by the definition of reduced units the ballistic regime is the same at all state points. At long times both figures exhibit a diffusive regime where the MSD is proportional to t. Only along the isomorph do the data collapse in both regimes. Data are shown for 20 state points with 2.30<ρ<2.78 and 5<T<43.
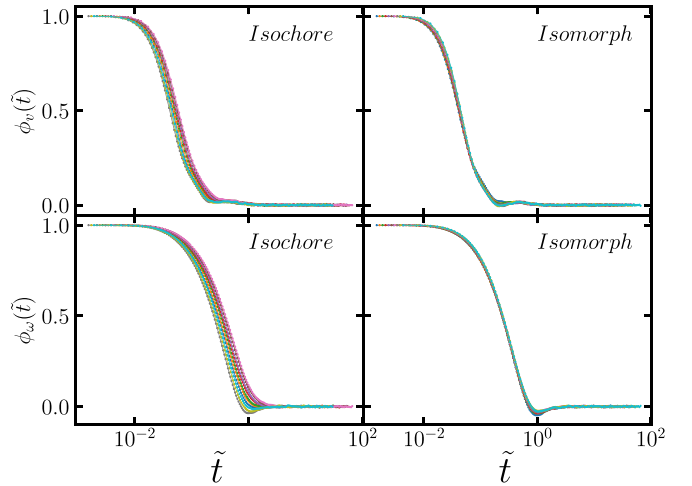
Fig. 4. Upper panel: center-of-mass velocity autocorrelation function as a function of the reduced time. Lower panel: angular velocity autocorrelation function.

starting from the reference state point (ρ, T) = (2.3,5.0). We proceed to investigate how different probes of structure and dynamics vary along this isomorph.

4. Comparing the isomorph to the ρ=2.3 isochore

The discotic GB model has more structural and dynamic signatures than a simple liquid for which there is basically just the radial distribution function (RDF) $g(r)$ and the time-dependent mean-square displacement (MSD). This section investigates to which degree structure and dynamics are invariant along the isomorph (white line in Fig. 2). Quantities are reported in reduced units (Sec. II.E). In order to put the isomorph findings into perspective, we compare to the variation of the same quantities along the ρ=2.3 isochore over the same temperature range as along the isomorph (5<T<43). Table 1 gives data for the isomorph state points studied.
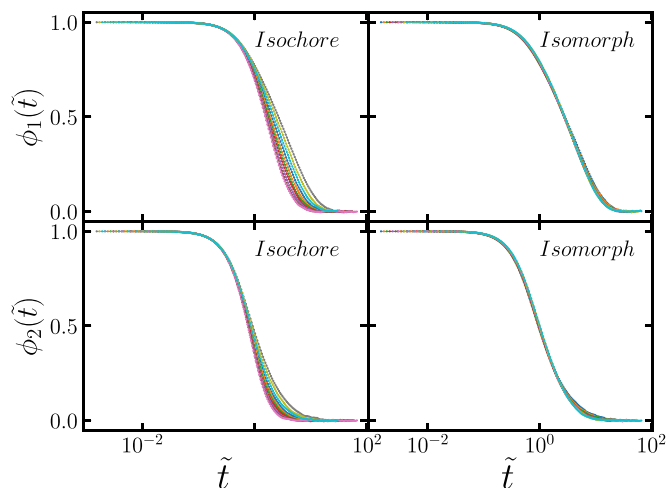
Fig. 5. First order (upper panel) and second order (lower panel) orientational autocorrelation functions (Eq. (7)).
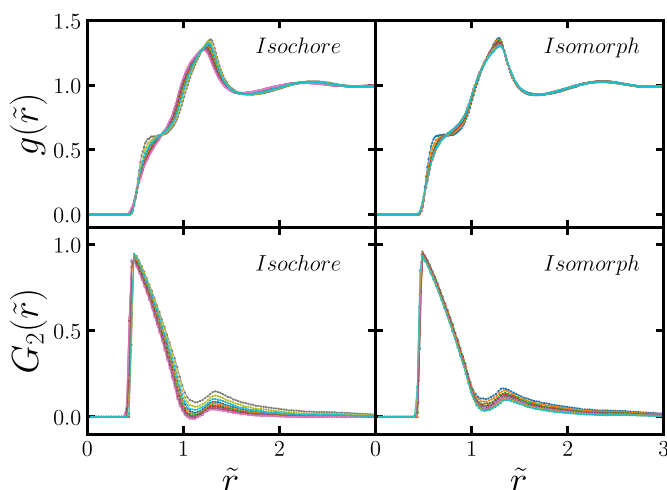
Fig. 6. Radial distribution function and orientational correlation function plotted as functions of the reduced distance along the isochore and the isomorph.

4.1. Dynamics

Fig. 3 compares the reduced-unit MSD along the isochore and the isomorph. Only along the isomorph is there invariance. Such data are typical for systems with isomorphs, so-called R-simple systems, and the data confirm the prediction of invariant dynamics along an isomorph [18]. One can think of an isomorph as a line in the phase diagram along which all physics relating to the positions and motion of the particles relative to one another is the same. Thus if one imagines filming the molecules at two different state points on a given isomorph, the same movie is recorded except for a scaling of space and time. This is the prediction for perfect isomorphs which, however, only exist in systems for which the potential-energy function is homogenous (implying $R=1$). For more realistic systems, isomorph invariance is approximate.

Fig. 4 gives data for two different velocity autocorrelation functions. The upper row shows the reduced center-of-mass velocity autocorrelation function along the isochore (left) and along the isomorph (right). We see data collapse along the latter, but not along the former. This is not surprising in view of Fig. 3 because the velocity autocorrelation function is two times the second derivative of the MSD. The two lower figures report the angular velocity autocorrelation functions, a quantity that has no analog in the standard Lennard-Jones model. Again we
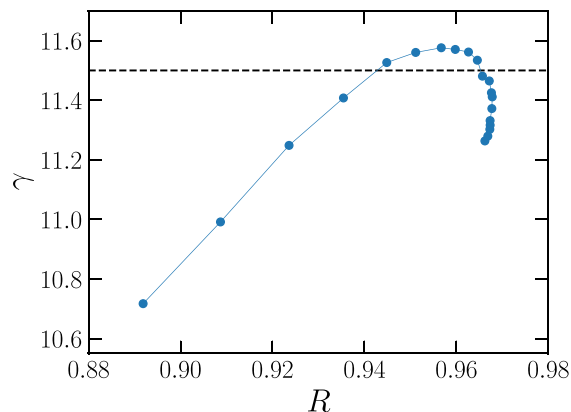
Fig. 7. Plot of γ versus R along the isomorph. The lower left corner is the reference state point $(\rho, T) = (2.3, 5.0)$; moving to higher temperatures and densities corresponds to moving to the upper right.

observe dynamic invariance along the isomorph, but not along the isochore.

Fig. 5 shows data for the first- and second-order orientational time-autocorrelation functions. In all cases, the function is unity at short times and decays to zero at long times. Only along the isomorph is the decay invariant to a good approximation.

We conclude that the reduced-unit dynamic characteristics are approximately invariant along the isomorph, but not along an isochore with the same temperature variation. This confirms the isomorph-theory prediction.

4.2. Structure

Next we report data for the reduced-unit structure. The upper panel of Fig. 6 shows the ordinary center-of-mass RDF along the isochore and the isomorph. The data are more invariant along the latter, but this time the difference is less striking. A similar observation is made for the spatial orientational correlation function (Eq. (8)) plotted in the lower figures.

Isomorph invariance of the isotropic phase of the discotic GB model is more pronounced for the dynamics than for the structure. A similar observation has been made in some liquids for which the height of the first peak of the radial distribution function may vary along an isomorph if the density-scaling exponent varies significantly [27]. This is consistent with the recent finding that the so-called bridge function is isomorph invariant [28], because an invariant bridge function implies that the RDF cannot be rigorously invariant.

5. Applying the constant-exponent density-scaling framework

Turning back to the dynamics, we now seek to interpret it in terms of density-scaling in its classical version for which the density-scaling exponent γ is assumed to be a material constant, i.e., not to vary with state point [29,30]. In this version, dynamic quantities are predicted to be a unique function of ρ^γ/T when plotted in reduced units.

In isomorph theory γ is the generally state-point-dependent quantity defined in Eq. (5). Fig. 7 shows how this γ and the virial potential-energy correlation coefficient R vary along the isomorph. The correlation coefficient increases as temperature and density are increased moving toward the upper right corner. At the same time, γ increases and goes through a maximum.

We calculated the average value of the isomorph-theory density-scaling exponent (Eq. (5)) along the four isochores given by $\rho=2.2$, $\rho=2.3$, $\rho=2.4$, and $\rho=2.5$ with temperatures obeying $T \in [5,43], [4,32], [10,32],$ and $[11,43]$, respectively. The results is
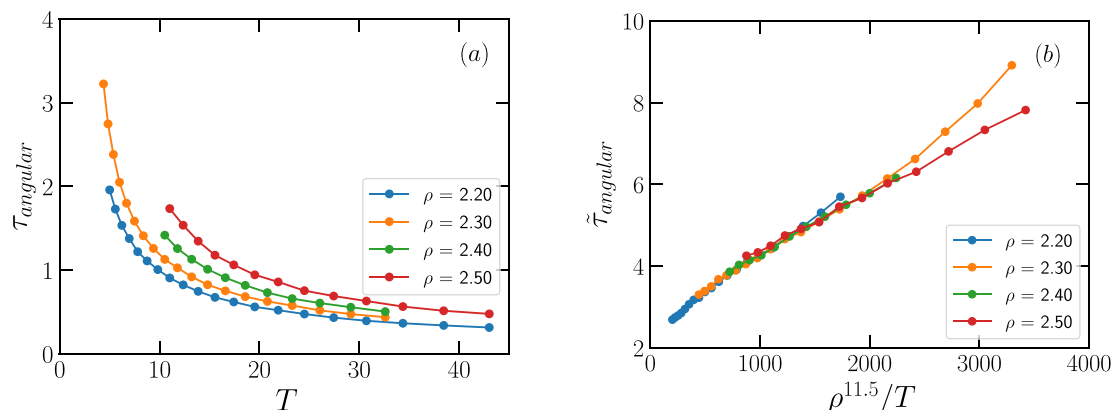
Fig. 8. (a) Average angular relaxation time as a function of temperature along four isochores with density varying from ρ=2.2 to ρ=2.5. (b) The same data for the average angular relaxation time plotted in reduced units as a function of the constant-exponent density-scaling variable ρ^γ/T with γ=11.5.
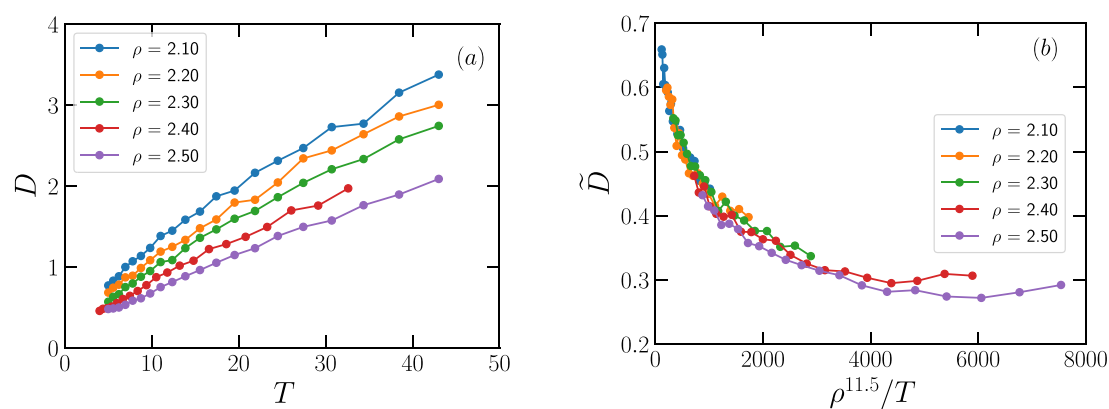
Fig. 9. (a) Diffusion coefficient as a function of temperature along five isochores with density varying from ρ=2.1 to ρ=2.5. (b) The same data plotted in reduced units as a function of the density-scaling variable ρ^γ/T with γ=11.5.

$$\gamma = 11.5. \tag{10}$$

This number is much larger than the density-scaling exponents found in standard Lennard-Jones models, which are never above 6 [17,18,31]. This emphasizes how different the GB model is from point-particle Lennard-Jones models, which also have isomorphs [32]. We conclude that the existence of isomorphs of the GB model is not inherited in a trivial way from the standard Lennard-Jones model.

Fig. 8(a) shows the average relaxation time of the angular autocorrelation function identified as the time at which this has reached the value 0.2, plotted as a function of the temperature along four isochores. Fig. 8(b) tests the constant-exponent version of density scaling with the average γ of Eq. (10). We find a good collapse for most data, with deviations at the longest relaxation times (lowest temperatures). This is where the density-scaling exponent deviates most from its average value 11.5, compare Fig. 7, i.e., where the constant-exponent approximation is expected to work less well.

Fig. 9 shows a similar figure for the center-of-mass diffusion coefficient D (with the additional isochore $\rho = 2.1$), extracted from the long-time behavior of the MSD. Fig. 9(a) shows the data for D as a function of the temperature and (b) shows the reduced-unit diffusion coefficient as a function of $\rho^{11.5}/T$. We again see a good data collapse.

6. Discussion

This paper has demonstrated the applicability of isomorph theory to the high-temperature isotropic phase of the discotic Gay-Berne model. We have traced out an isomorph and shown that along it the reduced-

unit dynamics is invariant to a good approximation, while it is not invariant along an isochore with the same temperature variation. Dynamic invariance applies not only for the standard mean-square displacement and velocity autocorrelation functions as a function of the reduced time (note that these are not independent quantities), invariance applies also for the first- and second-order orientational time-autocorrelation functions. The reduced-unit structure quantified by the radial distribution function and the corresponding spatial orientational correlation function are also isomorph invariant to a good approximation, although these quantities vary relatively little even along the isochore.

The isomorph-theory density-scaling exponent γ varies between 10.7 and 11.6, with the majority of exponents found close to 11.6 when studied along, e.g., the ρ=2.5 isochore. The density-scaling exponent averaged over the four isochores is 11.5. It is not clear why this value is so much larger than density-scaling exponents of the standard and various binary Lennard-Jones models. Constant-exponent density scaling applies with this value of γ, i.e., a good collapse is observed when the reduced-unit angular relaxation time and the reduced-unit diffusion coefficient are plotted as functions of $\rho^{11.5}/T$.

This paper presented the first application of isomorph theory to a liquid-crystal model. Future works will focus on other GB models and on the possibility of extending isomorph theory to ordered phases such as the nematic phase. In Ref. 14 density scaling was shown to apply for the GB model in the nematic phase with parameters corresponding to rod-like particles. For the current GB discotic liquid-crystal model we needed to go to high temperatures to find strong virial potential-energy correlations, but the fact that density scaling applies for the ordered

phases of the GB model for other parameters than those studied here suggests that isomorphs may also exist in the model's ordered phases. This is the subject of an ongoing investigation.

7. Conclusion

We have demonstrated the existence of isomorphs in the isotropic phase of the Gay-Berne liquid-crystal model. This shows that the model has the hidden-scale-invariance symmetry [33] that basically removes one dimension from the two-dimensional thermodynamic phase diagram. In other systems like supercooled molecular liquids, the existence of isomorphs implies specific predictions of how the system behaves under high pressure [34]; we expect that similar predictions can be made for high-pressure experiments on liquid crystals.

Declaration of Competing Interest

None.

Acknowledgments

References

[1] G.R. Luckhurst, G.W. Gray (Eds.), The Molecular Physics of Liquid Crystals, Academic Press, New York, 1979.
[2] M.P. Allen, Molecular simulation of liquid crystals, Mol. Phys. 117 (2019) 2391.
[3] Wikipedia article "Liquid Crystal", (2021).
[4] S. Kumar, Discotic liquid crystal-nanoparticle hybrid systems, NPG Asia Mater. 6 (2014), e82.
[5] S. Laschat, A. Baro, N. Steinke, F. Giesselmann, C. Haegele, G. Scalia, R. Judele, E. Kapatsina, S. Sauer, A. Schreivogel, M. Tosoni, Discotic liquid crystals: from tailor-made synthesis to plastic electronics, Angew. Chem. Int. Ed. 46 (2007) 4832.
[6] T. Wöhrle, I. Wurzbach, J. Kirres, A. Kostidou, N. Kapernaum, J. Litterscheidt, J. C. Haenle, P. Staffeld, A. Baro, F. Giesselmann, S. Laschat, Discotic liquid crystals, Chem. Rev. 116 (2016) 1139.
[7] R.J. Bushby, K. Kawata, Liquid crystals that affected the world: discotic liquid crystals, Liq. Cryst. 38 (2011) 1415.
[8] M.A. Kolmangadi, A. Yildirim, K. Sentker, M. Butschies, A. Bühlmeyer, P. Huber, S. Laschat, A. Schönhals, Molecular dynamics and electrical conductivity of guanidinium based ionic liquid crystals: influence of cation headgroup configuration, J. Mol. Liq. 330 (2021), 115666.
[9] A. Yildirim, M.A. Kolmangadi, A. Buühlmeyer, P. Huber, S. Laschat, A. Schönhals, Electrical conductivity and multiple glassy dynamics of crown ether-based columnar liquid crystals, J. Phys. Chem. B 124 (2020) 8728.
[10] J.G. Gay, B.J. Berne, Modification of the overlap potential to mimic a linear site–site potential, J. Chem. Phys. 74 (1981) 3316.
[11] E. De Miguel, L.F. Rull, M.K. Chalam, K.E. Gubbins, Liquid crystal phase diagram of the Gay-Berne fluid, Mol. Phys. 74 (1991) 405.
[12] M.A. Bates, G.R. Luckhurst, Computer simulation studies of anisotropic systems. XXVI. Monte Carlo investigations of a Gay–Berne discotic at constant pressure, J. Chem. Phys. 104 (1996) 6696.
[13] S. Ravichandran, A. Perera, M. Moreau, B. Bagchi, Universality in the fast orientational relaxation near isotropic–nematic transition, J. Chem. Phys. 109 (1998) 7349.
[14] K. Satoh, Thermodynamic scaling of dynamic properties of liquid crystals: verifying the scaling parameters using a molecular model, J. Chem. Phys. 139 (2013), 084901.
[15] A. Humpert, M.P. Allen, Elastic constants and dynamics in nematic liquid crystals, Mol. Phys. 113 (2015) 2680.
[16] V. Kapko, Z. Zhao, D.V. Matyushov, C.A. Angell, Ideal glassformers vs ideal glasses: studies of crystal-free routes to the glassy state by "potential tuning" molecular dynamics, and laboratory calorimetry, J. Chem. Phys. 138 (2013) 12A549.
[17] N.P. Bailey, U.R. Pedersen, N. Gnan, T.B. Schrøder, J.C. Dyre, Pressure-energy correlations in liquids. I. Results from computer simulations, J. Chem. Phys. 129 (2008), 184507.
[18] N. Gnan, T.B. Schrøder, U.R. Pedersen, N.P. Bailey, J.C. Dyre, Pressure-energy correlations in liquids. IV. "Isomorphs" in liquid phase diagrams, J. Chem. Phys. 131 (2009), 234504.
[19] T.S. Ingebrigtsen, T.B. Schrøder, J.C. Dyre, What is a simple liquid? Phys. Rev. X 2 (2012), 011011.
[20] T.B. Schrøder, J.C. Dyre, Simplicity of condensed matter at its core: generic definition of a Roskilde-simple system, J. Chem. Phys. 141 (2014), 204502.
[21] A.P.J. Emerson, G.R. Luckhurst, S.G. Whatling, Computer simulation studies of anisotropic systems. XXIII. The Gay-Berne discogen, Mol. Phys. 82 (1994) 113.
[22] O. Cienega-Cacerez, J.A. Moreno-Razo, E. Diaz-Herrera, E.J. Sambriski, Phase equilibria, fluid structure, and diffusivity of a discotic liquid crystal, Soft Matter 10 (2014) 3171.
[23] W.G. Hoover, Canonical dynamics: equilibrium phase-space distributions, Phys. Rev. A 31 (1985) 1695.
[24] D. Fincham, Leapfrog rotational algorithms for linear molecules, Mol. Simul. 11 (1993) 79.
[25] D. Fincham, Leapfrog rotational algorithms, Mol. Simul. 8 (1992) 165.
[26] E. Attia, J.C. Dyre, U.R. Pedersen, Extreme case of density scaling: the Weeks-Chandler-Andersen system at low temperatures, Phys. Rev. E 103 (2021), 062140.
[27] A.K. Bacher, T.B. Schrøder, J.C. Dyre, The EXP pair-potential system. II. Fluid phase isomorphs, J. Chem. Phys. 149 (2018), 114502.
[28] F.L. Castello, P. Tolias, J.C. Dyre, Testing the isomorph invariance of the bridge functions of Yukawa one-component plasmas, J. Chem. Phys. 154 (2021), 034501.
[29] A. Tölle, Neutron scattering studies of the model glass former ortho-terphenyl, Rep. Prog. Phys. 64 (2001) 1473.
[30] C. Alba-Simionesco, A. Cailliaux, A. Alegría, G. Tarjus, Scaling out the density dependence of the α relaxation in glass-forming polymers, Europhys. Lett. 68 (2004) 58.
[31] N.P. Bailey, U.R. Pedersen, N. Gnan, T.B. Schrøder, J.C. Dyre, Pressure-energy correlations in liquids. II. Analysis and consequences, J. Chem. Phys. 129 (2008), 184508.
[32] T.B. Schrøder, N. Gnan, U.R. Pedersen, N.P. Bailey, J.C. Dyre, Pressure-energy correlations in liquids. V. Isomorphs in generalized lennard-jones systems, J. Chem. Phys. 134 (2011), 164505.
[33] J.C. Dyre, Hidden scale invariance in condensed matter, J. Phys. Chem. B 118 (2014) 10007.
[34] H.W. Hansen, A. Sanz, K. Adrjanowicz, B. Frick, K. Niss, Evidence of a one-dimensional thermodynamic phase diagram for simple glass-formers, Nat. Commun. 9 (2018) 518.

Hidden scale invariance in the Gay-Berne model

Saeed Mehri ⬤, Jeppe C. Dyre ⬤,* and Trond S. Ingebrigtsen ⬤†

Glass and Time, IMFUFA, Department of Science and Environment, Roskilde University, P.O. Box 260, DK-4000 Roskilde, Denmark

This paper presents a numerical study of the Gay-Berne liquid crystal model with parameters corresponding to calamitic (rod-shaped) molecules. The focus is on the isotropic and nematic phases at temperatures above unity, where we find strong correlations between the virial and potential-energy thermal fluctuations, reflecting the hidden scale invariance symmetry. This implies the existence of isomorphs, which are curves in the thermodynamic phase diagram of approximately invariant physics. We study numerically one isomorph in the isotropic phase and one in the nematic phase. In both cases, good invariance of the dynamics is demonstrated via data for the mean-square displacement and the reduced-unit time-autocorrelation functions of the velocity, angular velocity, force, torque, and first- and second-order Legendre polynomial orientational order parameters. Deviations from isomorph invariance are observed at short times for the orientational time-autocorrelation functions, which reflects the fact that the moment of inertia is assumed to be constant and thus not isomorph-invariant in reduced units. Structural isomorph invariance is demonstrated from data for the radial distribution functions of the molecules and their orientations. For comparison, all quantities were also simulated along an isochore of similar temperature variation, in which case invariance is not observed. We conclude that the thermodynamic phase diagram of the calamitic Gay-Berne model is essentially one-dimensional in the studied regions as predicted by isomorph theory, a fact that potentially allows for simplifications of future theories and numerical studies.

I. INTRODUCTION

Liquid crystals (LCs), rodlike polymers, and disk-formed particles all involve molecules with a high degree of shape anisotropy [1]. LCs occur in many contexts, ranging from the well-known display applications to biological systems [2–4]. Depending on the density and the temperature, the anisotropy of LCs may lead to different structural phases. For the thermometric LCs in focus here, changing temperature and density may cause transitions from the ordinary crystalline state to smectic, nematic, and isotropic phases [2].

Pure fluids and mixtures consisting of aspherical particles have been the subject of many theoretical, experimental, and simulations studies [5–8]. Theoretical studies are typically based on the Fokker-Planck equation [9,10], generalized Langevin equations [11,12], Onsager theory [13], density-functional theory [14], or generalized van der Waals descriptions [15]. Different numerical techniques such as Monte Carlo and molecular dynamics (MD) have been applied for studying the phase behavior, thermodynamics, structure, and dynamics of rigid anisotropic molecules forming LCs [16].

Depending on the type of interaction between the molecules, one can classify LC models into two main groups [17]. The first group considers models of hard particles with a nonspherical shape [18]. In such models, there are no attractive interactions, i.e., the potential is purely repulsive and short-ranged. The main motivation for this approach is the success of the hard-sphere model in explaining the properties of simple liquids [19,20]. Extensive simulation studies have used this approach to investigate the structure and dynamics of LC fluids for different shape anisotropies (prolate ellipsoids, spherocylinders, rods, disks, etc.) [21–23]. In the other main class of LC models, both short-range repulsive and long-range attractive interactions are taken into account. Several models for fluids of aspherical particles have been introduced for LC studies, e.g., the Kihara potential [24], the site-site potential [25], the Gaussian overlap model [26], and the Gay-Berne (GB) model [27]. By using site-site potentials, one can realistically mimic the structure of LC molecules and compare results to experiments [28–33], but unfortunately such models usually require huge computational resources. This is why most simulations so far have been conducted for relatively small system sizes. An exception is the GB model based on the Lennard-Jones (LJ) pair interaction, which is computationally cheap and still realistic. For this reason, the GB model has become a generic LC model. The GB model gives rise to a rich mesogenic behavior [4]. Previous numerical studies of this model focused on its phase behavior [34–40], per-particle translational and orientational dynamics [41], interfacial properties [42], elastic constants [43], thermal conductivity [44,45], and viscosity [46,47]. Analytical perturbation theories have also been applied in order to explore the phase diagram of GB fluids [48,49].

The GB model allows one to describe different shape anisotropy, spanning from elongated ellipsoids to thin disks [27]. The GB potential depends on four dimensionless parameters, which is often indicated by the notation $GB(\kappa, \kappa', \mu, \nu)$.

---

*dyre@ruc.dk
†trond@ruc.dk

The four parameters control the shape of the molecules and the strength of the interaction between them. GB(3, 5, 2, 1) is the most studied case, mimicking rod-shaped molecules, and in this case the phase diagram and orientational order parameter are known [50]. Moreover, the velocity time-autocorrelation function [41], viscosity [47], elastic constants [51], free energies and enthalpy [14], isotropic-nematic transition [36], liquid-vapor coexistence curve [52], stress-tensor components [53], and self-diffusion coefficient [54] have been studied for the GB(3, 5, 2, 1) model.

This paper presents a study of the Gay-Berne model with the above parameters corresponding to calamitic, i.e., rod-shaped elongated molecules (GB(3,5,2,1)) at high temperatures, where the model is shown to obey the symmetry of hidden scale invariance. According to this symmetry, the system is expected to have isomorphs, which are curves in the thermodynamic phase diagram along which structure and dynamics are almost invariant when given in properly reduced units. A recent study of ours showed this for the more exotic discotic Gay-Berne model GB(0.345, 0.2, 1, 2) in the isotropic phase [55]; the present paper demonstrates the existence of isomorphs in both the isotropic and the nematic phase of a more standard Gay-Berne model. The study given below nicely confirms a recent work by Liszka and co-workers [56], although that paper focused more on density-scaling (a specific consequence of isomorph theory) than on demonstrating isomorph invariance of structure and dynamics.

II. GAY-BERNE POTENTIAL

The GB potential between pairs of particles ("molecules"), GB($\kappa, \kappa', \mu, \nu$), is characterized by four dimensionless parameters: $\kappa \equiv \sigma_e/\sigma_s$ where σ_e and σ_s are lengths, $\kappa' \equiv \varepsilon_{ss}/\varepsilon_{ee}$ where ε_{ss} and ε_{ee} are energies, while μ and ν are exponents.

The GB pair potential v_{GB}, which is basically a direction-dependent LJ pair potential, is defined as follows:

$$v_{GB}(\mathbf{r}_{ij}, \hat{\mathbf{e}}_i, \hat{\mathbf{e}}_j) = 4\varepsilon(\hat{\mathbf{r}}, \hat{\mathbf{e}}_i, \hat{\mathbf{e}}_j)[(\sigma_s/\rho_{ij})^{12} - (\sigma_s/\rho_{ij})^6],$$
(1a)

$$\rho_{ij} = r_{ij} - \sigma(\hat{\mathbf{r}}, \hat{\mathbf{e}}_i, \hat{\mathbf{e}}_j) + \sigma_s.$$
(1b)

Here, r_{ij} is the distance between molecules i and j, $\hat{\mathbf{r}} \equiv \mathbf{r}_{ij}/r_{ij}$ is the unit vector along the vector from molecule i to molecule j denoted by $\mathbf{r}_{ij}$, and $\hat{\mathbf{e}}_i$ and $\hat{\mathbf{e}}_j$ are unit vectors along the major axes of molecules i and j. The GB molecule is roughly an ellipsoid of two diameters σ_s and σ_e, and one defines

$$\sigma(\hat{\mathbf{r}}, \hat{\mathbf{e}}_i, \hat{\mathbf{e}}_j) = \sigma_s \left[1 - \frac{\chi}{2} \left(\frac{(\hat{\mathbf{e}}_i \cdot \hat{\mathbf{r}} + \hat{\mathbf{e}}_j \cdot \hat{\mathbf{r}})^2}{1 + \chi(\hat{\mathbf{e}}_i \cdot \hat{\mathbf{e}}_j)} \right. \right.$$
$$\left. \left. + \frac{(\hat{\mathbf{e}}_i \cdot \hat{\mathbf{r}} - \hat{\mathbf{e}}_j \cdot \hat{\mathbf{r}})^2}{1 - \chi(\hat{\mathbf{e}}_i \cdot \hat{\mathbf{e}}_j)} \right) \right]^{-1/2},$$
(2a)

$$\chi = \frac{\kappa^2 - 1}{\kappa^2 + 1}.$$
(2b)

Physically, χ is a shape anisotropy parameter and κ quantifies the molecular elongation. The case $\kappa = 1$ ($\chi = 0$) represents spherical molecules, the case $\kappa \to \infty$ ($\chi \to 1$) corresponds

to very long rods, and the case $\kappa \to 0$ ($\chi \to -1$) corresponds to very thin disks. The energy term is given as follows:

$$\varepsilon(\hat{\mathbf{r}}, \hat{\mathbf{e}}_i, \hat{\mathbf{e}}_j) = \varepsilon_0 \left[\varepsilon_1(\hat{\mathbf{e}}_i, \hat{\mathbf{e}}_j) \right]^\nu [\varepsilon_2(\hat{\mathbf{r}}, \hat{\mathbf{e}}_i, \hat{\mathbf{e}}_j)]^\mu$$
(3a)

in which

$$\varepsilon_1(\hat{\mathbf{e}}_i, \hat{\mathbf{e}}_j) = (1 - \chi^2(\hat{\mathbf{e}}_i \cdot \hat{\mathbf{e}}_j)^2)^{-1/2},$$
(3b)

$$\varepsilon_2(\hat{\mathbf{r}}, \hat{\mathbf{e}}_i, \hat{\mathbf{e}}_j) = 1 - \frac{\chi'}{2} \left(\frac{(\hat{\mathbf{e}}_i \cdot \hat{\mathbf{r}} + \hat{\mathbf{e}}_j \cdot \hat{\mathbf{r}})^2}{1 + \chi'(\hat{\mathbf{e}}_i \cdot \hat{\mathbf{e}}_j)} \right.$$
$$\left. + \frac{(\hat{\mathbf{e}}_i \cdot \hat{\mathbf{r}} - \hat{\mathbf{e}}_j \cdot \hat{\mathbf{r}})^2}{1 - \chi'(\hat{\mathbf{e}}_i \cdot \hat{\mathbf{e}}_j)} \right),$$
(3c)

and the energy anisotropy parameter is given by

$$\chi' = \frac{\kappa'^{1/\mu} - 1}{\kappa'^{1/\mu} + 1}.$$
(3d)

The energies ε_{ss} and ε_{ee} are the well depths of the potential in the side-side and end-end configurations, respectively. Henceforth, unless isomorph-theory reduced units are used (see Sec. III), σ_s defines the length unit and ε_0 defines the energy unit. The density ρ and the temperature T are always given in these units.

The GB(3, 5, 2, 1) model was introduced in 1981 by Gay and Berne, inspired by the Gaussian overlap model of Berne and Pechukas [26,27]. For realistic LCs, the length-to-width ratio is at least 3, leading to the choice of $\kappa = 3$ by Gay and Berne [27]. To obtain the other parameters, the GB pair potential was compared to the case of a pair of linear molecules consisting of four LJ particles placed on a line such that the length-to-width ratio equals 3. This results in $\kappa' = 5$, $\mu = 2$, and $\nu = 1$ [27].

As mentioned, the GB(3, 5, 2, 1) model shows a rich phase behavior with isotropic, nematic, and smectic-B phases [34,35,50]. Actually, the model (occasionally with slightly different parameters) also has the following phases: smectic A [35], tilted smectic B [50], and rippled smectic B [40]. In some cases, more involved versions of the GB potential have been investigated by introducing, e.g., dipolar forces [57], flexibility [58], more complex shapes [59], or biaxial molecules [60]. Other sets of parameters have also been studied, and other properties have been examined, e.g., the effect of the ν exponent on the orientational order parameter [61], the elastic constant for GB(3, 5, 1, 3) [62], the diffusion coefficient in the smectic-A phase of GB(4.4, 20, 1, 1) [63], the stability of the smectic phase, the radial distribution function, the orientational order parameter [64], and the rotational viscosity coefficient [65]. Satoh *et al.* studied the effect of an external magnetic field on GB fluids [66]. The isotropic-nematic region has been explored for different values of κ [67,68]. Varying κ' while keeping the other parameters fixed at $\kappa = 3$, $\mu = 2$, and $\nu = 1$ has been investigated in detail. The liquid-vapor region has been analyzed [69,70], and so has the equation of state, structure, and diffusion coefficient [71]. For discotic GB fluids, the phase diagram has been obtained for different κ and κ' parameters [55,72–74]. The most studied discotic model is GB(0.345, 0.2, 1, 2) [75], which incidentally led to an improvement of the angle of view of liquid-crystal displays [76].
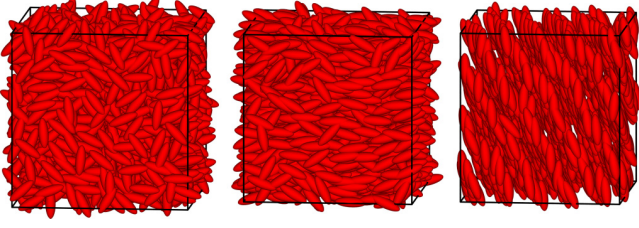
FIG. 1. Snapshots of the calamitic GB model GB(3, 5, 2, 1) at three state points. Panel (a) shows the isotropic liquid phase at the state point $(\rho, T) = (0.27, 1.2)$; (b) shows the nematic phase at $(\rho, T) = (3.3, 1.2)$; (c) shows the smectic phase at $(\rho, T) = (3.9, 1.2)$.

In this work, we study the GB(3, 5, 2, 1) model because, as already mentioned, its phase diagram, structure, and dynamics are known. Figure 1 presents snapshots of the system at equilibrium in the isotropic, nematic, and smectic phases. There is no positional or orientational ordering in the isotropic phase. In the nematic phase there is no positional ordering, but some long-range orientational ordering. In the smectic phase the molecules form parallel layers with long-range orientational ordering within the layers.

III. *R*-SIMPLE SYSTEMS AND ISOMORPHS

Recalling that the virial W quantifies the part of the pressure p deriving from molecular interactions via the defining identity $pV = Nk_BT + W$ (in which V is the volume and N is the number of molecules) [77], liquids and solids may be classified according to the correlation between the equilibrium fluctuations of the virial and the potential energy U [78]. The so-called *R*-simple systems, which are those with strong such correlations, are particularly simple because the thermodynamic phase diagram is basically one-dimensional instead of two-dimensional in regard to structure and dynamics [78–81].

Isomorph theory dealing with *R*-simple systems was developed over the past decade [82–85]. The WU Pearson correlation coefficient is defined by

$$R(\rho, T) = \frac{\langle \Delta W \Delta U \rangle}{\sqrt{\langle (\Delta W)^2 \rangle \langle (\Delta U)^2 \rangle}}. \qquad (4)$$

Here the angular brackets denote NVT ensemble averages, Δ is the deviation from the equilibrium mean value, and ρ is the density. Many systems, including the LJ fluid, have strong WU correlations in the liquid and solid phases, whereas $R(\rho, T)$ usually decreases significantly below the critical density [86]. A system is considered to be *R*-simple whenever $R > 0.9$ at the state points in question. The density-scaling exponent γ, which is characterized by $\Delta U \cong \gamma \Delta W$, is found from linear-regression fits to a WU scatter plot as shown in Fig. 2 or using the equation

$$\gamma = \frac{\langle \Delta W \Delta U \rangle}{\langle (\Delta U)^2 \rangle}. \qquad (5)$$

R-simple systems have curves in the phase diagram along which structure and dynamics are approximately invariant, and these curves are termed *isomorphs*. It is important to emphasize that isomorph invariance only applies when data
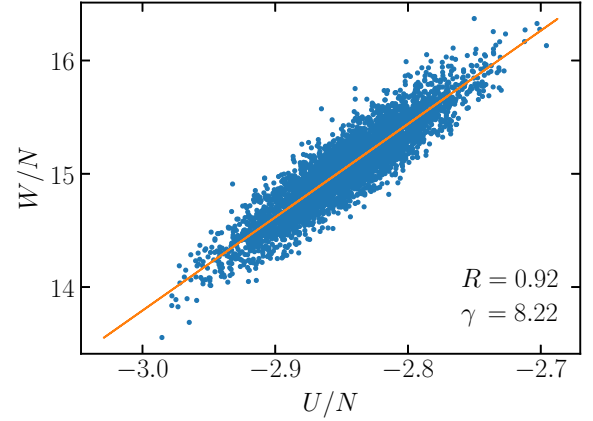
FIG. 2. Scatter plot of WU correlations for the GB(3, 5, 2, 1) model at the state point $(\rho, T) = (0.33, 1.2)$. The system is strongly correlating here with $R = 0.92$; the density-scaling exponent γ is 8.22.

are presented in so-called reduced units. In the system of reduced units, which in contrast to ordinary units is state-point-dependent, the density $\rho \equiv N/V$ defines the length unit l_0, the temperature defines the energy unit e_0, and the density and thermal velocity define the time unit t_0:

$$l_0 = \rho^{-1/3}, \quad e_0 = k_B T, \quad t_0 = \rho^{-1/3}\sqrt{m/k_B T}.$$

Here m is the molecule mass. Quantities given in isomorph-theory reduced units are marked with a tilde.

Strong virial potential-energy correlations arise whenever the hidden-scale-invariance symmetry applies. This is the condition in which the potential-energy ordering of same-density configurations is maintained under a uniform scaling of all coordinates [87], which is formally expressed as follows:

$$U(\mathbf{R}_a) < U(\mathbf{R}_b) \Rightarrow U(\lambda\mathbf{R}_a) < U(\lambda\mathbf{R}_b), \qquad (6)$$

where λ is the scaling factor. Consider two configurations with the same potential energy, i.e., $U(\mathbf{R}_a) = U(\mathbf{R}_b)$. After a uniform scaling, one has by Eq. (6) $U(\lambda\mathbf{R}_a) = U(\lambda\mathbf{R}_b)$. By taking the derivative of this with respect to λ, one easily derives $W(\mathbf{R}_a) = W(\mathbf{R}_b)$ [87]; thus same potential energy implies same virial, i.e., 100% correlation between W and U. Equation (6) only applies approximately for realistic systems, however, so in practice one observes strong but not perfect virial potential-energy correlations.

It can be shown that Eq. (6) implies that the reduced-unit structure and dynamics are invariant along the lines of constant excess entropy, which are by definition the isomorphs [87]. Recall that a system's entropy S can be expressed as that of an ideal gas plus a term derived from the intermolecular interactions, $S = S_{id} + S_{ex}$. For an ideal gas, one has $S_{ex} = 0$; for all other systems, $S_{ex} < 0$ because these are less disordered than an ideal gas.

Along an isomorph one has

$$dS_{ex} = \left(\frac{\partial S_{ex}}{\partial T}\right)_V dT + \left(\frac{\partial S_{ex}}{\partial V}\right)_T dV = 0. \qquad (7)$$

Using Maxwell's volume-temperature relation for the configurational degrees of freedom, $(\partial S_{ex}/\partial V)_T = [\partial(W/V)/\partial T]_V$,

we can rewrite Eq. (7) as

$$\left(\frac{\partial S_{\text{ex}}}{\partial T} \right)_V T \, d \ln T = \left(\frac{\partial W}{\partial T} \right)_V d \ln \rho. \tag{8}$$

Using $dU = T \, dS_{\text{ex}} - (W/V) dV$ leads to

$$\left(\frac{\partial U}{\partial T} \right)_V d \ln T = \left(\frac{\partial W}{\partial T} \right)_V d \ln \rho, \tag{9}$$

which via the fluctuation relations $(\partial W / \partial T)_V = -\langle \Delta W \Delta U \rangle / k_B T^2$ and $(\partial U / \partial T)_V = -\langle (\Delta U)^2 \rangle / k_B T^2$ for γ leads to the above Eq. (5),

$$\gamma \equiv \left(\frac{\partial \ln T}{\partial \ln \rho} \right)_{S_{\text{ex}}} = \frac{\langle \Delta W \Delta U \rangle}{\langle (\Delta U)^2 \rangle}. \tag{10}$$

Equation (10) is completely general [83]. This equation is of particular interest, however, when the system has isomorphs because the equation can then be used for tracing out isomorphs without knowing the equation of state, which is done as follows. At a given state point (ρ_1, T_1) one first calculates γ from the equilibrium fluctuations of the potential energy and virial. Then, by scaling the system to a slightly different density ρ_2 and numerically calculating $(\partial \ln T / \partial \ln \rho)_{S_{\text{ex}}}$ from Eq. (10), one predicts the temperature T_2 with the property that (ρ_2, T_2) is on the same isomorph as (ρ_1, T_1). In the simulations of this paper we used fourth-order Runge-Kutta integration to generate isomorphs [88] involving density step sizes of approximately 1%.

IV. PROPERTIES STUDIED

We simulated a system of 1372 molecules. The pair potential was cut and shifted at $r_c = 4.0$ and the time step was $\Delta t = 0.001$. Because of the shape anisotropy, supplementing the standard NVT Nose-Hoover algorithm for the center-of-mass motion, we used the IMP algorithm for the rotational motion [89]. Different thermostats were applied for translational and rotational motion (we eventually concluded that using a single thermostat did not result in any noticeable differences, however). The molecular moment of inertia was set to $I = 1$. At each simulated state point, 20 million time steps were taken to equilibrate the system before the production runs, each of which involved 67 million time steps. As a consistency check of our GB implementation, we compared the simulation results with those of the literature and found good agreement in all cases. The quantities evaluated in these comparisons, which are all defined below, were the following [where we also list the reference(s) to which data were compared]: the radial distribution function $g(r)$ [50,90], the radial distribution orientational correlation function $G_2(r)$ [34,36,50], the S_2 orientational order parameter [36,50,91], and various time-autocorrelation functions [41,92].

An order parameter is a physical quantity that distinguishes between two phases. We proceed to define the second-rank orientational order parameter S_2 that quantifies how much the molecular orientations vary throughout the system [93]. For a uniaxial phase, S_2 is defined as the following sum over all molecules:

$$S_2 = \left\langle \frac{1}{N} \sum_i P_2(\hat{\mathbf{e}}_i \cdot \hat{\mathbf{e}}_d) \right\rangle. \tag{11}$$

Here P_2 is the second-order Legendre polynomial, $\hat{\mathbf{e}}_d$ is the director of the phase, and the angular brackets denote a time or ensemble average. This quantity takes values between 0 and 1; for a perfectly aligned system, $S_2 = 1$, whereas $S_2 = 0$ implies an isotropic system.

In a simulation, $\hat{\mathbf{e}}_d$ is unknown. Here the order parameter can be evaluated by maximizing S_2 with respect to $\hat{\mathbf{e}}_d$, which is done by rewriting Eq. (11) as follows [21,93]:

$$S_2 = \langle \hat{\mathbf{e}}_d \cdot \mathbf{Q} \cdot \hat{\mathbf{e}}_d \rangle. \tag{12}$$

If $\otimes$ denotes a tensor product and **I** is the unity matrix, **Q** is defined by

$$\mathbf{Q} = \frac{1}{2N} \sum_i (3 \hat{\mathbf{e}}_i \otimes \hat{\mathbf{e}}_i - \mathbf{I}). \tag{13}$$

It can be shows that S_2 is the largest eigenvalue, $\lambda_{\max}$, of the **Q** tensor.

Figure 3 shows a "heat-map" phase diagram of the GB(3, 5, 2, 1) model with respect to the virial potential-energy correlation coefficient R and the orientational order parameter S_2. By definition, the regions with $R > 0.9$ are R-simple; this is where one expects isomorph theory to apply. This is not a sharp distinction, however, and many systems with R between 0.8 and 0.9 have also been found to have good isomorphs. In Fig. 3, I stands for the isotropic, N for the nematic, and S for the smectic phase; regions in-between are those of coexisting phases. The dark green triangles marking the phase boundaries were extracted from Ref. [94]. Selected isomorphs are marked as solid yellow lines, each of which starts from a "reference state point" marked as a red full circle. The main paper presents results for two isomorphs (black): one in the isotropic phase and one in the nematic phase. Results for the remaining five isomorphs are reported in Ref. [95].

We conclude from Fig. 3(a) that there are strong correlations whenever the temperature is above unity, which is where the nematic phase becomes relevant. The isomorph reference state points were selected to obey $R > 0.9$; from here on R increases when density and temperature are increased along each isomorph (except at the highest densities). The Appendix gives details in the form of tables of the two isomorphs studied, listing for each isomorph several state points and the corresponding values of R and γ. Note that invariance of the physics along the isomorphs—the main focus of this paper—is manifested already in Fig. 3(b) as regards the orientational ordering because S_2 is clearly approximately isomorph-invariant. In particular, the phase boundary approximately follows an isomorph [83,96]. Based on this, the light blue triangles mark the expected isotropic-nematic phase boundary. This gives an example of how isomorph theory may be used for estimating the phase boundary by allowing one to go beyond the numerical phase-boundary data of Ref. [94] without having to perform extensive additional simulations.

Having established the phase diagram of the GB(3, 5, 2, 1) model, we next define the quantities studied. We probed the system's dynamics at the different state points by calculating the mean-square displacement (MSD) as a function of time, as well as time-autocorrelation functions defined by

$$\phi_A(t) = \langle \mathbf{A}(t_0) \cdot \mathbf{A}(t_0 + t) \rangle. \tag{14}$$
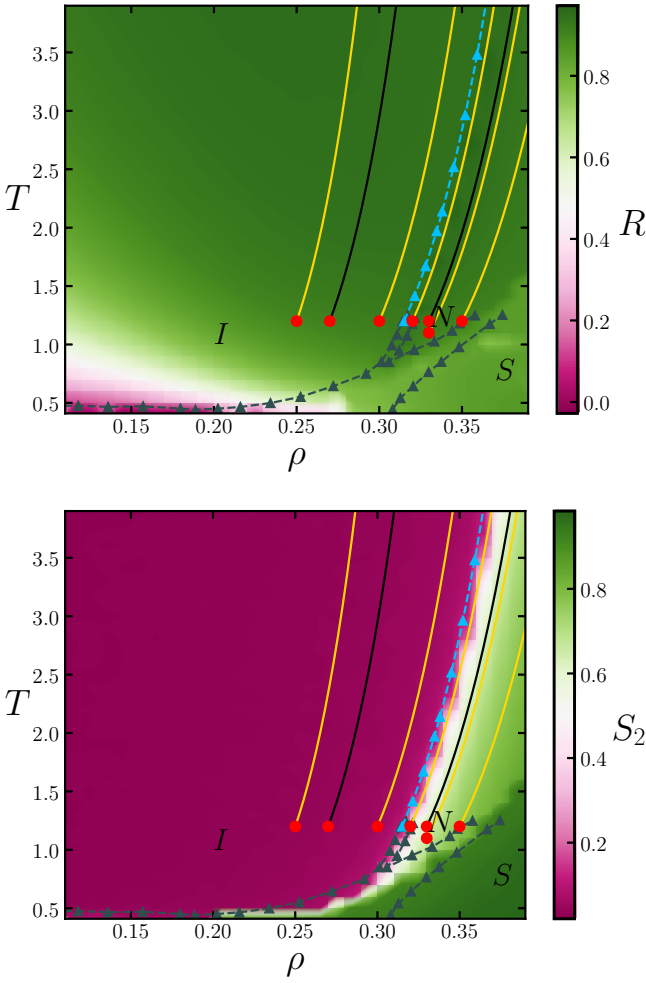
FIG. 3. Density-temperature phase diagram of the GB(3, 5, 2, 1) model with (a) showing the virial potential-energy correlation coefficient R [Eq. (4)] and (b) showing the second-order orientational order parameter S_2 [Eq. (12)]. Dark green triangles connected by dark green dashed lines delimit the phase boundaries [94]. I stands for the isotropic, N for the nematic, and S for the smectic phase. The solid yellow curves are isomorphs not investigated further here (results for these are presented in Ref. [95]); the two black curves are isomorphs for which results are reported below, one in the isotropic phase and one in the nematic phase. The light blue triangles mark the isomorph that continues the I-N phase boundary numerical data of Ref. [94]. The isomorphs were determined by numerical integration of Eq. (10) starting from the following reference state points marked by the red filled circles: $(\rho_{\text{ref}}, T_{\text{ref}}) = (0.25, 1.2)$, $(\rho_{\text{ref}}, T_{\text{ref}}) = (0.27, 1.2)$, $(\rho_{\text{ref}}, T_{\text{ref}}) = (0.30, 1.2)$, $(\rho_{\text{ref}}, T_{\text{ref}}) = (0.32, 1.2)$, $(\rho_{\text{ref}}, T_{\text{ref}}) = (0.33, 1.1)$, $(\rho_{\text{ref}}, T_{\text{ref}}) = (0.33, 1.2)$, and $(\rho_{\text{ref}}, T_{\text{ref}}) = (0.35, 1.2)$.

Here $\mathbf{A}(t)$ is a vector or scalar molecular property, and the angular brackets denote an ensemble and particle average. Below we evaluate Eq. (14) from simulations for $\mathbf{A}$ equal to velocity, angular velocity, force, and torque. We also study the first- and second-order orientational order-parameter time-correlation function defined by

$$\phi_l(t) = \langle P_l[\hat{\mathbf{e}}_i(t_0) \cdot \hat{\mathbf{e}}_i(t_0 + t)]\rangle, \quad (15)$$

in which P_l is a Legendre polynomial ($l = 1$ and 2). To quantify the structure, we measured the standard radial distribution function, $g(r)$, as well as the radial-distribution orientational correlation function defined by

$$G_2(r) \equiv \langle P_2(\hat{\mathbf{e}}_i \cdot \hat{\mathbf{e}}_j)\rangle, \quad (16)$$

where the angular brackets imply an average over all pairs of molecules i and j that are the distance r apart.

V. RESULTS

This section investigates to which degree the reduced-unit structure and dynamics are invariant along two isomorphs. We present data for one isomorph in the isotropic phase and one in the nematic phase (the black lines in Fig. 3). In realistic models isomorph invariance is only approximate, so in order to put the findings into perspective we compare the results for each isomorph with results for the isochore defined by the reference-state-point density (red points in Fig. 3) with the same temperature variation as that of the isomorph. For the isotropic-phase isomorph, the reference state point is $(\rho_{\text{ref}}, T) = (0.27, 1.2)$; here we cover a density variation of about 40% with temperatures in the range $1.2 < T < 27$. For the nematic-phase isomorph, the reference state point is $(\rho_{\text{ref}}, T) = (0.33, 1.2)$; here the density varies by about 35% with temperatures in the range $1.2 < T < 16$.

Figure 4 provides data for the reduced-unit MSD along the isochore and the isomorph in the isotropic and nematic phases, respectively. The level of invariance in the center-of-mass dynamics is clearly higher along the isomorph than along the isochore. At long times, the MSD is proportional to time, and the diffusion coefficients may be extracted from these data. Figure 5 shows the reduced diffusion coefficient as a function of temperature along the isochores and isomorphs—approximate isomorph invariance is again clearly visible.

Next we show data for four time-autocorrelation functions. Figure 6 gives in the two upper figures the velocity (v) and angular velocity (ω) time-autocorrelation functions, while the two lower figures give the force and torque time-autocorrelation functions. As in Fig. 4, all functions are given in reduced units as functions of the reduced time $\tilde{t}$. Overall, we see in both the isotropic and the nematic phases good isomorph invariance and a sizable variation along the corresponding isochores. The short-time angular velocity and torque time-autocorrelation functions violate isomorph invariance significantly, however. This is due to the fact that the moment of inertia in the simulations was kept fixed, implying that this quantity is not constant in reduced units. As a consequence, the short-time ballistic motion is not isomorph-invariant. At intermediate and long times, we do find good isomorph invariance also for the rotational time-autocorrelation functions; here the moment of inertia plays little role for the dynamics, which for a given molecule is dominated by interactions with the surrounding GB molecules. A weaker but still clearly visible violation of isomorph invariance occurs at short times for the force autocorrelation function. In our understanding, this reflects the fact that the density-scaling exponent γ changes with density along an isomorph, resulting in a changing effective inverse-power-law interaction. The lowest densities have the largest

Isotropic phase
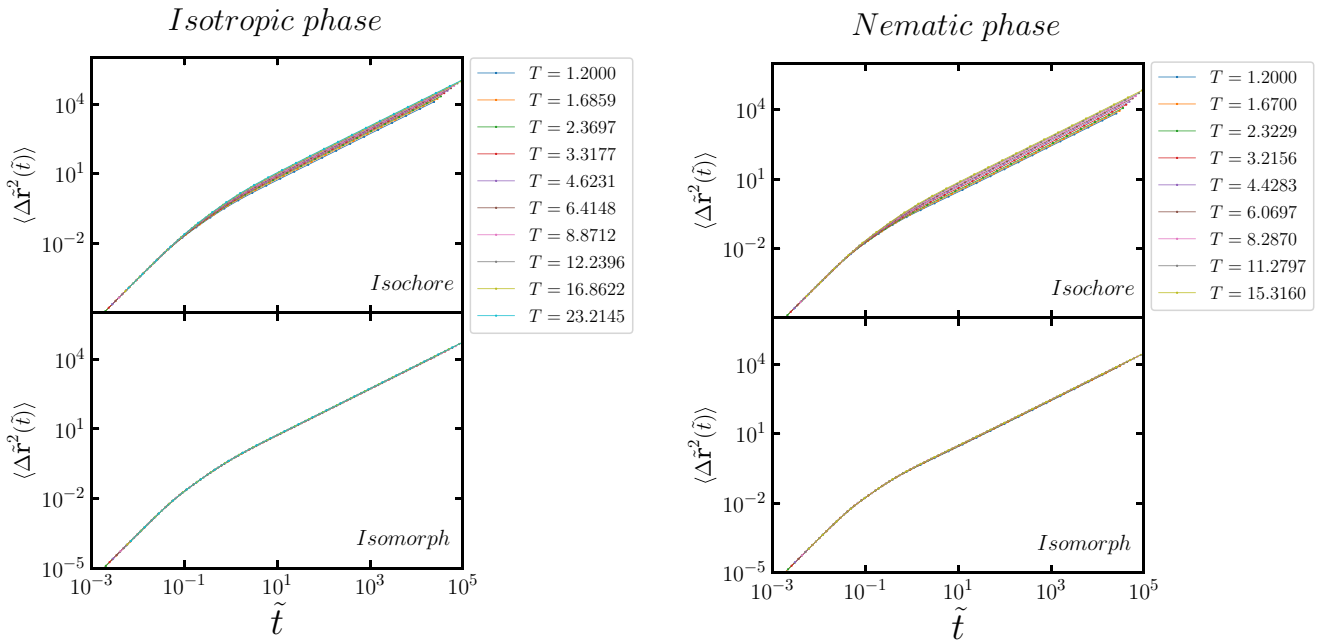
Nematic phase

FIG. 4. Reduced mean-square displacement as a function of the reduced time $\tilde{t}$ along an isochore and an isomorph in the isotropic phase (left) and likewise in the nematic phase (right). In both cases, the data collapse to a good approximation along the isomorph but not along the isochore.

γ (see the Appendix), leading to the highest average force squared coming from collisions. The collapse of the isochore angular velocity time-autocorrelation functions at short times is a consequence of the definition of reduced units, as is the short-time reduced-unit MSD collapse.
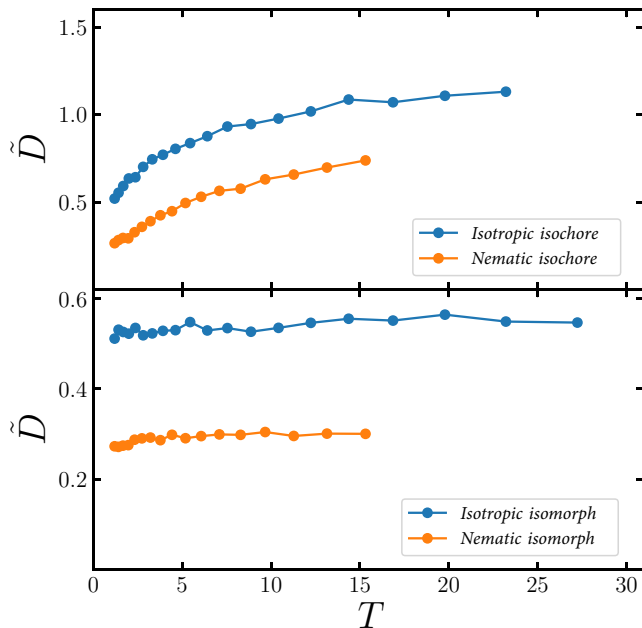
FIG. 5. Reduced diffusion coefficient as a function of temperature along the isochores (upper panel) and the isomorphs (lower panel). Approximate invariance in the latter case is clearly visible.

Figure 7 shows data for the first- and second-order orientational time-autocorrelation function, again plotted as functions of the reduced time. In the isotropic phase, these functions go to zero at long times, confirming that there are no preferred orientations. This is not the case, of course, in the nematic phase. In both phases, we observe good isomorph invariance. According to the phase diagram (Fig. 3), the isochore defined from the nematic isomorph reference state point enters the isotropic phase at high temperatures; this is reflected in the figures by the fact that both time-autocorrelation functions go to zero at long times as the temperature increases.

So far we have discussed different dynamic signals and seen good isomorph invariance. The isomorph theory, however, also predicts that the reduced-unit structure should be invariant. This is tested in Fig. 8, in which the upper panels show the center-of-mass radial distribution function along the isochores and isomorphs. The data are close to invariant along the isomorph, though with visible deviations around the first peak. This is often observed when isomorph theory is tested over a large density range; it reflects a noninvariance arising when the density-scaling exponent γ varies along the isomorph (similar to the noninvariance of the short-time force time-autocorrelation function discussed above). A large γ implies a large effective inverse-power-law exponent, which decreases the probability of near contacts and is "compensated" by a higher peak in order to arrive at the same coordination number (defined by integration of the radial distribution function over its first peak). This phenomenon was recently rationalized in terms of isomorph invariance of the so-called bridge function of liquid-state theory [97]. Confirming this interpretation, the highest first peaks along the isomorphs correspond to the lowest densities where γ is largest (see the Appendix).
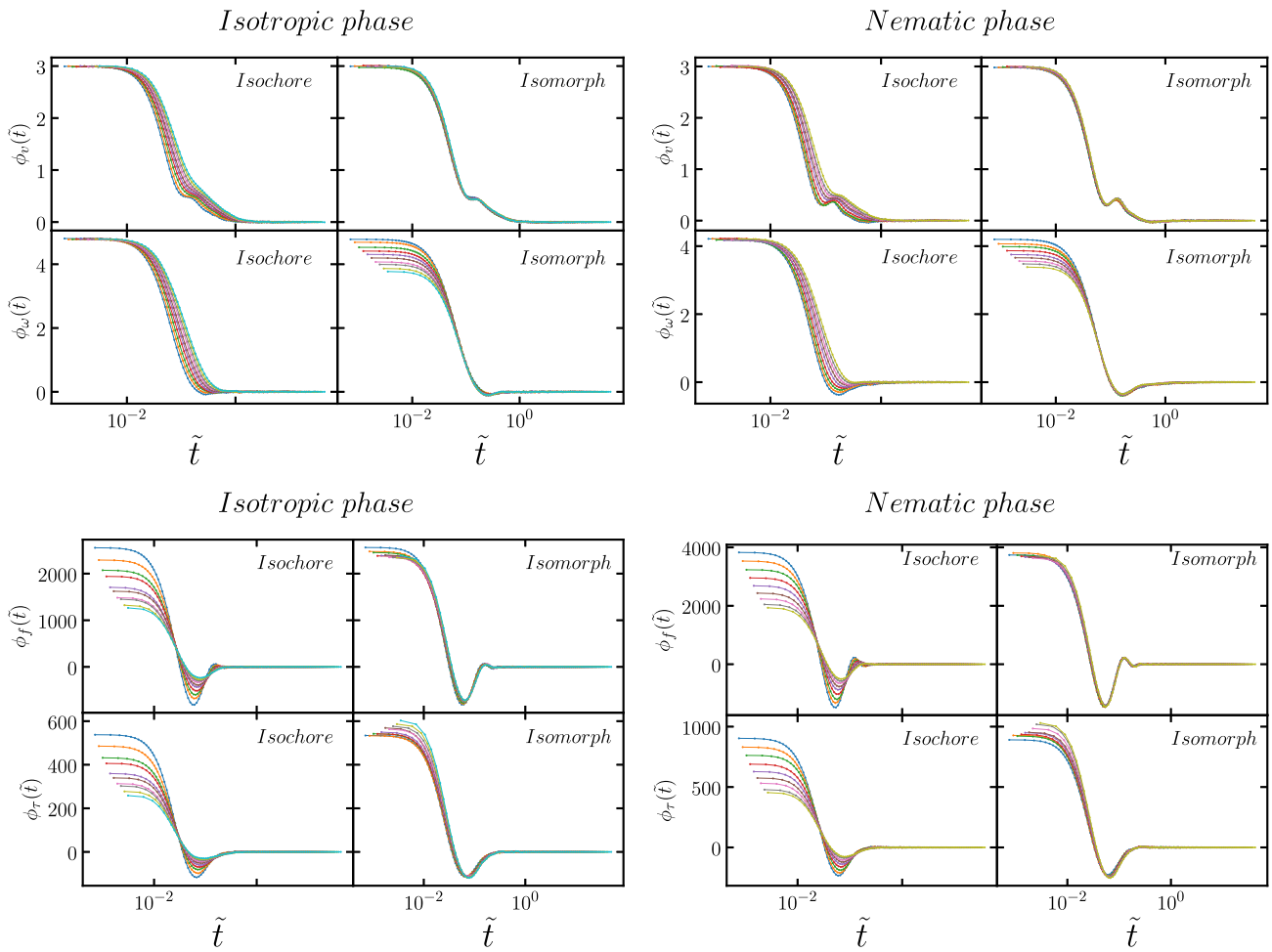
FIG. 6. The upper figures show the reduced-unit time-autocorrelation functions of the velocity v and the angular velocity ω along the isochore and the isomorph in the isotropic (left) and the nematic phases (right). The lower figures show the analogous results for the reduced-unit time-autocorrelation functions of the force f and the torque τ. The color codes are the same as in Fig. 4. Good isomorph invariance is generally observed except for significant short-time deviations for the two rotational autocorrelation functions (see the text).
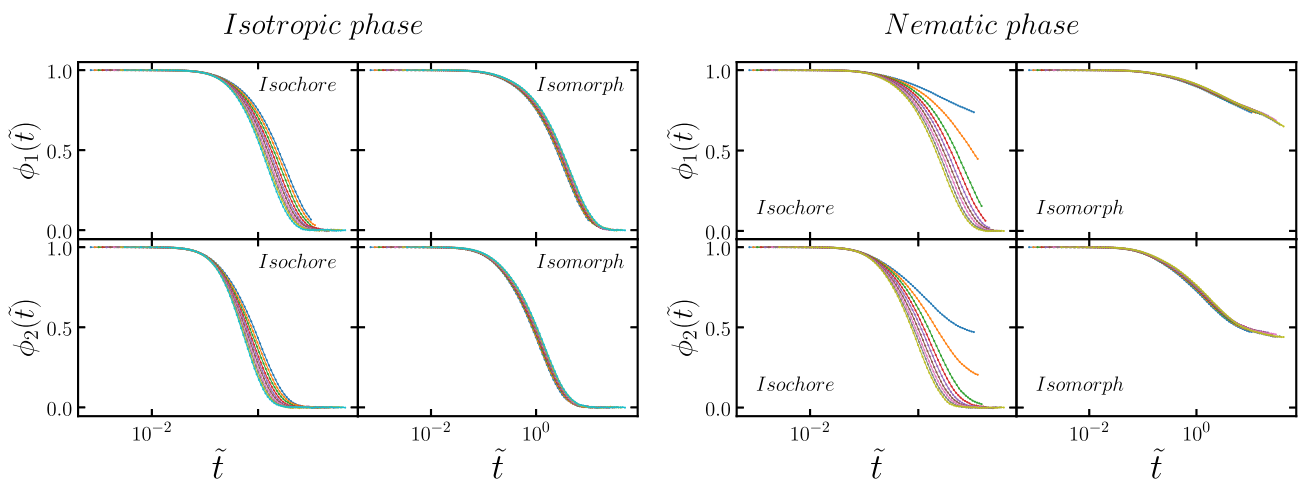
FIG. 7. The left figures show the first- and second-order orientational order parameter time-autocorrelation function in the isotropic phase; the right figures show the same in the nematic phase. Good isomorph invariance is observed in both phases.
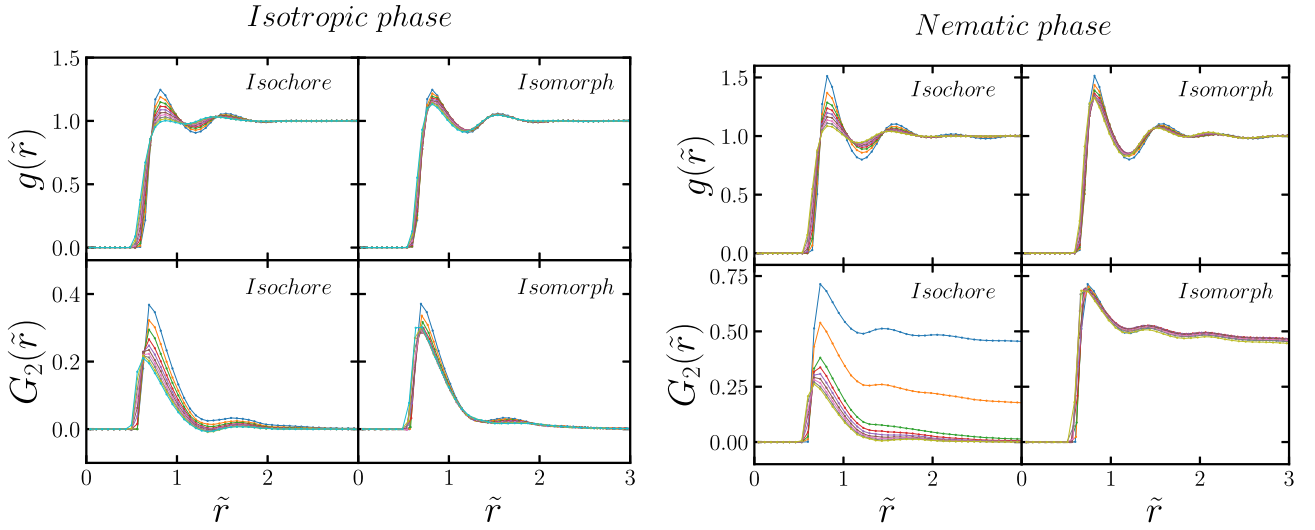
FIG. 8. Reduced-unit radial distribution functions (upper figures) and radial-distribution orientational correlation function [Eq. (16), lower figures] along the isochore and the isomorph in the isotropic (left) and nematic phases (right). Good isomorph invariance is observed in both phases, with some deviation at the first peak (see the text).

Data for the orientational structure quantified in terms of $G_2(r)$ are given in the lower panels of Fig. 8. In the nematic phase, this function does not converge to zero at long times as in the isotropic phase. Nevertheless, except for the first peak in the isotropic phase, there is good isomorph invariance of the structure. Note that the tail of $G_2(r)$ goes to zero as the temperature is increased along the isochore in the nematic phase. This reflects a phase transition into the isotropic phase. In contrast, the tail is invariant as we increase the temperature along the isomorph.

VI. CONCLUSIONS

When given in reduced units, the dynamic and structural properties of the GB(3, 5, 2, 1) model are invariant to a good approximation along isomorphs in both the isotropic and the nematic phases, with some deviations at short times for orientational time-autocorrelation functions reflecting that the moment of inertia was assumed to be constant and thus not isomorph-invariant in reduced units. In contrast, structure and dynamics are not invariant along isochores with the same temperature variation. Overall, our findings confirm isomorph-theory predictions and are consistent with the fact that the calamitic GB(3, 5, 2, 1) model obeys hidden scale invariance at relevant temperatures in both phases, i.e., has a virial potential-energy correlation coefficient above 0.9. For future work, it would be interesting to investigate the smectic B phase of the model for which, based on Fig. 3, we expect good isomorphs even at temperatures lower than unity.

ACKNOWLEDGMENT

APPENDIX: ISOMORPH STATE POINTS

This Appendix provides details of the two isomorphs studied (Tables I and II), giving for each of these at several state points: density, temperature, virial potential-energy correlation coefficient R [Eq. (4)], and density-scaling exponent γ [Eq. (10)].

TABLE I. Variation of density, temperature, correlation coefficient R, and density-scaling exponent γ for the state points on the isotropic-phase isomorph generated from the reference state point $(\rho_{\text{ref}}, T_{\text{ref}}) = (0.27, 1.2)$.

ρ	T	R	γ
0.2700	1.2000	0.9077	8.4553
0.2727	1.3057	0.9158	8.5107
0.2754	1.4215	0.9231	8.5535
0.2782	1.5480	0.9285	8.5737
0.2810	1.6859	0.9330	8.5795
0.2838	1.8361	0.9367	8.5756
0.2866	1.9995	0.9396	8.5615
0.2895	2.1770	0.9416	8.5383
0.2924	2.3697	0.9433	8.5126
0.2953	2.5788	0.9445	8.4820
0.2982	2.8056	0.9457	8.4555
0.3012	3.0514	0.9461	8.4252
0.3042	3.3177	0.9467	8.3962
0.3073	3.6062	0.9469	8.3646
0.3104	3.9186	0.9468	8.3364
0.3135	4.2570	0.9469	8.3084
0.3166	4.6231	0.9465	8.2815
0.3198	5.0194	0.9463	8.2542
0.3230	5.4483	0.9460	8.2276
0.3262	5.9125	0.9456	8.2032
0.3295	6.4148	0.9450	8.1802
0.3327	6.9583	0.9446	8.1647

TABLE I. (*Continued.*)

ρ	T	R	γ
0.3361	7.5463	0.9442	8.1479
0.3394	8.1827	0.9436	8.1289
0.3428	8.8712	0.9428	8.1121
0.3463	9.6164	0.9423	8.0987
0.3497	10.4226	0.9416	8.0867
0.3532	11.2953	0.9410	8.0735
0.3567	12.2396	0.9403	8.0628
0.3603	13.2616	0.9396	8.0562
0.3639	14.3680	0.9390	8.0462
0.3676	15.5657	0.9383	8.0443
0.3712	16.8622	0.9376	8.0396
0.3749	18.2660	0.9370	8.0345
0.3787	19.7859	0.9362	8.0315
0.3825	21.4318	0.9356	8.0285
0.3863	23.2145	0.9350	8.0295
0.3902	25.1457	0.9342	8.0295
0.3941	27.2379	0.9335	8.0343

TABLE II. Variation of density, temperature, correlation coefficient R, and density-scaling exponent γ for the state points on the nematic-phase isomorph generated from the reference state point $(\rho_{\mathrm{ref}}, T_{\mathrm{ref}}) = (0.33, 1.2)$.

ρ	T	R	γ
0.3300	1.2000	0.9169	8.2217
0.3333	1.3027	0.9230	8.2809
0.3366	1.4149	0.9274	8.3187
0.3400	1.5371	0.9315	8.3349
0.3434	1.6700	0.9342	8.3301
0.3468	1.8142	0.9359	8.3183
0.3503	1.9705	0.9375	8.2957
0.3538	2.1398	0.9385	8.2664
0.3573	2.3229	0.9389	8.2333
0.3609	2.5209	0.9393	8.2066
0.3645	2.7349	0.9394	8.1697
0.3682	2.9660	0.9392	8.1395
0.3719	3.2156	0.9393	8.1057
0.3756	3.4851	0.9387	8.0731
0.3793	3.7759	0.9384	8.0433
0.3831	4.0898	0.9375	8.0058
0.3870	4.4283	0.9367	7.9788
0.3908	4.7934	0.9362	7.9487
0.3947	5.1873	0.9354	7.9212
0.3987	5.6119	0.9345	7.8922
0.4027	6.0697	0.9337	7.8677
0.4067	6.5632	0.9321	7.8438
0.4108	7.0953	0.9315	7.8229
0.4149	7.6689	0.9306	7.7996
0.4190	8.2870	0.9296	7.7791
0.4232	8.9533	0.9286	7.7620
0.4274	9.6715	0.9277	7.7464
0.4317	10.4455	0.9264	7.7286
0.4360	11.2797	0.9258	7.7155
0.4404	12.1786	0.9244	7.6942
0.4448	13.1473	0.9232	7.6844
0.4492	14.1912	0.9223	7.6712
0.4537	15.3160	0.9209	7.6535
0.4583	16.5277	0.9197	7.6442

[1] M. Jurásek and R. Vácha, Self-assembled clusters of patchy rod-like molecules, Soft Matter **13**, 7492 (2017).

[2] S. J. Woltman, G. P. Crawford, and G. D. Jay, *Liquid Crystals: Frontiers in Biomedical Applications* (World Scientific, Singapore, 2007)

[3] A. de la Cotte, C. Wu, M. Trevisan, A. Repula, and E. Grelet, Rod-like virus-based multiarm colloidal molecules, ACS Nano **11**, 10616 (2017).

[4] Y. Tian and Z. Niu, Self-assembly of rod-like bionanoparticles at interfaces and in solution, in *Virus-Derived Nanoparticles for Advanced Technologies* (Springer, Berlin, 2018).

[5] D. Antypov and D. J. Cleaver, The role of attractive interactions in rod–sphere mixtures, J. Chem. Phys. **120**, 10307 (2004).

[6] M. Cifelli, G. Cinacchi, and L. De Gaetani, Smectic order parameters from diffusion data, J. Chem. Phys. **125**, 164912 (2006).

[7] R. Berardi, A. Costantini, L. Muccioli, S. Orlandi, and C. Zannoni, A computer simulation study of the formation of liquid crystal nanodroplets from a homogeneous solution, J. Chem. Phys. **126**, 044905 (2007).

[8] R. Vadnais, M.-A. Beaudoin, and A. Soldera, Study of the influence of ester orientation on the thermal stability of the smectic c phase: Simulation investigation, J. Chem. Phys. **129**, 164908 (2008).

[9] J. Méndez-Bermúdez and I. Santamaría-Holek, Relaxation in homogeneous and non-homogeneous polarized systems. A mesoscopic entropy approach, Physica A **389**, 1819 (2010).

[10] M. Doi, S. F. Edwards, and S. F. Edwards, *The Theory of Polymer Dynamics* (Oxford University Press, Oxford, 1988).

[11] Y. P. Kalmykov, Rotational Brownian motion and nonlinear dielectric relaxation of asymmetric top molecules in strong electric fields, Phys. Rev. E **65**, 021101 (2001).

[12] M. Hernández-Contreras and M. Medina-Noyola, Rotational diffusion of nonspherical Brownian particles in a suspension of spheres, Phys. Rev. E **54**, 6586 (1996).

[13] S. Szabolcs, G. Jackson, and I. Szalai, External field induced paranematic–nematic phase transitions in rod-like systems, Mol. Phys. **93**, 377 (1998).

[14] E. M. del Rio, M. T. Da Gama, E. De Miguel, and L. Rull, Wetting and interfacial order at nematic free surfaces, Europhys. Lett. **35**, 189 (1996).

[15] E. M. del Rio, M. M. Telo da Gama, E. De Miguel, and L. F. Rull, Surface-induced alignment at model nematic interfaces, Phys. Rev. E **52**, 5028 (1995).

[16] M. P. Allen, J. T. Brown, and M. A. Warren, Computer simulation of liquid crystals, J. Phys.: Condens. Matter **8**, 9433 (1996).

[17] M. P. Allen, Simulations and phase behaviour of liquid crystals, in *Observation, Prediction and Simulation of Phase Transitions in Complex Fluids* (Springer, Berlin, 1995).

[18] M. P. Allen, G. T. Evans, D. Frenkel, and B. M. Mulder, Hard convex body fluids, Adv. Chem. Phys. **86**, 1 (1993).

[19] J. Hansen and I. McDonald, *Theory of Simple Liquids* (Academic, New York, 1986).

[20] J. C. Dyre, Simple liquids' quasiuniversality and the hard-sphere paradigm, J. Phys.: Condens. Matter **28**, 323001 (2016).

[21] R. Eppenga and D. Frenkel, Monte carlo study of the isotropic and nematic phases of infinitely thin hard platelets, Mol. Phys. **52**, 1303 (1984).

[22] M. P. Allen and D. Frenkel, Observation of Dynamical Precursors of the Isotropic-Nematic Transition by Computer Simulation, Phys. Rev. Lett. **58**, 1748 (1987).

[23] D. Frenkel, Computer simulation of hard-core models for liquid crystals, Mol. Phys. **60**, 1 (1987).

[24] T. Kihara, Convex molecules in gaseous and crystalline states, Adv. Chem. Phys. **5**, 147 (1963).

[25] W. Streen and K. Gubbins, Liquids of linear molecules: Computer simulations and theory, Annu. Rev. Phys. Chem. **28**, 373 (1977).

[26] B. J. Berne and P. Pechukas, Gaussian model potentials for molecular interactions, J. Chem. Phys. **56**, 4213 (1972).

[27] J. Gay and B. Berne, Modification of the overlap potential to mimic a linear site–site potential, J. Chem. Phys. **74**, 3316 (1981).

[28] E. Egberts and H. Berendsen, Molecular dynamics simulation of a smectic liquid crystal with atomic detail, J. Chem. Phys. **89**, 3718 (1988).

[29] A. Komolkin, Y. V. Molchanov, and P. Yakutseni, Computer simulation of a real liquid crystal, Liq. Cryst. **6**, 39 (1989).

[30] M. R. Wilson and M. P. Allen, Computer simulations of mesogenic molecules using realistic atom-atom potentials, Mol. Cryst. Liq. Cryst. **198**, 465 (1991).

[31] M. Wilson and M. Allen, Structure of trans-4-(trans-4-n-pentylcyclohexyl) cyclohexylcarbonitrile (cch5) in the isotropic and nematic phases: a computer simulation study, Liq. Cryst. **12**, 157 (1992).

[32] G. V. Paolini, G. Ciccotti, and M. Ferrario, Simulation of site-site soft-core liquid crystal models, Mol. Phys. **80**, 297 (1993).

[33] S. S. Patnaik, S. J. Plimpton, R. Pachter, and W. W. Adams, Modelling a nematic liquid crystal, Liq. Cryst. **19**, 213 (1995).

[34] D. Adams, G. Luckhurst, and R. Phippen, Computer simulation studies of anisotropic systems: XVII. The Gay-Berne model nematogen, Mol. Phys. **61**, 1575 (1987).

[35] G. Luckhurst, R. Stephens, and R. Phippen, Computer simulation studies of anisotropic systems. XIX. mesophases formed by the Gay-Berne model mesogen, Liq. Cryst. **8**, 451 (1990).

[36] E. de Miguel, L. F. Rull, M. K. Chalam, K. E. Gubbins, and F. Van Swol, Location of the isotropic-nematic transition in the Gay-Berne model, Mol. Phys. **72**, 593 (1991).

[37] J. Alejandre, J. Emsley, D. Tildesley, and P. Carlson, Molecular dynamics simulations of a flexible molecule in a liquid crystalline solvent, J. Chem. Phys. **101**, 7027 (1994).

[38] M. K. Chalam, K. E. Gubbins, E. D. Miguel, and L. F. Rull, A molecular simulation of a liquid-crystal model: bulk and confined fluid, Mol. Simul. **7**, 357 (1991).

[39] R. Berardi *et al.*, Monte Carlo investigations of a Gay-Berne liquid crystal, J. Chem. Soc., Faraday Trans. **89**, 4069 (1993).

[40] R. Hashim, G. Luckhurst, and S. Romano, Computer-simulation studies of anisotropic systems. XXIV. Constant-pressure investigations of the smectic b phase of the Gay-Berne mesogen, J. Chem. Soc., Faraday Trans. **91**, 2141 (1995).

[41] E. de Miguel, L. F. Rull, and K. E. Gubbins, Dynamics of the Gay-Berne fluid, Phys. Rev. A **45**, 3813 (1992).

[42] E. M. del Río, E. de Miguel, and L. F. Rull, Computer simulation of the liquid-vapour interface in liquid crystals, Physica A **213**, 138 (1995).

[43] J. Stelzer, L. Longa, and H.-R. Trebin, Molecular dynamics simulations of a Gay-Berne nematic liquid crystal: elastic properties from direct correlation functions, J. Chem. Phys. **103**, 3098 (1995).

[44] S. Sarman, Molecular dynamics of heat flow in nematic liquid crystals, J. Chem. Phys. **101**, 480 (1994).

[45] S. Sarman and D. J. Evans, Self-diffusion and heat flow in isotropic and liquid crystal phases of the Gay-Berne fluid, J. Chem. Phys. **99**, 620 (1993).

[46] S. Sarman and D. J. Evans, Statistical mechanics of viscous flow in nematic fluids, J. Chem. Phys. **99**, 9021 (1993).

[47] A. M. Smondyrev, G. B. Loriot, and R. A. Pelcovits, Viscosities of the Gay-Berne Nematic Liquid Crystal, Phys. Rev. Lett. **75**, 2340 (1995).

[48] S. Gupta, Computer simulation and perturbation theory of fluids modelled using three-and six-site Lennard-Jones potentials, Mol. Phys. **68**, 699 (1989).

[49] E. Velasco, A. Somoza, and L. Mederos, Liquid-crystal phase diagram of the Gay-Berne fluid by perturbation theory, J. Chem. Phys. **102**, 8107 (1995).

[50] E. De Miguel, L. F. Rull, M. K. Chalam, and K. E. Gubbins, Liquid crystal phase diagram of the Gay-Berne fluid, Mol. Phys. **74**, 405 (1991).

[51] M. P. Allen, M. A. Warren, M. R. Wilson, A. Sauron, and W. Smith, Molecular dynamics calculation of elastic constants in Gay-Berne nematic liquid crystals, J. Chem. Phys. **105**, 2850 (1996).

[52] L. F. Rull and J. M. Romero-Enrique, Computer simulation study of the nematic–vapour interface in the Gay-Berne model, Mol. Phys. **115**, 1214 (2017).

[53] S. Sarman, Y.-L. Wang, and A. Laaksonen, Non-Newtonian rheological properties of shearing nematic liquid crystal model

systems based on the Gay-Berne potential, Phys. Chem. Chem. Phys. **17**, 16615 (2015).

[54] S. Sarman, Y.-L. Wang, and A. Laaksonen, Self-diffusion in the non-Newtonian regime of shearing liquid crystal model systems based on the Gay-Berne potential, J. Chem. Phys. **144**, 054901 (2016).

[55] S. Mehri, M. A. Kolmangadi, J. C. Dyre, and T. S. Ingebrigtsen, Lines of invariant physics in the isotropic phase of the discotic Gay-Berne model, J. Non-Cryst. Solids: X **14**, 100085 (2022).

[56] K. Liszka, A. Grzybowski, K. Koperwas, and M. Paluch, Density scaling of translational and rotational molecular dynamics in a simple ellipsoidal model near the glass transition, Int. J. Mol. Sci. **23**, 4546 (2022).

[57] K. Satoh, S. Mita, and S. Kondo, Monte carlo simulations on mesophase formation using dipolar Gay-Berne model, Liq. Cryst. **20**, 757 (1996).

[58] G. La Penna, D. Catalano, and C. A. Veracini, A rigid core-flexible chain model for mesogenic molecules in molecular dynamics simulations of liquid crystals, J. Chem. Phys. **105**, 7097 (1996).

[59] B. M. Neal, A. Parker, and C. Care, A molecular dynamics study of a steric multipole model of liquid crystal molecular geometry, Mol. Phys. **91**, 603 (1997).

[60] D. J. Cleaver, C. M. Care, M. P. Allen, and M. P. Neal, Extension and generalization of the Gay-Berne potential, Phys. Rev. E **54**, 559 (1996).

[61] N. Mori, H. Fujioka, R. Semura, and K. Nakamura, Brownian dynamics simulations for suspension of ellipsoids in liquid crystalline phase under simple shear flows, Rheol. Acta **42**, 102 (2003).

[62] G. Germano, M. P. Allen, and A. J. Masters, Simultaneous calculation of the helical pitch and the twist elastic constant in chiral liquid crystals from intermolecular torques, J. Chem. Phys. **116**, 9422 (2002).

[63] M. A. Bates and G. R. Luckhurst, Studies of translational diffusion in the smectic a phase of a Gay-Berne mesogen using molecular dynamics computer simulation, J. Chem. Phys. **120**, 394 (2004).

[64] E. d. Miguel Agustino, E. F. Martin del Rio, F. Jimenez Blas *et al.*, Stability of smectic phases in the Gay-Berne model, J. Chem. Phys. **121**, 11183 (2004).

[65] K. Satoh, Characteristic behavior of short-term dynamics in reorientation for Gay-Berne particles near the nematic-isotropic phase transition temperature, J. Chem. Phys. **125**, 204902 (2006).

[66] K. Satoh, Molecular dynamics simulation of the nematic liquid crystal phase in the presence of an intense magnetic field, J. Chem. Phys. **124**, 144901 (2006).

[67] A. J. McDonald, M. P. Allen, and F. Schmid, Surface tension of the isotropic-nematic interface, Phys. Rev. E **63**, 010701(R) (2000).

[68] C.-C. Huang, S. Ramachandran, and J.-P. Ryckaert, Calculation of the absolute free energy of a smectic-a phase, Phys. Rev. E **90**, 062506 (2014).

[69] E. de Miguel, L. F. Rull, and K. E. Gubbins, Effect of molecular elongation on liquid-vapour properties: computer simulation and virial approximation, Physica A **177**, 174 (1991).

[70] E. de Miguel, E. Martín del Rio, J. T. Brown, and M. P. Allen, Effect of the attractive interactions on the phase behavior of the Gay-Berne liquid crystal model, J. Chem. Phys. **105**, 4234 (1996).

[71] J. He, Z. Niu, R. Tangirala, J.-Y. Wang, X. Wei, G. Kaur, Q. Wang, G. Jutz, A. Böker, B. Lee *et al.*, Self-assembly of tobacco mosaic virus at oil/water interfaces, Langmuir **25**, 4979 (2009).

[72] N. Akino, F. Schmid, and M. P. Allen, Molecular-dynamics study of the nematic-isotropic interface, Phys. Rev. E **63**, 041706 (2001).

[73] D. Caprion, L. Bellier-Castella, and J.-P. Ryckaert, Influence of shape and energy anisotropies on the phase diagram of discotic molecules, Phys. Rev. E **67**, 041703 (2003).

[74] T. Yamamoto, T. Suga, and N. Mori, Brownian dynamics simulation of orientational behavior, flow-induced structure, and rheological properties of a suspension of oblate spheroid particles under simple shear, Phys. Rev. E **72**, 021509 (2005).

[75] O. Cienega-Cacerez, J. A. Moreno-Razo, E. Díaz-Herrera, and E. J. Sambriski, Phase equilibria, fluid structure, and diffusivity of a discotic liquid crystal, Soft Matter **10**, 3171 (2014).

[76] R. J. Bushby and K. Kawata, Liquid crystals that affected the world: discotic liquid crystals, Liq. Cryst. **38**, 1415 (2011).

[77] N. P. Bailey, L. Bøhling, A. A. Veldhorst, T. B. Schrøder, and J. C. Dyre, Statistical mechanics of Roskilde liquids: Configurational adiabats, specific heat contours, and density dependence of the scaling exponent, J. Chem. Phys. **139**, 184506 (2013).

[78] T. S. Ingebrigtsen, T. B. Schrøder, and J. C. Dyre, What Is a Simple Liquid? Phys. Rev. X **2**, 011011 (2012).

[79] T. S. Ingebrigtsen, T. B. Schrøder, and J. C. Dyre, Isomorphs in model molecular liquids, J. Phys. Chem. B **116**, 1018 (2012).

[80] J. C. Dyre, Hidden scale invariance in condensed matter, J. Phys. Chem. B **118**, 10007 (2014).

[81] J. C. Dyre, Perspective: Excess-entropy scaling, J. Chem. Phys. **149**, 210901 (2018).

[82] N. P. Bailey, U. R. Pedersen, N. Gnan, T. B. Schrøder, and J. C. Dyre, Pressure-energy correlations in liquids. I. results from computer simulations, J. Chem. Phys. **129**, 184507 (2008).

[83] N. Gnan, T. B. Schrøder, U. R. Pedersen, N. P. Bailey, and J. C. Dyre, Pressure-energy correlations in liquids. IV. "Isomorphs" in liquid phase diagrams, J. Chem. Phys. **131**, 234504 (2009).

[84] A. A. Veldhorst, J. C. Dyre, and T. B. Schrøder, Scaling of the dynamics of flexible Lennard-Jones chains, J. Chem. Phys. **141**, 054904 (2014).

[85] L. Costigliola, T. B. Schrøder, and J. C. Dyre, Freezing and melting line invariants of the Lennard-Jones system, Phys. Chem. Chem. Phys. **18**, 14678 (2016).

[86] I. H. Bell, R. Messerly, M. Thol, L. Costigliola, and J. C. Dyre, Modified entropy scaling of the transport properties of the Lennard-Jones fluid, J. Phys. Chem. B **123**, 6345 (2019).

[87] T. B. Schrøder and J. C. Dyre, Simplicity of condensed matter at its core: Generic definition of a Roskilde-simple system, J. Chem. Phys. **141**, 204502 (2014).

[88] E. Attia, J. C. Dyre, and U. R. Pedersen, Extreme case of density scaling: The Weeks-Chandler-Andersen system at low temperatures, Phys. Rev. E **103**, 062140 (2021).

[89] D. Fincham, More on rotational motion of linear molecules, CCP5 Quarterly **12**, 47 (1984).

[90] M. Bates and G. Luckhurst, Computer simulation studies of anisotropic systems. xxx. the phase behavior and structure of a Gay-Berne mesogen, J. Chem. Phys. **110**, 7087 (1999).

[91] J. G. Méndez-Bermúdez, I. Guillén-Escamilla, J. C. Mixteco-Sánchez, G. A. Méndez-Maldonado, and M. González-Melchor, Equation of state, structure and diffusion coefficients of Gay-Berne fluids: the cases $\kappa' = 5$; 10; 15; 20, arXiv:1911.07366.

[92] P. P. Jose and B. Bagchi, Multiple short time power laws in the orientational relaxation of nematic liquid crystals, J. Chem. Phys. **125**, 184901 (2006).

[93] M. P. Allen and D. J. Tildesley, *Computer Simulation of Liquids* (Oxford University Press, Oxford, 2017).

[94] E. de Miguel and C. Vega, The global phase diagram of the Gay-Berne model, J. Chem. Phys. **117**, 6313 (2002).

[95] S. Mehri, Computer simulations of the Gay-Berne liquid crystal model and of physical aging, Ph.D. thesis, Roskilde University (2022).

[96] U. R. Pedersen, L. Costigliola, N. P. Bailey, T. B. Schrøder, and J. C. Dyre, Thermodynamics of freezing and melting, Nat. Commun. **7**, 12386 (2016).

[97] F. L. Castello, P. Tolias, and J. C. Dyre, Testing the isomorph invariance of the bridge functions of Yukawa one-component plasmas, J. Chem. Phys. **154**, 034501 (2021).

Article
Single-Parameter Aging in the Weakly Nonlinear Limit

Saeed Mehri, Lorenzo Costigliola and Jeppe C. Dyre *

Glass and Time, IMFUFA, Department of Science and Environment, Roskilde University, P.O. Box 260, DK-4000 Roskilde, Denmark; mehri@ruc.dk (S.M.); lorenzoc@ruc.dk (L.C.)
* Correspondence: dyre@ruc.dk

Abstract: Physical aging deals with slow property changes over time caused by molecular rearrangements. This is relevant for non-crystalline materials such as polymers and inorganic glasses, both in production and during subsequent use. The Narayanaswamy theory from 1971 describes physical aging—an inherently nonlinear phenomenon—in terms of a linear convolution integral over the so-called material time ξ. The resulting "Tool–Narayanaswamy (TN) formalism" is generally recognized to provide an excellent description of physical aging for small, but still highly nonlinear, temperature variations. The simplest version of the TN formalism is single-parameter aging according to which the clock rate $d\xi/dt$ is an exponential function of the property monitored. For temperature jumps starting from thermal equilibrium, this leads to a first-order differential equation for property monitored, involving a system-specific function. The present paper shows analytically that the solution to this equation to first order in the temperature variation has a universal expression in terms of the zeroth-order solution, $R_0(t)$. Numerical data for a binary Lennard–Jones glass former probing the potential energy confirm that, in the weakly nonlinear limit, the theory predicts aging correctly from $R_0(t)$ (which by the fluctuation–dissipation theorem is the normalized equilibrium potential-energy time-autocorrelation function).

Keywords: physical aging; binary Lennard-Jones glass former; first-order perturbation theory

1. Introduction

The properties of non-crystalline materials, such as polymers and inorganic glasses, change slightly over time. In many cases, the aging is so slow that it cannot be observed, but sometimes it results in unwanted degradation of material properties. When aging is exclusively due to molecular rearrangements, with no chemical reactions involved, one speaks about physical aging [1–14]. The present-day understanding of physical aging is based on the century-old observation [15] that any glass is in an out-of-equilibrium state and, as a consequence, relaxes continuously toward the equilibrium state.

During physical aging, the system's volume decreases slightly. This reflects the fact that the equilibrium metastable liquid is denser than the glass at the same temperature. Likewise, the enthalpy decreases during aging. Both effects are extremely difficult to observe because they are minute and take place over a very long time. Defining a glass as any non-equilibrium state of a liquid resulting from a thermodynamic perturbation, a good way of studying physical aging is the following: First, equilibrate the glass-forming liquid at some "annealing" temperature just below the calorimetric glass-transition temperature. Depending on the viscosity of the liquid, this may take long time—experiments often study liquids at temperatures for which the equilibrium relaxation time is hours or days [16–21]; if the equilibrium relaxation time is one day, annealing the sample for a week ensures virtually complete thermal equilibrium. Once the sample has been equilibrated, the temperature is changed rapidly to a new value and kept there for a time long enough to allow for monitoring virtually the entire equilibration process. This defines an "ideal aging experiment" [17,22]. Such an experiment requires the ability to monitor some quantity accurately and continuously as a function of time, excellent temperature control,

and the ability to change temperature rapidly [17]. Aging may be probed by measuring any property that can be monitored precisely, e.g., the electrical capacitance at a particular frequency [21,23–26]; in conjunction with a Peltier-element-based fast and accurate temperature control, this is our favorite method in Roskilde [21]. Other quantities that have been monitored during physical aging include, e.g., density [27,28], enthalpy [29,30], Young's modulus [31], gas permeability [32], high-frequency mechanical moduli [16,33], dc conductivity [2], X-ray photon correlation spectroscopy [34], and nonlinear dielectric susceptibility [35].

The present paper develops the theory of aging by studying the so-called single-parameter aging framework, which is the simplest realization of the concept of a material time that controls aging in the Tool-–Narayanaswamy (TN) formalism [3]. An important prediction of the TN formalism is that if the aging rate is known as a function of the property monitored, knowledge of the linear limit of physical aging, e.g., following an infinitesimal temperature jump, is enough to quantitatively determine the aging that results from any time-dependent temperature variation. According to the fluctuation–dissipation (FD) theorem, any linear-response property is determined by thermal-equilibrium fluctuations quantified in terms of a time-autocorrelation function. The prospect for future experimental investigations is that one can make quantitative predictions about aging from the knowledge of equilibrium fluctuations.

Single-parameter aging results in a first-order differential equation for the normalized relaxation function following a temperature jump [18]. This equation involves an *a priori* unknown, system-specific function that determines the linear limit of aging. In order to predict aging, however, it is enough to know the linear-limit relaxation function that, by the FD theorem, is the relevant equilibrium time-autocorrelation function. This paper derives an explicit expression for the weakly nonlinear limit of aging based on the relevant equilibrium time-autocorrelation function. After developing the theory in Section 2, we provide an example of how to calculate a quantity similar to the fragility of glass science in Section 3; this section can be skipped in a first reading of the paper. The general first-order solution to single-parameter aging following a temperature jump is derived in Section 4. The validity of the formalism is illustrated in Section 5 by results from computer simulations of a binary Lennard–Jones system; the final section provides a brief discussion.

2. The TN Formalism and Single-Parameter Aging

The quantity probed during aging is denoted by $\chi(t)$. Following a temperature jump at $t = 0$, $\chi(t)$ gradually approaches its equilibrium value χ_{eq} at the new temperature T_0. We define the normalized relaxation function $R(t)$ by

$$R(t) \equiv \frac{\chi(t) - \chi_{eq}}{\chi(0) - \chi_{eq}}. \tag{1}$$

By definition, $R(t)$ is unity at $t = 0$ and approaches zero as $t \to \infty$. Thus for both temperature up and down jumps, $R(t)$ is a decreasing function of time. In practice, in experiments as well as simulations, there is always a rapid initial change of $\chi(t)$ immediately after $t = 0$ deriving from χ's dependence on the fast, vibrational degrees of freedom and/or one or more fast relaxation processes decoupled from the main and slowest (α) relaxation. For this reason, workers in the field often normalize the relaxation function by defining $R(t)$ to be unity after the initial rapid change of $\chi(t)$. That is different from what is done in Equation (1) and below, which is our preference because it avoids introducing the extra parameter that comes from estimating the value of the short-time "plateau" of $\chi(t)$.

The TN *material time* is denoted by ξ. This quantity, which may be thought of as the time measured on a clock with a clock rate $\gamma(t)$ that changes as the material ages, is related to the clock rate as follows

$$d\xi = \gamma(t)dt. \tag{2}$$

According to the TN formalism, the material time ξ controls the physical aging in such a way that the variation of χ, denoted by

$$\Delta\chi(t) \equiv \chi(t) - \chi_{\text{eq}}, \tag{3}$$

is a *linear* convolution integral over the temperature variation history $T(t) - T_0$ in which T_0 is the "reference" temperature [3,29].

Single-parameter aging (SPA) is the simplest version of the TN formalism [18]. SPA assumes that the clock rate $\gamma(t)$ is an exponential function of the monitored property, i.e.,

$$\gamma(t) = \gamma_{\text{eq}} \exp\left(\frac{\Delta\chi(t)}{\chi_0}\right). \tag{4}$$

Here, γ_{eq} is the equilibrium relaxation rate at T_0 and χ_0 is a constant with the same dimension as χ. In conjunction with the TN prediction that physical aging is linear in the temperature variation when formulated in terms of the material time, SPA may be applied to any relatively small (continuous or discontinuous) temperature variation around T_0, not just for the discontinuous temperature jumps to which the below discussion is limited. Since $\Delta\chi(t) = \Delta\chi(0)R(t)$ by the definition of $R(t)$, Equation (4) may be rewritten as

$$\gamma(t) = \gamma_{\text{eq}} \exp\left(\frac{\Delta\chi(0)}{\chi_0} R(t)\right). \tag{5}$$

For temperature jumps the TN fundamental result is that [3,29]

$$R(t) = \Phi(\xi) \tag{6}$$

in which the function $\Phi(\xi)$ is the same for all temperature jumps of a given system. In view of the nonlinearity of physical aging, this is a highly nontrivial prediction. Keeping in mind the definition of $\gamma(t)$ (Equation (2)), Equation (6) implies $\dot{R}(t) = \Phi'(\xi)\gamma(t)$. Since, according to Equation (6), ξ is the same function of R for all jumps, defining $F(R) \equiv -\Phi'(\xi(R))$ leads to the "jump differential equation"

$$\dot{R}(t) = -F(R)\gamma(t) = -\gamma_{\text{eq}} F(R) \exp\left(\frac{\Delta\chi(0)}{\chi_0} R(t)\right) \tag{7}$$

in which $F(R)$ is the same function for all jumps of a given system. The negative sign in the definition of $F(R)$ is introduced in order to make $F(R)$ positive.

Equation (7) has been confirmed in experiments on a silicone oil and several organic liquids [18,20,21] aged to equilibrium just below their calorimetric glass transition temperature. Even though the largest temperature jumps studied were just a few percent, this is enough to exhibit a strongly nonlinear response with more than one decade of relaxation-time variation. One experimental test of Equation (7) involved rewriting it as [18,20]

$$-\frac{\dot{R}(t)}{\gamma_{\text{eq}}} \exp\left(-\frac{\Delta\chi(0)}{\chi_0} R(t)\right) = F(R) \tag{8}$$

and showing that the left-hand side is the same function of R for different jumps. A second test confirmed the consequence of Equation (7) that the $R(t)$ for an arbitrary jump may be predicted from data of a single jump [18,20,21].

This paper develops the SPA formalism based on Equation (7) that, for simplicity, is rewritten by adopting the unit system in which $\gamma_{\text{eq}} = 1$ at the temperature T_0:

$$\dot{R} = -F(R)\, e^{\Lambda R} \tag{9}$$

with

$$\Lambda \equiv \frac{\Delta\chi(0)}{\chi_0}. \tag{10}$$

3. Calculation of a Generalized Fragility

Each value of Λ leads to a unique solution denoted by $R(t, \Lambda)$ of the jump differential equation, Equation (9), with the initial condition $R(0, \Lambda) = 1$. As a first illustration of how perturbation theory may be applied whenever $|\Lambda| \ll 1$, we determine the Λ dependence of the average relaxation time defined by

$$\tau(\Lambda) \equiv \int_0^\infty R(t, \Lambda) dt. \tag{11}$$

From $\tau(\Lambda)$, a fragility-like [36] parameter m_a (subscript "a" for aging) may be defined by

$$m_a \equiv -\frac{d}{d\Lambda} \ln \tau \bigg|_{\Lambda=0}. \tag{12}$$

The minus ensures that $m_a > 0$ because $\Lambda > 0$ from Equation (9) leads to a faster relaxation.

We proceed to derive the following expression in which $R_0(t) \equiv R(t, \Lambda = 0)$

$$m_a = \frac{\int_0^\infty R_0^2(t) dt}{\int_0^\infty R_0(t) dt}. \tag{13}$$

Note that whenever $0 < R_0(t) < 1$, which is usually the case [18], one has $m_a < 1$. Note also that, since $\gamma_{eq}(\Lambda) = \exp(\Lambda)$ from Equation (9), the equilibrium relaxation time $\tau_{eq}(\Lambda) \equiv 1/\gamma_{eq}(\Lambda)$ obeys $d \ln \tau_{eq} = -d\Lambda$. Using this, one can transform Equation (13) into an expression for how the relative change of $\tau(\Lambda)$ from its value at T_0 depends on the relative change of the equilibrium relaxation time between the two temperatures involved in the jump, i.e.,

$$\frac{d \ln \tau}{d \ln \tau_{eq}} \bigg|_{T=T_0} = \frac{\int_0^\infty R_0^2(t) dt}{\int_0^\infty R_0(t) dt} = m_a. \tag{14}$$

The fact that $m_a < 1$ is now intuitively obvious, since the graph of $R(t)$ obviously falls between the equilibrium relaxation function graphs at the two temperatures.

To derive Equation (13), note that Equation (9) implies $dt = -\exp(-\Lambda R) dR/F(R)$. Thus

$$\tau(\Lambda) = -\int_1^0 \frac{R e^{-\Lambda R}}{F(R)} dR = \int_0^1 \frac{R e^{-\Lambda R}}{F(R)} dR. \tag{15}$$

From this we get

$$\tau(\Lambda = 0) = \int_0^1 \frac{R}{F(R)} dR. \tag{16}$$

and

$$\frac{d\tau}{d\Lambda} \bigg|_{\Lambda=0} = -\int_0^1 \frac{R^2}{F(R)} dR. \tag{17}$$

By substituting $R = R_0$ into both integrals and switching back to time as the integration variable, one finds

$$m_a = \frac{\int_0^1 \frac{R_0^2}{F(R_0)} dR_0}{\int_0^1 \frac{R_0}{F(R_0)} dR_0} = \frac{\int_0^\infty R_0^2(t) dt}{\int_0^\infty R_0(t) dt}. \tag{18}$$

An alternative proof of Equation (13) makes use of an integral criterion derived in Ref. [18] (Appendix A).

For the calculation of m_a from experimental or computer simulation data on $R_0(t)$, one proceeds as follows. Given a sequence of times $(\Delta t, 2\Delta t, 3\Delta t, \ldots, n\Delta t)$ at which the equilibrium normalized relaxation function $(R_{0,1}, R_{0,2}, R_{0,3}, \ldots, R_{0,n})$ is known, we have

$$m_a = \frac{\sum_{j=1}^{n} R_{0,j}^2}{\sum_{j=1}^{n} R_{0,j}}. \tag{19}$$

As an example of the above, we consider the case in which the linear-limit relaxation function is a stretched exponential with exponent β (for simplicity, a dimensionless time is used below),

$$R_0(t) = e^{-t^\beta}. \tag{20}$$

Defining the function

$$f(\alpha, \beta) = \int_0^\infty e^{-\alpha t^\beta} dt, \tag{21}$$

we have $m_a = f(2, \beta)/f(1, \beta)$. Since

$$f(2, \beta) = \int_0^\infty e^{-2t^\beta} dt = 2^{-1/\beta} \int_0^\infty e^{-2t^\beta} d(2^{1/\beta} t) = 2^{-1/\beta} f(1, \beta), \tag{22}$$

we get

$$m_a = 2^{-1/\beta}. \tag{23}$$

If the normalized relaxation function in the experimental time window is described by a stretched exponential with the short-time plateau $C < 1$, i.e., by the function $C \exp(-t^\beta)$, one finds

$$m_a = C \, 2^{-1/\beta}. \tag{24}$$

4. Solving the Jump Differential Equation to First Order in the Temperature Change ΔT

To find the solution, $R(t, \Lambda)$, of the jump differential equation in first-order perturbation theory we proceed as follows. A first-order expansion of $R(t)$,

$$R(t) = R_0(t) + \Lambda R_1(t), \tag{25}$$

is substituted into Equation (9) where $R_0(t)$ is the normalized relaxation function corresponding to an infinitesimal jump, i.e., to the linear limit of aging (this function is discussed below in Section 5.1). To first order in Λ, one has $F(R) = F(R_0) + F'(R_0)\Lambda R_1$ and $\exp(\Lambda R) = 1 + \Lambda R = 1 + \Lambda R_0$. This results in

$$\dot{R}_0 + \Lambda \dot{R}_1 = -\big(F(R_0) + F'(R_0)\Lambda R_1\big)\big(1 + \Lambda R_0\big), \tag{26}$$

which leads to the following zeroth- and first-order equations:

$$\dot{R}_0 = -F(R_0) \tag{27}$$
$$\dot{R}_1 = -F(R_0)R_0 - F'(R_0)R_1. \tag{28}$$

Due to the zero-time normalization of both $R(t)$ and $R_0(t)$, the initial condition of R_1 is $R_1(0) = 0$. For $t > 0$, one has $R_1(t) < 0$ because $\Lambda > 0$, as mentioned, implies a faster relaxation toward equilibrium, i.e., $R(t) < R_0(t)$. Consequently, since $R_1(0) = R_1(t \to \infty) = 0$, the function $R_1(t)$ is non-monotonous.

The solution to Equation (28), obeying the initial condition $R_1(0) = 0$, is

$$R_1(t) = \dot{R}_0(t) \int_0^t R_0(t') dt'. \tag{29}$$

To derive this, we proceed as follows. First, note that the inverse of $R(t, \Lambda)$ is given by

$$t(R, \Lambda) = - \int_1^R e^{-\Lambda R'} \frac{dR'}{F(R')}, \tag{30}$$

which follows by rewriting Equation (9) as $dt = -\exp(-\Lambda R)\, dR/F(R)$ and integrating. Next, we note that because $R(t,0) = R_0(t)$, one has

$$R_1(t) = \left(\frac{\partial R}{\partial \Lambda}\right)_t = -\frac{\left(\frac{\partial t}{\partial \Lambda}\right)_R}{\left(\frac{\partial t}{\partial R}\right)_\Lambda} \tag{31}$$

in which it here and henceforth is understood that all functions are evaluated at $\Lambda = 0$, implying that one should put $R = R_0$ in the final evaluations. Since $dR_0/F(R_0) = -dt$, using Equation (30) the numerator is evaluated as follows

$$\left(\frac{\partial t}{\partial \Lambda}\right)_R = \int_1^R R' \frac{dR'}{F(R')} = -\int_0^t R_0\, dt'. \tag{32}$$

For $\Lambda = 0$, the denominator of Equation (31) is given by

$$\left(\frac{\partial t}{\partial R}\right)_\Lambda = \frac{1}{\dot{R}_0(t)}. \tag{33}$$

Combining these results, one arrives at Equation (29). To confirm that Equation (29) indeed solves Equation (28), one differentiates:

$$\dot{R}_1(t) = \ddot{R}_0(t) \int_0^t R_0(t')dt' + \dot{R}_0(t)R_0(t). \tag{34}$$

Since $\ddot{R}_0 = -F'(R_0)\dot{R}_0$ by Equation (27), we see that $\dot{R}_1 = -F'(R_0)R_1 - F(R_0)R_0$ as required.

As an illustration, we show how Equation (29) leads to Equation (13). From Equations (11), (12) and (25) one easily derives

$$m_a = -\frac{\int_0^\infty R_1(t)dt}{\int_0^\infty R_0(t)dt}. \tag{35}$$

This is simplified by performing a partial integration:

$$\begin{aligned}
-\int_0^\infty R_1(t)dt &= -\int_0^\infty \dot{R}_0(t)\left(\int_0^t R_0(t')dt'\right)dt \\
&= -\left[R_0(t)\left(\int_0^t R_0(t')dt'\right)\right]_0^\infty + \int_0^\infty R_0^2(t)dt \\
&= \int_0^\infty R_0^2(t)dt.
\end{aligned} \tag{36}$$

We thus arrive at Equation (13).

5. Numerical Results for a Binary Lennard–Jones Model

5.1. The Relevant Fluctuation–Dissipation Theorem

When the externally controlled variable is temperature itself, a slightly modified derivation of the FD theorem is required [37]. In the end, however, the result looks much like in the standard FD case: If $\Delta\beta(t)$ is the variation of $\beta \equiv 1/k_B T$ from its equilibrium value at the reference temperature, $\delta\beta(t) \equiv \beta(t+dt) - \beta(t)$, and sharp brackets denote standard canonical averages, the variation of the potential energy is given [37] by

$$\Delta U(t) = -\langle(\Delta U)^2\rangle \Delta\beta(t) + \int_{-\infty}^t \langle\Delta U(0)\Delta U(t-t')\rangle \delta\beta(t'). \tag{37}$$

Following a small inverse-temperature jump of magnitude $\Delta\beta$, $\Delta U(t) \to -\langle(\Delta U)^2\rangle \Delta\beta$ for $t \to \infty$. Since $\Delta\beta = -\Delta T_0/k_B T_0^2$, this leads to the well-known Einstein expression for the specific heat, $c = \langle(\Delta U)^2\rangle/k_B T_0^2$.

Equation (37) implies that the response to a jump at $t = 0$ for $t > 0$ is given by $\Delta U(t) = \left[-\langle(\Delta U)^2\rangle + \langle\Delta U(0)\Delta U(t)\rangle\right]d\beta$ (note that right after the temperature jump one has $\Delta U(t) \cong 0$ because of continuity). Therefore, the linear-response normalized relaxation function, $R_0(t)$, is given by

$$R_0(t) \;=\; \frac{\Delta U(t) - \Delta U(t=\infty)}{\Delta U(0) - \Delta U(t=\infty)} \;=\; \frac{\langle\Delta U(0)\Delta U(t)\rangle}{\langle(\Delta U)^2\rangle}. \tag{38}$$

5.2. Simulation Results

We simulated the well-known Kob–Andersen binary Lennard–Jones (KA) 80/20 mixture of A and B particles [38] with the standard Nose–Hoover thermostat [39] by means of the GPU-software RUMD [40]. The pair potentials of the KA system are Lennard–Jones potentials defined by $v_{ij}(r) = \varepsilon_{ij}[(\sigma_{ij}/r)^{12} - (\sigma_{ij}/r)^6]$ $(i,j = A,B)$ with the following parameters: $\sigma_{AA} = 1$, $\sigma_{AB} = 0.80$, $\sigma_{BB} = 0.88$, $\varepsilon_{AA} = 1$, $\varepsilon_{AB} = 1.5$, and $\varepsilon_{BB} = 0.5$. All masses are set to unity. A system of $N = 8000$ particles was simulated. In the units based on σ_{AA} and ε_{AA}, the time step was $\Delta t = 0.0025$, and the thermostat relaxation time was 0.2. The potentials were cut and shifted at $r_c = 2.5\sigma_{ij}$.

The potential-energy time-autocorrelation function appearing in Equation (38) was calculated at the reference temperature $T_0 = 0.60$ as follows. First, 10^7 time steps were taken for equilibration, which was confirmed from two consecutive runs comparing the self-part of the intermediate scattering function. After that, a run of 5×10^6 time steps was carried out, dumping the potential energy every 32 time steps. The potential-energy time-autocorrelation function was calculated using Fast Fourier Transform as implemented in RUMD [41].

In SPA, the constant Λ of Equation (9) is assumed to be proportional to the change in the monitored property, *in casu* ΔU. Λ was determined using the integral criterion of Ref. [18], which considers two jumps to the same temperature: an up and a down jump. For this we used the jumps from the temperatures 0.55 and 0.65 to $T_0 = 0.60$ [21], leading to

$$\Lambda \;=\; \frac{\Delta U}{0.0404}. \tag{39}$$

Here, ΔU is the equilibrium potential energy at the starting temperature minus the corresponding quantity at the final temperature (following the tradition in the field). The Λ of Equation (39) was used for all predictions.

Temperature-jump simulations were carried out as follows. First, 5×10^8 time steps were taken to ensure equilibration at the starting temperature. A total of 1000 configurations were generated from a subsequent 5×10^8 simulation by dumping configurations every 2^{19} time steps. This ensures that the configurations are statistically independent at the lowest temperature studied ($T = 0.50$). For each of the 1000 configurations, an aging simulation of 10^6 time steps was performed and the potential energy was dumped every eighth time step. The curves shown in Figure 1 represent averages over these 1000 aging simulations.
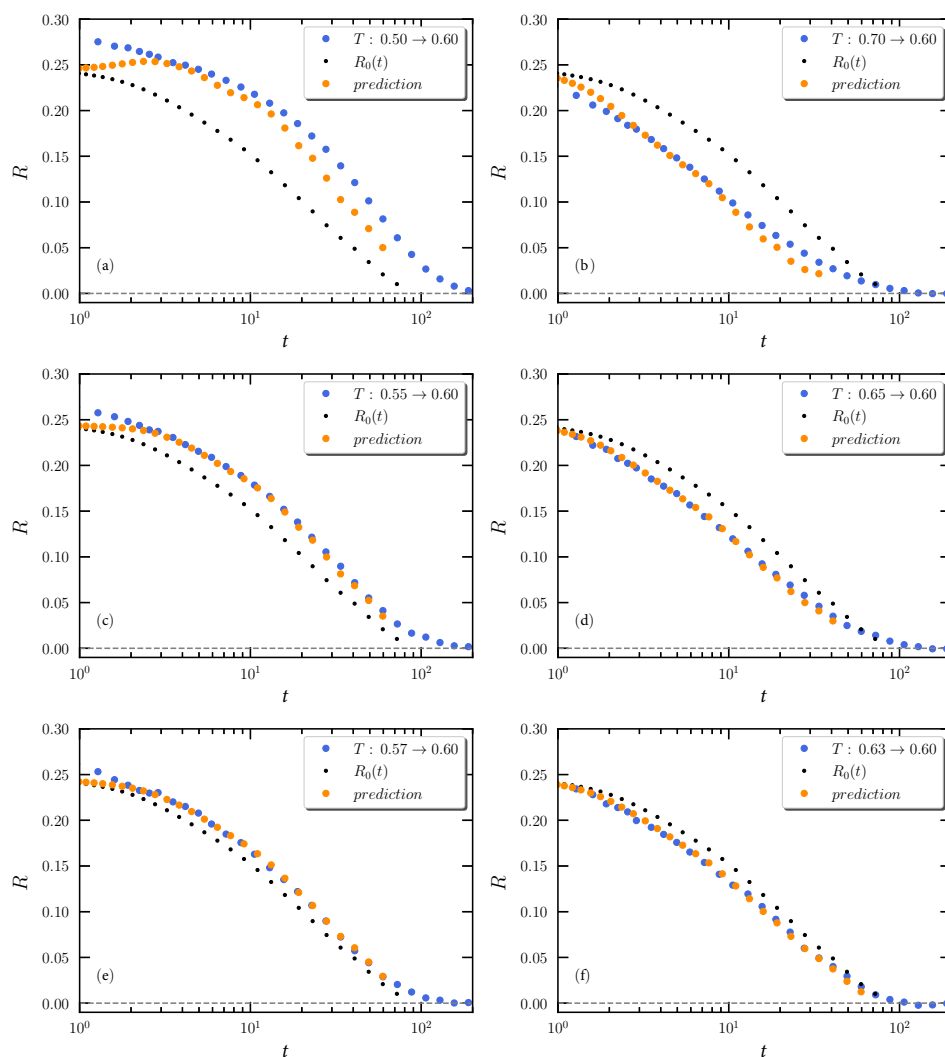
Figure 1. Results from computer simulations of the Kob–Andersen binary Lennard–Jones model. The figures show the normalized relaxation function $R(t)$ (Equations (25) and (29)) defined from the potential energy U after a temperature jump at $t = 0$ starting from a state of thermal equilibrium (blue filled circles): (**a**,**b**) show results for magnitude 0.10 temperature up and down jumps to the reference temperature $T_0 = 0.60$; (**c**,**d**) show results for magnitude 0.05 temperature up and down jumps to $T_0 = 0.60$; (**e**,**f**) show results for magnitude 0.03 temperature up and down jumps to $T_0 = 0.60$. The orange filled circles are the first-order predictions of the jump differential equation Equation (9) (given in Equation (25) in which $R_0(t)$ is the normalized equilibrium potential-energy time-autocorrelation function at $T_0 = 0.60$, $R_1(t)$ is given by Equation (29), and Λ is given by Equation (39)). For reference, in all figures $R_0(t)$ is plotted as small black filled circles.

The averages were smoothed using a Gaussian function. Each point represents an average calculated over all the data points using $R_{\text{avg}}(t) = \sum_{t'} R(t') \exp(-(t - t')^2/\sigma) / \sum_{t'} \exp(-(t - t')^2/\sigma)$ in which t' is the time-step number and $\sigma = 15{,}000$. In order to reduce the number of points in Figure 1, the data were divided into 24 bins per decade.

Figure 1 shows the simulation results (blue circles) for the normalized relaxation function of the potential energy for up and down jumps to $T_0 = 0.60$. The orange circles are the predictions of the first-order theory. In all figures the small black filled circles are the normalized equilibrium potential-energy time-autocorrelation function at $T_0 = 0.60$, which is the linear-limit normalized relaxation function $R_0(t)$ (Equation (38)). This function is faster than $R(t)$ for up jumps and slower for down jumps. This is expected since relaxation

is initially slow for the up jumps to $T_0 = 0.60$ because the fictive temperature [3] in this case is below 0.60, while the opposite happens for the down jumps to $T_0 = 0.60$.

We see that the theory generally fits the data well, even for the fairly large temperature jumps of magnitude 0.05. Deviations between prediction and simulations is observed for larger up jumps, though. A similar pattern has been observed in experiments but there the observed relaxation function is faster than predicted, not slower [21]. In both cases, these deviations serve to emphasize that SPA does is not accurate for large jumps.

The TN formalism implies that the long-time decay of the normalized relaxation function for infinitesimal jumps to different temperatures are identical except for an overall scaling of the time, i.e., it obeys time–temperature superposition (TTS) [42]. In other words, TTS is a necessary condition for TN to apply and thus, in particular, for SPA to apply. We test TTS by plotting the normalized potential-energy time-autocorrelation functions $R_0(t)$ at temperatures ranging from 0.50 to 0.70 (Figure 2a) and scaling these on the time axis (Figure 2b). Except for the short-time signals that are not relevant to aging, we see that TTS indeed applies to a very good approximation.
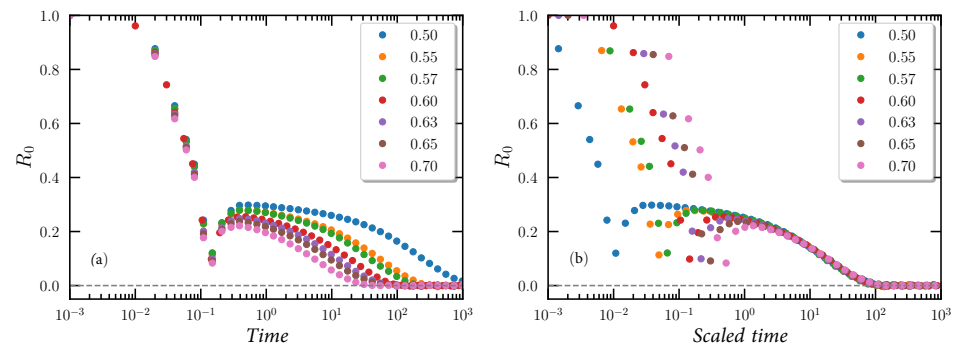
Figure 2. Test of time–temperature superposition for the normalized potential-energy time-autocorrelation function $R_0(t)$ at the temperatures indicated in the legends: (**a**) shows the simulation data and (**b**) shows the same data empirically scaled on the time axis. We conclude that TTS applies except at the shortest times.

6. Summary and Outlook

We solved the jump differential equation analytically to first order. The solution is Equation (25) in which $R_1(t)$ is given by Equation (29). The solution does not explicitly involve the function $F(R)$; indeed $R_1(t)$ has a universal expression in terms of the zeroth-order solution, $R_0(t)$. Since the latter, by the fluctuation–dissipation theorem, is an equilibrium time-autocorrelation function, our results imply that, within the single-parameter aging scheme, knowledge of equilibrium fluctuations is enough to predict aging. The expression of $R_1(t)$ relevant for the weakly nonlinear limit was confirmed by computer simulations of the Kob–Andersen binary Lennard–Jones glass former monitoring the aging of potential energy following temperature jumps of varying magnitudes.

For future development of the TN single-parameter aging formalism, it would be most interesting to monitor the equilibrium fluctuations in experiments in order to check whether aging is predicted correctly from these fluctuations. This is experimentally very challenging, but should not be impossible. It would also be interesting to monitor other quantities in simulations than the potential energy used here, although it should be mentioned that many quantities relax in a very similar way for the Kob–Andersen system [43].

Institutional Review Board Statement: Not applicable.

Informed Consent Statement: Not applicable.

Data Availability Statement: The data of this study are available upon request.

Conflicts of Interest: The authors declare no conflict of interest.

Appendix A

Equation (13) is derived here from the integral criterion of Ref. [18] that considers two jumps to the same temperature: an up and a down jump. For two small jumps of same magnitude to the temperature T_0, denoted by a and b, one has the two normalized relaxation functions

$$
\begin{aligned}
R_a &= R_0 + \Lambda R_1 \\
R_b &= R_0 - \Lambda R_1.
\end{aligned}
\tag{A1}
$$

The integral criterion [18] is

$$
\int_0^\infty \left(e^{\Lambda_{ab} R_a} - 1 \right) dt + \int_0^\infty \left(e^{\Lambda_{ba} R_b} - 1 \right) dt = 0.
\tag{A2}
$$

Here, $\Lambda_{ab} = -\Lambda_{ba}$ is the difference in the value of Λ jumping from above and below, implying that $\Lambda_{ab} = 2\Lambda$ and $\Lambda_{ba} = -2\Lambda$. When Equation (A1) is substituted into Equation (A2), we get

$$
\int_0^\infty \left(e^{2\Lambda(R_0 + \Lambda R_1)} - 1 \right) dt + \int_0^\infty \left(e^{-2\Lambda(R_0 - \Lambda R_1)} - 1 \right) dt = 0.
\tag{A3}
$$

Expanding to second order in Λ leads to

$$
\int_0^\infty \left(2\Lambda(R_0 + \Lambda R_1) + 2\Lambda^2 R_0^2 + (-2\Lambda(R_0 - \Lambda R_1)) + 2\Lambda^2 R_0^2 \right) dt = 0.
\tag{A4}
$$

This reduces to

$$
\int_0^\infty \left(4\Lambda^2 R_1 + 4\Lambda^2 R_0^2 \right) dt = 0,
\tag{A5}
$$

which implies Equation (36) and, therefore, Equation (13).

References

1. Mazurin, O. Relaxation phenomena in glass. *J. Non-Cryst. Solids* **1977**, *25*, 129–169. [CrossRef]
2. Struik, L.C.E. *Physical Aging in Amorphous Polymers and Other Materials*; Elsevier: Amsterdam, The Netherland, 1978.
3. Scherer, G.W. *Relaxation in Glass and Composites*; Wiley: New York, NY, USA, 1986.
4. Hodge, I.M. Physical aging in polymer glasses. *Science* **1995**, *267*, 1945–1947. [CrossRef]
5. Chamon, C.; Kennett, M.P.; Castillo, H.E.; Cugliandolo, L.F. Separation of time scales and reparametrization invariance for aging systems. *Phys. Rev. Lett.* **2002**, *89*, 217201. [CrossRef]
6. Priestley, R.D. Physical aging of confined glasses. *Soft Matter* **2009**, *5*, 919–926. [CrossRef]
7. Grassia, L.; Simon, S.L. Modeling volume relaxation of amorphous polymers: Modification of the equation for the relaxation time in the KAHR model. *Polymer* **2012**, *53*, 3613–3620. [CrossRef]
8. Cangialosi, D.; Boucher, V.M.; Alegria, A.; Colmenero, J. Physical aging in polymers and polymer nanocomposites: Recent results and open questions. *Soft Matter* **2013**, *9*, 8619–8630. [CrossRef]
9. Dyre, J.C. Aging of CKN: Modulus versus conductivity analysis. *Phys. Rev. Lett.* **2013**, *110*, 245901. [CrossRef] [PubMed]
10. Micoulaut, M. Relaxation and physical aging in network glasses: A review. *Rep. Prog. Phys.* **2016**, *79*, 066504. [CrossRef] [PubMed]
11. McKenna, G.B.; Simon, S.L. 50th anniversary perspective: Challenges in the dynamics and kinetics of glass-forming polymers. *Macromolecules* **2017**, *50*, 6333–6361. [CrossRef]
12. Roth, C.B. (Ed.) *Polymer Glasses*; CRC Press: Boca Raton, FL, USA, 2017.
13. Ruta, B.; Pineda, E.; Evenson, Z. Relaxation processes and physical aging in metallic glasses. *J. Phys. Condens. Mat.* **2017**, *29*, 503002. [CrossRef]
14. Mauro, J.C. *Materials Kinetics: Transport and Rate Phenomena*; Elsevier: Amsterdam, The Netherlands, 2021.
15. Simon, F. Über den Zustand der unterkühlten Flüssigkeiten und Gläser. *Z. Anorg. Allg. Chem.* **1931**, *203*, 219–227. [CrossRef]

16. Olsen, N.B.; Dyre, J.C.; Christensen, T. Structural relaxation monitored by instantaneous shear modulus. *Phys. Rev. Lett.* **1998**, *81*, 1031–1033. [CrossRef]

17. Hecksher, T.; Olsen, N.B.; Niss, K.; Dyre, J.C. Physical aging of molecular glasses studied by a device allowing for rapid thermal equilibration. *J. Chem. Phys.* **2010**, *133*, 174514. [CrossRef] [PubMed]

18. Hecksher, T.; Olsen, N.B.; Dyre, J.C. Communication: Direct tests of single-parameter aging. *Chem. Phys.* **2015**, *142*, 241103. [CrossRef] [PubMed]

19. Hecksher, T.; Olsen, N.B.; Dyre, J.C. Fast contribution to the activation energy of a glass-forming liquid. *Proc. Natl. Acad. Sci. USA* **2019**, *116*, 16736–16741. [CrossRef]

20. Roed, L.A.; Hecksher, T.; Dyre, J.C.; Niss, K. Generalized single-parameter aging tests and their application to glycerol. *J. Chem. Phys.* **2019**, *150*, 044501. [CrossRef]

21. Riechers, B.; Roed, L.A.; Mehri, S.; Ingebrigtsen, T.S.; Hecksher, T.; Dyre, J.C.; Niss, K. Predicting nonlinear physical aging of glasses from equilibrium relaxation via the material time. *Sci. Adv.* **2022**, *8*, eabl9809. [CrossRef] [PubMed]

22. Kolla, S.; Simon, S.L. The t-effective paradox: New measurements towards a resolution. *Polymer* **2005**, *46*, 733–739. [CrossRef]

23. Schlosser, E.; Schönhals, A. Dielectric relaxation during physical aging. *Polymer* **1991**, *32*, 2135–2140. [CrossRef]

24. Leheny, R.L.; Nagel, S.R. Frequency-domain study of physical aging in a simple liquid. *Phys. Rev. B* **1998**, *57*, 5154–5162. [CrossRef]

25. Lunkenheimer, P.; Wehn, R.; Schneider, U.; Loidl, A. Glassy aging dynamics. *Phys. Rev. Lett.* **2005**, *95*, 055702. [CrossRef]

26. Richert, R. Supercooled liquids and glasses by dielectric relaxation spectroscopy. *Adv. Chem. Phys.* **2015**, *156*, 101–195.

27. Kovacs, A.J. Transition vitreuse dans les polymeres amorphes. Etude phenomenologique. *Fortschr. Hochpolym.-Forsch.* **1963**, *3*, 394–507.

28. Spinner, S.; Napolitano, A. Further studies in the annealing of a borosilicate glass. *J. Res. NBS* **1966**, *70*, 147–152. [CrossRef] [PubMed]

29. Narayanaswamy, O.S. A model of structural relaxation in glass. *J. Amer. Ceram. Soc.* **1971**, *54*, 491–498. [CrossRef]

30. Moynihan, C.T.; Easteal, A.J.; DeBolt, M.A.; Tucker, J. Dependence of the fictive temperature of glass on cooling rate. *J. Am. Ceram. Soc.* **1976**, *59*, 12–16. [CrossRef]

31. Chen, H.S. The influence of structural relaxation on the density and Young's modulus of metallic glasses. *J. Appl. Phys.* **1978**, *49*, 3289–3291. [CrossRef]

32. Huang, Y.; Paul, D.R. Physical aging of thin glassy polymer films monitored by gas permeability. *Polymer* **2004**, *45*, 8377–8393. [CrossRef]

33. Leonardo, R.D.; Scopigno, T.; Ruocco, G.; Buontempo, U. Spectroscopic cell for fast pressure jumps across the glass transition line. *Rev. Sci. Instrum.* **2004**, *75*, 2631–2637. [CrossRef]

34. Ruta, B.; Chushkin, Y.; Monaco, G.; Cipelletti, L.; Pineda, E.; Bruna, P.; Giordano, V.M.; Gonzalez-Silveira, M. Atomic-scale relaxation dynamics and aging in a metallic glass probed by x-ray photon correlation spectroscopy. *Phys. Rev. Lett.* **2012**, *109*, 165701. [CrossRef]

35. Brun, C.; Ladieu, F.; L'Hote, D.; Biroli, G.; Bouchaud, J.-P. Evidence of growing spatial correlations during the aging of glassy glycerol. *Phys. Rev. Lett.* **2012**, *109*, 175702. [CrossRef] [PubMed]

36. Angell, C.A. Formation of glasses from liquids and biopolymers. *Science* **1995**, *267*, 1924–1935. [CrossRef] [PubMed]

37. Nielsen, J.K.; Dyre, J.C. Fluctuation-dissipation theorem for frequency-dependent specific heat. *Phys. Rev. B* **1996**, *54*, 15754–15761. [CrossRef] [PubMed]

38. Kob, W.; Andersen, H.C. Testing mode-coupling theory for a supercooled binary Lennard-Jones mixture I: The van Hove correlation function. *Phys. Rev. E* **1995**, *51*, 4626–4641. [CrossRef]

39. Nose, S. A unified formulation of the constant temperature molecular dynamics methods. *J. Chem. Phys.* **1984**, *81*, 511. [CrossRef]

40. Bailey, N.P.; Ingebrigtsen, T.S.; Hansen, J.S.; Veldhorst, A.A.; Bøhling, L.; Lemarchand, C.A.; Olsen, A.E.; Bacher, A.K.; Costigliola, L.; Pedersen, U.R.; et al. RUMD: A general purpose molecular dynamics package optimized to utilize GPU hardware down to a few thousand particles. *Scipost Phys.* **2017**, *3*, 38. [CrossRef]

41. Allen, M.P.; Tildesley, D.J. *Computer Simulation of Liquids*; Oxford Science Publications: Oxford, UK, 1987.

42. Olsen, N.B.; Christensen, T.; Dyre, J.C. Time-temperature superposition in viscous liquids. *Phys. Rev. Lett.* **2001**, *86*, 1271–1274. [CrossRef]

43. Mehri, S.; Ingebrigtsen, T.S.; Dyre, J.C. Single-parameter aging in a binary Lennard-Jones system. *J. Chem. Phys.* **2021**, *154*, 094504. [CrossRef]

Hidden scale invariance in the Gay-Berne model. II. Smectic-*B* phase

Saeed Mehri ⬤, Jeppe C. Dyre ⬤,* and Trond S. Ingebrigtsen†

Glass and Time, IMFUFA, Department of Science and Environment, Roskilde University, P.O. Box 260, DK-4000 Roskilde, Denmark

This paper complements a previous study of the isotropic and nematic phases of the Gay-Berne liquid-crystal model [Mehri *et al.*, Phys. Rev. E **105**, 064703 (2022)] with a study of its smectic-*B* phase found at high density and low temperatures. We find also in this phase strong correlations between the virial and potential-energy thermal fluctuations, reflecting hidden scale invariance and implying the existence of isomorphs. The predicted approximate isomorph invariance of the physics is confirmed by simulations of the standard and orientational radial distribution functions, the mean-square displacement as a function of time, and the force, torque, velocity, angular velocity, and orientational time-autocorrelation functions. The regions of the Gay-Berne model that are relevant for liquid-crystal experiments can thus fully be simplified via the isomorph theory.

I. INTRODUCTION

Liquid crystals involve molecules with a high degree of shape anisotropy [1,2]. This interesting state of matter is relevant in many different contexts, ranging from display applications to biological systems [3–5]. Depending on temperature and pressure, the molecular anisotropy leads to different structural phases, e.g., nematic and smectic phases with long-range orientational ordering [1].

Gay-Berne (GB) models describe molecules of varying shape anisotropy spanning from elongated ellipsoids to thin disks, and GB models have become standard liquid-crystal models [6]. The GB pair potential depends on four dimensionless parameters. This is reflected in the notation $GB(\kappa, \kappa', \mu, \nu)$ in which the four parameters quantify the shape of the molecules and the strength of their interactions. A previous paper studied the isotropic and nematic phases of a GB model with parameters corresponding to rod-shaped elongated molecules [7]. It was found that this model has isomorphs in the isotropic and nematic phases, which are curves in the thermodynamic phase diagram along which the physics is approximately invariant. This paper presents a study of the same GB model in its smectic-*B* phase, demonstrating that isomorphs exist also here.

II. THE GAY-BERNE POTENTIAL AND SIMULATION DETAILS

The $GB(\kappa, \kappa', \mu, \nu)$ pair potential is characterized by the following four dimensionless parameters: $\kappa \equiv \sigma_e/\sigma_s$, where σ_e and σ_s are lengths, $\kappa' \equiv \varepsilon_{ss}/\varepsilon_{ee}$, where ε_{ss} and ε_{ee} are

energies, and two exponents μ and ν. The GB pair potential v_{GB} is defined as follows [6]:

$$v_{GB}(\mathbf{r}_{ij}, \hat{\mathbf{e}}_i, \hat{\mathbf{e}}_j) = 4\varepsilon(\hat{\mathbf{r}}, \hat{\mathbf{e}}_i, \hat{\mathbf{e}}_j)[(\sigma_s/\rho_{ij})^{12} - (\sigma_s/\rho_{ij})^6], \quad (1a)$$

$$\rho_{ij} = r_{ij} - \sigma(\hat{\mathbf{r}}, \hat{\mathbf{e}}_i, \hat{\mathbf{e}}_j) + \sigma_s. \quad (1b)$$

Here, r_{ij} is the distance between molecules i and j, $\hat{\mathbf{r}} \equiv \mathbf{r}_{ij}/r_{ij}$ is the unit vector from molecule i to molecule j, and $\hat{\mathbf{e}}_i$ and $\hat{\mathbf{e}}_j$ are unit vectors along the major axes of the molecules. The GB molecule mimics an ellipsoid of two diameters, σ_s and σ_e. Specifically, one defines

$$\sigma(\hat{\mathbf{r}}, \hat{\mathbf{e}}_i, \hat{\mathbf{e}}_j) = \sigma_s \left[1 - \frac{\chi}{2} \left(\frac{(\hat{\mathbf{e}}_i \cdot \hat{\mathbf{r}} + \hat{\mathbf{e}}_j \cdot \hat{\mathbf{r}})^2}{1 + \chi(\hat{\mathbf{e}}_i \cdot \hat{\mathbf{e}}_j)} \right. \right.$$
$$\left. \left. + \frac{(\hat{\mathbf{e}}_i \cdot \hat{\mathbf{r}} - \hat{\mathbf{e}}_j \cdot \hat{\mathbf{r}})^2}{1 - \chi(\hat{\mathbf{e}}_i \cdot \hat{\mathbf{e}}_j)} \right) \right]^{-1/2}, \quad (2a)$$

$$\chi = \frac{\kappa^2 - 1}{\kappa^2 + 1}. \quad (2b)$$

Here, χ is a shape anisotropy parameter, and κ quantifies the molecular asymmetry such that $\kappa = 1$ ($\chi = 0$) represents spherical molecules, $\kappa \to \infty$ ($\chi \to 1$) corresponds to very long rods, and $\kappa \to 0$ ($\chi \to -1$) corresponds to very thin disks. The energy term is given by

$$\varepsilon(\hat{\mathbf{r}}, \hat{\mathbf{e}}_i, \hat{\mathbf{e}}_j) = \varepsilon_0 (\varepsilon_1(\hat{\mathbf{e}}_i, \hat{\mathbf{e}}_j))^{\nu} (\varepsilon_2(\hat{\mathbf{r}}, \hat{\mathbf{e}}_i, \hat{\mathbf{e}}_j))^{\mu}, \quad (3a)$$

in which

$$\varepsilon_1(\hat{\mathbf{e}}_i, \hat{\mathbf{e}}_j) = (1 - \chi^2(\hat{\mathbf{e}}_i \cdot \hat{\mathbf{e}}_j)^2)^{-1/2}, \quad (3b)$$

$$\varepsilon_2(\hat{\mathbf{r}}, \hat{\mathbf{e}}_i, \hat{\mathbf{e}}_j) = 1 - \frac{\chi'}{2} \left(\frac{(\hat{\mathbf{e}}_i \cdot \hat{\mathbf{r}} + \hat{\mathbf{e}}_j \cdot \hat{\mathbf{r}})^2}{1 + \chi'(\hat{\mathbf{e}}_i \cdot \hat{\mathbf{e}}_j)} \right.$$
$$\left. + \frac{(\hat{\mathbf{e}}_i \cdot \hat{\mathbf{r}} - \hat{\mathbf{e}}_j \cdot \hat{\mathbf{r}})^2}{1 - \chi'(\hat{\mathbf{e}}_i \cdot \hat{\mathbf{e}}_j)} \right). \quad (3c)$$

---

*dyre@ruc.dk
†trondingebrigtsen@hotmail.com
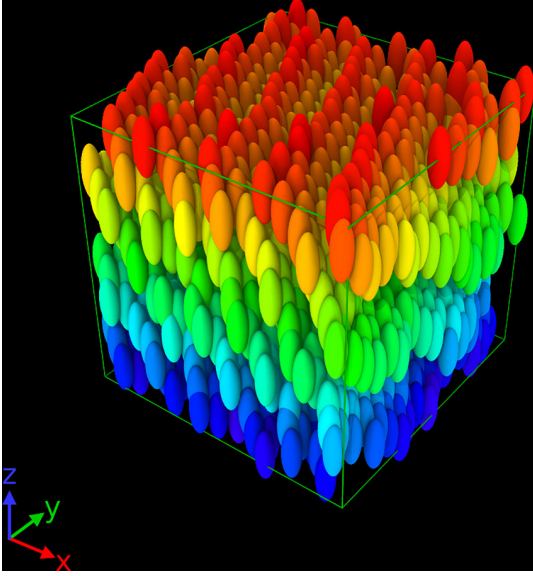
FIG. 1. Snapshot of the smectic-B phase at density 0.4 and temperature 1.2. A color coding is introduced here to visualize the individual planes.

Here,

$$\chi' = \frac{\kappa'^{1/\mu} - 1}{\kappa'^{1/\mu} + 1} \tag{3d}$$

is an energy anisotropy parameter. The energies ε_{ss} and ε_{ee} are the well depths of the potential in the side-side and end-end configurations, respectively. Unless otherwise stated, σ_s defines the length and ε_0 defines the energy unit used below.

We simulated a system of 1372 particles of the GB(3, 5, 2, 1) model studied previously in Ref. [7]. The GB pair potential was cut and shifted at $r_c = 4.0$, and the time step used was $\Delta t = 0.001$. The standard NVT Nosé-Hoover algorithm was used for the center-of-mass motion and the Fincham algorithm was used for the rotational motion [8,9]. Different thermostats were applied for the translational and rotational motions [7]. The molecular moment of inertia was set to unity. A homemade code for graphics processing unit (GPU) computing was used; at each simulated state point, 20×10^6 time steps were taken to equilibrate the system before the production run of 67×10^6 time steps.

If $\mathbf{R} \equiv (\mathbf{r}_1, \ldots, \mathbf{r}_N)$ is the vector of particle coordinates and $\rho \equiv N/V$ is the particle density, the microscopic virial $W(\mathbf{R})$ is defined by $W(\mathbf{R}) \equiv \partial U(\mathbf{R})/\partial \ln \rho$ in which the density is changed by a uniform scaling of all particle coordinates. For an inverse power-law pair potential, $v(r) = \varepsilon(r/\sigma)^{-n}$, it is easy to see that this implies that $W(\mathbf{R})$ is a sum of pair virial contributions equal to $(n/3)v(r)$. Because the vectors $\hat{\mathbf{r}}$, $\hat{\mathbf{e}}_i$, and $\hat{\mathbf{e}}_j$ do not change under a uniform expansion, a related result applies for the GB pair potential. Specifically, the GB pair virial is $4\varepsilon(\hat{\mathbf{r}}, \hat{\mathbf{e}}_i, \hat{\mathbf{e}}_j)[4(\sigma_s/\rho_{ij})^{12} - 2(\sigma_s/\rho_{ij})^6](r/\rho_{ij})$ and the total microscopic virial $W(\mathbf{R})$ is calculated as the sum of all pair virials.

The GB(3,5,2,1) phase diagram is shown in Fig. 3 of Ref. [7]. Figure 1 shows a snapshot of the system at equilibrium in the smectic-B phase.

III. PROPERTIES STUDIED

The quantities evaluated numerically in this paper are as follows: the standard radial distribution function $g(r)$ [10,11], the below-defined orientational radial distribution function $G_l(r)$ ($l = 2$) [11–14], and a number of single-molecule time-autocorrelation functions [15,16]. The latter two observables are defined by

$$G_l(r) = \langle P_l(\hat{\mathbf{e}}_i \cdot \hat{\mathbf{e}}_j) \rangle, \tag{4}$$

$$\phi_A(t) = \langle \mathbf{A}(t_0) \cdot \mathbf{A}(t_0 + t) \rangle. \tag{5}$$

Here, P_l is the lth Legendre polynomial, $\mathbf{A}(t)$ is a vector defined for each molecule, and the angular brackets denote an ensemble and particle average, which in the case of $G_l(r)$ is restricted to pairs of particles the distance r apart. We study the cases of $\mathbf{A}$ being the velocity, angular velocity, force, and torque. We also study the first- and second-order molecular orientational order parameter time-autocorrelation functions defined by

$$\phi_l(t) = \langle P_l(\hat{\mathbf{e}}_i(t_0) \cdot \hat{\mathbf{e}}_i(t_0 + t)) \rangle. \tag{6}$$

IV. R-SIMPLE SYSTEMS AND ISOMORPHS

The virial W quantifies the part of the pressure p that derives from molecular interactions via the defining identity $pV = Nk_BT + W$. Liquids and solids may be classified according to the degree of correlation between the constant-volume thermal-equilibrium fluctuations of virial W and potential energy U [17]. "R-simple systems" are those with strong WU correlations; such systems are simple because their thermodynamic phase diagram is basically one dimensional in regard to structure and dynamics [17–20]. The "isomorph theory" of R-simple systems was developed over the last decade [21,22].

The WU Pearson correlation coefficient (which depends on the state point in question) is defined by

$$R = \frac{\langle \Delta W \Delta U \rangle}{\sqrt{\langle (\Delta W)^2 \rangle \langle (\Delta U)^2 \rangle}}. \tag{7}$$

Here, Δ gives the deviation from the equilibrium mean value. Many systems, including the standard Lennard-Jones and Yukawa fluids, have strong WU correlations in their liquid and solid phases, whereas R usually decreases significantly for densities below the critical density [23]. A system is considered to be R-simple whenever $R > 0.9$ at the state points of interest [21]. This is a pragmatic criterion, however, and, e.g., the simulations presented in this paper go below this value at high temperatures without significantly affecting the degree of isomorph invariance.

As mentioned, R-simple systems have curves in the phase diagram along which structure and dynamics are approximately invariant. These curves are termed *isomorphs*. Isomorph invariance applies when data are presented in so-called reduced units. These units, which in contrast to ordinary units are state-point dependent, are given by letting the density ρ define the length unit l_0, the temperature define the energy unit e_0, and density and thermal velocity define the time

unit t_0,

$$l_0 = \rho^{-1/3}, \quad e_0 = k_B T, \quad t_0 = \rho^{-1/3}\sqrt{m/k_B T}. \quad (8)$$

Here, m is the molecule mass. Quantities made dimensionless by reference to these units are termed "reduced" and marked with a tilde.

Strong virial potential-energy correlations arise whenever hidden scale invariance applies. This is the condition that the potential-energy ordering of same-density configurations is maintained under a uniform scaling of all coordinates [24]. This is formally expressed as follows:

$$U(\mathbf{R}_a) < U(\mathbf{R}_b) \Rightarrow U(\lambda\mathbf{R}_a) < U(\lambda\mathbf{R}_b), \quad (9)$$

in which λ is a scaling factor. Consider two configurations with the same potential energy, i.e., $U(\mathbf{R}_a) = U(\mathbf{R}_b)$. After a uniform scaling one has by Eq. (9) $U(\lambda\mathbf{R}_a) = U(\lambda\mathbf{R}_b)$. By taking the derivative of this with respect to λ one derives $W(\mathbf{R}_a) = W(\mathbf{R}_b)$ [24]. Thus the same potential energy implies the same virial, resulting in a 100% correlation between the W and U constant-volume fluctuations. For realistic systems, Eq. (9) is fulfilled only approximately, however, and one rarely experiences perfect virial potential-energy correlations [this only applies when $U(\mathbf{R})$ is an Euler-homogeneous function].

Recall that a system's entropy S is equal to that of an ideal gas at the same density and temperature plus an "excess" term deriving from the intermolecular interactions: $S = S_{id} + S_{ex}$. It can be shown that Eq. (9) implies that the reduced structure and dynamics are invariant along the lines of constant excess entropy; these are by definition the system's isomorphs [24]. The so-called density-scaling exponent γ is defined by

$$\gamma \equiv \left(\frac{\partial \ln T}{\partial \ln \rho}\right)_{S_{ex}} = \frac{\langle \Delta W \Delta U \rangle}{\langle (\Delta U)^2 \rangle}. \quad (10)$$

The second equality here is a general identity [22], which is useful when the system is R-simple because Eq. (10) can then be applied for tracing out isomorphs without knowing the equation of state. For the simple Euler algorithm this is done by proceeding as follows. At a given state point (ρ_1, T_1), by means of Eq. (10) one calculates γ from the equilibrium fluctuations of the potential energy and virial. From Eq. (10) one then predicts the temperature T_2 with the property that (ρ_2, T_2) is on the same isomorph as (ρ_1, T_1). If $\gamma = 7$, for instance, for a 1% density increase a 7% temperature increase will ensure that the new state point is on the same isomorph. In the simulations of this paper, in order to increase the accuracy of the generated isomorph, following Ref. [25] we used instead the fourth-order Runge-Kutta algorithm for solving numerically Eq. (10) (involving density changes of order 1%). The resulting isomorph state points are given in Table I. We note that the density-scaling exponent is generally significantly larger than for point-particle Lennard-Jones models where it is in the range 4–6. This must be a consequence of the spherical asymmetry because the same increase has been seen, e.g., for the asymmetric dumbbell and Lewis-Wahnström ortho-terphenyl models built of Lennard-Jones particles [18,21,26]. A quantitative explanation of this is missing, however, because a full isomorph theory of molecules is still not available.

TABLE I. Variation of density ρ, temperature T, virial potential-energy correlation coefficient R [Eq. (7)], and density-scaling exponent γ [Eq. (10)] for nine state points on the isomorph generated from the reference state point $(\rho, T) = (0.4, 0.4)$.

ρ	T	R	γ
0.400	0.400	0.956	9.46
0.416	0.578	0.946	9.04
0.433	0.823	0.936	8.74
0.451	1.160	0.925	8.50
0.469	1.619	0.905	8.28
0.488	2.240	0.887	8.06
0.508	3.079	0.868	7.92
0.529	4.211	0.854	7.85
0.550	5.770	0.854	8.00

V. STRUCTURE AND DYNAMICS MONITORED ALONG AN ISOCHORE AND AN ISOMORPH

We begin the study by presenting results for the mean-square displacement as a function of time, which is predicted to be isomorph invariant in reduced units. Figure 2 shows the results along the $\rho = 0.4$ isochore (upper panel) and the isomorph generated from the reference state point $(\rho, T) = (0.4, 0.4)$ (lower panel), in both cases for the same nine temperatures. The isomorph data involve state points of more than a third density change and more than a factor of 10 temperature change (Table I). Note that the smectic-B phase of the GB(5,3,2,1) model is found at higher densities than those of the isotropic and nematic phases studied in Ref. [7].
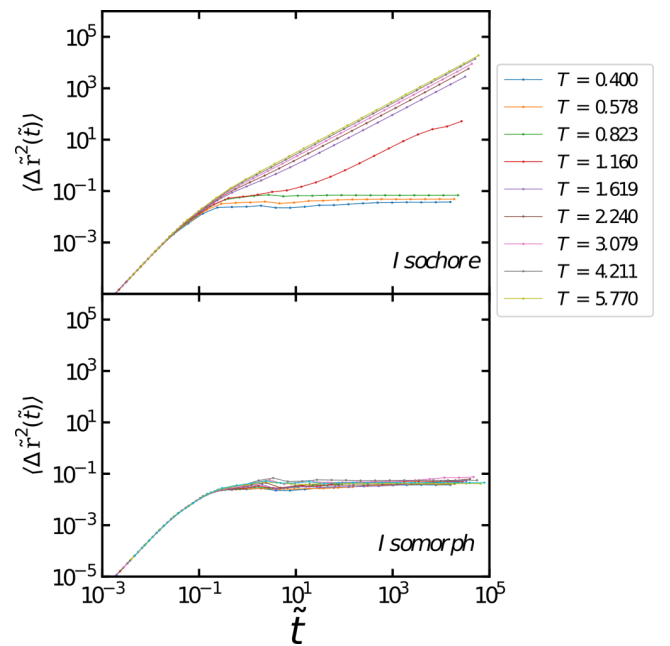
FIG. 2. Reduced mean-square displacement as a function of reduced time along the $\rho = 0.4$ isochore and along the isomorph generated from the reference state point $(\rho, T) = (0.4, 0.4)$ (Table I).
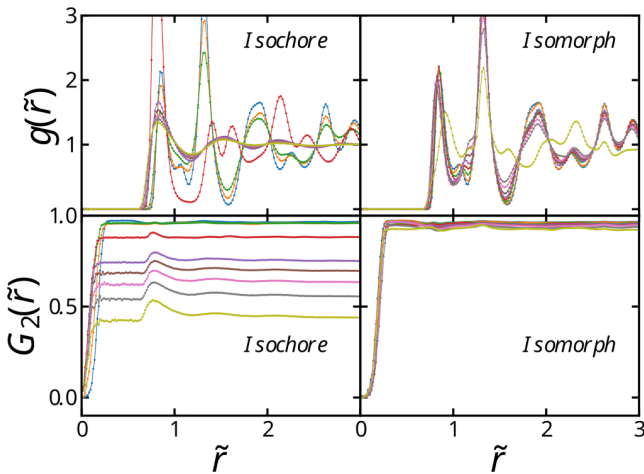
FIG. 3. Structure along the isochore and the isomorph probed via the standard radial distribution function (upper panels) and the orientational radial distribution function defined in Eq. (4) (lower panels), in both cases plotted as a function of the reduced pair distance $\tilde{r}$. The colors used here and henceforth for the different temperatures are the same as those of Fig. 2.

FIG. 4. Normalized force (upper panels) and torque (lower panels) time-autocorrelation functions along the same isochore and isomorph as in the previous figures, plotted as functions of reduced time $\tilde{t}$.

The low-temperature state points along the isochore of Fig. 2 are in the solid state as evident from the fact that the long-time mean-square displacement is constant. The high-temperature isochore state points, on the other hand, show diffusive long-time behavior and are liquid. The fact that all mean-square displacement data collapse at short times in the ballistic regime for both the isochore and the isomorph is a consequence of the use of reduced units, which leads to a reduced-unit thermal velocity that is the same at all state points. For the isomorph data, we see a fairly good collapse at all times, not just at short times. The minor deviations from perfect collapse are consistent with the fact that the virial potential-energy correlation coefficient R is not very close to unity; in fact, R goes below 0.9 at the four highest temperatures (Table I). This feature might have to do with the short-time librational motion of the rods, which as shown below does not scale well in the isomorph sense.

Figure 3 shows reduced-unit data for the radial distribution function $g(r)$ and the orientational radial distribution function $G_2(r)$ [Eq. (4)] along the same isochore and isomorph. Figure 3 shows no invariance along the isochore, but fair invariance along the isomorph. An exception to this is the highest temperature isomorph radial distribution function that deviates notably from the eight others. We have found that at this (and higher) temperatures, the smectic-B phase undergoes a further transition involving a tilt of the average molecular orientation with respect to the smectic layers, similar to what has been reported by de Miguel *et al.* [11]. Interestingly, this does not affect the isomorph invariance of quantities other than the radial distribution function [compare the $G_2(r)$ data of Fig. 3, as well as the data of later figures].

Returning to dynamic properties, the normalized force and torque time-autocorrelation functions, i.e., the functions $\phi_A(t)/\phi_A(0)$ of Eq. (5) for **A** equal to the force and torque
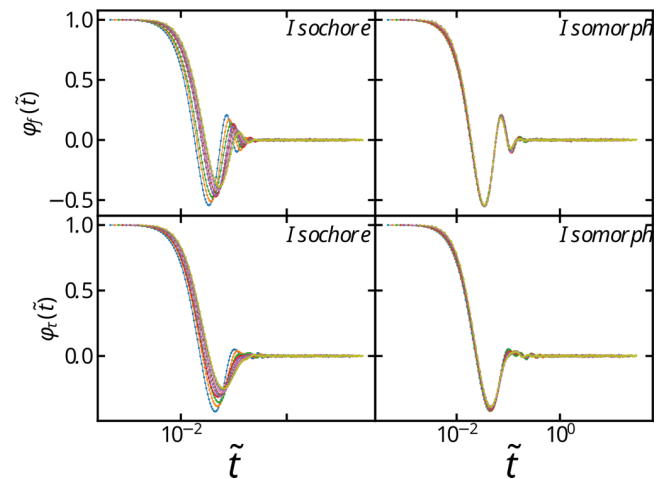
on the individual particles, respectively, are shown in Fig. 4 as functions of the reduced time. Near-perfect scaling is observed for both functions along the isomorph, but not along the isochore.

Figure 5 shows the first- and second-order orientational time-autocorrelation functions along the isochore and isomorph. These functions both decay to zero at the highest density studied on the isochore, which is not the case for the isomorph along which invariant dynamics is observed.

We finish the study by showing the normalized velocity and angular velocity time-autocorrelation functions in Fig. 6. Again, good isomorph invariance is observed at all times, though with minor deviation at intermediate times for the velocity time-autocorrelation function.
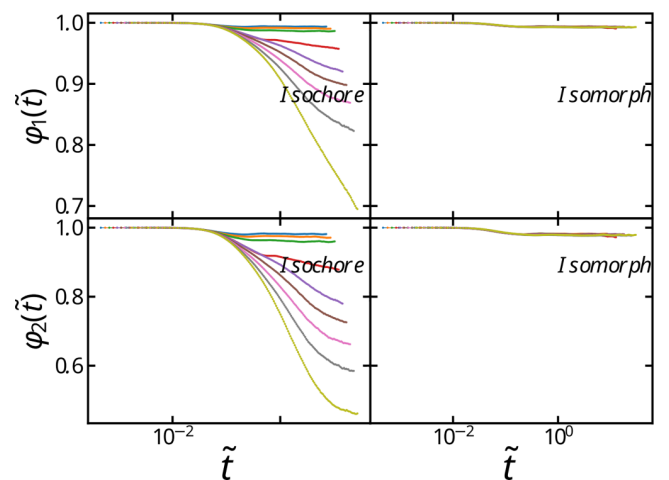
FIG. 5. First- and second-order orientational order parameter time-autocorrelation functions along the isochore and isomorph, plotted as functions of reduced time.
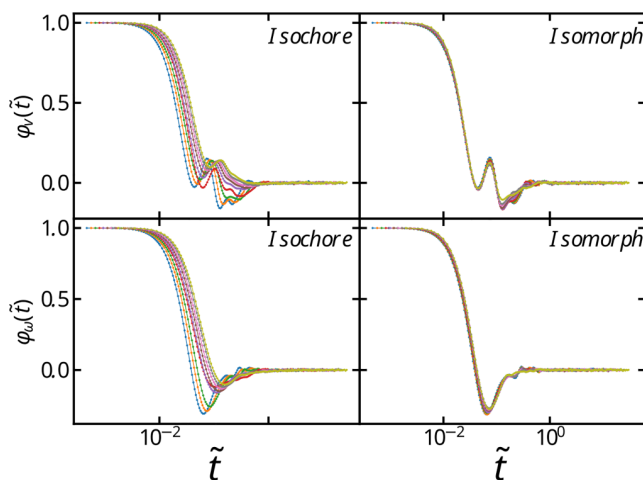
FIG. 6. Normalized velocity and angular velocity time-autocorrelation functions along the isochore and isomorph, plotted as functions of reduced time.

VI. SUMMARY

We have shown that the isomorph theory can be used to understand GB liquid crystals in the smectic-*B* phase, because the thermodynamic phase diagram is here effectively one dimensional in the sense that the reduced-unit structure and dynamics are approximately invariant along the isomorphs. Our previous paper [7] showed that the same applies for the isotropic and nematic phases of the GB(3,5,2,1) model. This means that most of the GB(3,5,2,1) phase diagram is effectively one dimensional in regard to structure and dynamics. We note that this property is not limited to a particular GB model; thus an earlier publication demonstrated the existence of isomorphs in the GB(0.345,0.2,1,2) model that forms a discotic liquid-crystal phase at low temperatures [27]. The GB potential is unique in the field of liquid-crystal models in that through a gradual reduction of the parameters χ and χ' of Eqs. (2) and (3), the Lennard-Jones potential is recovered. It is an interesting question whether one would find isomorph invariance behavior in other models of rods, such as a rigid line of Lennard-Jones interaction centers.

We demonstrated above that the GB(3,5,2,1) model exhibits good invariance of the reduced-unit structure and dynamics along the studied isomorph. In conjunction with our previous study [7], the existence of isomorphs in the GB model can now be used to explain the observed behavior of liquid crystals, for instance, the so-called density scaling, which is the fact that the reduced dynamics is invariant along lines of constant ρ^γ / T [28,29]. Studies remain to investigate whether other smectic phases of the GB model also exhibit strong virial potential-energy correlations and thus the existence of isomorphs. It would be interesting, in particular, to investigate the effect of varying the moment of inertia, given the fact that fixing this quantity upon a density change formally violates isomorph invariance of the dynamics, but was found above to have little effect in practice. Also, it would be interesting to investigate systematically the vast parameter space of the GB potential from the hidden-scale-invariance perspective.

[1] P. G. de Gennes and J. Prost, *The Physics of Liquid Crystals*, 2nd ed. (Oxford University Press, Oxford, 1993).

[2] M. Jurásek and R. Vácha, Self-assembled clusters of patchy rod-like molecules, Soft Matter **13**, 7492 (2017).

[3] S. J. Woltman, G. P. Crawford, and G. D. Jay, *Liquid Crystals: Frontiers in Biomedical Applications* (World Scientific, Singapore, 2007).

[4] A. de la Cotte, C. Wu, M. Trevisan, A. Repula, and E. Grelet, Rod-like virus-based multiarm colloidal molecules, ACS Nano **11**, 10616 (2017).

[5] Y. Tian and Z. Niu, Self-assembly of rod-like bionanoparticles at interfaces and in solution, in *Virus-Derived Nanoparticles for Advanced Technologies* (Springer, New York, 2018), pp. 159–167.

[6] J. Gay and B. Berne, Modification of the overlap potential to mimic a linear site–site potential, J. Chem. Phys. **74**, 3316 (1981).

[7] S. Mehri, J. C. Dyre, and T. S. Ingebrigtsen, Hidden scale invariance in the Gay-Berne model, Phys. Rev. E **105**, 064703 (2022).

[8] D. Fincham, N. Quirke, and D. J. Tildesley, Computer simulation of molecular liquid mixtures. I. A diatomic Lennard-Jones model mixture for CO_2/C_2H_6, J. Chem. Phys. **84**, 4535 (1986).

[9] D. Fincham, Leapfrog rotational algorithms, Mol. Simul. **8**, 165 (1992).

[10] M. A. Bates and G. R. Luckhurst, Computer simulation studies of anisotropic systems. XXX. The phase behavior and structure of a Gay-Berne mesogen, J. Chem. Phys. **110**, 7087 (1999).

[11] E. De Miguel, L. F. Rull, M. K. Chalam, and K. E. Gubbins, Liquid crystal phase diagram of the Gay-Berne fluid, Mol. Phys. **74**, 405 (1991).

[12] B. J. Berne and G. D. Harp, On the calculation of time correlation functions, in *Advances in Chemical Physics*, Advances in Chemical Physics Series Vol. 17 (Wiley, New York, 1970), pp. 63–227.

[13] E. de Miguel, L. F. Rull, M. K. Chalam, K. E. Gubbins, and F. Van Swol, Location of the isotropic-nematic transition in the Gay-Berne model, Mol. Phys. **72**, 593 (1991).

[14] D. Adams, G. Luckhurst, and R. Phippen, Computer simulation studies of anisotropic systems: XVII. The Gay-Berne model nematogen, Mol. Phys. **61**, 1575 (1987).

[15] E. de Miguel, L. F. Rull, and K. E. Gubbins, Dynamics of the Gay-Berne fluid, Phys. Rev. A **45**, 3813 (1992).

[16] P. P. Jose and B. Bagchi, Multiple short time power laws in the orientational relaxation of nematic liquid crystals, J. Chem. Phys. **125**, 184901 (2006).

[17] T. S. Ingebrigtsen, T. B. Schrøder, and J. C. Dyre, What Is a Simple Liquid? Phys. Rev. X **2**, 011011 (2012).

[18] T. S. Ingebrigtsen, T. B. Schrøder, and J. C. Dyre, Isomorphs in model molecular liquids, J. Phys. Chem. B **116**, 1018 (2012).

[19] J. C. Dyre, Hidden scale invariance in condensed matter, J. Phys. Chem. B **118**, 10007 (2014).

[20] J. C. Dyre, Perspective: Excess-entropy scaling, J. Chem. Phys. **149**, 210901 (2018).

[21] N. P. Bailey, U. R. Pedersen, N. Gnan, T. B. Schrøder, and J. C. Dyre, Pressure-energy correlations in liquids. I. Results from computer simulations, J. Chem. Phys. **129**, 184507 (2008).

[22] N. Gnan, T. B. Schrøder, U. R. Pedersen, N. P. Bailey, and J. C. Dyre, Pressure-energy correlations in liquids. IV. "Isomorphs" in liquid phase diagrams, J. Chem. Phys. **131**, 234504 (2009).

[23] I. H. Bell, R. Messerly, M. Thol, L. Costigliola, and J. C. Dyre, Modified entropy scaling of the transport properties of the Lennard-Jones fluid, J. Phys. Chem. B **123**, 6345 (2019).

[24] T. B. Schrøder and J. C. Dyre, Simplicity of condensed matter at its core: Generic definition of a Roskilde-simple system, J. Chem. Phys. **141**, 204502 (2014).

[25] E. Attia, J. C. Dyre, and U. R. Pedersen, Extreme case of density scaling: The Weeks-Chandler-Andersen system at low temperatures, Phys. Rev. E **103**, 062140 (2021).

[26] L. J. Lewis and G. Wahnström, Molecular-dynamics study of supercooled ortho-terphenyl, Phys. Rev. E **50**, 3865 (1994).

[27] S. Mehri, M. A. Kolmangadi, J. C. Dyre, and T. S. Ingebrigtsen, Lines of invariant physics in the isotropic phase of the discotic Gay-Berne model, J. Non-Cryst. Solids: X **14**, 100085 (2022).

[28] C. M. Roland, S. Hensel-Bielowka, M. Paluch, and R. Casalini, Supercooled dynamics of glass-forming liquids and polymers under hydrostatic pressure, Rep. Prog. Phys. **68**, 1405 (2005).

[29] K. Satoh, Characteristic behavior of short-term dynamics in reorientation for Gay-Berne particles near the nematic-isotropic phase transition temperature, J. Chem. Phys. **125**, 204902 (2006).

Bibliography

1. Tabor, D. *Gases, liquids and solids: and other states of matter* (Cambridge university press, 1991).

2. Wikipedia contributors. *Phase diagram — Wikipedia, The Free Encyclopedia* Link. [Online; accessed 16-December-2022]. 2022.

3. Collings, P. J. & Goodby, J. W. *Introduction to liquid crystals: chemistry and physics* (Crc Press, 2019).

4. Huang, C. Introduction to Liquid Crystals: Chemistry and Physics by Peter J. Collings and Michael Hird. *AMERICAN JOURNAL OF PHYSICS* **66,** 551–551 (1998).

5. Chen, R. H. *Liquid crystal displays: fundamental physics and technology* (John Wiley & Sons, 2011).

6. Demus, D., Goodby, J. W., Gray, G. W., Spiess, H. W. & Vill, V. *Handbook of Liquid Crystals* (John Wiley & Sons, 2008).

7. Allen, M. P. *Computer Simulations of Liquids* 1987.

8. Alba-Simionesco, C., Cailliaux, A, Alegria, A & Tarjus, G. Scaling out the density dependence of the α relaxation in glass-forming polymers. *EPL (Europhysics Letters)* **68,** 58 (2004).

9. Roland, C., Hensel-Bielowka, S, Paluch, M & Casalini, R. Supercooled dynamics of glass-forming liquids and polymers under hydrostatic pressure. *Reports on Progress in Physics* **68,** 1405 (2005).

10. López, E. R., Pensado, A. S., Fernández, J. & Harris, K. R. On the density scaling of pVT data and transport properties for molecular and ionic liquids. *The Journal of Chemical Physics* **136** (2012).

11. Adrjanowicz, K, Pionteck, J & Paluch, M. Isochronal superposition and density scaling of the intermolecular dynamics in glass-forming liquids with varying hydrogen bonding propensity. *RSC advances* **6,** 49370–49375 (2016).

12. Satoh, K. Thermodynamic scaling of dynamic properties of liquid crystals: Verifying the scaling parameters using a molecular model. *The Journal of Chemical Physics* **139,** 084901 (2013).

13. Satoh, K. Thermodynamic Scaling of Miesowicz Viscosity Coefficients via Molecular Dynamics Simulation. *Molecular Crystals and Liquid Crystals* **615,** 78–88 (2015).

14. Bailey, N. P., Pedersen, U. R., Gnan, N., Schrøder, T. B. & Dyre, J. C. Pressure-energy correlations in liquids. I. Results from computer simulations. *The Journal of chemical physics* **129,** 184507 (2008).

15. Tool, A. Q. RELATION BETWEEN INELASTIC DEFORMABILITY AND THERMAL EXPANSION OF GLASS IN ITS ANNEALING RANGE*. *Journal of the American Ceramic Society* **29,** 240–253. eprint: Link. Link (1946).

16. NARAYANASWAMY, O. S. A Model of Structural Relaxation in Glass. *Journal of the American Ceramic Society* **54,** 491–498. eprint: Link. Link (1971).

17. Scherer, G. W. Relaxation in glass and composites (1986).

18. Viasnoff, V. & Lequeux, F. Rejuvenation and overaging in a colloidal glass under shear. *Physical Review Letters* **89,** 065701 (2002).

19. Narayanaswamy, O. A model of structural relaxation in glass. *Journal of the American Ceramic Society* **54,** 491–498 (1971).

20. Tool, A. Q. Relation between inelastic deformability and thermal expansion of glass in its annealing range. *Journal of the American Ceramic society* **29,** 240–253 (1946).

21. Dyre, J. C. Narayanaswamy's 1971 aging theory and material time. *The Journal of chemical physics* **143,** 114507 (2015).

22. Roed, L. A., Hecksher, T., Dyre, J. C. & Niss, K. Generalized single-parameter aging tests and their application to glycerol. *The Journal of chemical physics* **150,** 044501 (2019).

23. Hecksher, T., Olsen, N. B. & Dyre, J. C. Communication: Direct tests of single-parameter aging. *The Journal of Chemical Physics* **142,** 241103. eprint: Link. Link (2015).

24. Bailey, N. P., Pedersen, U. R., Gnan, N., Schrøder, T. B. & Dyre, J. C. Pressure-energy correlations in liquids. II. Analysis and consequences. *The Journal of chemical physics* **129,** 184508 (2008).

25. Gnan, N., Schrøder, T. B., Pedersen, U. R., Bailey, N. P. & Dyre, J. C. Pressure-energy correlations in liquids. IV."Isomorphs" in liquid phase diagrams. *The Journal of chemical physics* **131,** 234504 (2009).

26. Ingebrigtsen, T. S., Schrøder, T. B. & Dyre, J. C. What is a simple liquid? *Physical Review X* **2,** 011011 (2012).

27. Schrøder, T. B., Bailey, N. P., Pedersen, U. R., Gnan, N. & Dyre, J. C. Pressure-energy correlations in liquids. III. Statistical mechanics and thermodynamics of liquids with hidden scale invariance. *The Journal of chemical physics* **131,** 234503 (2009).

28. Schrøder, T. B. & Dyre, J. C. Simplicity of condensed matter at its core: Generic definition of a Roskilde-simple system. *The Journal of Chemical Physics* **141,** 204502 (2014).

29. Pedersen, U. R., Bailey, N. P., Schrøder, T. B. & Dyre, J. C. Strong pressure-energy correlations in van der Waals liquids. *Physical review letters* **100,** 015701 (2008).

30. Dyre, J. C. Hidden scale invariance in condensed matter. *The Journal of Physical Chemistry B* **118,** 10007–10024 (2014).

31. Dyre, J. C. Isomorph theory beyond thermal equilibrium. *The Journal of Chemical Physics* **153,** 134502 (2020).

32. Bailey, N. P., Bøhling, L., Veldhorst, A. A., Schrøder, T. B. & Dyre, J. C. Statistical mechanics of Roskilde liquids: Configurational adiabats, specific heat contours, and density dependence of the scaling exponent. *The Journal of Chemical Physics* **139,** 184506 (2013).

33. Flenner, E., Staley, H. & Szamel, G. Universal features of dynamic heterogeneity in supercooled liquids. *Physical review letters* **112,** 097801 (2014).

34. Prasad, S. & Chakravarty, C. Onset of simple liquid behaviour in modified water models. *The Journal of Chemical Physics* **140,** 164501 (2014).

35. Veldhorst, A. A., Dyre, J. C. & Schrøder, T. B. Scaling of the dynamics of flexible Lennard-Jones chains. *The Journal of Chemical Physics* **141,** 054904 (2014).

36. Albrechtsen, D. E., Olsen, A. E., Pedersen, U. R., Schrøder, T. B. & Dyre, J. C. Isomorph invariance of the structure and dynamics of classical crystals. *Physical Review B* **90,** 094106 (2014).

37. Bacher, A. K., Schrøder, T. B. & Dyre, J. C. The EXP pair-potential system. II. Fluid phase isomorphs. *The Journal of Chemical Physics* **149,** 114502 (2018).

38. Costigliola, L., Schrøder, T. B. & Dyre, J. C. Freezing and melting line invariants of the Lennard-Jones system. *Physical Chemistry Chemical Physics* **18,** 14678–14690 (2016).

39. Xiao, W., Tofteskov, J., Christensen, T. V., Dyre, J. C. & Niss, K. Isomorph theory prediction for the dielectric loss variation along an isochrone. *Journal of Non-Crystalline Solids* **407,** 190–195 (2015).

40. Wase Hansen, H., Sanz, A., Adrjanowicz, K., Frick, B. & Niss, K. Evidence of a one-dimensional thermodynamic phase diagram for simple glass-formers. *arXiv e-prints,* arXiv–1709 (2017).

41. Friedeheim, L., Dyre, J. C. & Bailey, N. P. Hidden scale invariance at high pressures in gold and five other face-centered-cubic metal crystals. *Physical Review E* **99,** 022142 (2019).

42. Costigliola, L. *Isomorph theory and extensions* PhD thesis (Roskilde University, 2016).

43. Costigliola, L., Schrøder, T. B. & Dyre, J. C. Communication: Studies of the Lennard-Jones fluid in 2, 3, and 4 dimensions highlight the need for a liquid-state 1/d expansion. *The Journal of Chemical Physics* **144,** 231101 (2016).

44. Fragiadakis, D. & Roland, C. M. On the density scaling of liquid dynamics. *The Journal of chemical physics* **134,** 044504 (2011).

45. Koperwas, K., Grzybowski, A & Paluch, M. The effect of molecular architecture on the physical properties of supercooled liquids studied by MD simulations: Density scaling and its relation to the equation of state. *The Journal of Chemical Physics* **150,** 014501 (2019).

46. Fragiadakis, D & Roland, C. Intermolecular distance and density scaling of dynamics in molecular liquids. *The Journal of Chemical Physics* **150,** 204501 (2019).

47. Vetterling, W. T., Press, W. H., Teukolsky, S. A. & Flannery, B. P. *Numerical recipes example book (c++): The art of scientific computing* (Cambridge University Press, 2002).

48. De Gennes, P.-G. & Prost, J. *The physics of liquid crystals* **83** (Oxford university press, 1993).

49. Barón, M. Definitions of basic terms relating to low-molar-mass and polymer liquid crystals (IUPAC Recommendations 2001). *Pure and Applied Chemistry* **73,** 845–895 (2001).

50. Garti, N., Somasundaran, P. & Mezzenga, R. *Self-assembled supramolecular architectures: lyotropic liquid crystals* (John Wiley & Sons, 2012).

51. Collings, P. J. & Hird, M. *Introduction to liquid crystals chemistry and physics* (Crc Press, 2017).

52. Demus, D., Goodby, J. W., Gray, G. W., Spiess, H. W. & Vill, V. *Handbook of liquid crystals, volume 2A: low molecular weight liquid crystals I: calamitic liquid crystals* (John Wiley & Sons, 2011).

53. *Electronics & DIY lab* May 1, 2011. Link.

54. Reinitzer, F. Beiträge zur kenntniss des cholesterins. *Monatshefte für Chemie* **9,** 421–441 (1888).

55. Whatling, S. *Computer simulation studies of liquid crystals* PhD thesis (University of Southampton, 1997). Link.

56. Raynes, P. *LIQUID CRYSTALS—Second Edition, by S CHANDRASEKHAR, Cambridge University Press,(1992), ISBN 0-521-41747-3 (HB), ISBN 0-521-42741-X (PB)* 1993.

57. Vorländer, D. Die Erforschung der molekularen Gestalt mit Hilfe der kristallinischen Flüssigkeiten. *Zeitschrift für Physikalische Chemie* **105,** 211–254 (1923).

58. Chandrasekhar, S, Sadashiva, B. & Suresh, K. Liquid crystals of disc-like molecules. *pramana* **9,** 471–480 (1977).

59. Tinh, N. H., Destrade, C. & Gasparoux, H. Nematic disc-like liquid crystals. *Physics letters A* **72,** 251–254 (1979).

60. Giroud-Godquin, A. & Billard, J. Un Organométallique Disquogĕne Thermotrope. *Molecular Crystals and Liquid Crystals* **66,** 147–150 (1981).

61. Ohta, K., Muroki, H., Takagi, A., Hatada, K.-I., Ema, H., Yamamoto, I. & Matsuzaki, K. Discotic liquid crystals of transition metal complexes, 3: the first-established discotic lamellar phase in bis [1, 3-di (pn-alkoxyphenyl) propane-1, 3-dionato] copper (II). *Molecular Crystals and Liquid Crystals* **140,** 131–152 (1986).

62. Ribeiro, A., Martins, A. & Giroud-Godquin, A. Evidence of a smectic phase of disc-like molecules. *Molecular Crystals and Liquid Crystals Letters* **5,** 133–139 (1988).

63. Allen, M. P. & Warren, M. A. Simulation of structure and dynamics near the isotropic-nematic transition. *Physical review letters* **78,** 1291 (1997).

64. Sarman, S. Flow properties of liquid crystal phases of the Gay–Berne fluid. *The Journal of chemical physics* **108,** 7909–7916 (1998).

65. Wu, C., Qian, T. & Zhang, P. Non-equilibrium molecular-dynamics measurement of the Leslie coefficients of a Gay–Berne nematic liquid crystal. *Liquid Crystals* **34,** 1175–1184 (2007).

66. Cuetos, A., Ilnytskyi, J. M. & Wilson, M. R. Rotational viscosities of gay-berne mesogens. *Molecular Physics* **100,** 3839–3845 (2002).

67. Phuong, N. H., Germano, G. & Schmid, F. Elastic constants from direct correlation functions in nematic liquid crystals: A computer simulation study. *The Journal of Chemical Physics* **115,** 7227–7234 (2001).

68. Stelzer, J., Longa, L. & Trebin, H.-R. Molecular dynamics simulations of a Gay–Berne nematic liquid crystal: elastic properties from direct correlation functions. *The Journal of chemical physics* **103,** 3098–3107 (1995).

69. Allen, M. P., Warren, M. A., Wilson, M. R., Sauron, A. & Smith, W. Molecular dynamics calculation of elastic constants in Gay–Berne nematic liquid crystals. *The Journal of chemical physics* **105,** 2850–2858 (1996).

70. Frenkel, D. & Smit, B. *Understanding molecular simulation: from algorithms to applications* (Elsevier, 2001).

71. Humpert, A. *Computer simulations of siquid crystals* PhD thesis (University of Warwick, 2016).

72. Verlet, L. Computer" experiments" on classical fluids. I. Thermodynamical properties of Lennard-Jones molecules. *Physical review* **159,** 98 (1967).

73. Levesque, D. & Verlet, L. Molecular dynamics and time reversibility. *Journal of Statistical Physics* **72,** 519–537 (1993).

74. Nosé, S. A unified formulation of the constant temperature molecular dynamics methods. *The Journal of chemical physics* **81,** 511–519 (1984).

75. Nosé, S. A molecular dynamics method for simulations in the canonical ensemble. *Molecular physics* **52,** 255–268 (1984).

76. Hoover, W. G. Canonical dynamics: Equilibrium phase-space distributions. *Physical review A* **31,** 1695 (1985).

77. Hoover, W. G. & Hoover, C. G. *Time reversibility, computer simulation, algorithms, chaos* (World Scientific, 2012).

78. Fincham, D. Leapfrog rotational algorithms for linear molecules. *Molecular Simulation* **11,** 79–89 (1993).

79. Toxvaerd, S. Algorithms for canonical molecular dynamics simulations. *Molecular Physics* **72,** 159–168 (1991).

80. Weeks, J. D., Chandler, D. & Andersen, H. C. Role of repulsive forces in determining the equilibrium structure of simple liquids. *The Journal of chemical physics* **54,** 5237–5247 (1971).

81. Frenkel, D. Computer simulation of hard-core models for liquid crystals. *Molecular physics* **60,** 1–20 (1987).

82. Onsager, L. The effects of shape on the interaction of colloidal particles. *Annals of the New York Academy of Sciences* **51,** 627–659 (1949).

83. Frenkel, D. Columnar ordering as an excluded volume effect. *Liquid crystals* **5,** 929–940 (1989).

84. Frenkel, D, Mulder, B. & McTague, J. Phase diagram of a system of hard ellipsoids. *Physical review letters* **52,** 287 (1984).

85. Frenkel, D & Mulder, B. The hard ellipsoid-of-revolution fluid: I. Monte Carlo simulations. *Molecular physics* **55,** 1171–1192 (1985).

86. Vieillard-Baron, J. The equation of state of a system of hard spherocylinders. *Molecular Physics* **28,** 809–818 (1974).

87. Frenkel, D. Onsager's spherocylinders revisited. *Journal of physical chemistry* **91,** 4912–4916 (1987).

88. Stroobants, A, Lekkerkerker, H. & Frenkel, D. Evidence for smectic order in a fluid of hard parallel spherocylinders. *Physical review letters* **57,** 1452 (1986).

89. Frenkel, D, Lekkerkerker, H. & Stroobants, A. Thermodynamic stability of a smectic phase in a system of hard rods. *Nature* **332,** 822–823 (1988).

90. Veerman, J. & Frenkel, D. Phase diagram of a system of hard spherocylinders by computer simulation. *Physical review A* **41,** 3237 (1990).

91. Veerman, J. & Frenkel, D. Phase behavior of disklike hard-core mesogens. *Physical Review A* **45,** 5632 (1992).

92. Kihara, T. Convex molecules in gaseous and crystalline states. *Advances in chemical Physics,* 147–188 (1963).

93. Streen, W. & Gubbins, K.-E. Liquids of linear molecules: computer simulations and theory. *Annual Review of Physical Chemistry* **28,** 373–410 (1977).

94. Berne, B. J. & Pechukas, P. Gaussian model potentials for molecular interactions. *The Journal of Chemical Physics* **56,** 4213–4216 (1972).

95. Gay, J. & Berne, B. Modification of the overlap potential to mimic a linear site–site potential. *The Journal of Chemical Physics* **74,** 3316–3319 (1981).

96. Egberts, E & Berendsen, H. Molecular dynamics simulation of a smectic liquid crystal with atomic detail. *The Journal of chemical physics* **89,** 3718–3732 (1988).

97. Komolkin, A., Molchanov, Y. V. & Yakutseni, P. Computer simulation of a real liquid crystal. *Liquid Crystals* **6,** 39–45 (1989).

98. Picken, S., Van Gunsteren, W., Duijnen, P. T. V. & De Jeu, W. A molecular dynamics study of the nematic phase of 4-n-pentyl-4′-cyanobiphenyl. *Liquid Crystals* **6,** 357–371 (1989).

99. Wilson, M. R. & Allen, M. P. Computer simulations of mesogenic molecules using realistic atom-atom potentials. *Molecular Crystals and Liquid Crystals* **198,** 465–477 (1991).

100. Wilson, M. & Allen, M. Structure of trans-4-(trans-4-n-pentylcyclohexyl) cyclohexylcarbonitrile (CCH5) in the isotropic and nematic phases: a computer simulation study. *Liquid Crystals* **12,** 157–176 (1992).

101. Paolini, G. V., Ciccotti, G. & Ferrario, M. Simulation of site-site soft-core liquid crystal models. *Molecular Physics* **80,** 297–312 (1993).

102. Patnaik, S. S., Plimpton, S. J., Pachter, R. & Adams, W. W. Modelling a nematic liquid crystal. *Liquid Crystals* **19,** 213–220 (1995).

103. Corner, J. & Lennard-Jones, J. E. The second virial coefficient of a gas of non-spherical molecules. *Proceedings of the Royal Society of London. Series A. Mathematical and Physical Sciences* **192,** 275–292. eprint: Link. Link (1948).

104. Kushick, J. & Berne, B. J. Computer simulation of anisotropic molecular fluids. *The Journal of Chemical Physics* **64,** 1362–1367 (1976).

105. Decoster, D., Constant, E. & Constant, M. Computer Simulation of Molecular Dynamics of Anisotropic Fluids. *Molecular Crystals and Liquid Crystals* **97,** 263–276 (1983).

106. Walmsley, S. Gaussian model potentials for molecular interactions and their development. *Chemical Physics Letters* **49,** 390–392 (1977).

107. Tsykalo, A. & Bagmet, A. Molecular dynamics study of the nematic liquid crystals. *Molecular Crystals and Liquid Crystals* **46,** 111–119 (1978).

108. Kihara, T. The second virial coefficient of non-spherical molecules. *Journal of the Physical Society of Japan* **6,** 289–296 (1951).

109. Emerson, A., Luckhurst, G. & Whatling, S. Computer simulation studies of anisotropic systems: XXIII. The Gay-Berne discogen. *Molecular Physics* **82,** 113–124 (1994).

110. Adams, D., Luckhurst, G. & Phippen, R. Computer simulation studies of anisotropic systems: XVII. The Gay-Berne model nematogen. *Molecular Physics* **61,** 1575–1580 (1987).

111. Luckhurst, G., Stephens, R. & Phippen, R. Computer simulation studies of anisotropic systems. XIX. Mesophases formed by the Gay-Berne model mesogen. *Liquid Crystals* **8,** 451–464 (1990).

112. De Miguel, E., Rull, L. F., Chalam, M. K., Gubbins, K. E. & Van Swol, F. Location of the isotropic-nematic transition in the Gay-Berne model. *Molecular physics* **72,** 593–605 (1991).

113. De Miguel, E., Rull, L. F., Chalam, M. K. & Gubbins, K. E. Liquid crystal phase diagram of the Gay-Berne fluid. *Molecular Physics* **74,** 405–424 (1991).

114. Alejandre, J, Emsley, J., Tildesley, D. & Carlson, P. Molecular dynamics simulations of a flexible molecule in a liquid crystalline solvent. *The Journal of chemical physics* **101,** 7027–7036 (1994).

115. Chalam, M. K., Gubbins, K. E., Miguel, E. D. & Rull, L. F. A molecular simulation of a liquid-crystal model: bulk and confined fluid. *Molecular Simulation* **7,** 357–385 (1991).

116. Andrew, P. *et al.* Monte Carlo investigations of a Gay—Berne liquid crystal. *Journal of the Chemical Society, Faraday Transactions* **89,** 4069–4078 (1993).

117. Hashim, R, Luckhurst, G. & Romano, S. Computer-simulation studies of anisotropic systems. Part XXIV.—Constant-pressure investigations of the smectic B phase of the Gay–Berne mesogen. *Journal of the Chemical Society, Faraday Transactions* **91,** 2141–2148 (1995).

118. De Miguel, E., Rull, L. F. & Gubbins, K. E. Dynamics of the Gay-Berne fluid. *Physical Review A* **45,** 3813 (1992).

119. Del Rio, E. M., de Miguel, E. & Rull, L. F. Computer simulation of the liquid-vapour interface in liquid crystals. *Physica A-statistical Mechanics and Its Applications* **213,** 138–147 (1995).

120. Sarman, S. Molecular dynamics of heat flow in nematic liquid crystals. *The Journal of chemical physics* **101,** 480–489 (1994).

121. Sarman, S. & Evans, D. J. Self-diffusion and heat flow in isotropic and liquid crystal phases of the Gay–Berne fluid. *The Journal of chemical physics* **99,** 620–627 (1993).

122. Sarman, S. & Evans, D. J. Statistical mechanics of viscous flow in nematic fluids. *The Journal of chemical physics* **99,** 9021–9036 (1993).

123. Sarman, S. Microscopic theory of liquid crystal rheology. *The Journal of chemical physics* **103,** 393–416 (1995).

124. Tjipto-Margo, B & Sullivan, D. Molecular interactions and interface properties of nematic liquid crystals. *The Journal of chemical physics* **88,** 6620–6630 (1988).

125. Velasco, E, Somoza, A. & Mederos, L. Liquid-crystal phase diagram of the Gay–Berne fluid by perturbation theory. *The Journal of chemical physics* **102,** 8107–8113 (1995).

126. De Miguel, E. & Vega, C. The global phase diagram of the Gay–Berne model. *The Journal of chemical physics* **117,** 6313–6322 (2002).

127. Smondyrev, A., Loriot, G. B. & Pelcovits, R. A. Viscosities of the Gay-Berne nematic liquid crystal. *Physical review letters* **75,** 2340 (1995).

128. Del Rio, E. M., Da Gama, M. T., De Miguel, E & Rull, L. Wetting and interfacial order at nematic free surfaces. *EPL (Europhysics Letters)* **35,** 189 (1996).

129. Rull, L. F. & Romero-Enrique, J. M. Computer simulation study of the nematic–vapour interface in the Gay–Berne model. *Molecular Physics* **115,** 1214–1224 (2017).

130. Sarman, S., Wang, Y.-L. & Laaksonen, A. Non-Newtonian rheological properties of shearing nematic liquid crystal model systems based on the Gay–Berne potential. *Physical Chemistry Chemical Physics* **17,** 16615–16623 (2015).

131. Sarman, S., Wang, Y.-L. & Laaksonen, A. Self-diffusion in the non-Newtonian regime of shearing liquid crystal model systems based on the Gay-Berne potential. *The Journal of Chemical Physics* **144,** 054901 (2016).

132. Berardi, R., Emerson, A. P. J. & Zannoni, C. Monte Carlo investigations of a Gay—Berne liquid crystal. *J. Chem. Soc., Faraday Trans.* **89,** 4069–4078. Link (22 1993).

133. Caprion, D., Bellier-Castella, L & Ryckaert, J.-P. Influence of shape and energy anisotropies on the phase diagram of discotic molecules. *Physical Review E* **67,** 041703 (2003).

134. Akino, N., Schmid, F. & Allen, M. P. Molecular-dynamics study of the nematic-isotropic interface. *Physical Review E* **63,** 041706 (2001).

135. Coussaert, T. & Baus, M. Density-functional theory of the columnar phase of discotic Gay–Berne molecules. *The Journal of chemical physics* **116,** 7744–7751 (2002).

136. Yamamoto, T., Suga, T. & Mori, N. Brownian dynamics simulation of orientational behavior, flow-induced structure, and rheological properties of a suspension of oblate spheroid particles under simple shear. *Phys. Rev. E* **72,** 021509. Link (2 2005).

137. Cienega-Cacerez, O., Moreno-Razo, J. A., Díaz-Herrera, E. & Sambriski, E. J. Phase equilibria, fluid structure, and diffusivity of a discotic liquid crystal. *Soft Matter* **10,** 3171–3182 (2014).

138. Bushby, R. J. & Kawata, K. Liquid crystals that affected the world: discotic liquid crystals. *Liquid Crystals* **38,** 1415–1426 (2011).

139. Kabadi, V. N. & Steele, W. A. Molecular dynamics of fluids: the Gaussian overlap model. *Berichte der Bunsengesellschaft für physikalische Chemie* **89,** 2–9 (1985).

140. Kabadi, V. N. Molecular dynamics of fluids: the Gaussian overlap model II. *Berichte der Bunsengesellschaft für physikalische Chemie* **90,** 327–332 (1986).

141. Sediawan, W., Gupta, S & McLaughlin, E. Simulation and theory of fluids of axisymmetric molecules. *Molecular Physics* **62,** 141–159 (1987).

142. Sediawan, W. B., Gupta, S. & McLaughlin, E. Computer modeling of naphthalene. *The Journal of chemical physics* **90,** 1888–1900 (1989).

143. Eppenga, R & Frenkel, D. Monte Carlo study of the isotropic and nematic phases of infinitely thin hard platelets. *Molecular physics* **52,** 1303–1334 (1984).

144. Wikipedia. *Radial distribution function — Wikipedia, The Free Encyclopedia* Link. [Online; accessed 07-June-2022]. 2022.

145. Bates, M. & Luckhurst, G. Computer simulation studies of anisotropic systems. XXX. The phase behavior and structure of a Gay-Berne mesogen. *J. Chem. Phys.* **110,** 7087–7108 (1999).

146. Méndez-Bermúdez, J. G., Guillén-Escamilla, I., Mixteco-Sánchez, J. C., Méndez-Maldonado, G. A. & González-Melchor, M. Equation of state, structure and diffusion coefficients of Gay-Berne fluids: the cases $\kappa'=$ 5; 10; 15; 20. *arXiv:1911.07366* (2019).

147. Jose, P. P. & Bagchi, B. Multiple short time power laws in the orientational relaxation of nematic liquid crystals. *J. Chem. Phys.* **125,** 184901 (2006).

148. Tölle, A. Neutron scattering studies of the model glass former orthoterphenyl. *Reports on Progress in Physics* **64,** 1473 (2001).

149. Cangialosi, D. Dynamics and thermodynamics of polymer glasses. *Journal of Physics: Condensed Matter* **26,** 153101 (2014).

150. Hodge, I. M. Physical Aging in Polymer Glasses. *Science* **267,** 1945–1947. ISSN: 0036-8075. eprint: Link. Link (1995).

151. Moynihan, C. T., Easteal, A. J., De BOLT, M. A. & Tucker, J. Dependence of the fictive temperature of glass on cooling rate. *Journal of the American Ceramic Society* **59,** 12–16 (1976).

152. Olsen, N. B., Dyre, J. C. & Christensen, T. Structural relaxation monitored by instantaneous shear modulus. *Physical review letters* **81,** 1031 (1998).

153. Mauro, J. C., Loucks, R. J. & Gupta, P. K. Fictive temperature and the glassy state. *Journal of the American Ceramic Society* **92,** 75–86 (2009).

154. Cugliandolo, L. F. & Kurchan, J. On the out-of-equilibrium relaxation of the Sherrington-Kirkpatrick model. *Journal of Physics A: Mathematical and General* **27,** 5749 (1994).

155. Kob, W. & Barrat, J.-L. Fluctuations, response and aging dynamics in a simple glass-forming liquid out of equilibrium. *The European Physical Journal B-Condensed Matter and Complex Systems* **13,** 319–333 (2000).

156. Adolf, D. B., Chambers, R. S., Flemming, J., Budzien, J. & McCoy, J. Potential energy clock model: Justification and challenging predictions. *Journal of Rheology* **51,** 517–540 (2007).

157. Castillo, H. E. & Parsaeian, A. Local fluctuations in the ageing of a simple structural glass. *Nature physics* **3,** 26–28 (2007).

158. Parsaeian, A. & Castillo, H. E. Equilibrium and nonequilibrium fluctuations in a glass-forming liquid. *Physical review letters* **102,** 055704 (2009).

159. Kolvin, I. & Bouchbinder, E. Simple nonlinear equation for structural relaxation in glasses. *Physical Review E* **86,** 010501 (2012).

160. Qiao, J. & Pelletier, J.-M. Dynamic mechanical relaxation in bulk metallic glasses: a review. *Journal of Materials Science & Technology* **30,** 523–545 (2014).

161. Song, L., Xu, W., Huo, J., Li, F., Wang, L.-M., Ediger, M. & Wang, J.-Q. Activation entropy as a key factor controlling the memory effect in glasses. *Physical Review Letters* **125,** 135501 (2020).

162. Lundgren, L, Svedlindh, P, Nordblad, P & Beckman, O. Dynamics of the relaxation-time spectrum in a CuMn spin-glass. *Physical review letters* **51,** 911 (1983).

163. Berthier, L. & Bouchaud, J.-P. Geometrical aspects of aging and rejuvenation in the Ising spin glass: A numerical study. *Physical Review B* **66,** 054404 (2002).

164. Cangialosi, D., Boucher, V. M., Alegría, A. & Colmenero, J. Physical aging in polymers and polymer nanocomposites: recent results and open questions. *Soft Matter* **9,** 8619–8630 (2013).

165. Spinner, S. & Napolitano, A. Further studies in the annealing of a borosilicate glass. *Journal of Research of the National Bureau of Standards. Section A, Physics and Chemistry* **70,** 147 (1966).

166. Schlosser, E & Schönhals, A. Dielectric relaxation during physical ageing. *Polymer* **32,** 2135–2140 (1991).

167. Leheny, R. L. & Nagel, S. R. Frequency-domain study of physical aging in a simple liquid. *Physical Review B* **57,** 5154 (1998).

168. Lunkenheimer, P., Wehn, R., Schneider, U. & Loidl, A. Glassy aging dynamics. *Physical review letters* **95,** 055702 (2005).

169. Richert, R. Supercooled liquids and glasses by dielectric relaxation spectroscopy. *Adv. Chem. Phys* **156,** 101–195 (2015).

170. Hecksher, T., Olsen, N. B., Niss, K. & Dyre, J. C. Physical aging of molecular glasses studied by a device allowing for rapid thermal equilibration. *The Journal of chemical physics* **133,** 174514 (2010).

171. Wehn, R, Lunkenheimer, P. & Loidl, A. Broadband dielectric spectroscopy and aging of glass formers. *Journal of non-crystalline solids* **353,** 3862–3870 (2007).

172. Dyre, J. C. & Olsen, N. B. Minimal model for beta relaxation in viscous liquids. *Physical review letters* **91,** 155703 (2003).

173. Kovacs, A. J. in *Fortschritte der hochpolymeren-forschung* 394–507 (Springer, 1964).

174. Di, X., Win, K. Z., McKenna, G. B., Narita, T., Lequeux, F., Pullela, S. R., Cheng, Z., *et al.* Signatures of structural recovery in colloidal glasses. *Physical review letters* **106,** 095701 (2011).

175. McKenna, G. B. & Simon, S. L. 50th anniversary perspective: Challenges in the dynamics and kinetics of glass-forming polymers. *Macromolecules* **50,** 6333–6361 (2017).

176. Struik, L. *Physical aging in amorphous polymers and other materials* in (1978).

177. Mazurin, O. Relaxation phenomena in glass. *Journal of Non-Crystalline Solids* **25,** 129–169 (1977).

178. McKenna, G. B. On the physics required for prediction of long term performance of polymers and their composites. *Journal of Research-National Institute of Standards and Technology* **99,** 169–169 (1994).

179. Hodge, I. M. Enthalpy relaxation and recovery in amorphous materials. *Journal of Non-Crystalline Solids* **169,** 211–266 (1994).

180. Avramov, I. Kinetics of structural relaxation of glass-forming melts. *Thermochimica acta* **280,** 363–382 (1996).

181. Dyre, J. C. Colloquium: The glass transition and elastic models of glass-forming liquids. *Reviews of modern physics* **78,** 953 (2006).

182. Kob, W. & Andersen, H. C. Testing mode-coupling theory for a supercooled binary Lennard-Jones mixture. *Transport Theory and Statistical Physics* **24,** 1179–1198 (1995).

183. Ingebrigtsen, T. S., Dyre, J. C., Schrøder, T. B. & Royall, C. P. Crystallization instability in glass-forming mixtures. *Physical Review X* **9,** 031016 (2019).

184. Pedersen, U. R., Schrøder, T. B. & Dyre, J. C. Phase diagram of Kob-Andersen-type binary Lennard-Jones mixtures. *Physical review letters* **120,** 165501 (2018).

185. Bell, I. H., Dyre, J. C. & Ingebrigtsen, T. S. Excess-entropy scaling in supercooled binary mixtures. *Nature communications* **11,** 1–12 (2020).

186. Powles, J., Rickayzen, G & Heyes*, D. Temperatures: old, new and middle aged. *Molecular Physics* **103,** 1361–1373 (2005).

187. Nielsen, J. K. & Dyre, J. C. Fluctuation-dissipation theorem for frequency-dependent specific heat. *Physical Review B* **54,** 15754 (1996).

188. Bailey, N., Ingebrigtsen, T., Hansen, J. S., Veldhorst, A., Bøhling, L., Lemarchand, C., Olsen, A., Bacher, A., Costigliola, L., Pedersen, U., *et al.* RUMD: A general purpose molecular dynamics package optimized to utilize GPU hardware down to a few thousand particles. *SciPost Physics* **3,** 038 (2017).

Declaration of co-authorship

Co-authors should fulfill the requirements of the Vancouver rules

1. Title of article *Single parameter aging in a binary Lennard-Jones system*

2. Declaration of the individual elements

The extent of the candidate's contribution to the article is assessed on the following scale.

   A. has contributed to the work (0-33\%)

   B. has made a substantial contribution (34-66\%)

   C. did the majority of the work (67-100\%)

Saeed   Trond   Jeppe

	Author 1	Author 2	Author 3	Author 4	Author 5
1. Formulation in the concept phase of the basic scientific problem on the basis of theoretical questions which require clarification, including a summary of the general questions which it is assumed will be answered via analyses or actual experiments/investigations.	A,B or C A	A,B or C A	A,B or C C	A,B or C	A,B or C
2. Planning of experiments/analyses and formulation of investigative methodology in such a way that the questions asked under (1) can be expected to be answered, including choice of method and independent methodological development.	A,B or C A	A,B or C A	A,B or C C	A,B or C	A,B or C
3. Involvement in the analysis or the actual experiments/investigation.	A,B or C C	A,B or C A	A,B or C B	A,B or C	A,B or C
4. Presentation, interpretation and discussion of the results obtained in the form of an article or manuscript.	A,B or C B	A,B or C A	A,B or C B	A,B or C	A,B or C

3. Signatures

Date	Name	Author #	Signature
14/6-22	Saeed Mehri	1	Saeed Mehri
19/6-22	Trond Ingebrigtsen	2	Trond Ingebrigtsen
14/6-22	Jeppe Dyre	3	Jeppe Dyre

ROSKILDE UNIVERSITY
Roskilde Doctoral Schools (RDS)

RUC

Declaration of co-authorship

Co-authors should fulfill the requirements of the Vancouver rules

1. Title of article *Predicting nonlinear physical aging of glasses from equilibrium*

2. Declaration of the individual elements *relaxation via the material time*

The extent of the candidate's contribution to the article is assessed on the following scale.

- A. has contributed to the work (0-33\%)
- B. has made a substantial contribution (34-66\%)
- C. did the majority of the work (67-100\%)

	Saeed Author 1	Trond Author 2	Tina Author 3	Jeppe Author 4	Kristine Author 5
1. Formulation in the concept phase of the basic scientific problem on the basis of theoretical questions which require clarification, including a summary of the general questions which it is assumed will be answered via analyses or actual experiments/investigations.	A,B or C A	A,B or C A	A,B or C B	A,B or C B	A,B or C B
2. Planning of experiments/analyses and formulation of investigative methodology in such a way that the questions asked under (1) can be expected to be answered, including choice of method and independent methodological development.	A,B or C A	A,B or C A	A,B or C B	A,B or C B	A,B or C B
3. Involvement in the analysis or the actual experiments/investigation.	A,B or C B	A,B or C A	A,B or C A	A,B or C B	A,B or C B
4. Presentation, interpretation and discussion of the results obtained in the form of an article or manuscript.	A,B or C A	A,B or C A	A,B or C A	A,B or C B	A,B or C B

3. Signatures

Date	Name	Author #	Signature
14/6 - 22	Saeed Mehri	3	Saeed Mehri
14/6 - 22	Trond Ingebrigtsen	4	Trond Ingebrigtsen
15/6 - 22	Tina Hecksher	5	
14/6 - 22	Jeppe Dyre	6	Jeppe Dyre
15/6 - 22	Kristine Niss	7	Kristine Niss

ROSKILDE UNIVERSITY
Roskilde Doctoral Schools (RDS)

RUC

Declaration of co-authorship

Co-authors should fulfill the requirements of the Vancouver rules

1. Title of article *Lines of invariant physics in the isotropic phase of the*

2. Declaration of the individual elements *discotic Gay-Berne model.*

The extent of the candidate's contribution to the article is assessed on the following scale.

   A. has contributed to the work (0-33\%)
   B. has made a substantial contribution (34-66\%)
   C. did the majority of the work (67-100\%)

Saeed Muh. Jeppe Trond

	Author 1	Author 2	Author 3	Author 4	Author 5
1. Formulation in the concept phase of the basic scientific problem on the basis of theoretical questions which require clarification, including a summary of the general questions which it is assumed will be answered via analyses or actual experiments/investigations.	A,B or C B	A,B or C A	A,B or C A	A,B or C C	A,B or C
2. Planning of experiments/analyses and formulation of investigative methodology in such a way that the questions asked under (1) can be expected to be answered, including choice of method and independent methodological development.	A,B or C B	A,B or C A	A,B or C A	A,B or C C	A,B or C
3. Involvement in the analysis or the actual experiments/investigation.	A,B or C C	A,B or C B	A,B or C A	A,B or C B	A,B or C
4. Presentation, interpretation and discussion of the results obtained in the form of an article or manuscript.	A,B or C C	A,B or C A	A,B or C A	A,B or C B	A,B or C

3. Signatures

Date	Name	Author #	Signature
14/6 -22	Saeed Mehri	1	Saeed Mehri
14.6.22	Mohamed Kolmangadi	2	K. Joseph
14/6 -22	Jeppe Dyre	3	Jeppe Dyre
14/6 -22	Trond Ingebrigtsen	4	Trond Ingebrigtsen

ROSKILDE UNIVERSITY
Roskilde Doctoral Schools (RDS)

RUC

Declaration of co-authorship

Co-authors should fulfill the requirements of the Vancouver rules

1. Title of article *Hidden scale invariance in the Gay-Berne model*

2. Declaration of the individual elements

The extent of the candidate's contribution to the article is assessed on the following scale.

A. has contributed to the work (0-33\%)
B. has made a substantial contribution (34-66\%)
C. did the majority of the work (67-100\%)   *Saeed   Jeppe   Trond*

	Author 1	Author 2	Author 3	Author 4	Author 5
1. Formulation in the concept phase of the basic scientific problem on the basis of theoretical questions which require clarification, including a summary of the general questions which it is assumed will be answered via analyses or actual experiments/investigations.	A,B or C B	A,B or C A	A,B or C C	A,B or C	A,B or C
2. Planning of experiments/analyses and formulation of investigative methodology in such a way that the questions asked under (1) can be expected to be answered, including choice of method and independent methodological development.	A,B or C B	A,B or C A	A,B or C C	A,B or C	A,B or C
3. Involvement in the analysis or the actual experiments/investigation.	A,B or C AC	A,B or C A	A,B or C B	A,B or C	A,B or C
4. Presentation, interpretation and discussion of the results obtained in the form of an article or manuscript.	A,B or C C	A,B or C A	A,B or C B	A,B or C	A,B or C

3. Signatures

Date	Name	Author #	Signature
14/6-22	Saeed Mehri	1	Saeed Mehri
14/6-22	Jeppe Dyre	2	Jeppe Dyre
14/6-22	Trond Ingebrigtsen	3	Trond Ingebrigtsen

ROSKILDE UNIVERSITY

Roskilde Doctoral Schools (RDS)

RUC

Declaration of co-authorship

Co-authors should fulfill the requirements of the Vancouver rules

1. Title of article *Single parameter aging in the weakly nonlinear limit*

2. Declaration of the individual elements

The extent of the candidate's contribution to the article is assessed on the following scale.

- A. has contributed to the work (0-33\%)
- B. has made a substantial contribution (34-66\%)
- C. did the majority of the work (67-100\%)

	Author 1	Author 2	Author 3	Author 4	Author 5
1. Formulation in the concept phase of the basic scientific problem on the basis of theoretical questions which require clarification, including a summary of the general questions which it is assumed will be answered via analyses or actual experiments/investigations.	A,B or C A	A,B or C A	A,B or C C	A,B or C	A,B or C
2. Planning of experiments/analyses and formulation of investigative methodology in such a way that the questions asked under (1) can be expected to be answered, including choice of method and independent methodological development.	A,B or C A	A,B or C A	A,B or C C	A,B or C	A,B or C
3. Involvement in the analysis or the actual experiments/investigation.	A,B or C C	A,B or C A	A,B or C B	A,B or C	A,B or C
4. Presentation, interpretation and discussion of the results obtained in the form of an article or manuscript.	A,B or C B	A,B or C A	A,B or C B	A,B or C	A,B or C

3. Signatures

Date	Name	Author #	Signature
14/6 – 22	Saeed Mehri	1	Saeed Mehri
15/6 – 22	LORENZO COSTIGLIOLA	2	Lorenzo Costigliola
14/6 – 22	Jeppe Dyre	3	Jeppe Dyre